

NASA CR-134596



FRACTURE CONTROL METHODS FOR SPACE VEHICLES

Volume I

Fracture Control Design Methods

By
A. F. Liu

REPRODUCED BY
**NATIONAL TECHNICAL
INFORMATION SERVICE**
U. S. DEPARTMENT OF COMMERCE
SPRINGFIELD, VA. 22161

Prepared for

NATIONAL AERONAUTICS AND SPACE ADMINISTRATION

NASA Lewis Research Center

Contract NAS 3-16765

N74-35279

Unclas
51052

G3/31

(NASA-CR-134596) FRACTURE CONTROL METHODS
FOR SPACE VEHICLES. VOLUME 1: FRACTURE
CONTROL DESIGN METHODS Contractor
Report, (Rockwell International Corp.,
Downey, Calif.) CSC1 22B

FRACTURE CONTROL METHODS
FOR
SPACE VEHICLES

Volume I
Fracture Control Design Methods

by

A. F. Liu

Contract NAS3-16765
NASA Lewis Research Center
Cleveland, Ohio

August 1974

1. Report No. NASA CR-134596	2. Government Accession No.	3. Recipient's Catalog No.	
4. Title and Subtitle Fracture Control Methods for Space Vehicles Volume I, Fracture Control Design Methods		5. Report Date August 1974	
		6. Performing Organization Code	
7. Author(s) A.F. Liu		8. Performing Organization Report No. SD 73-SH-0171-1	
		10. Work Unit No.	
9. Performing Organization Name and Address Space Division Rockwell International Corporation Downey, CA 90241		11. Contract or Grant No. NAS 3-16765	
		13. Type of Report and Period Covered Contractor Report June 1972 through March 1974	
12. Sponsoring Agency Name and Address National Aeronautics and Space Administration 21000 Brookpark Rd. Lewis Research Center, Cleveland, OH 44135		14. Sponsoring Agency Code	
15. Supplementary Notes Project Manager, Gordon T. Smith NASA Lewis Research Center Cleveland, OH 44135			
16. Abstract This report is concerned with a systematic approach for applying methods for fracture control in the structural components of space vehicles. Four major steps are required to complete the fracture control sequence. The first step is to define the primary load-carrying structural elements and the type of load, environment, and design stress levels acting upon them. The second step is to identify the potential fracture-critical parts by means of a selection logic flow diagram. The third step is to evaluate the safe-life and fail-safe capabilities of the specified part. The last step in the sequence is to apply the control procedures that will prevent damage to the fracture-critical parts. The fracture control methods discussed herein include fatigue design and analysis methods, methods for preventing crack-like defects, fracture mechanics analysis methods, and nondestructive evaluation methods; however, emphasis is placed on the fracture mechanics analysis methods. To illustrate the use of fracture mechanics methodology, an example problem is presented for evaluation of the safe-crack-growth capability of the Space Shuttle crew compartment skin structure. <p style="text-align: right;">PRICES SUBJECT TO CHANGE</p>			
17. Key words (Suggested by Author(s)) Fracture Mechanics Space Vehicle Structure Fracture Control Procedures		18. Distribution Statement Unclassified, Unlimited	
19. Security Classif. (of this report) Unclassified	20. Security Classif. (of this page) Unclassified	21. No. of Pages	22. Price*

FOREWORD

The work described in this report was performed by the Space Division of Rockwell International Corporation under Contract NAS3-16765, Fracture Control Methods for Space Shuttle Vehicles, for the Lewis Research Center of the National Aeronautics and Space Administration. The investigation was conducted under the technical direction of Mr. Gordon T. Smith of NASA/LeRC. The project study manager at the Space Division of Rockwell International Corporation was Mr. A. F. Liu, with Dr. Paul C. Paris of Del Research Corporation and Dr. Matthew Creager of Del West Associates, Inc., acting as primary technical consultants.

This report consists of three volumes:

Volume I. Fracture Control Design Methods (prepared by A. F. Liu)

Volume II. Assessment of Fracture Mechanics Technology for Space Shuttle Applications (prepared by R. M. Ehret)

Volume III. Space Shuttle Configurations (prepared by A. F. Liu and E. J. Mulcahy)

Mr. James E. Collipriest, Jr., provided overall technical guidance in the preparation of Volume II. Mr. Edward J. Mulcahy and Mr. A. S. Musicman contributed significantly to the preparation of Section 1.1 (Space Shuttle Vehicle Structural Description) of Volume I. Mr. John Mamon and Mr. F. Stuckenberg aided substantially in the preparation of the nondestructive evaluation sections in Volumes I and II. Mr. R. E. O'Brien and Mr. R. M. Ehret contributed, respectively, Section 2.2 (Prevention of Cracks and Crack-Like Defects in Shuttle Vehicle Structure) and Section 2.3.8 (Required Material Properties Data for Space Shuttle Fracture Mechanics Analysis) of Volume I. Dr. Matthew Creager contributed Section 2.3.6 (Failure Under Complex Loading Conditions) and Section 2.3.7.4 (Damage Tolerance Analysis for Pressure Vessels) of Volume I and Section 2.2 (Thin Sheet Behavior) and a discussion of fracture behavior under combined in-plane loading in Section 1.2 (Linear Elastic Concepts of Fracture Behavior) of Volume II.

Mr. R. W. Westrup prepared the original proposal response to the RFP and established the basic frame work for the study program. The managerial guidance provided by Mr. R. P. Olsen, Engineering Manager, Materials and Processes, Space Division, is acknowledged by the authors.

CONTENTS

Section		Page
	INTRODUCTION	1
1.0	APPRAISAL OF SPACE SHUTTLE VEHICLE STRUCTURES	3
	1.1 Space Shuttle Vehicle Structural Description	3
	1.1.1 Solid Rocket Booster	4
	1.1.2 External Tank	5
	1.1.3 Mid Fuselage	7
	1.1.4 Wing	8
	1.1.5 Forward Fuselage and Crew Compartment	9
	1.1.6 Aft Fuselage	11
	1.1.7 Vertical Stabilizer	11
	1.1.8 Landing Gear	12
	1.2 Critical Part Selection Logic	27
	1.2.1 Loss of Assembly (Step 4)	27
	1.2.2 Loss of Vehicle (Step 6)	29
	1.2.3 Redundant Member or Multiload Path (Step 5)	29
	1.2.4 Accessibility Requirements (Step 9)	29
	1.2.5 Evaluation of Potentially Fracture- Critical Parts (Step 7)	30
	1.2.6 Critical Part Selection Logic Application Examples	31
2.0	FRACTURE CONTROL METHODS	33
	2.1 Fatigue Design and Analysis Methods	35
	2.1.1 Fatigue Performance	35
	2.1.2 Detail Design Considerations	39
	2.1.3 Fatigue Analysis Methods	46
	2.2 Prevention of Cracks and Crack-Like Defects in Space Vehicle Structure	49
	2.2.1 Administrative Controls and Activities	49
	2.2.2 Technical Activities	50
	2.3 Fracture Control Methods for Initially Cracked Structures	52
	2.3.1 Safe-Crack-Growth and Fail-Safe Structures	53

Section	Page
2.3.2 Classification of Space Shuttle Structural Elements	55
2.3.3 Monolithic Structure	55
2.3.4 Crack Arrest Structure	95
2.3.5 Multiple Element Structure	116
2.3.6 Failure Under Complex Loading Conditions	122
2.3.7 Failure of Pressure Vessels and Shells	125
2.3.8 Required Material Property Data for Space Shuttle Fracture Mechanics Analysis	150
2.3.9 Recommendations on Fracture Mechanics Research and Development	152
2.4 Nondestructive Evaluation	153
3.0 FRACTURE CONTROL PROCEDURES	181
3.1 Fracture Mechanics Procedure	181
3.2 An Example Problem	185
3.2.1 Design Stress Level, Material and Structural Dimensions	185
3.2.2 Crack Geometry	187
3.2.3 Stress Intensity Factors	190
3.2.4 Initial Crack Lengths	194
3.2.5 Crack Growth Predictions	194
4.0 SUMMARY AND RECOMMENDATIONS	203
5.0 REFERENCES.	205
APPENDIX SYMBOLS AND SUBSCRIPTS.	215

ILLUSTRATIONS

Figure		Page
1-1	Critical Part Selection Logic	28
2-1	Fracture Control Program Elements	34
2-2	Elements for Fatigue Design and Analysis	36
2-3	Double-Scarf Joint Specimen	40
2-4	Double-Shear Joint Specimen	41
2-5	Stepped Double Shear Joint Specimen	42
2-6	Plain-Scarf Joint Specimen	43
2-7	Single-Shear Joint Specimen	44
2-8	Continuous Member Tension Design	45
2-9	Examples for the Definition of GAG Cycle	47
2-10	Comparison of Fatigue Crack Growth Characteristics for Monolithic Structure and Crack Arrest Structure	56
2-11	Comparison of Fatigue Crack Growth Characteristics for Monolithic Structure and Multiple Element Structure	57
2-12	Crack Growth Characteristics Under Monotonic Increasing Load	58
2-13	Cross-Sectional Views of Common Crack Geometries	61
2-14	Through-the-Thickness Crack Loaded in Tension	62
2-15	Stress Intensity Factors for Eccentrically Cracked Plate	64
2-16	Through-the-Thickness Edge Crack in a Plate Loaded in Tension	65
2-17	Failure Analysis Using an R-Curve	67
2-18	R-Curves for Aluminum Alloys	69
2-19	Failure of Aluminum Alloy Sheets Predicted From R-Curve	70
2-20	Fracture Toughness of Bare 2024-T3 Sheets	71
2-21	Geometries of Truncated Elliptical Cracks	75
2-22	Front Free Surface Influence Factor M_1	78
2-23	Front Surface Influence Factor M_1'/ϕ for $a/c \leq 1$	79
2-24	Front Surface Influence Factor M_1'/ϕ for $a/c \geq 1$	80
2-25	Change of Flaw Shape in Propagation of Surface Crack	82
2-26	Surface Flaw Fatigue Crack Propagation Data	84
2-27	Free Surface Correction Factor for Corner Flaw	87
2-28	Crack or Cracks Emanating From a Hole	89

Figure		Page
2-29	Flaw Shape Factor M/ϕ	90
2-30	Bowie's Factors for Influence of a Hole	91
2-31	Stress Intensity Factor Versus Crack Length for a Lug	93
2-32	Stress Intensity Factor for a Pin-Loaded Hole	94
2-33	Through- the-Thickness Cracks in Skin-Stiffened Panel	96
2-34	Stress Intensity Analysis of Unstiffened and Stiffened Structure	98
2-35	Stress Intensity Factor for Crack Extending Equally on Both Sides of Point Midway Between Two Stringers (NASA TR R-358)	99
2-36	Stress Intensity Factor for Crack Extending Equally on Both Sides of Stringer (NASA TR R-358)	100
2-37	Stiffener Stiffness Parameter as a Function of Effective Stiffener Area	102
2-38	Stiffener Efficiency Factor for a One-Bay Crack as a Function of Stiffener Stiffness Parameter	104
2-39	Stiffener Efficiency Factor for a Crack Extended Symmetrically on Both Sides of a Stringer	106
2-40	Effects of Applied Stress Levels on the Stiffener Efficiency.	107
2-41	The Effects of Broken Stiffener and Stiffener Yielding on Crack Tip Stress Intensity	109
2-42	The Effect of Broken Stiffener on the Stress Intensity Factor	110
2-43	The Effect of Broken Stiffener on the Stress Intensity Factor	112
2-44	Stiffener Efficiency Factor for a Two-Bay Crack With a Center Broken Stiffener	113
2-45	Design Curves for Reinforced Flat Panels	114
2-46	Relationship Between Stress Intensity Factor and Crack Length for Panel With Integral Stiffeners	117
2-47	Stress Distribution Across a Three-Plank Fail-Safe Test Panel With the Middle Plank Broken.	119
2-48	Effective Width in Side Planks for Flat Panels With Longitudinal Splices	121
2-49	Failure Under Combined Tension and Shear	124
2-50	Evaluation of Bowie Factor for Biaxial Loading.	126
2-51	Paris Failure Criteria for Cylindrical Pressure Vessels With Axial Through- the-Thickness Crack	128
2-52	Hahn's Failure Criteria for Cylindrical Pressure Vessels With Axial Through- the-Thickness Crack	130
2-53	Curvature Effect Coefficients in Symmetrically Loaded Shells	133

Figure		Page
2-54	Curvature Effect Coefficients in Symmetrically Loaded Shells	134
2-55	Curvature Effect Coefficients in Shells Under Torsion	136
2-56	The Membrane Stress Singularities for a Cylindrical Shell Containing an Axial Crack ($N_0 = 0$, $M = 0$), Comparison of Three Analytical Results	137
2-57	Stress Intensity Multiplication Factor for Axially Cracked Cylindrical Shell	138
2-58	Stress Intensity Multiplication Factor for Circumferentially Cracked Shell.	140
2-59	Plastic Zone Instability Failure Strength of Pressure Vessels	141
2-60	Thickness Versus Design Life	144
2-61	Initial Flaw Size Determination	144
2-62	Initial and Critical Flaws.	146
2-63	Typical Transition Criteria	146
2-64	Fatigue Crack Propagation Rate Representations	147
2-65	Crack Growth Calculation	149
3-1	Fracture Control Functions	182
3-2	Missions to Failure as a Function of Applied Stress Levels and Crack Geometry.	184
3-3	Effect of Initial Flaw Size on Wing Weight for Safe-Life (B-9U Booster)	184
3-4	Crew Compartment Configuration	186
3-5	Crack Geometries	188
3-6	Stress Intensity Factor for Integrally Stiffened Skin	192
3-7	Stress Intensity Factor for Integrally Stiffened Skin	193
3-8	Stress Intensity Factor for Integrally Stiffened Skin	195
3-9	Predicted Fatigue Crack Growth History for a Longitudinal Crack in the Crew Compartment Skin.	197
3-10	Predicted Fatigue Crack Growth History for a Circumferential Crack in the Crew Compartment Skin	198
3-11	Predicted Fatigue Crack Growth History for a Circumferential Crack at Bottom of an Integral Stiffener in the Crew Compartment Skin	199
3-12	Predicted Fatigue Crack Growth History for Crack Emanating from Rivet Hole	200

TABLES

Table		Page
1-1	Space Shuttle Orbiter Reusable Tankages	14
1-2	Space Shuttle Solid Rocket Booster (SRB)	16
1-3	Space Shuttle Orbiter External Tank System	17
1-4	Space Shuttle Orbiter Mid Fuselage	18
1-5	Space Shuttle Orbiter Wing	20
1-6	Space Shuttle Orbiter Crew Cabin and Forward Fuselage	21
1-7	Space Shuttle Orbiter Aft Fuselage	22
1-8	Space Shuttle Orbiter Vertical Stabilizer and Rudder	24
1-9	Space Shuttle Orbiter Landing Gears	25
2-1	Classification of Cracked Structure	59
2-2	Comparison Between the Actual and the Predicted Values for Fracture Tests of X7475-T61 Aluminum Panels	73
2-3	Orbiter Reusable Tankage Structural Elements and Applicable NDE Methods	156
2-4	Solid Rocket Booster Structural Elements and Applicable NDE Methods	158
2-5	External Tank Structural Elements and Applicable NDE Methods	160
2-6	Mid Fuselage Structural Elements and Applicable NDE Methods	164
2-7	Wing Structural Elements and Applicable NDE Methods	167
2-8	Crew Cabin and Forward Fuselage Structural Elements and Applicable NDE Methods	169
2-9	Aft Fuselage Structural Elements and Applicable NDE Methods	172
2-10	Vertical Stabilizer and Rudder Structural Elements and Applicable NDE Methods	175
2-11	Main and Nose Landing Gears Structural Elements and Applicable NDE Methods	177
2-12	Crack Detection Capabilities	180
3-1	Safe-Crack-Growth Predictions for Crew Compartment Skin	201

PRECEDING PAGE BLANK NOT FILMED

INTRODUCTION

The development of an effective system to prevent premature fracture of aerospace vehicle structures resulting from cracks or crack-like defects is an area of deep concern and extensive effort by both Air Force and NASA agencies. This concern has been stimulated by failures in recent years, some of them catastrophic, on high-performance aircraft in operational service and on some space vehicles during test.

When this problem is considered with respect to the Space Shuttle, it is apparent that failures of this type are intolerable because of the limited number of vehicles to be constructed and the resulting programmatic, economic, and political consequences of such a failure. It is absolutely essential that an effective fracture control system be developed for application to the Shuttle. This requirement presents significant challenges because of the unprecedented service environments of ascent and atmospheric entry applied to a reusable manned vehicle. At the same time, a high sensitivity exists between payload weight and vehicle structural weight. Therefore, an overly conservative design approach is not an acceptable solution to fracture control.

The objectives of this study were to provide an organized review and evaluation of current technology applicable to space vehicle fracture control and to apply the most appropriate methods and data defined by this review to obtain an early identification of fracture control requirements and procedures that will be compatible with the attainment of high structural efficiency for space vehicles. This study is therefore considered to be a vital part of Shuttle development. Early evaluation of the fracture problem is essential so that the most effective and efficient selections can be made in terms of fracture control approach, structural materials, and design configuration. If fracture control considerations are not integrated with other design requirements early in the design phase, it may be difficult to achieve either an efficient structure or an effective fracture control program.

The scope of effort included in this study program was (1) to identify the fracture critical elements of the Space Shuttle vehicle and (2) to assess the capabilities of current fracture mechanics technology to provide adequate analysis methods and data and effective fracture control procedures. The study effort was divided into four major technical task areas.

Task I involved establishing basic configurations for Shuttle vehicle stages to serve as a reference for the study, identifying and characterizing all major load-carrying structural elements of these configurations, determining service load and environments for these elements, and defining the types of fracture control requirements and information to be considered in subsequent phases of the study.

Concurrent with this effort, Task II was performed to review fracture mechanics technology and other fracture prevention concepts that are applicable to Space Shuttle fracture control requirements. The technology areas selected for consideration were directed toward the structural configurations, materials, loadings, environments, and general fracture control requirements identified in Task I. Problems, uncertainties, and limitations associated with current fracture mechanics concepts and methods were identified, and the sensitivity of Shuttle design to these factors was assessed.

Task III consisted of reviews and evaluations of currently available methods to achieve fracture control. It was primarily concerned with defining the manner in which the technical concepts and methods of Task II are used in practical application to the types of structural elements and environments identified in Task I so as to achieve fracture control objectives. General definition of these methods, as well as the specific characterization and evaluation of relative merits, suitability for various types of structure, and deficiencies or uncertainties present were accomplished.

Task IV is the final phase of the study; it summarized a recommended fracture control plan for the Space Shuttle and identified areas where fracture technology development is needed to support the Shuttle program. The task involved detailed fracture analyses of critical structural elements, using the most appropriate fracture analysis and fracture control methods, as determined from the results of Tasks II and III. Results of these analyses were used to establish specific fracture control requirements for each structural element and to define technology development requirements.

1.0 APPRAISAL OF SPACE SHUTTLE VEHICLE STRUCTURES

The primary purpose of this task is to identify the potential fracture critical structural elements in the Space Shuttle vehicle and to describe the structural characteristics, environments, and loadings applicable to each of these elements. Preliminary design drawings for each major structural component in the Space Shuttle vehicle are provided in Volume III (Space Shuttle Configurations) of this report. The structural elements are identified by numbers, and the detailed descriptions of each of the elements are listed in Tables 1-1 to 1-9 in this volume (page 14). The criticality classification of these structural elements was determined by using a systematically constructed Critical Part Selection logic diagram. The philosophy and applicability of this logic diagram are discussed in Section 1.2.

1.1 SPACE SHUTTLE VEHICLE STRUCTURAL DESCRIPTION

The current Space Shuttle concept involves a flyback orbiter vehicle mounted on top of a large, expendable, liquid oxygen/hydrogen propellant tank (called the external tank). Additional thrust for liftoff and a portion of the ascent trajectory is provided by two solid rocket motors (SRB) mounted to the sides of the external tank (ET). Under the current concept, the SRB's are recoverable and reusable; parachutes are used to control water impact attitude and velocity. The orbiter vehicle is separated from the external liquid propellant tank after orbit insertion. The tank is not recovered. Figure 1.1.1 of Volume III shows a view of the current configuration. Major orbiter components and equipment are listed in Figure 1.1.2 and their locations are identified in Figures 1.1.3 and 1.1.4. The structural configurations described in these figures and in this volume are based on preliminary design information available as of (on or before) June 1973. Some of the structural configurations, design stress levels, and design environments may have been changed or will be changed in the future.

The Space Shuttle orbiter is conveniently divided into six component assemblies, as follows:

1. Mid fuselage
2. Wing
3. Forward fuselage and crew compartment
4. Aft fuselage
5. Vertical stabilizer and rudder
6. Nose and main landing gears

In addition to the primary load carrying structures in the orbiter, more than 30 pressure vessels are located inside the orbiter to supply propellant or fuel for the following orbiter subsystems:

1. Electrical power
2. Mechanical power (auxiliary power unit)
3. Environmental control and life support
4. Propulsion
 - a. Main propulsion
 - b. Orbital maneuvering
 - c. Reaction control
 - d. Airbreathing propulsion

The geometries, operating pressure levels, and failure consequences for these pressurized tankages are summarized in Table 1-1.

General descriptions of the SRB, the external tank, and the orbiter structural arrangements are given in the following sections. Characterization of specific structural elements in these structural assemblies are summarized in Tables 1-2 to 1-9. The structural elements in each part were numbered (e. g. , 5-1 for wing skin, 8-11 for rudder honeycomb panel, etc.) and identified on the drawings in Figures 1.2.1 to 1.9.2 (Volume III). The materials, product form, environment, loading conditions, and approximate design stress levels for each of these elements are given in Tables 1-1 to 1-9.

1.1.1 Solid Rocket Booster (Table 1-2 and Figures 1.2.1 to 1.2.3 in Volume III)

The main structural element of the solid rocket booster is the motor case. The 3.6-meter (142-inch) diameter cylindrical section of the case is comprised of segments mechanically joined to obtain a length of 34.5 meters (1358 inches). The segments are fabricated from D6-AC steel to a thickness of approximately 1.27 centimeters (one-half inch) by the shear forming process. Segment splicing is implemented by a tongue-and-groove joint secured with shear pins.

A cylindrical shell structure with a conical nose fairing is attached to the forward end of the motor case. This assembly contains provisions for attachment and thrust transfer to the external tank and houses the recovery system. A cylindrical shell and flared cone assembly is attached to the aft end of the motor case to provide aerodynamic fairing for the gimballed nozzles.

1.1.2 External Tank (Table 1-3 and Figure 1.3.1 in Volume III)

The external tank contains all of the propellants for the Shuttle main propulsion system and also houses and supports related subsystems components. The tank is of circular cross-section with 7.7-meter (304-inch) maximum diameter. The total external tank is comprised of three major structural assemblies; the LO₂ tank, the LH₂ tank, and an intertank assembly. These components are discussed in more detail in the following sections.

1.1.2.1 LO₂ Tank

The LO₂ tank is a ring-stiffened monocoque structure of 2219 aluminum alloy; skin panels, rings, and bulkhead gores are joined by fusion welding. The forward portion of the tank is of ogive shape to provide satisfactory aerodynamic contour. The ogive extends from a forward ring 1.04 meters (41 inches) in diameter to a point where it becomes tangent to the basic 7.7-meter (304-inch) diameter of the cylindrical portion of the tank. The ogive is fabricated from five panels of 2219-T87 aluminum alloy, which are explosive formed to the desired contour and are joined by longitudinal fusion welds. The forward ring is a machined member of 2219 aluminum fusion-welded to the ogive shell. It provides for bolted attachment of the forward dome of the LO₂ tank and the deorbit motor support structure. A shell stability ring is provided at the junction of ogive and cylindrical shells and is joined to these segments of the tank shell by circumferential fusion welds.

The aft bulkhead is of ellipsoidal contour, with an aspect ratio of 0.75. It is a welded assembly of 2219-T87 aluminum alloy. Six gore panels are explosive-formed to the desired contour and chem-milled to provide the desired weld land reinforcement and variation of membrane thickness over the surface. The gores are then joined by welding to form the complete bulkhead shell. The LO₂ feedline outlet and an access cover are incorporated in the aft bulkhead assembly. The bulkhead is attached to the cylindrical wall by a circumferential weld joint to a Y-ring member. The Y-ring also provides for attachment of the inter-tank shell structure. The Y-ring will either be a roll ring forging or a component made of plate segments rolled to contour and joined by welding to form a complete ring.

Structural temperatures in the LO₂ tank will vary from -183C (-297F) for portions in contact with liquid oxygen to 121C (+250F) on the forward shell structure at the time of deorbit. The forward portion of the tank is protected from ascent heating by cork ablative insulation. The temperature of 121C represents the maximum allowable bondline temperature between the cork and the aluminum wall.

1.1.2.2 LH₂ Tank

The LH₂ tank is a cylindrical shell of basic ring-stiffened monocoque construction. The cylindrical skin sections are welded assemblies of 2219-T87 aluminum alloy. Major ring frames are provided at the orbiter and SRB aft attachment point; the orbiter forward attachment point; and the orbiter thrust assembly support points. Smaller stability rings are provided at the remaining cylinder segment joints. The end bulkheads are ellipsoidal domes of the same shape and basic construction as the LO₂ tank aft bulkhead.

Integral longitudinal stiffening is provided only in the local region associated with the transfer of orbiter thrust loads to the LH₂ tanks. The thrust longerons are forged members of 7075-T73 aluminum alloy, bolted into one of the cylindrical shell segments. The adjacent skin panels incorporate integral longitudinal stiffness to meet the stability requirements of the high local shear and compression stresses associated with the orbiter thrust transfer.

The outer surface of the LH₂ tank is covered with spray-on foam insulation (SOFI) to limit the heat transfer to the liquid hydrogen during pad hold and initial ascent. However, in areas of high interference heating it is expected that the SOFI will be degraded during the ascent trajectory, and the structural temperature may increase to a maximum of 260C (500F) at the time of deorbit. But, the tank internal pressure at this time is much less than the design value; the present mission operations plan provides for depressurization of the tanks immediately after completion of the orbit insertion burn. The maximum structural temperature expected at the time of tank depressurization is approximately 93C (200F).

1.1.2.3 Intertank

The intertank assembly maintains the structural shell continuity between the LO₂ and LH₂ tanks and provides for thrust load transfer from the solid rocket boosters (SRB's). It is of conventional semimonocoque construction, employing 2024-T86 aluminum alloy as the primary material. Skin panels are machined from plate stock of this alloy to incorporate integral longitudinal stiffness. A major ring frame is provided at the SRB forward attach point to accept normal and tangential loads from the boosters. Additional stability frames are provided at approximately 1.016-meter (40-inch) spacing. These ring frames are of conventional construction of built-up 2024 aluminum alloy in the appropriate temper. Thrust longerons are located on each side of the intertank to accept the concentrated forces from the SRB and to distribute the load to the shell structure. These members are forgings, probably of 7075-T73 aluminum alloy.

Cork insulation is applied on the external surface in local areas as required to protect from interference heating effects resulting from the proximity of the SRB's. Structural temperatures will be limited to a maximum of 176C (350F); however, the temperature at the time of maximum thrust load transfer from the SRB's will be much lower.

1.1.3 Mid Fuselage (Table 1-4 and Figures 1.4.1 to 1.4.12 in Volume III)

The mid fuselage section is designed around the cargo payload requirements of an envelope. A minimum clearance of 7.62 centimeters (three inches) is maintained around the envelope. Alternate attachment locations are provided to accommodate variations in cargo sizes. The entire structure is covered with a thermal protection system (TPS).

The mid fuselage is a conventional semimonocoque shell construction, fabricated from 2024 aluminum alloy and consisting of skin panels, stringers, longerons, and frames. The lower section of the fuselage is the primary structural element. Body bending and shear and torsion loads from the wing, nose, and aft fuselage sections are reacted by the shell. Conventional fasteners are used for assembly. The cargo bay doors do not react any of the body loadings except torsion.

The mid fuselage is a U-shaped structure approximately 5.33 meters (17.5 feet) wide, 3.96 meters (13 feet) high, 18.89 meters (62 feet) long, and weighs approximately 6350.4 kilograms (14,000 pounds). It extends from $X_0=578.0$ to $X_0=1307$ and interfaces with the forward and aft fuselages, the wing structure, and the payload bay doors. (Note: the bulkheads at $X_0=578$ and 1307 are not a part of the mid fuselage task.)

The mid fuselage is also the primary structural attach system for the wings. A multi-spar carry-through structure is built integrally into the lower section. Four truss-type spars, machined from aluminum alloy, serve as fuselage lower frames.

Seventeen frames are located in the mid fuselage structure and are defined in three categories: wing support, glove support, and intermediate frames. Two of the wing support frames and two intermediate frames are in the wing carry-through torque box area ($X_0=1191$ to $X_0=1307$). The remaining 13 frames are forward of the torque box. Fourteen frames are also designed to react payload attachment loads, which are introduced at nine locations between frames.

The structural skin panels are machined integrally stiffened panels. Because of fuselage bending and axial loads, the stringers are located in a longitudinal direction except in the area of the wing ($X_0=1191$ to $X_0=1307$), where they are oriented in the lateral directions, since the wing loads are dominant.

The mid fuselage longerons consist of the sill and lower corner longerons. They are machined from extrusions or plate stock.

Frame support ribs extend longitudinally along the mid fuselage at $Y_0=0.00$ and $Y_0\pm 52.5$ and at two positions on the side. The primary purpose of these ribs is to stabilize the frame inner caps. The $Y_0=0.00$ position rib has diagonal members in each bay between $X_0=578$ through $X_0=1191$. At the other locations, members are provided in random bay positions to clear subsystem equipment.

The glove fairing is a built-up sheet metal subassembly. It will be riveted and bolted to the mid fuselage in final assembly.

The payload bay liner is a coated flexible fabric configuration with bonded peripheral aluminum edge members and elastomeric seals. The liner panels are attached to the inside of the payload bay with mechanical fasteners.

Two large segmented deployable doors cover the payload bay. These doors are designed to carry direct pressure loads only. The doors are hinged near the horizontal reference plane of the payload and open clear of that reference plane. The mating edges of the doors have slotted fairings for stowage of the manipulator arms and thermal protection through the launch and reentry portions of flight. The manipulator deployment and cargo door opening geometry is designed to provide for a full door travel in the event of a failure to release the manipulators from their stowed position. The door design is on the basis of "on-board systems" opening in space or in the vertical position while shielded from wind only. For all other opening cases, GSE is required.

1.1.4 Wing (Table 1-5 and Figures 1.5.1 to 1.5.4 in Volume III)

The wing is of delta planform, with a 45-degree leading edge sweep and a symmetrical NACA 0010-64 airfoil. It has a thickness/chord ratio of 10 percent at the root and 12 percent at the tip, with maximum thickness occurring along the 40-percent chord line. The wing is composed of outer panels and elevons. The outer panels comprise the entire exposed surface of the wing and can be detached at the fuselage interface; this method of attaching the wing to the fuselage is an outgrowth of a producibility/assembly sequence study which revealed major program savings. In addition, the outer panels provide mounting features for the main landing gear and the elevons and their subsystems.

Primary structural members include the skins and ribs, a main front spar, and a main rear spar. The structural arrangement is conventional design, fabricated from 2024 aluminum alloy and covered with a thermal

protective system (TPS). The wing skins are primarily fabricated of sheet metal, stiffened with formed sheet metal hat section stiffeners, riveted together.

The main spars outboard of the fuselage attachment are built-up of machined caps riveted to corrugated webs. This yields a light shear resistant structure that also simplifies the fabrication. The spars are aligned parallel to the fuselage station planes.

The ribs are built-up of tube trusses, except those subject to high loads such as the ribs that carry the elevon hinges or main landing gear. These are constructed similar to the spars.

The elevon is a two-piece structure spanning nearly all of the trailing edge of the wing. It is of aluminum bonded sandwich construction. Provisions have been incorporated into the design for "droop" of the elevon beyond the normal actuation travel, which will allow easy installation or removal of the actuators without having to remove the elevons. In the areas of the elevon/wing gap, hot-structure seals exclude the hot plasmas from the internal structure.

The leading and trailing edges are essentially closeout fairings completing the aerodynamic shape of the wing. They are cantilevered off the forward and rear spars. The skins of the trailing edge section are designed as access panels, which will permit ease of inspection and servicing of the elevon actuation system. For installation and removal of the actuators, access doors are located in the upper skin of the main wing box. Hoisting and jacking points are situated in the wing along the root and tip ribs and are accessible through door panels provided for the wing-to-fuselage mating bolts.

1. 1. 5 Forward Fuselage and Crew Compartment (Table 1-6 and Figures 1. 6. 1 and 1. 6. 2 in Volume III)

The forward fuselage is the primary load-carrying structure forward of the payload bay. Structural support is provided for the crew module, mid fuselage, nose landing gear, and hoisting/jacking provisions. It is a semimonocoque design, fabricated from 2024-T86 aluminum alloy except in the windshield area where high temperature alloys are required. The aluminum structure is covered with a thermal protective system (TPS).

The stretch-formed skins are stiffened by riveted-on stringers, in conventional aircraft fashion. The fuselage frames are either built-up from formed sheet metal or integrally machined in the higher load areas. The aft pressure bulkhead of the crew compartment closes out the forward fuselage at the interface with the mid fuselage, providing structural support for the manipulator arms, the cargo bay door closeout, and the external

oxygen-hydrogen tank forward attachment. The nose landing gear is supported by two longitudinal beams which also provide hinge support for the landing gear doors.

The crew module is a semimonocoque aluminum structure incorporating interior rings and exterior longitudinal stringers. Five openings are located in the structure: the windshield, the cupola, and three hatches, i. e., (1) payload bay access hatch, (2) mid section side hatch, and (3) the flight section side hatch.

The crew module has been arranged in three sections: (1) the flight section, which serves as the control and operational area; (2) the mid section, accommodating the avionics equipment and the crew; and (3) the lower section, which accommodates the ECLSS equipment. An airlock in the middle section provides the EVA/IVA capability for the orbiter.

The crew module is a pressure vessel design, fabricated from 2219 aluminum alloy panels that are joined by fusion welding. This crew module corresponding to the 7D Shuttle orbiter is a floating module with four attach points to the forward fuselage structure. The module is cantilevered from the midbody forward bulkhead (Station 576) utilizing four attach fittings and a fiberglass shear web. The flight section floor consists of honeycomb panels supported by beams; the midsection floor also consists of honeycomb panels, removable at the center to provide access to the ECLSS equipment.

The basic shell is conical in shape with fore and aft flat bulkheads. The conical portion of the shell is an integrally machined skin-stringer arrangement with the stiffeners located externally. The stability frames are placed internally and are attached to the shell by mechanical fasteners tapped into bosses provided in the shell. The bulkheads are integrally machined flat panels with auxiliary stiffening members mechanically attached. The upper floor is used as a structural tie across the conical pressure shell. Above the flight deck, the cockpit enclosure is made up of flat panels with cutouts for windows and hatches. These panels are of integrally machined waffle design. The window assemblies are installed from the inside for accessibility. Each window assembly contains three panes of glass for thermal and pressure redundancy except the upper windows and hatch windows, which have two panes. The airlock section of the crew module is spherical in shape and is attached to the forward fuselage structure to react docking loads. A bellows-type adapter between the airlock section and basic crew module allows for any relative movement. The shell is an integrally machined waffle configuration. A bulkhead with a docking hatch is located in the upper area with a docking ring attached to the outboard side of the hatch.

1. 1. 6 Aft Fuselage (Table 1-7 and Figures 1. 7. 1 to 1. 7. 5 in Volume III)

The orbiter aft fuselage structurally supports the main propulsion system (MPS), the orbital maneuvering system (OMS), the auxiliary propulsion system (APU), and various avionics, launch umbilical, and thermal control equipment. The aft fuselage also furnishes structural support for the vertical fin and the rear wing spar and thermal protection for all installed equipment. To accomplish these purposes, the aft fuselage consists of a thrust structure assembly, two removable outer panel assemblies, two removable OMS pod assemblies, an outer shell assembly, a bulkhead assembly, a floor assembly, and an aft heat shield assembly.

The thrust structure consists of two machined titanium "shelves" which transfer in-plane thrust loads from the main engines to the mid fuselage longerons. These shelves are attached by machined titanium I-beam and diffusion-bonded square-shaped titanium tubing (reinforced with boron epoxy) truss members.

The forward spar of the vertical fin is attached directly to the forward bulkhead. Both fin spars connect to their aft fuselage support points through machined aluminum multilug clevis fittings. The aft spar support structure consists of a frame which is attached directly to the thrust structure through two posts.

The removable side panels and OMS pods are of built-up 2024 aluminum alloy sheet-stringer construction in conjunction with formed 2024 aluminum alloy frames. Machined tank support members are used on both the removable panels and the pods in local areas. The outer shell is also of built-up aluminum sheet-stringer construction with formed sheet aluminum frames, except in high load areas such as below the fin aft spar and at the vertical shear tie for the rear wing spar. Both these areas are machined assemblies. The wing vertical shear is transferred to the mid fuselage by a machined aluminum sidewall which extends below the lower thrust shelf.

The forward bulkhead of the aft fuselage is machined in three large pieces rather than one because of plate size limitations. These pieces are bolted together to form a single assembly which includes the aft moment-carrying spar of the wing.

The aft fuselage floor assembly is of stiffened-sheet aluminum construction similar to the side panels except that the more highly loaded frames are built-up of sheet webs and extruded stiffeners and caps.

1. 1. 7 Vertical Stabilizer (Table 1-8 and Figures 1. 8. 1 to 1. 8. 4 in Volume III)

The vertical stabilizer is a symmetrical 60/40 wedge shape, with the rudder hinge line at the 60-percent chord. The rudder is in two spanwise

sections to reduce binding in the hinges from spanwise bending deflections. The rudder is split along the chord plane to act as a speed brake for velocity modulation during atmospheric flight.

System components mounted in the vertical stabilizer consist of an APU exhaust duct, ram air duct inlet for vapor cycle package, and the hydraulic and flight control systems to operate the rudder/speed brake. The vertical stabilizer structure is basically comprised of a two-spar multirib stiffened skin box assembly. The skin panels are stiffened by hat sections or "Z" sections riveted to the skin. The rudder/speed brake skin panels are bonded aluminum honeycomb.

The structural material used is generally 2024-T86 or 2124-T851 aluminum, and the exposed surfaces are covered by a thermal protective system (TPS). The primary attachment of vertical stabilizer to the body is made at the front and rear spar through machined fittings attached to the main thrust structure. Each rudder/speed brake assembly is mounted on two hinges and driven by tandem actuators.

The vertical surface leading edge is removable in order to provide inspection and, if necessary, replacement. Access panels also allow installation and removal of rudder/speed brake actuators. During rudder/speed brake actuation, high-temperature seals are required to exclude the hot plasma flows from the internal structure. Design will be similar to the wing/elevon seals.

1. 1. 8 Landing Gear (Table 1-9 and Figures 1.9.1 and 1.9.2 in Volume III)

1. 1. 8. 1 Main Landing Gear

The main landing gear shock strut is a semicantilevered, conventional, air-oil piston-type of such design that the passage of hydraulic fluid through an orifice will absorb the energy of impact and in which dry nitrogen is the elastic medium to provide the spring force. A floating piston separates the hydraulic fluid and the nitrogen. The floating piston is mounted coaxially inside the shock strut piston with an upper extension of the floating piston mounted coaxially inside the metering pin. This extension also serves as a means of locating the position of the floating piston to assure that it is in its proper position for servicing of the shock strut. The principal members of the drag brace include the upper drag brace, the lower drag brace, and the support beam. The support beam, a tubular member, is the torque and tension carrying member for the upper drag brace whose two members are identical arms fabricated as a three-piece tubular flash-welded construction to achieve the best strength-weight-cost ratio. The lower drag brace is also an efficient tubular two-piece flash-welded construction. Self-aligning bearings are provided in each end.

The lock brace consists of three major components: the support beam, lower lock brace, and upper lock brace. The support beam is a "bottle" bored tube. Two identical tension springs are connected between the upper lock brace and shock strut cylinder. These springs each are designed to provide sufficient force to maintain the lock braces in an overcenter position against any tendency of the retract actuator to uplock the braces due to back pressure surges in the hydraulic system.

1.1.8.2 Nose Landing Gear

The shock strut is a semicantilevered, conventional, air-oil piston-type of such design that the passage of hydraulic fluid through an orifice will absorb the energy of impact and in which dry nitrogen is the elastic medium to provide the spring force. It was determined that the optimum design would be one with a 13.9 centimeter (5-1/2 inch) piston diameter and with the lower shock strut bearings moved down as close to the axle as possible. This configuration significantly reduced the piston bending moment and the shock strut bearing pressures.

A floating piston separates the hydraulic fluid and the nitrogen. The floating piston is inside the shock strut piston and the nitrogen is contained in the chamber below the floating piston. An air valve is located at the bottom of the shock strut piston for pressurizing this chamber. A guided and grooved metering pin is incorporated in conjunction with an orifice to accommodate energy absorption requirements. Nose wheel centering within ± 0.25 degree of center as the piston extends prior to gear retraction is provided by two internal mating face cams operated by the load generated by the strut internal pressure tending to extend the piston. The upper cam is keyed to the piston, and the lower cam is keyed to the cylinder.

The drag brace includes the upper drag brace, the lower drag brace, and the support beam as its principal members. The support beam, a machined tube, acts as the torque-carrying member for the upper drag brace whose two members consist of identical three-piece flash welded tubular assemblies. The lower drag brace is also an efficient tubular design of two-piece flash-welded construction.

The lock brace consists of three major components: the yoke, the lower brace, and the upper brace. The yoke is fabricated from aluminum alloy, while both braces are fabricated from high strength steel. The yoke is a simple member connecting the lock brace linkage to the knee joint of the drag brace. The upper lock brace is basically an I-beam in shape, which terminates in a tube at one end. Protruding from the tube are the lugs which attach the linkage to the shock strut. Extending from the tube at one end is the retraction actuator stud with its associated attaching hardware.

Table 1-1. Space Shuttle Orbiter Reusable Tankages

System	Item No. ^Δ	Tankage Size and Shape	Tank Material	Tank Thickness cm (in.)	Operating Pressure N/m ² x 10 ⁶ (psi)	Max Relief Pressure N/m ² x 10 ⁶ (psi)	Structural Temp Range °C (°F)	Material Contained	Location ^Δ	Availability for Removal	Consequence of Leakage	Consequence of Burst	Possible Design Approach	Selection Logic
Electrical power generation	439 and 441	1.168 m (46 in.) dia sphere (outer shell); 1.066 m (42 in.) dia sphere (inner shell)	2219 AL	0.190 (0.075)	2.0 (285)	2.3 (335)	-252-- -101 (-423-- -150)	Supercritical LH ₂	Fwd-midbody	Can be removed but not desirable due to extensive testing associated with installation	Potential fire hazard ^Δ	Catastrophic ^Δ	Safe-life	1-7
			2219 AL	0.190 (0.075)										
	438 and 440	1.016 m (40 in.) dia sphere (outer shell); 0.914 m (36 in.) dia sphere (inner shell)	2219 AL	0.266 (0.105)	6.6 (950)	7.2 (1,050)	-183-- 26 (-297-- 80)	Supercritical LO ₂	Fwd-midbody					
			718 Inconel	0.266 (0.105)										
Auxiliary power unit	563	0.736 m (29 in.) dia sphere	Ti-6AL-4V	0.096 (0.038)	3.0 (435)	-	4 -65 (40 -150)	N ₂ H ₂	Aft body	Tanks are removed after each flight for servicing and refueling	Potential hazard of soaking into TPS and igniting on re-entry ^Δ	Catastrophic ^Δ	Safe-life	1-7
Main propulsion system	544	0.642 m (25.3 in.) dia sphere	Ti-6AL-4V	1.016 (0.400)	27.6 (4,000)	31.0 (4,500)	104 (220)	He	Engine compartment	Can be re-removed through aft structure	No potential hazard with loss of one tank	Catastrophic ^Δ	Safe-life	1-7
Environmental control system	414, 415 and 416	Oblate spheroid	Glass epoxy or metal	TBD	20.7 (3,000)	-	-54--68 (-65--155)	N ₂	Lower body aft of crew compartment	Tanks can be removed	Potential fire hazard with O ₂ leakage ^Δ	Catastrophic ^Δ	Safe-life	1-7
		413	Oblate spheroid	Glass epoxy or metal	TBD	6.2 (900)	-	-54--68 (-65--155)						
Orbital maneuvering system	572	Cylinder with hemispherical heads, 1.117 m (44 in.) dia x 2.514 m (99 in.) long	Ti-6AL-4V	0.129 (0.051)	1.5 (215)	1.9 (273)	37 (100)	N ₂ O ₄	OMS pods	Pods are removed after each flight for servicing	Potential fire hazard ^Δ	Catastrophic ^Δ	Safe-life	1-7
	570	Cylinder with hemispherical heads, 1.117 m (44 in.) dia x 2.514 m (99 in.) long	Ti-6AL-4V	0.129 (0.051)	1.5 (215)	1.9 (273)	37 (100)	MMH	OMS pods					
	569	0.958 m (37.75 in.) dia sphere	Ti-6AL-4V	0.952 (0.375)	27.579 (4,070)	29.8 (4,315)	37 (100)	He	OMS pods					

Table 1-1. Space Shuttle Orbiter Reusable Tankages (Cont)

System	Item [△]	Tankage Size and Shape	Tank Material	Tank Thickness cm (in.)	Operating Pressure N/m ² x 10 ⁶ (psi)	Max Relief Pressure N/m ² x 10 ⁶ (psi)	Structural Temp Range °C (°F)	Material Contained	Location [△]	Availability for Removal	Consequence of Leakage	Consequence of Burst	Possible Design Approach	Selection
Reaction control system	205 579	0.487 m (19.2 in.) dia sphere	Ti-6AL-4V	0.477 (0.188)	24.8 (3,600)	27.6 (4,000)	21--176 (70--350)	He	Vehicle nose and aft fuselage	Modules are removed after each flight for servicing	Potential fire hazard [△]	Catastrophic [△]	Safe-life	1-7
	204 578	Cylinder with ellipsoidal head, 0.711 m (28 in.) dia x 1.117 m (44 in.) long	Ti-6AL-4V	0.149 (0.059)	1.9 (280)	3.0 (435)		MMH						
	204 578	Cylinder with ellipsoidal head, 0.711 m (28 in.) dia x 1.117 m (44 in.) long	Ti-6AL-4V	0.149 (0.059)	1.9 (280)	3.0 (435)		N ₂ O ₄						
Airbreathing engine system [△]	Not shown	Cylinder 3.556 m (140 in.) dia x 1.473 m (58 in.) long and end cones 3.556 m (140 in.) dia x 2.413 m (95 in.) long	Aluminum	0.635 (0.250)	0.14 (20)	-	-54--71 (-65--160)	JP fuel	Aft cargo bay	Tank removable after ferry flight and flight tests	Potential fire hazard [△]	Catastrophic [△]	Safe-life	1-7

[△] Item No. refers to nomenclature No. on Drawing VL72-000091 (Figure 1.1.2 in Volume III).
[△] See Figure 1.1.4 in Volume III.
[△] Loss of vehicle.
[△] ABES not used in orbital flights.

Table 1-2. Space Shuttle Solid Rocket Booster (SRB)

I. D. No.	Structural Element	Type of Construction	Material	Typical Thickness Range cm (in.)	Design Mode			Other Design Condition			Structural Temp Range °C (°F)	Typical Structural Joint	Consequence of Failure		Possible Design Approach		Selection Logic
					Loading Condition	Type of Load	Stress, N/m ² x 10 ⁶ (ksi)	Loading Condition	Type of Load	Stress, N/m ² x 10 ⁶ (ksi)			Loss of Assembly	Loss of Vehicle	Fail-Safe	Safe-Life	
2-1	Nose cone	Skin-stringer	2024-T81 or T86	0.381 (0.150)	Max q	Buckling	TBD				21 - 176 (70 - 350)	Mechanically fastened	No	No	-	-	1-2, 10
2-2	Recovery system support structure	TBD	TBD	TBD	Recovery	TBD	TBD				21 (70)		No	No	-	-	1-4, 9, 10
2-3	Forward cylinder	Skin-stringer	2024-T81 or T86	0.474 (0.187)	Max q	Tension	275.7 (40)				21 - 176 (70 - 350)		Yes	No	•	•	1-6, 9, 10
2-4	Forward thrust fitting	Machined forging	D6AC or 18% Ni maraging	TBD	Max q	Tension	344.7 (50)				15 - 148 (60 - 300)		Yes	No		•	1-6, 9, 10
2-5	Forward closure	Machined forging		0.584 - 1.193 (0.230 - 0.470)	Flight	Tension	1344.4 (195)				15 (60)		Yes	Yes		•	1-7
2-6	Cylindrical body	Shear spun or rolled and welded plate		1.193 (0.470)	Flight	Tension	1344.4 (195)				15 (60)		Yes	Yes		•	1-7
2-7	ET/SRB aft attachment frame	Machined forging		TBD	TBD	Bending	TBD				21 - 176 (70 - 350)		Yes	No		•	1-6, 9, 10
2-8	Aft closure	Machined forging	D6AC or 18% Ni maraging	0.584 - 1.193 (0.230 - 0.470)	Flight	Tension	1344.4 (195)				15 (60)		Yes	Yes		•	1-7
2-9	Nozzle	Shear spun plate	4340	TBD	Flight	Tension	TBD				15 (60)		No	No	-	-	1-4, 9, 10
2-10	Aft skirt	Skin-stringer	2024-T81 or T86	0.254 - 0.508 (0.100 - 0.200)	Launch	Tension	344.7 (50)	Pre-launch	Compression	344.7 (50)	21 - 176 (70 - 350)	Mechanically fastened	No	No	-	-	1-4, 9, 10

Table 1-3. Space Shuttle Orbiter External Tank System

I.D. No	Structural Element	Type of Construction	Material	Typical Thickness Range cm (in)	Design Mode			Other Design Condition			Structural Temp Range °C (°F)	Typical Structural Joint	Consequence of Failure		Possible Design Approach		Selection Logic
					Loading Condition	Type of Load	Stress, N/m ² x 10 ⁶ (ksi)	Loading Condition	Type of Load	Stress, N/m ² x 10 ⁶ (ksi)			Loss of Assembly	Loss of Vehicle	Fail-Safe	Safe-Life	
3-1	LO ₂ tank, nose cone	Stretch formed sheet	2219-T87	0.127 - 0.330 (0.050 - 0.130)	Proof test	Tension	344.7 (50)				-183 - 21 (-297 - 70)	Welded, mechanically fastened	Yes	Yes		•	1-7
3-2	LO ₂ tank, cylindrical body	Rolled and machined sheet	2219-T87	0.381 - 0.436 (0.150 - 0.172)	Proof test	Tension	344.7 (50)				-195 - 21 (-320 - 70)	Welded	Yes	Yes		•	1-7
3-3	LO ₂ tank frame, Y-ring	Machined ring, roll forging	2219-T62	0.254 - 0.381 (0.100 - 0.150)	Proof test	Tension	344.7 (50)	Max q	Bending	344.7 (50)	-195 - 21 (-320 - 70)	Welded and mechanically fastened	Yes	Yes		•	1-7
3-4	LO ₂ tank, bulkhead	Machined sheet, stretch-formed	2219-T87	0.279 - 0.373 (0.110 - 0.147)	Max q	Tension	TBD				-195 - 21 (-320 - 70)	Welded	Yes	Yes		•	1-7
3-5	LO ₂ tank frame (XT 715)	Machined ring, formed web	2219-T62	0.325 - 0.386 (0.128 - 0.152)	Proof test	Tension	344.7 (50)				-195 - 21 (-320 - 70)	Welded mechanically fastened	Yes	Yes		•	1-7
3-6	Intertank, skin/stringer	Integrally machined skin/stringer, rolled-formed	2024-T86	0.254 (0.100)	Max q post-staging	Compression	206.8 (30)	Max q	Shear	206.8 (30)	21 - 148 (70 - 300)	Welded and mechanically fastened	Yes	No		•	1-6, 9, 10
3-7	Intertank, frames (6 places)	Machined flanges, formed web	2024-T62	0.127 - 0.317 (0.050 - 0.125)	Max q post-staging	Compression	206.8 (30)				21 - 148 (70 - 300)	Mechanically fastened	No	No		-	1-2, 10
3-8	Intertank, frame (XT 947)	Machined ring	2024-T62	TBD	Max q	Bending	TBD				21 - 148 (70 - 300)	Mechanically fastened	Yes	No		•	1-6, 9, 10
3-9	SRB thrust longeron	Forging	7075-T73	TBD	Max q	Tension	TBD				-45 - 93 (-50 - 200)	Bolted	Yes	No		•	1-6, 9, 10
3-10	LH ₂ tank, fwd bulkhead	Machined sheet, stretch-formed	2219-T87	0.210 - 0.266 (0.083 - 0.105)	Deorbiting	Tension	427.4 (62)				-128 - 93 (-200 - 200)	Welded	Yes	Yes		•	1-7
3-11	LH ₂ tank frame (XT 1078)	Machined ring	2219-T62	TBD	Proof test	Tension	TBD	Max q	Bending	TBD	-252 - 21 (-423 - 70)	Welded and mechanically fastened	Yes	Yes		•	1-7
3-12	LH ₂ tank, fwd cylinder body	Machined plate, brake-formed	2219-T87	0.330 - 0.787 (0.130 - 0.310)	Pneumostat	Tension	344.7 (50)				-252 - 21 (-423 - 70)	Welded	Yes	Yes		•	1-7
3-13	LH ₂ tank, aft cylinder body	Machined plate, brake-formed	2219-T87	0.347 - 0.787 (0.137 - 0.310)	Pneumostat	Tension	344.7 (50)				-252 - 21 (-423 - 70)	Welded	Yes	Yes		•	1-7
3-14	LH ₂ tank, aft bulkhead	Machined sheet, stretch-formed	2219-T81	0.210 - 0.284 (0.083 - 0.112)	Pneumostat	Tension	344.7 (50)				-252 - 21 (-423 - 70)	Welded	Yes	Yes		•	1-7
3-15	ET/orbiter attachment structure	Tubing, machined fittings	T1-5AL-2.5 Sn	TBD	Flight loads	Tension	689.4 (100)	Flight loads	Compression	551.5 (80)	21 - 148 (70 - 300)	Mechanically fastened	Yes	Yes		•	1-7
3-16	LH ₂ tank, frame (XT 2058)	Machined ring	2219-T62	0.254 - 1.27 (0.100 - 0.500)	Flight loads	Tension	TBD				-252 - 21 (-423 - 70)	Welded and mechanically fastened	Yes	Yes		•	1-7
3-17	Compression strut	Thin wall tube	2219-T87	0.127 (0.050)	Flight loads	Compression	206.8 (30)				-252 - 21 (-423 - 70)	Mechanically fastened	No	No		-	1, 2, 10

Table 1-4. Space Shuttle Orbiter Mid Fuselage

I. D. No.	Structural Element	Type of Construction	Material	Typical Thickness Range cm (in.)	Design Mode			Other Design Condition			Structural Temp Range °C (°F)	Typical Structural Joint	Consequence of Failure		Possible Design Approach		Selection Logic
					Loading Condition	Type of Load	Stress, N/m ² x 10 ⁶ (ksi)	Loading Condition	Type of Load	Stress, N/m ² x 10 ⁶ (ksi)			Loss of Assembly	Loss of Vehicle	Fail-Safe	Safe-Life	
4-1	Forward sill longeron	Machined plate	2024-T851	0.279-1.676 (0.110-0.660)	High q boost	Compression	358.5 (52.0)	TBD	TBD	TBD	-128 - 162 (-200 - 325)	Mechanically fastened	Yes	Yes		•	1-7
4-2	Aft sill longeron	Machined plate and composite lay-up	Ti-6AL-4V and Boron/Epoxy	0.317-1.143 (0.125-0.450)	High q boost	Compression	689.4 (100.0)	TBD	TBD	TBD	-128 - 162 (-200 - 325)		Yes	Yes		•	1-7
4-3	Side skin panels	Machined plate, integrally stiffened	2024-T851	0.101-0.381 (0.040-0.150)	High q boost	Compression	241.3 (35.0)	Tail-down landing	Shear	206.8 (30.0)	-112 - 176 (-170 - 350)		Yes	No	•	•	1-6, 9, 10
4-4	Lower skin panels	Machined plate, integrally stiffened	2024-T851	0.101-0.381 (0.040-0.150)	Tail-down landing	Compression	206.8 (30.0)	2.5 g maneuver	Shear	193.0 (28.0)	-112 - 176 (-170 - 350)		Yes	Yes	•	•	1-7
4-5	Wing carry-thru skin panels	Machined plate, integrally stiffened	2024-T851	0.254-7.62 (0.100-3.000)	Tail-down landing	Tension	289.5 (42.0)	High q boost	Compression	289.5 (42.0)	-170 - 176 (-275 - 350)		Yes	No	•	•	1-6, 9, 10
4-6	Glove fairing skins	Formed sheets	2024-T81	0.081-0.635 (0.032-0.250)	High q boost	Tension	275.7 (40.0)				-112 - 176 (-170 - 350)		No	No	-	-	1-4, 9, 10
4-7	Glove fairing ribs	Extrusions and formed sheets	2024-T81 and T8511	0.127 (0.050)	High q boost	Bending	275.7 (40.0)				-112 - 176 (-170 - 350)		No	No	-	-	1-4, 9, 10
4-8	Lower forward longeron	Extrusion	2024-T8511	0.254-0.317 (0.100-0.125)	High q boost	Tension	324.0 (47.0)				-112 - 165 (-170 - 330)		Yes	Yes		•	1-7
4-9	Lower aft longeron	Machined plate	2024-T851	0.254-1.27 (0.100-0.500)	High q boost	Tension	324.0 (47.0)				-112 - 165 (-170 - 330)		Yes	Yes		•	1-7
4-10	Wing carry-thru spar frames	Machined plates	2024-T851	0.254-5.08 (0.100-2.000)	High q boost	Bending	289.5 (42.0)	2.5 g maneuver	Bending	289.5 (42.0)	-128 - 176 (-200 - 350)		Yes	Yes		•	1-7
4-11	Payload, glove and intermediate frame webs	Sheets	2024-T81	0.101-0.152 (0.040-0.060)	Landing	Shear	137.8 (20.0)				-128 - 176 (-200 - 350)		No	No	-	-	1-4, 9, 10
4-12	Payload, glove and intermediate frame caps, stiffeners and trusses	Extrusions, tubes	2024-T8511	TBD	Landing	Compression	275.7 (40.0)				-128 - 176 (-200 - 350)		No	No	-	-	1-2, 10
4-13	Frame support ribs	Tubes with end fittings	B/Al tubes Ti-6AL-4V	Tubes 0.073 (0.029)	Landing	Tension	103.4 (15.0)	Landing	Compression	103.4 (15.0)	-128 - 176 (-200 - 350)		No	No	-	-	1-3, 10
4-14	Access doors	Machined plates	2024-T851	0.101-0.381 (0.040-0.150)	Landing	Shear	117.2 (17.0)	Landing	Tension	68.9 (10.0)	-121 - 176 (-170 - 350)		No	No	-	-	1-3, 10
4-15	Fittings	Machined plates and forgings	2024-T851 2219-T6	TBD	TBD	TBD	TBD				TBD		Yes ^Δ	Yes ^Δ		•	1-7
4-16	Bracketry	Formed sheets	2024-T62 or T81	TBD	TBD	TBD	TBD				TBD		No	No	-	-	1-4, 9, 10
4-17	Payload bay liner	Fabric lamination	PDR-49-IV	TBD	TBD	TBD	TBD				TBD		No	No	-	-	1-4, 9, 10
4-18	MLG support	Machined plate	2024-T851	0.254-2.54 (0.100-1.000)	Landing	Bending	379.2 (55.0)	Turning	Bending	379.2 (55.0)	-156 - 93 (-250 - 200)	Mechanically fastened	Yes	Yes		•	1-7

Table 1-4. Space Shuttle Orbiter Mid Fuselage (Cont)

I. D. No.	Structural Element	Type of Construction	Material	Typical Thickness Range cm (in.)	Design Mode			Other Design Condition			Structural Temp Range °C (°F)	Typical Structural Joint	Consequence of Failure		Possible Design Approach		Selection Logic
					Loading Condition	Type of Load	Stress, N/m ² x 10 ⁶ (ksi)	Loading Condition	Type of Load	Stress, N/m ² x 10 ⁶ (ksi)			Loss of Assembly	Loss of Vehicle	Fail-Safe	Safe-Life	
4-19	Payload bay doors, skin	Formed sheets	2024-T86	0.063 - 0.101 (0.025 - 0.040)	High q boost	Shear	58.6 (8.5)				-128 - 176 (-200 - 350)	Mechanically fastened	No	No	-	-	1-3, 10
4-20	Payload bay doors, stringers	Extrusions	2024-T86	0.063 (0.025)	High q boost	Bending	190.9 (27.7)				-128 - 176 (-200 - 350)		No	No	-	-	1-5, 9, 10
4-21	Payload bay doors, frame web	Formed sheets	2024-T86	0.304 (0.120)	High q boost	Bending + axial	279.2 (40.5)				-128 - 176 (-200 - 350)		No	No	-	-	1-5, 9, 10
4-22	Payload bay doors, frame cap	Extrusions	2024-T86	0.381 (0.150)	High q boost	Bending + axial	286.8 (41.6)				-128 - 176 (-200 - 350)		No	No	-	-	1-5, 9, 10
4-23	Payload bay doors, hinges	Machined plate	Titanium 6AL-4V	0.152 - 0.355 (0.060 - 0.140)	High q boost	Compression	79.3 (11.5)	Door open	Bending	TBD	-128 - 176 (-200 - 350)		Mechanically fastened	Yes	Yes		•

△ Depend on location

Table 1-5. Space Shuttle Orbiter Wing

I. D. No.	Structural Element	Type of Construction	Material	Typical Thickness Range cm (in.)	Design Mode			Other Design Condition			Structural Temp Range °C (°F)	Typical Structural Joint	Consequence of Failure		Possible Design Approach		Selection Logic	
					Loading Condition	Type of Load	Stress, N/m ² x 10 ⁶ (ksi)	Loading Condition	Type of Load	Stress, N/m ² x 10 ⁶ (ksi)			Loss of Assembly	Loss of Vehicle	Fail-Safe	Safe-Life		
5-1	Skin	Formed sheet	2024-T81	0.101 - 0.254 (0.040 - 0.100)	High q	Compression	253.0 (36.7)	Head wind	Tension	196.5 (28.5)	-128 - 176 (-200 - 350)	Mechanically fastened	Yes	Yes	•	•	1-7	
5-2	Stringers	Formed sheets	2024-T81	0.050 - 0.254 (0.020 - 0.100)		Compression	253.0 (36.7)	Head wind	Tension	196.5 (28.5)	-128 - 176 (-200 - 350)		No	No	-	-	1-5, 9, 10	
5-3	Spar caps	Formed sheets	2024-T81	0.101 - 0.177 (0.040 - 0.070)		Tension	253.0 (36.7)				-128 - 176 (-200 - 350)		No	No	-	-	1-5, 9, 10	
5-4	Rib caps	Formed sheets	2024-T81	0.101 - 0.254 (0.040 - 0.100)		Tension	253.0 (36.7)				-128 - 176 (-200 - 350)		No	No	-	-	1-5, 9, 10	
5-5	Rib EMF tubes	Tubing	2024-T81	0.101 - 0.203 (0.040 - 0.080)		Compression	253.0 (36.7)	Head wind	Tension	253.0 (36.7)	-128 - 176 (-200 - 350)		No	No	-	-	1-5, 9, 10	
5-6	Rib EMF tube fittings	Machined plate	2124-T851	1.27 - 11.43 (0.500 - 4.50)		Compression	253.0 (36.7)	Head wind	Tension	253.0 (36.7)	-128 - 176 (-200 - 350)		No	No	-	-	1-5, 9, 10	
5-7	Rib/skin shear channels	Formed sheet	2024-T81	0.101 - 0.177 (0.040 - 0.070)		Tension	253.0 (36.7)				-128 - 176 (-200 - 350)		No	No	-	-	1-5, 9, 10	
5-8	Spar/rib splice	Formed sheet	2024-T81	0.254 - 0.635 (0.100 - 0.250)		Tension	253.0 (36.7)				-128 - 176 (-200 - 350)		No	No	-	-	1-5, 9, 10	
5-9	Elevon web	Formed sheet	Titanium 6AL-6V-2Sn	0.101 - 0.177 (0.040 - 0.070)		Shear	TBD				-128 - 426 (-200 - 800)		No	No	-	-	1-5, 9, 10	
5-10	Elevon web stiffeners	Formed sheet	Titanium 6AL-6V-2Sn	0.127 - 0.203 (0.050 - 0.080)		Tension	620.5 (90.0)				-128 - 426 (-200 - 800)		Yes	Yes	•	•	1-7	
5-11	Access doors	Machined plate	2124-T851	0.254 - 0.635 (0.100 - 0.250)		Compression	253.0 (36.7)	Head wind	Tension	253.0 (36.7)	-128 - 176 (-200 - 350)		No	No	-	-	1-5, 9, 10	
5-12	Wing fuselage attachment	Machined plate	2124-T851	0.254 - 5.08 (0.100 - 2.00)		Tension	253.0 (36.7)	Head wind	Compression	253.0 (36.7)	-128 - 176 (-200 - 350)		Yes	Yes	•	•	1-7	
5-13	Hinge fittings	Machined plate	Titanium 6AL-6V-2Sn	1.27 - 10.16 (0.500 - 4.00)		Tension	620.5 (90.0)	Head wind	Compression	620.5 (90.0)	-128 - 426 (-200 - 800)		Yes	Yes	•	•	1-7	
5-14	Actuator fittings	Machined plate	Titanium 6AL-6V-2Sn	1.27 - 10.16 (0.500 - 4.00)		Compression	620.5 (90.0)	Head wind	Tension	620.5 (90.0)	-128 - 426 (-200 - 800)	Mechanically fastened	Yes	Yes	•	•	1-7	
5-15	Elevon skins	Honeycomb panels	Titanium 6AL-6V-2Sn	0.025 - 0.040 (0.010 - 0.016)	High q	Tension	620.5 (90.0)	Head wind	Compression	620.5 (90.0)	-128 - 426 (-200 - 800)	Brazed	Yes	Yes	•	•	1-7	
5-16																		
5-17																		
5-18																		

Table 1-6. Space Shuttle Orbiter Crew Cabin and Forward Fuselage

I. D. No.	Structural Element	Type of Construction	Material	Typical Thickness Range cm (in.)	Design Mode			Other Design Condition			Structural Temp Range °C (°F)	Typical Structural Joint	Consequence of Failure		Possible Design Approach		Selection Logic
					Loading Condition	Type of Load	Stress, N/m ² x 10 ⁶ (Ksi)	Loading Condition	Type of Load	Stress, N/m ² x 10 ⁶ (Ksi)			Loss of Assembly	Loss of Vehicle	Fatigue	Safe-Life	
6-1	Cabin, forward bulkhead	Waffle grid, machined plate	2219-T87	0.081 — 0.508 (0.032 — 0.2)	Internal pressure	Tension	213.7 (31)				15 — 51 (60 — 125)	Welded	Yes	Yes	•	•	1-7
6-2	Cabin, floor bulkhead beams	Machined plate	2219-T87	0.635 — 1.27 (0.250 — 0.500)	Internal pressure	Tension	213.7 (31)				15 — 51 (60 — 125)	Mechanically fastened	Yes	Yes	•	•	1-7
6-3	Cabin, skin panels	Machined plate, integrally stiffened	2219-T851	0.081 — 0.279 (0.032 — 0.110)	Internal pressure	Tension	213.7 (31)				15 — 51 (60 — 125)	Welded	Yes	Yes	•	•	1-7
6-4	Cabin, frame webs	Formed sheet	2024-T81	0.050 — 0.127 (0.020 — 0.050)	Internal pressure	Tension	227.5 (33)				15 — 51 (60 — 125)	Mechanically fastened	No	No	—	—	1-5, 9, 10
6-5	Cabin, frame caps	Rolled extrusion	2024-T8511	0.254 — 0.635 (0.100 — 0.250)	Internal pressure	Tension	227.5 (33)				15 — 51 (60 — 125)	Mechanically fastened	No	No	—	—	1-5, 9, 10
6-6	Cabin, mfg access panels	Machined plates	2219-T87	0.254 — 0.635 (0.100 — 0.250)	Internal pressure	Tension	213.7 (31)				15 — 51 (60 — 125)	Mechanically fastened	Yes	Yes		•	1-7
6-7	Cabin, canopy panels	Formed sheets	2219-T851	0.254 — 0.635 (0.100 — 0.250)	Internal pressure	Tension	213.7 (31)				15 — 51 (60 — 125)	Welded	Yes	Yes	•	•	1-7
6-8	Cabin, aft bulkhead	Machined plate, waffle grid	2219-T87	0.081 — 0.076 (0.032 — 0.03)	Internal pressure	Tension	213.7 (31)				15 — 51 (60 — 125)	Welded	Yes	Yes	•	•	1-7
6-9	Fwd fuselage, skins	Formed sheets	2024-T81	0.050 — 0.101 (0.020 — 0.040)	Flight loads	Tension	206.8 (30)				-128 — 176 (-200 — 350)	Mechanically fastened	Yes	Yes	•	•	1-7
6-10	Fwd fuselage, stringers	Formed sheets and extrusion	2024-T81	0.076 — 0.381 (0.030 — 0.150)	Flight loads	Tension	206.8 (30)				-128 — 176 (-200 — 350)	Mechanically fastened	No	No	—	—	1-5, 9, 10
6-11	Fwd fuselage, frame webs	Formed sheets	2024-T81	0.050 — 0.152 (0.020 — 0.060)	Flight loads	Shear	137.8 (20)				-128 — 176 (-200 — 350)	Mechanically fastened	No	No	—	—	1-5, 9, 10
6-12	Fwd fuselage, frame caps	Extrusion	2024-T8511	0.152 — 0.317 (0.060 — 0.125)	Flight loads	Tension	124.1 (18)				-128 — 176 (-200 — 350)	Mechanically fastened	Yes	Yes		•	1-7
6-13	Fwd fuselage, longerons	Extrusion	2024-T8511	0.228 — 0.635 (0.090 — 0.250)	Flight loads	Tension	206.8 (30)				-128 — 176 (-200 — 350)	Mechanically fastened	Yes	Yes		•	1-7
6-14	Fwd fuselage, fwd bulkhead	Formed sheet	2219-T86	0.635 — 1.27 (0.250 — 0.500)	Flight loads	Tension	TBD				-128 — 176 (-200 — 350)	Mechanically fastened	No	No	—	—	1-4, 9, 10
6-15	Fwd fuselage, link brackets	Machined plate	Titanium 6AL-4V	0.635 — 1.27 (0.250 — 0.500)	Flight loads	Compression	758.4 (110)	Flight loads	Tension	TBD	-128 — 176 (-200 — 350)	Mechanically fastened	Yes	Yes		•	1-7
6-16	Link assembly	Machined plate	Titanium 6AL-4V	0.076 — 2.54 (0.030 — 1.00)	Flight loads	Compression	758.4 (110)	Flight loads	Tension	TBD	-128 — 176 (-200 — 350)	Mechanically fastened	Yes	Yes		•	1-7
6-17	Cabin, link bracket attachment	Machined plates	Titanium 6AL-4V	0.635 — 1.27 (0.25 — 0.500)	Flight loads	Compression	758.4 (110)	Flight loads	Tension	TBD	15 — 51 (60 — 125)	Mechanically fastened	Yes	Yes		•	1-7

Table 1-7. Space Shuttle Orbiter Aft Fuselage

I. D. No	Structural Element	Type of Construction	Material	Typical Thickness Range cm (in.)	Design Mode			Other Design Condition			Structural Temp Range °C (°F)	Typical Structural Joint	Consequence of Failure		Possible Design Approach		Selection Logic
					Loading Condition	Type of Load	Stress, N/m ² x 10 ⁶ (ksi)	Loading Condition	Type of Load	Stress, N/m ² x 10 ⁶ (ksi)			Loss of Assembly	Loss of Vehicle	Fail-Safe	Safe-Life	
7-1	Aft bulkhead	Machined plate	2124-T851	0.081 - 2.54 (0.032 - 1.00)	Pressure	Tension or compression	241.3-344.7 (35 - 50)				-106 - 121 (-160 - 250)	Mechanically fastened	Yes	Yes	•	•	1-7
7-2	Canted frame	Diffusion bonded	Ti-6AL-4V	0.381 - 2.54 (0.150 - 1.00)	Vertical fin	Tension or compression	241.3-827.3 (35 - 120)				-106 - 93 (-160 - 200)		Yes	Yes		•	1-7
7-3	Vertical stabilizer support frame	Machined plate	2124-T851	0.381 - 5.08 (0.150 - 2.00)	Vertical fin	Tension or compression	241.3-344.7 (35 - 50)				-106 - 176 (-160 - 350)		Yes	Yes		•	1-7
7-4	Fuselage frames	Formed sheets	2024-T86	0.101 - 0.152 (0.040 - 0.060)	Pressure	Tension or compression	241.3-344.7 (35 - 50)				-106 - 176 (-160 - 350)		Yes	Yes		•	1-7
7-5	Skin/stringer	Machined plate	2124-T851	0.081 - 0.304 (0.032 - 0.120)	Pressure and engine out	Compression with shear	241.3-241.3 (35 - 35)				-106 - 176 (-160 - 350)		Yes	Yes	•	•	1-7
7-6	Floor (waffle plate)	Machined plate	2124-T851	0.081 - 0.304 (0.032 - 0.120)	Pressure and engine out	Compression with shear	241.3-241.3 (35 - 35)				-106 - 176 (-160 - 350)		Yes	Yes	•	•	1-7
7-7	Floor beam caps	Extrusion	2024-T8511	0.254 (0.100)	Pressure and engine out	Tension or compression	241.3-344.7 (35 - 50)				-106 - 176 (-160 - 350)		No	No	-	-	1-5, 9, 10
7-8	Floor beam webs	Formed sheets	2024-T86	0.050 - 0.228 (0.020 - 0.090)	Pressure and engine out	Shear	68.9-206.8 (10 - 30)				-106 - 176 (-160 - 350)		No	No	-	-	1-5, 9, 10
7-9	Body flap skins	Honeycomb panels	2219-T85	0.040 (0.016)	Entry	Tension or compression	241.3-620.5 (35 - 90)				-106 - 176 (-160 - 350)		Yes	Yes		•	1-7
7-10	Upper shelf beam	Machined plate	Ti-6AL-4V	0.101 - 2.54 (0.040 - 1.00)	Engine out	Tension or compression	241.3-620.5 (35 - 90)				-106 - 176 (-160 - 350)		Yes	Yes		•	1-7
7-11	Lower shelf beam	Machined plate	Ti-6AL-4V	0.101 - 2.54 (0.040 - 1.00)	Engine out	Tension or compression	241.3-620.5 (35 - 90)				-106 - 176 (-160 - 350)		Yes	Yes		•	1-7
7-12	Truss tubing	Extruded tube/boron reinforced	Ti-6AL-4V and boron/epoxy	0.254 - 0.381 (0.100 - 0.150)	Engine out	Tension or compression	241.3-620.5 (35 - 90)				-106 - 176 (-160 - 350)		No	No	-	-	1-5, 9, 10
7-13	Actuator fittings	Machined plate	Ti-6AL-4V	0.304 - 2.54 (0.120 - 1.00)	Engine out	Tension or compression	241.3-620.5 (35 - 90)				-106 - 176 (-160 - 350)		Yes	Yes		•	1-7
7-14	Vertical trusses	Machined plate	Ti-6AL-4V	0.381 - 2.54 (0.150 - 1.00)	Engine out	Tension or compression	241.3-620.5 (35 - 90)				-106 - 176 (-160 - 350)	Mechanically fastened	Yes	Yes		•	1-7
7-15	Thrust tubes	Extruded tube/boron reinforced	Ti-6AL-4V and boron/epoxy	0.254 - 0.381 (0.100 - 0.150)	Engine out	Tension or compression	241.3-620.5 (35 - 90)				-106 - 176 (-160 - 350)	Welded and mechanically fastened	Yes	Yes		•	1-7

Table 1-7. Space Shuttle Orbiter Aft Fuselage (Cont)

I. D. No.	Structural Element	Type of Construction	Material	Typical Thickness Range cm (in.)	Design Mode			Other Design Condition			Structural Temp Range °C (°F)	Typical Structural Joint	Consequence of Failure		Possible Design Approach		Selection Logic
					Loading Condition	Type of Load	Stress, N/m ² x 10 ⁶ (ksi)	Loading Condition	Type of Load	Stress, N/m ² x 10 ⁶ (ksi)			Loss of Assembly	Loss of Vehicle	Fail-Safe	Safe-Life	
7-16	Fuel line support fittings	Machined plate	Ti-6AL-4V	0.254 — 2.54 (0.100 — 1.00)	Vibration and acceleration	Tension or compression	241.3-620.5 (35 — 90)				-106 -- 176 (-160 -- 350)	Mechanically fastened	Yes	Yes		•	1-7
7-17	Fuel line support beam web	Formed sheet	Ti-6AL-4V	0.081 — 0.304 (0.032 -- 0.120)	Vibration and acceleration	Tension or compression	241.3-620.5 (35 -- 90)				-106 -- 176 (-160 -- 350)	Mechanically fastened	Yes	Yes		•	1-7
7-18	Fuel line support beam caps	Extrusions	Ti-6AL-4V	0.254 (0.100)	Vibration and acceleration	Tension or compression	241.3-620.5 (35 -- 90)				-106 -- 176 (-160 -- 350)	Mechanically fastened	Yes	Yes		•	1-7
7-19	Thrust-hoist fitting	Diffusion bonded	Ti-6AL-4V	1.90 -- 2.54 (0.75 — 1.00)	Engine out	Tension or compression	241.3-620.5 (35 -- 90)				-106 -- 176 (-160 -- 350)	Mechanically fastened	Yes	Yes		•	1-7

Table 1-8. Space Shuttle Orbiter Vertical Stabilizer and Rudder

I. D. No.	Structural Element	Type of Construction	Material	Typical Thickness Range cm (in.)	Design Mode			Other Design Condition			Structural Temp Range °C (°F)	Typical Structural Joint	Consequence of Failure		Possible Design Approach		Selection Logic
					Loading Condition	Type of Load	Stress, N/m ² x 10 ⁶ (ksi)	Loading Condition	Type of Load	Stress, N/m ² x 10 ⁶ (ksi)			Loss of Assembly	Loss of Vehicle	Fail-Safe	Safe-Life	
8-1	Skin	Formed sheet	2024-T86 or T62	0.025-0.317 (0.010-0.125)	Entry glide back M = 0.9	Compression	330.9 (48.0)	Entry glide back M = 0.9	Shear	224.0 (32.5)	-101 to 176 (-150 to 350)	Mechanically fastened	Yes	Yes	•	•	1-7
8-2	Stringers	Formed sheet	2024-T86 or T62	0.050-0.254 (0.020-0.100)	Entry glide back M = 0.9	Compression	330.9 (48.0)						No	No	-	-	1-5, 9, 10
8-3	Nose ribs	Formed sheet	2024-T86 or T62	0.050-0.177 (0.020-0.070)	Max q boost	Compression	406.7 (59.0)						No	No	-	-	1-5, 9, 10
8-4	Ribs	Formed sheet	2024-T86 or T62	0.050-0.482 (0.020-0.190)	Entry glide back M = 0.9	Compression	330.9 (48.0)	Entry glide back M = 0.9	Shear	224.0 (32.5)			No	No	-	-	1-5, 9, 10
8-5	Spar caps	Extrusions	2024-T851	0.152-1.27 (0.060-0.500)	Entry glide back M = 0.9	Tension	TBD	Entry glide back M = 0.9	Compression shear	330.9 (48.0) 224.0 (32.5)			Yes	Yes		•	1-7
8-6	Spar web	Formed sheet	2024-T86 or T62	0.050-0.381 (0.020-0.150)	Entry glide back M = 0.9	Shear	224.0 (32.5)						No	No	-	-	1-5, 9, 10
8-7	Rubber actuator/hinge fitting	Machined plate	2124-T851	0.152-5.08 (0.060-2.00)	Approach and landing	Tension	TBD	Approach and landing	Bearing shear	TBD			Yes	No		•	1-5, 9, 10
8-8	Fuselage attachment plate	Machined plate	2124-T851	0.152-4.572 (0.060-1.80)	Entry glide back M = 0.9	Tension	206.8 (30.0)	Entry glide back M = 0.9	Compression shear	330.9 (48.0) 224.0 (32.5)			Yes	Yes		•	1-7
8-9	Stringers	Extrusions	2024-T8511	0.050-0.177 (0.020-0.070)	Entry glide back M = 0.9	Compression	330.9 (48.0)						No	No	-	-	1, 2, 10
8-10	Drag chute frame	Machined plate	2124-T851	TBD	Landing chute deployed	TBD	TBD					Mechanically fastened	Yes	No		•	1-6, 9, 10
8-11	Honeycomb panels	Adhesive bonded skin/core	2024-T86 or T62	0.040-0.101 (0.016-0.040)	Approach and landing	Compression shear	330.9 (48.0) 224.0 (32.5)	Entry glide back M = 0.9	Compression shear	330.9 (48.0) 224.0 (32.5)		Adhesive bond and mechanically fastened	Yes	Yes	•	•	1-7
8-12	Rudder ribs	Formed sheet	2024-T86 or T62	0.050-0.482 (0.020-0.190)								Mechanically fastened	Yes	No		•	1-5, 9, 10
8-13	Rudder front spar	Extrusion	2024-T8511	0.152-0.317 (0.060-0.125)								Mechanically fastened	Yes	Yes		•	1-7
8-14	Rudder rear spar	Formed sheet	2024-T86 or T62	0.050-0.228 (0.020-0.090)	Approach and landing	Compression shear	330.9 (48.0) 224.0 (32.5)	Entry glide back M = 0.9	Compression shear	330.9 (48.0) 224.0 (32.5)	-101 to 176 (-150 to 350)	Mechanically fastened	Yes	Yes		•	1-7

Table 1-9. Space Shuttle Orbiter Landing Gears

I. D. No.	Structural Element	Type of Construction	Material	Typical Thickness Range cm (in.)	Design Mode			Other Design Condition			Structural Temp Range °C (°F)	Typical Structural Joint	Consequence of Failure		Possible Design Approach		Selection Logic
					Loading Condition	Type of Load	Stress, N/m ² x 10 ⁶ (ksi)	Loading Condition	Type of Load	Stress, N/m ² x 10 ⁶ (ksi)			Loss of Assembly	Loss of Vehicle	Fail-Safe	Safe-Life	
MAIN LANDING GEAR																	
9-1	Upper drag brace	Flash-welded tube or forging	300 M	0.556 (0.219)	2-Pt brake roll	Shear	937.6 (136)	Reverse braking	Column compression	461.9 (67)	-54 → 121 (-65 → 250)	Welded and mechanically fastened	Yes	Yes		•	1-7
9-2	Lower drag brace	Flash-welded tube or forging	300 M	0.396 (0.156)	2-Pt brake roll	Shear	937.6 (136)	Reverse braking	Column compression	848.0 (123)		Welded and mechanically fastened	Yes			•	
9-3	Main cylinder	Forging	300 M	0.635 - 1.9 (0.250 - 0.750)	2-Pt brake roll	Bending + shear	1958.4 (284) 186.1 (27)	Turning	Hoop tension	1640.9 (238)		Mechanically fastened	Yes			•	
9-4	Main landing gear piston	Forging	300 M	0.396 - 1.112 (0.156 - 0.438)	Turning	Bending + shear	2158.0 (313) 110.3 (16)	Turning	Bending + shear	1930.5 (280) 191.0 (28)			Yes			•	
9-5	Upper lock brace	Forging	300 M	0.457 - 0.965 (0.180 - 0.380)	Retraction	Bending	1061.7 (154)	Retraction	Shear	717.0 (104)			Yes			•	
9-6	Lower lock brace	Forging	300 M or 7075-T6	(Alum) 2.54 (1.0)	Retraction	Shear	82.7 (12)						Yes			•	
9-7	Cross tube	Forging	300 M	1.193 (0.470)	Reverse braking	Tension	503.3 (73)	Retraction	Shear	110.3 (16)			Yes	Yes		•	1-7
9-8	Drag brace cross brace	Tubing	7049-T73	0.713 (0.281)	2-Pt brake roll	Column compression	158.5 (23)						No	No	-	-	1, 2, 10
9-9	Axle	Forging	300 M	0.566 - 1.109 (0.219 - 0.437)	Turning	Bending + shear	1572.0 (228) 799.7 (116)						Yes	Yes		•	1-7
9-10	Torque arm	Forging	300 M	0.635 - 3.492 (0.250 - 1.375)	Pivoting	Bending	1854.6 (269)	Pivoting	Shear	992.8 (144)	-54 → 121 (-65 → 250)	Mechanically fastened	Yes	Yes		•	1-7
NOSE LANDING GEAR																	
9-11	Upper drag brace	Flash-welded tube or forging	300 M	0.635 - 1.27 (0.250 - 0.500)	Spinup	Tension	827.3 (120)	Spring-back	Column compression	223.3 (32.4)	-54 → 121 (-65 → 250)	Welded and mechanically fastened	Yes	Yes		•	1-7
9-12	Lower drag brace	Flash-welded tube or forging	300 M	0.482 - 0.952 (0.190 - 0.375)	Spinup	Tension	1206.5 (175)	Spring-back	Column compression	985.9 (143)	-54 → 121 (-65 → 250)	Welded and mechanically fastened	Yes	Yes		•	1-7

REPRODUCIBILITY OF THE ORIGINAL PAGE IS POOR

Table 1-9. Space Shuttle Orbiter Landing Gears (Cont)

I.D. No.	Structural Element	Type of Construction	Material	Typical Thickness Range cm (in.)	Design Mode			Other Design Condition			Structural Temp Range °C (°F)	Typical Structural Joint	Consequence of Failure		Possible Design Approach		Selection Logic
					Loading Condition	Type of Load	Stress, N/mm ² x 10 ⁶ (ksi)	Loading Condition	Type of Load	Stress, N/mm ² x 10 ⁶ (ksi)			Loss of Assembly	Loss of Vehicle	Fail-Safe	Safe-Life	
9-13	Shock strut main cylinder	Forging	300 M	0.317 — 1.905 (0.125 — 0.750)	Spinup	Bending + shear	1813.3 (263) 75.8 (11)				-54 — 121 (-65 — 250)	Mechanically fastened	Yes	Yes		•	1-7
9-14	Shock strut piston	Forging	300 M	0.584 — 1.397 (0.230 — 0.550)	Spinup	Bending + shear	1909.8 (277) 255.1 (37)						Yes			•	
9-15	Axle	Forging	300 M	0.317 — 1.905 (0.125 — 0.750)	Turning	Bending + shear	537.7 (78) 806.6 (117)						Yes			•	
9-16	Torque links	Forging	300 M	0.533 — 0.635 (0.210 — 0.250)	Spinup	Bending	1096.2 (159)						Yes			•	
9-17	Down-lock brace, upper	Forging	300 M	0.635 — 0.792 (0.250 — 0.312)	Landing	Bending + shear	2213.2 (321) 103.4 (15)						Yes			•	
9-18	Down-lock brace, lower	Forging	7075-T6	0.317 — 0.787 (0.125 — 0.310)	Spring-back	Bending + shear	1254.8 (182) 89.6 (13)						Yes			•	
9-19	Drag brace cross tie	TBD	300 M or 7075-T6	(Steel) 0.317 (0.125)	Spinup	Bending	620.5 (90)				-54 — 121 (-65 — 250)	Mechanically fastened	Yes	Yes		•	1-7

1.2 CRITICAL PART SELECTION LOGIC

Sometimes it is convenient to use a selection logic diagram to evaluate the criticality of a given structural element. The selection logic diagram used for this study is presented in Figure 1-1. The criticality of a given part is generally evaluated by following through one of the six possible screening paths. These flow paths are illustrated in the following:

1. 1 → 2 → 10
2. 1 → 2 → 3 → 10
3. 1 → 2 → 3 → 4 → 9 → 10
4. 1 → 2 → 3 → 4 → 5 → 9 → 10*
5. 1 → 2 → 3 → 4 → 5 → 6 → 9 → 10*
6. 1 → 2 → 3 → 4 → 5 → 6 → 7 → 8(a) or 8(b) or 8(c)

*Alternate path

- 4a. 1 → 2 → 3 → 4 → 5 → 9 → 7 → 8(a) or 8(b) or 8(c)
- 5a. 1 → 2 → 3 → 4 → 5 → 6 → 9 → 7 → 8(a) or 8(b) or 8(c)

The sequence of steps outlined in each flow path is not a rigid requirement for application of this flow diagram, but it is suggested that these would be the natural steps and sequences when the subject diagram is being employed.

Prior to showing how to apply the Critical Part Selection logic diagram, it is necessary to discuss the rationale and the significance of the intermediate steps outlined in the flow diagram. Steps 1, 2, and 3 are self-explanatory. Other steps are discussed in the following paragraphs.

1.2.1 Loss of Assembly (Step 4)

A structural element, or a part, is a single item such as those listed in Tables 1-1 to 1-9. An assembly is considered to be a built-up structure which functions as a single unit in the Shuttle vehicle system. The external tank, the solid rocket booster, and the nose or main landing gears are obvious examples. Just for convenience, an assembly is regarded to be the structural sections or components entitled in Tables 1-1 to 1-9, except that the nose landing gear and the main landing gear are considered to be separate assemblies. The pressure vessels inside the orbiter are other exceptions because each of these pressure vessels acts as a single structural element as well as an individual structural assembly.

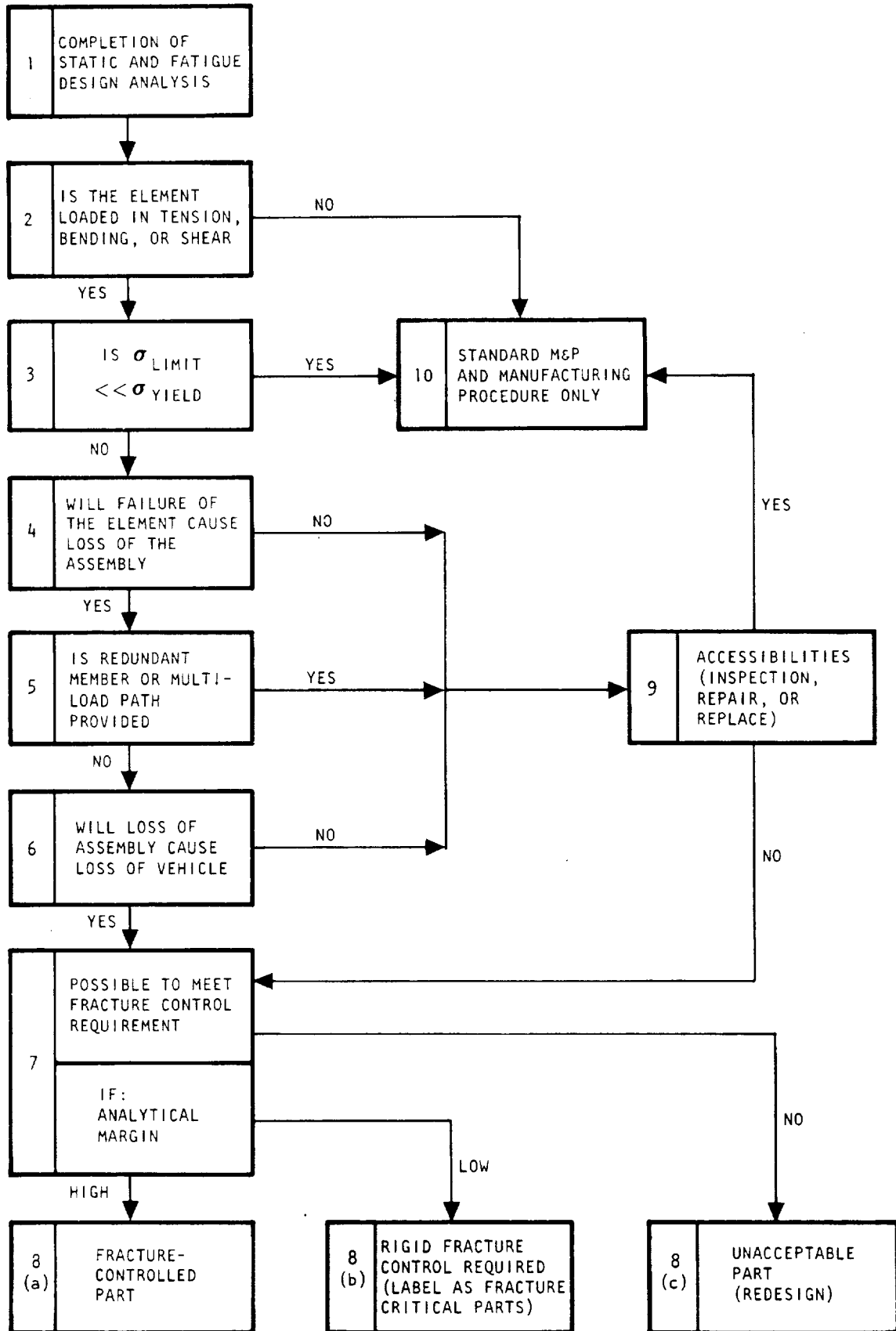


Figure 1-1. Critical Part Selection Logic

1.2.2 Loss of Vehicle (Step 6)

The impact on structural integrity because of failure of a single structural element and the subsequent effect caused by failure of a structural assembly depends largely on the nature of the failure mode and sometimes on engineering judgment. As a rule of thumb, failure of a primary structure (e.g., a skin panel or a longeron), any explosive type of failure, or failure of anything that would result in loss of the wing or a landing gear are considered detrimental to flight safety (will cause loss of vehicle). Except for the landing gears, structural assemblies that fail in the ground phases (after touchdown and during rollout) of a flight might be considered non-detrimental to flight safety (will not cause loss of vehicle).

1.2.3 Redundant Member or Multiload Path (Step 5)

The purpose of the Critical Part Selection logic diagram is to aid the designer in easily identifying the criticality of a given structural element without doing any calculations or analysis up to Step 7 or, alternatively, Step 10, as the case might be. Following Step 4, an idea is supplemented by Steps 5 and 9. The idea implies the following: Failure of a single structural element may not immediately cause catastrophic failure of the entire section of the structure. Redundant members or multiload paths (if there are any) adjacent to the failed member usually hold the local section of the structure together and thus temporarily maintain the integrity of the assembly. However, the failed member should be detectable and repairable; otherwise, catastrophic failure of the assembly might still occur in the subsequent missions. It should be noted that, unlike the conventional concept of fail-safe design, redundant members are not regarded as fail-safe structure here. Whether or not a given structural component be fail-safe, it is necessary to conduct a fail-safe analysis on the part and prove that the part meets fail-safe requirements. Therefore, in this step the redundancy of a given structure would be solely judged by its basic structural arrangements. A truss member in the wing box or stringers connected with splices and frames or sometimes the extra piece of hinge fittings, etc., are typical examples. The concept of fail-safe will be discussed in more depth in later sections.

1.2.4 Accessibility Requirements (Step 9)

It is observable in the selection logic diagram that the importance of the accessibility requirement has been emphasized a great deal. It implies that all the structural elements should be accessible. Regardless of the consequence of failure (will or will not cause loss of vehicle), a redundant element or an element which is intentionally designed for fail-safe will not be called redundant or fail-safe unless it is accessible for inspection, replacement, or repair.

1.2.5 Evaluation of Potentially Fracture-Critical Parts (Step 7)

By going through the screening operations starting from Step 1 to Step 6 (or alternatively Step 9), a given structural element will be identified as:

1. Noncritical part (Step 10), or
2. Potentially fracture-critical part (Step 7)

The consequences of the three possibilities that a structural element might be fracture-critical are as follows:

1. Failure of the element will cause loss of a section of the structure (or so-called assembly) and subsequently cause loss of the vehicle.
2. Failure of the element will cause loss of the assembly but may not cause loss of the vehicle. This element is neither repairable nor replaceable.
3. Failure of the element would normally cause loss of the assembly. This element is a member of a redundant structural system. However, this element is neither inspectable, repairable, nor replaceable.

Presumably these structural elements have already been sized to meet static and fatigue requirements as indicated in Step 1; in Step 7, the actual degree of criticality would be evaluated by fracture mechanics analysis. The result of fracture mechanics analysis determines and categorizes the part to be either:

1. Nonfracture-critical (or called the fracture-controlled part, Step 8a)
2. Fracture-critical (Step 8b), or
3. Unacceptable (Step 8c)

Here the fracture-controlled parts in Step 8a are basically the same as those noncritical parts in Step 10. The only difference is that the parts in Step 8a are considered to be potentially critical, but it has been proven by analysis that the parts will meet the residual strength and longevity (safe crack growth) design requirements.

Fracture-critical parts are those not obviously acceptable or rejectable parts. Rigid fracture control procedures are required for these parts. Procuring upgraded alloy, reducing design stress levels, applying stress intensity reduction methods, re-establishing reliable inspection intervals,

or compromising for shorter safe-life period, etc., are commonly usable fracture control methods. In some cases, especially for parts that have been chosen to incorporate with resizing or employment of crack stoppers, these parts are essentially redesigned and no longer fracture-critical.

1.2.6 Critical Part Selection Logic Application Examples

After examination of the geometry and loading condition and consideration of the possible failure modes applicable to the part and the rationale (just discussed in the previous sections), the selection logic diagram can be used to determine whether a given part is potentially fracture-critical or nonfracture critical. Each structural element listed in Tables 1-1 to 1-9 was evaluated and the logic selections were determined. The results are also listed in Tables 1-1 to 1-9.

The following examples are typical of those elucidated by the selection logic.

1. Element No. 2-4, Forward Thrust Fitting. Failure of the fitting will cause loss of the SRB. However, under normal circumstances the SRB will probably be dropped from the Shuttle system and leave the Shuttle orbiter unharmed. Therefore, the selection path would be Steps 1 to 6, then 9 and 10.
2. Element No. 3-2, LO₂ Tank Cylindrical Body. Explosive failure of the liquid oxygen tank will cause loss of the entire external tank system and also damage the Shuttle orbiter. Therefore, the selection path would be Steps 1 to 7.
3. Element No. 4-5, Wing Carry-Through Skin Panel. Whether failure of this skin panel will or will not cause loss of the entire mid-fuselage section, it certainly will cause loss of the wing. However, since the tension load only occurs at the landing phase of the mission, it can be assumed that failure of this element is tolerable. The selection path would be Steps 1 to 6, then 9 and 10.
4. Element No. 4-10, Wing Carry-Through Spar Frames. Again, failure of this element will cause loss of the wing. In this case, the bending loads occur at both the boost and maneuver phases of the mission. Therefore, it is potentially fracture-critical (selection path Steps 1 to 7).
5. Element No. 5-5, Rib EMF Tubes. Since these tubes form a redundant truss member system, the selection path would be Steps 1 to 5, then Steps 9 and 10.

(Note that the logic of selections have been based on the assumptions that accesses for inspection, repair, or replacement were adequately provided for all the structural elements listed. It is realized that alternate selection paths should be used on some elements for which access problems are identified.

2.0 FRACTURE CONTROL METHODS

Fracture control methods can be grouped under two general conceptual approaches:

1. Take all reasonable measures to prevent the occurrence or initiation of crack-like defects.
2. Establish design configurations, inspection requirements, etc., to ensure that any such defects will be detected and removed or repaired before they cause catastrophic failure during operational service.

Figure 2-1 is a diagram of major elements which might be involved in an overall fracture control program. This diagram illustrates the relationship and interaction between technical and functional activities in the application of basic fracture control methods.

Approaches under the first category generally relate to prevention of cracks from mechanical, chemical, or combined mechanical and chemical causes. The methods do not require application of fracture mechanics technology because, by definition, no crack-like flaws are assumed to be present. The methods are essentially concerned with the fatigue life of a structural element. Two major areas of interest are involved.

1. Design and its impact on fatigue life assurance
2. The role of material processing and manufacturing procedures on prevention of crack-like defects and material environmental resistance

Design and fatigue-life assurance are discussed in Section 2. 1. Discussions on material and manufacturing are presented in Section 2. 2.

The second category of the approaches is essentially fracture-mechanics-based design and analysis methodologies. It assumes that cracks or flaws could exist in the structure at the start of operational service. Fracture mechanics analyses and data are then applied to predict flaw growth and residual strength from this initial condition under the expected loads and environments of service operation. Methods for this kind of fracture control will be discussed in Section 2. 3.

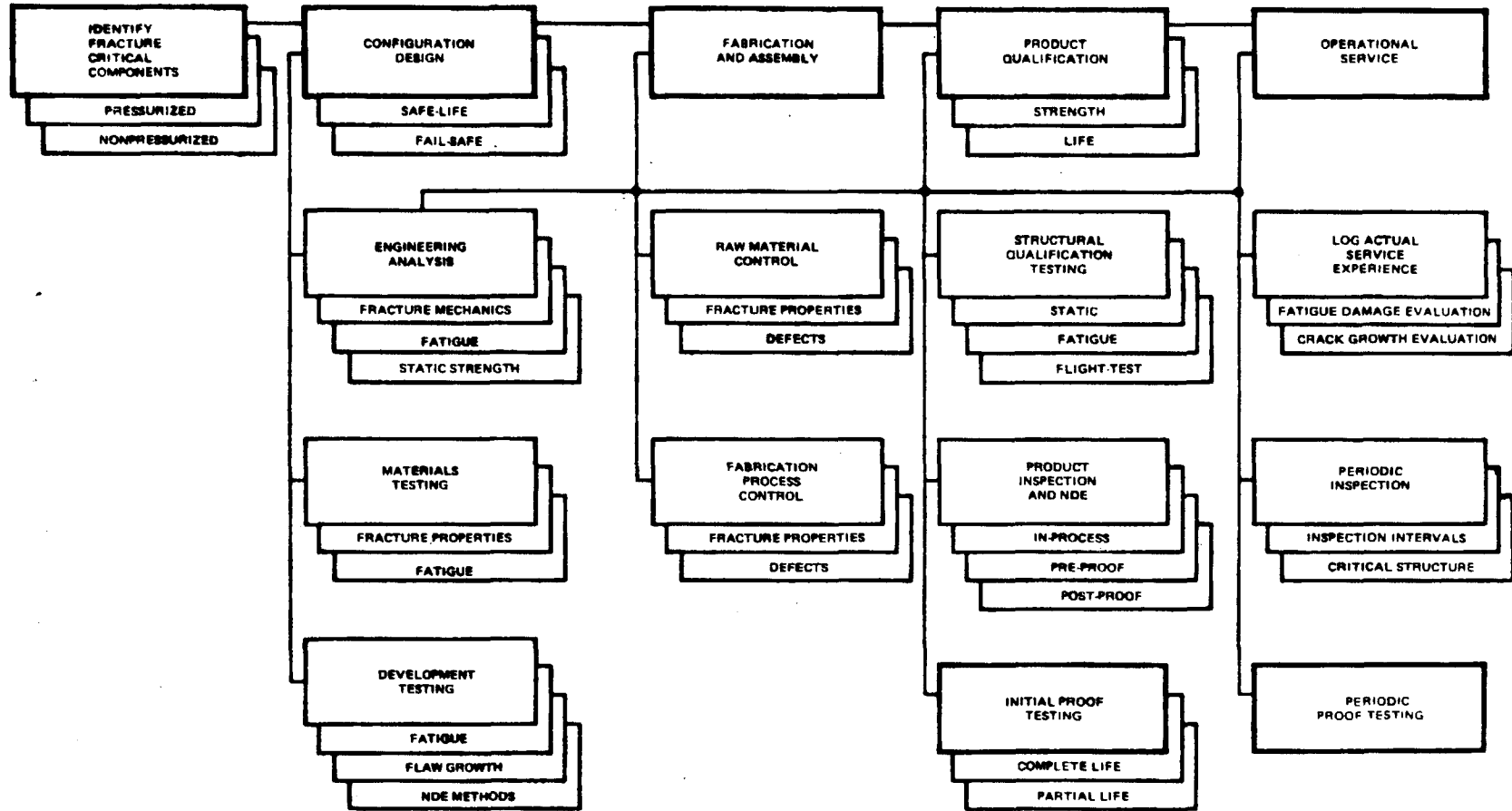


Figure 2-1. Fracture Control Program Elements

Successful implementation of these fracture control design methods, particularly for the fracture-mechanics-based approaches, requires a very important supplementary engineering tool: nondestructive evaluation (NDE). The ability to detect flaws significantly and directly affects the results of fracture mechanics analyses and the establishment of inspection intervals. The current NDE techniques available to Space Shuttle structure applications and the rationale for how, when, and where to apply these techniques onto actual Space Shuttle structural hardware are discussed in Section 2.4.

2.1 FATIGUE DESIGN AND ANALYSIS METHODS

Structural fatigue design criteria are established with the main objective of designing a primary structure which will experience no fatigue failures during its required lifetime. For this objective to be attained, within acceptable accuracy tolerances, the following information and analysis methods are required:

1. Service-life requirements and planned operational usage
2. Fatigue load input spectra representative of the required life and expected operational usage
3. Methods to calculate structural element fatigue load response spectra
4. Method to calculate fatigue damage for expected life and to predict the safe fatigue life
5. Structural element fatigue strength properties and the factors that affect the fatigue performance

Figure 2-2 illustrates the relationships among these five major areas in fatigue design and analysis. Items 1, 2, and 3 are not within the scope of the present study. Only the materials regarding items 4 and 5 will be discussed in the following sections.

2.1.1 Fatigue Performance

Fatigue properties of airframe structures are affected by many variables. They are not necessarily independent variables, many of them being interrelated and acting as fatigue performance functions. These variables can be considered in two parts: (1) the type of loading and environment and (2) design and materials where, in the material area, material processes, manufacture, and the material itself are included. The three areas—material, design and manufacture—are grouped because of the interrelationships of design, material utilization, and subsequent

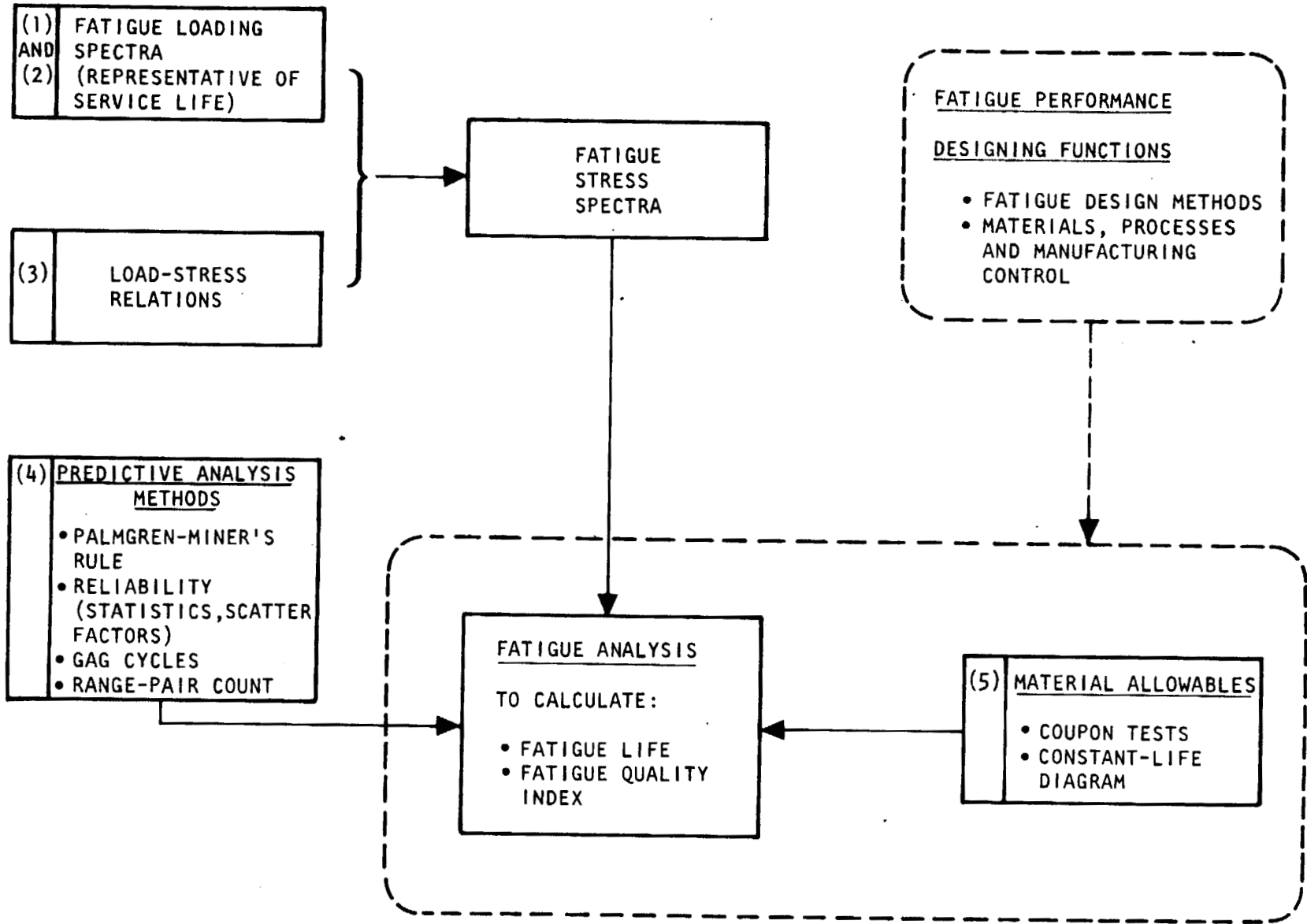


Figure 2-2. Elements for Fatigue Design and Analysis

manufacture. In the area of fatigue, the designer must consider the potential influence of not only his work in configuration, but also the very details of a fabrication process.

Some factors in these two major areas which can significantly affect the fatigue performance are:

1. Loads and environment (operational functions)
 - a. Flight profile
 - b. Load environment (gust load, maneuver load, etc.)
 - c. Directional effects
 - (1) Uniaxial (axial load, rotary bending, vibratory bending, etc.)
 - (2) Biaxial
 - (3) Triaxial
 - (4) Combination of the above
 - d. Stress ratio
 - e. Stress wave form
 - (1) Constant amplitude (sinusoidal, square, etc.)
 - (2) Varying amplitude (spectrum, sequence, random, etc.)
 - f. Temperature
 - g. Surroundings or foreign matter
 - (1) Vacuum
 - (2) Radiation
 - (3) Humidity
 - (4) Corrosive media
 - (5) Fretting corrosion

- h. Frequency
- i. Rest period
- j. Length of flight (i. e. , add more ground-air-ground cycles into the total expected life for the case of shorter flight usage)

2. Design and materials (designing functions)

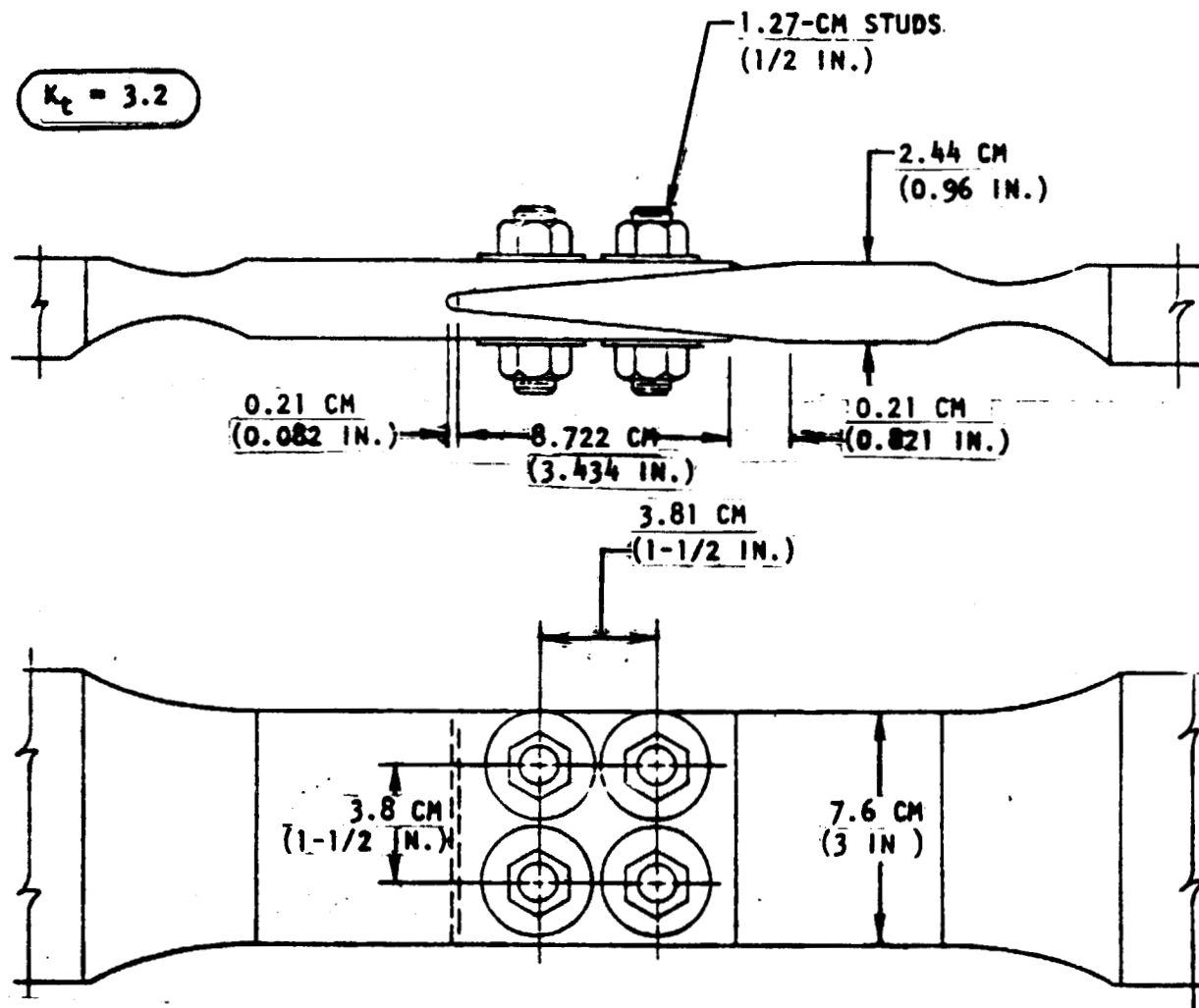
- a. Stress concentrations
 - (1) Local geometry
 - (2) Notches
 - (3) Joints
 - Mechanical (pin fastened)
 - Brazed
 - Adhesively bonded
- b. Size
- c. Shape
- d. Pre-stress and residual stress
- e. Surface condition
 - (1) Coating
 - (2) Roughness
- f. Manufacturing (machining, forming, etc.)
- g. Microstructure and substructure
 - (1) Chemistry
 - (2) Heat treatment
 - (3) Product form

2.1.2 Detail Design Considerations

There are many excellent textbooks and documents (References 1 to 8) discussing in detail the effects of the factors (listed in the previous section) on fatigue performance. In addition, metallurgical aspects of fatigue are thoroughly discussed in the literature. Therefore, it is not necessary to discuss every one of these subjects here. One very clear fact concerning fatigue performance is the importance of the very local stress, its stress field or gradients, and its variation with time. In other words, for a given structural element, the loads and environment that this piece of structure would experience are generally predetermined by the planned operational usage. Therefore, engineers are directly associated with the detail design and the subsequent manufacture of the structure. From the stress engineer's or the designer's point of view, the fatigue life of an airframe structure to withstand a given loading spectrum is expected to be controlled by the operational stress level and the quality of the detail design. Identification or visualization of the potential fatigue-critical areas and corrective actions on designs of these areas in the structure are important in all the design stages.

The well-known tests of Hartman et al. (References 9 and 10) are shown in Figures 2-3 to 2-7, where five joint configurations are presented. The fatigue quality index (effective K_t) for these joints was determined from the fatigue test results of these specimens. It is seen that the double-scarf joint specimen exhibited a K_t value of 3.2 (the best of all), while the double shear joint specimen and the stepped double shear joint specimen exhibited K_t values of 4.1 and 4.3, respectively. The K_t values for the plain-scarf joint specimens ranged from 4.1 to 8.1, depending upon the material. The worst is the single shear joint specimen, which exhibited a K_t value of 13.0. The better fatigue performance in the first three types of joints is partly a result of the configuration and partly because these specimens consisted of fewer fasteners in a row in these joints.

The second example is illustrated in Figure 2-8. It presents three designs for a spar chord which attaches the skin panel and the web. This example shows the importances of fastener pattern and notches in the sheet. Three degrees of accomplishments in these joints are cited: a best design, a conditionally acceptable design, and an unacceptable design.



(Reference 9)

Figure 2-3. Double-Scarf Joint Specimen

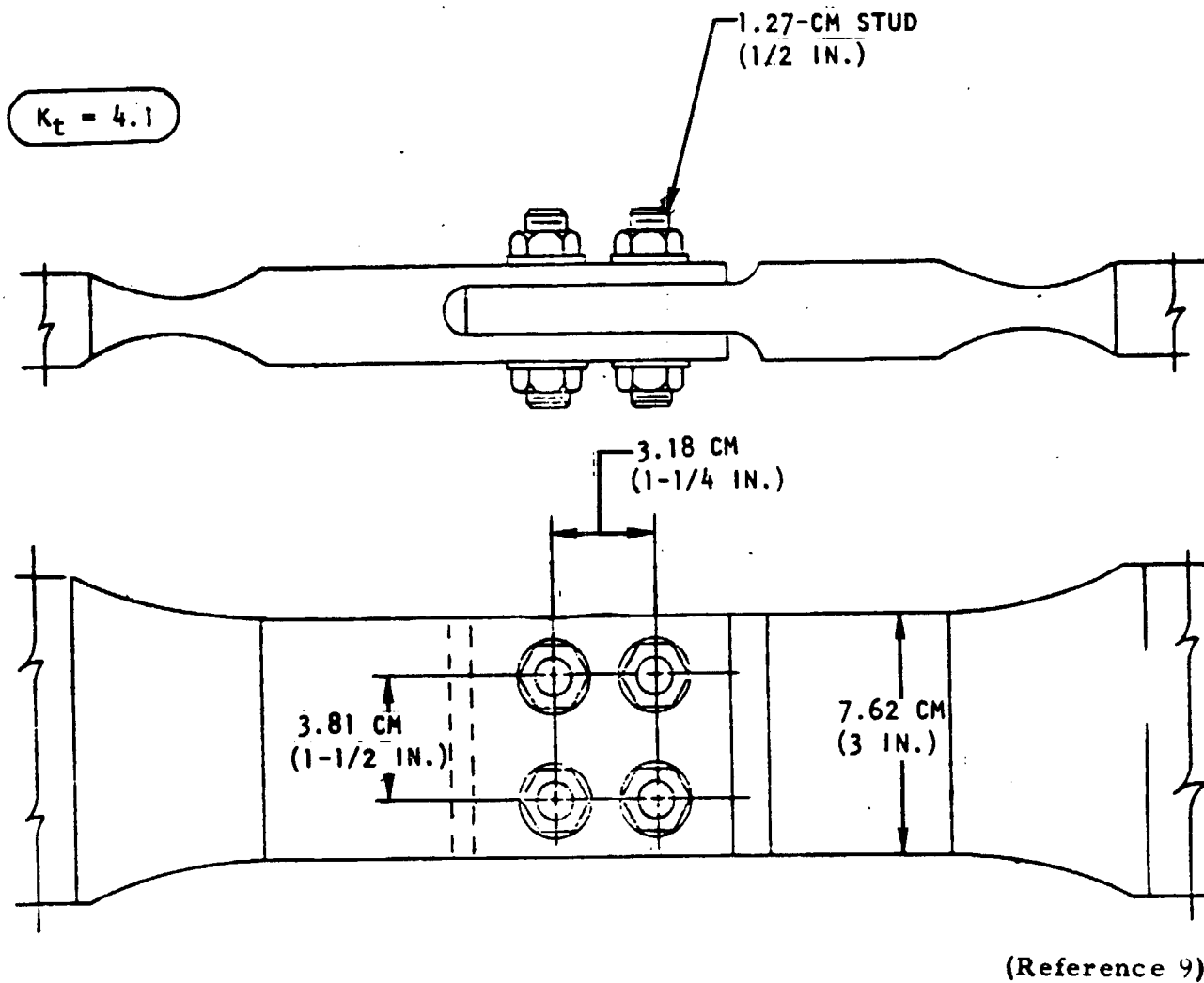
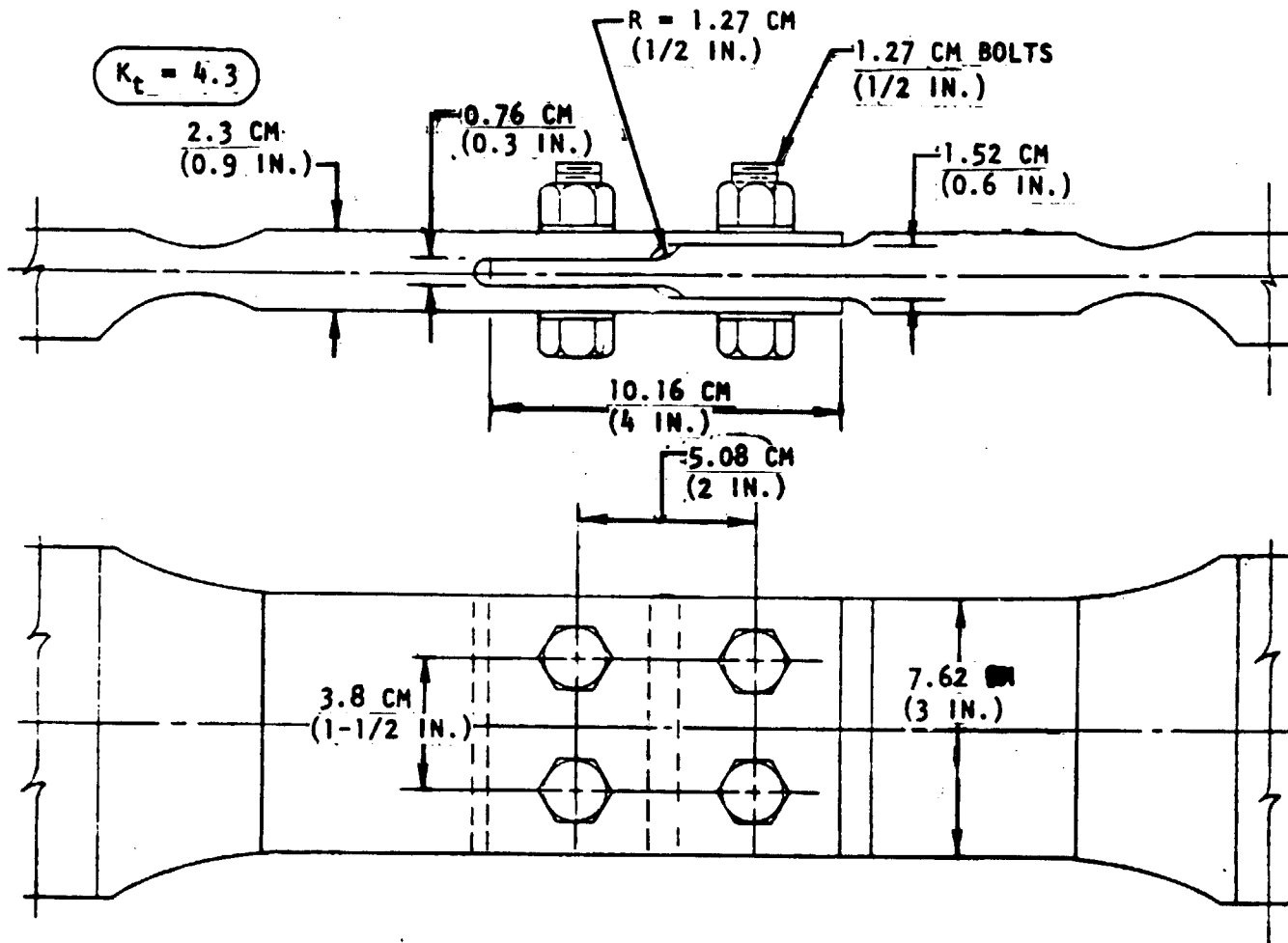


Figure 2-4. Double-Shear Joint Specimen

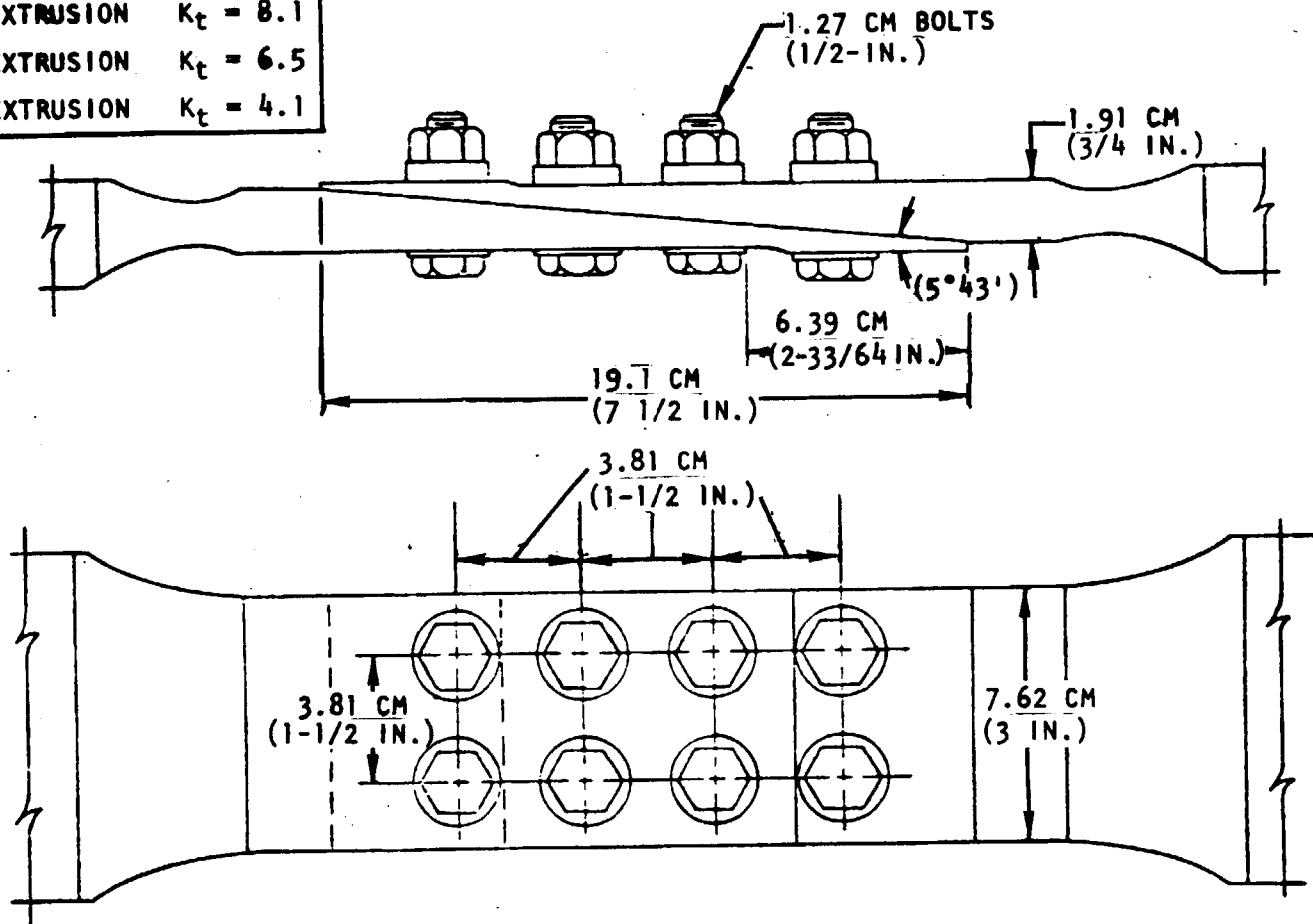
(Reference 9)



(Reference 10)

Figure 2-5. Stepped Double Shear Joint Specimen

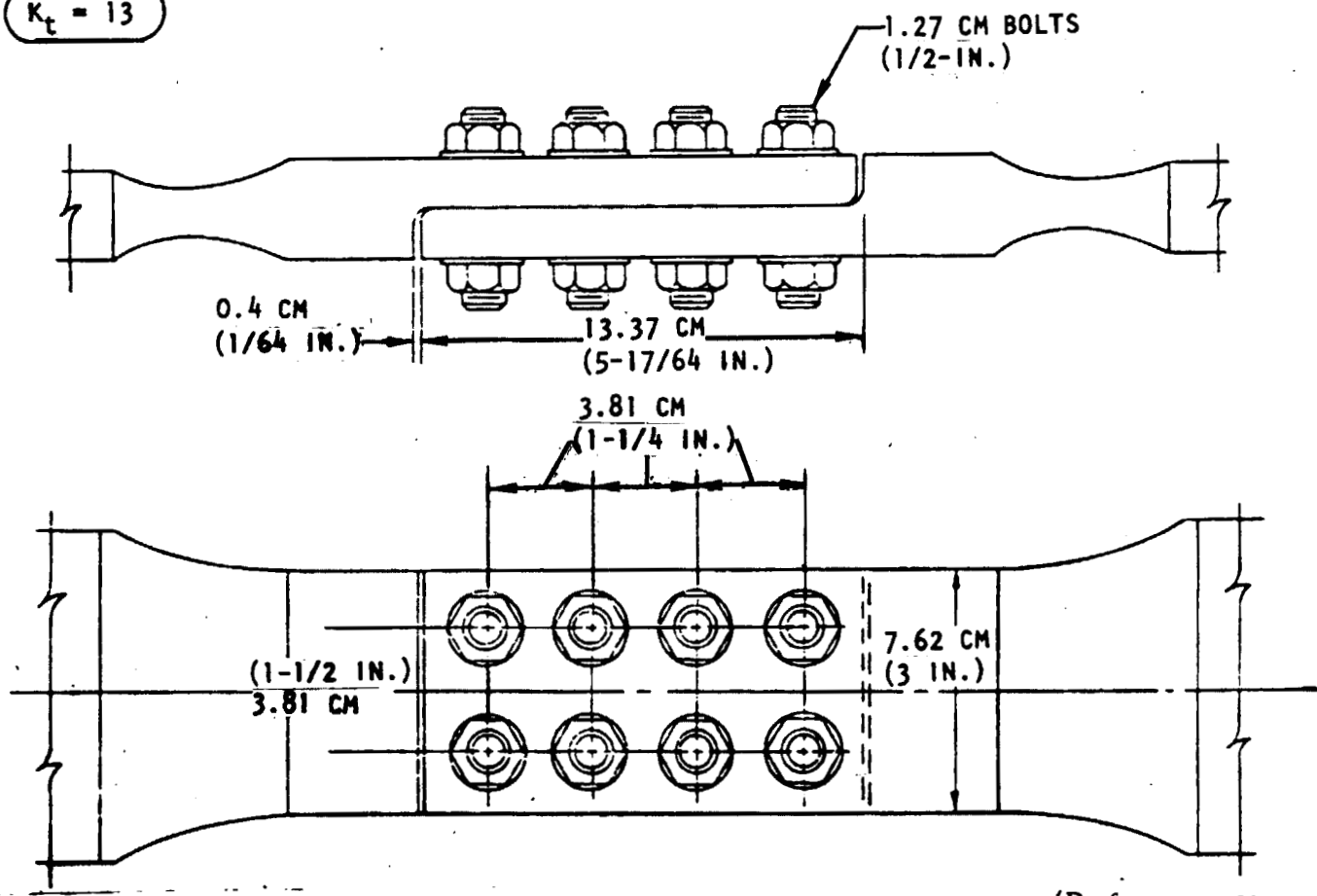
75S-T6 EXTRUSION	$K_t = 8.1$
14S-T6 EXTRUSION	$K_t = 6.5$
24S-T4 EXTRUSION	$K_t = 4.1$



(Reference 9)

Figure 2-6. Plain-Scarf Joint Specimen

$K_t = 13$



(Reference 9)

Figure 2-7. Single-Shear Joint Specimen

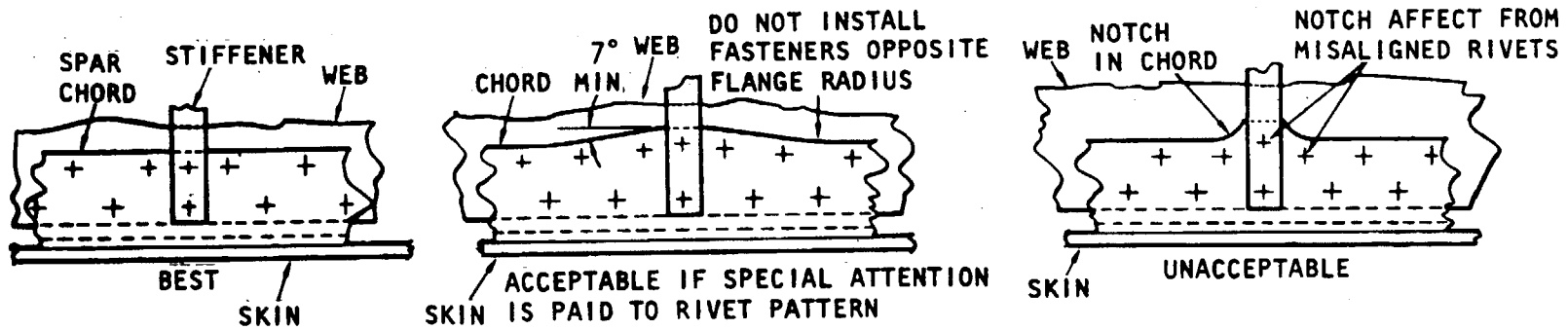


Figure 2-8. Continuous Member Tension Design

With the aid of the modern digital computer technology, fatigue performance can be analyzed for any complicated joint configurations in the airframe structure. Examples are the stress severity factor technique for modeling the multiple pin joint (Reference 11) and application of the graded-modulus bonding concept to analysis of a lap joint (Reference 12). It is anticipated that increasing work in this area will continue so that the structural component configuration, and correspondingly higher fatigue performance, can be optimized.

2. 1. 3 Fatigue Analysis Methods

Figure 2-2 illustrates the analysis procedure for predicting the fatigue life for a given design stress or the design stress for a given fatigue life. The fatigue loading spectra, together with the relationship between load and stress, are used to define the fatigue stress spectra. For preliminary design, various load-stress relationships are assumed so that the relationship between design stress and fatigue life can be obtained. Fatigue load spectra for wing, fuselage, or vertical stabilizer are usually presented as load-exceedance curves. A discrete loading distribution is needed to give the actual number of cycles to be applied at discrete load levels for the purpose of representing a cumulative loading or stress spectrum in fatigue tests and for fatigue analysis. The procedure for converting a cumulative stress spectrum to a discrete stress spectrum is to divide the load-exceedance curve into regular segments. The difference between excessive exceedances at each increment is the number of load occurrences within that increment. An average value of load within that increment is used to represent all load cycles that occur over that increment. For structural elements with a more discrete load cycle, such as landing gear and propellant tankages, the load spectra are defined directly (in the form of a table). For an accurate prediction of the fatigue lives and fatigue crack propagation rates, a correct representation of the fatigue loads or fatigue stress spectrum is essential. The load-exceedance curve only indicates the probabilities of occurrences that the applied stress level would equal or exceed certain values. The variation in stress from ground taxi to, and during, flight and back to ground taxi must be defined for the fatigue analysis. This stress variation, the ground-air-ground (GAG) cycle, is one of the most important stress cycles contributing to the fatigue damage of the structure. The examples given in Figure 2-9 illustrate the meaning of two GAG cycle definitions commonly used for fatigue analysis: the mean-to-mean GAG cycle and the once-per-flight peak-to-peak GAG cycle. Of these two definitions, the peak-to-peak GAG is generally used because it provides the best correlation between the spectrum fatigue test conducted on notched coupons and fatigue analysis. It should be noted that for the Space Shuttle orbiter, there are at least three kinds of GAG cycles. These GAG cycles represent the prelaunch to docking phase, and the undocking to reentering (all the way until touchdown) phase during the orbital flight, and the regular kind of GAG cycles for the ferry mission.

In addition to the GAG cycles, the peaks and valleys between every single load cycle, especially those connecting a climb from one lower stress level to a high stress level, are not reflected in the load-exceedance curve. In a recent survey conducted by Dowling (Reference 13), it was revealed that the so-called "range-pair cycle counting" method would properly account for these missed portions in the spectrum. A brief description of the "range-pair cycle counting" technique has been reported in Section 6 of Volume II and will not be pursued here. Note that the "range-pair cycle counting" technique permits identification and definition of the ground-air-ground load cycles and any other significant secondary load excursions; therefore, when this cycle-counting procedure is used, the ground-air-ground cycles do not have to be defined separately.

The fatigue stress spectra and the material fatigue allowables, in the form of S-N curves or constant-life diagrams, are the input data required for the fatigue analysis. The fatigue calculations are performed with the use of some damage rule which defines the relationship between the applied stresses and number of cycles and the allowable stresses and number of cycles required to cause failure.

Numerous cumulative damage methods have been proposed, and an extensive evaluation of the various methods was made in Reference 14. Of all the methods surveyed, all of which were based on experimental results, the linear cumulative damage procedure (Palmgren-Miner's rule) was recommended for its simplicity, versatility, availability of applicable S-N data, and accuracy commensurate with the available data for fatigue analysis in general. Although this theory does not account for the loading sequence and its effects, the survey conducted in Reference 14 has revealed that over a wide range of circumstances no other proposed method predicts the fatigue life significantly better. The basic equation, based on Palmgren-Miner's rule, for calculating fatigue damage is expressed as

$$D = \sum_{i=1}^k \frac{n_i}{N_i} \quad (1)$$

where

n_i = number of loading cycles at the i^{th} stress level

N_i = number of cycles to failure for the i^{th} stress level based on constant amplitude S-N data for the applicable material and K_t value

k = number of stress levels considered in the analysis.

Equation (1) implies that the total fatigue damage is the sum of the damage for each increment of the loading spectra. The ratio of the number of applied load cycles to allowable load cycles is the fatigue damage for a given increment of the loading spectra. Since the loading spectra represents a specified period of service life, e. g., 10,000 hours or 1000 missions, etc., ideally the calculated total damage factor, D, should equal unity or 0.25 if a safety factor of 4.0 is desired. The predicted fatigue life for a given fatigue stress spectra (based on a selected limit design stress level) would be

$$L_f = \frac{L}{F \cdot D} \quad (2)$$

where

L = hours or number of missions represented by the spectra used in the analysis

F = factor of safety

L_f = predicted fatigue life divided by a safety factor

Equation (1) can also be used to estimate the fatigue quality (effective K_t) of a given structural design. Generally, the fatigue quality of the structure is determined from results of fatigue tests of components or the complete air-frame structure. The fatigue quality index can be computed at each crack location developed during fatigue testing. Fatigue analyses are conducted with a set of constant amplitude S-N curves used for various values of K_t obtained from simple notched coupons. The stress spectrum that was sustained at each critical point to fatigue crack initiation in the test is determined from the spectra of applied loads. Results of the analyses are interpolated to determine the specific S-N curve which makes the D value in Equation (1) equal to unity for the test life. The value of K_t associated with the S-N curve is a measure of the fatigue quality index. The better structure is the structure with a lower effective K_t .

2.2 PREVENTION OF CRACKS AND CRACK-LIKE DEFECTS IN SPACE VEHICLE STRUCTURE

2.2.1 Administrative Controls and Activities

Initiation or propagation of cracks and crack-like defects in space vehicle structures should be minimized by implementation of controls and preferred practices such as those described in material specifications (MS's), material process specifications (MPS's), and material processing procedures

(MPP's). In addition, design manual (DM) practices have been developed to guide the designer toward selection and use of materials, fabrication processes, and parts that will preclude initiation or propagation of cracks during manufacturing, test, or use environments.

A material list document should be prepared and distributed in the in-house design engineering functions. This document describes the basic characteristics of preferred materials in several test and use environments and establishes minimum-maximum temperature usage for each of these preferred materials. A similar document should be prepared for subcontractor-furnished items.

Supplementing these documentary controls and practices will be the review and approval of drawings (release sign-off procedure) by knowledgeable disciplines involved with the selection, processing, and use of materials.

2.2.2 Technical Activities

Summarized in the paragraphs that follow are typical guidelines for construction of space vehicle structure to preclude cracks from the possible sources noted.

2.2.2.1 The Influence of Alloy Selection, Form, Temper, and Processes

Undisclosed defects can exist in the basic raw material and these defects may propagate during operations such as forming, heat treating, and chemical milling. As an example, grain orientation in metals, particularly in aluminum alloys, is a significant design consideration. **The mechanical properties, including elongation, are reduced in the short transverse direction of plate and bar products, which can cause cracking of stress-corrosion-susceptible material when it is loaded in this direction. High-strength, low-alloy steels are susceptible to process-induced cracks during heat treatment, cleaning, grinding, or plating operations.**

To preclude generation of propagation of cracks resulting from alloy selection, form, temper, and processing, the following procedures should be implemented:

1. Whenever possible, select materials which have inherent toughness and a tolerance to undisclosed defects. Selection will be by judgment, in some cases, based on experience with the material itself or on other recognized toughness criteria such as impact resistance, fatigue resistance, or plane strain fracture toughness, K_{IC} value.

2. Use forgings rather than castings in critical applications due to the preferred multidirectional uniformity of mechanical properties. The forging process has other inherent benefits, including the healing of small casting defects or, perhaps more significantly, eliminating gross defects by failure in the forging process.
3. Limit the minimum and maximum strength levels of low-alloy steels as a result of heat treatment to ensure safe, crack-free operation of parts at the intended use temperature.
4. Control the process parameters involved in manufacturing operations such as heat treatment, cleaning, grinding, chemical milling, and plating by invoking material processing procedures containing restraints and stringent quality assurance provisions and controls.
5. Using machine welding rather than hand weld methods, if applicable. Titanium weldments will be required in evacuated and inert gas backfilled chambers to preclude the pickup of and embrittlement of the titanium by interstitials.
6. Materials known to be susceptible to hydrogen embrittlement will be given a hydrogen relief thermal bake treatment following operations in which diffused hydrogen may have affected the part.
7. Drilled holes in titanium alloys and steels heat-treated to greater than 180 ksi will be lapped and honed and deburred before parts are installed in an effort to minimize the possibility of micro-cracks. Electrically discharged machined parts will be processed only after the successful demonstration of crack-free parts on like coupon material.

2. 2. 2. 2 The Influence of Part Geometry, Loads, Finish, Environmental Exposure, and Assembly Stresses

Frequently sharp notches or corner radii may be the source of cracks under either static or dynamic loads. Inadequate or improperly applied part protective finishes also have contributed to cracking and part failures in manufacturing, test, and use environments. Failure to assess the levels of stress or the type of loading adequately may result in failure of the part. Fatigue-type cracking has frequently occurred because of cyclic and/or acoustic conditions which were not accounted for in the design. Resultant tensile stresses imposed during manufacturing assembly buildups and fitups have been the source of numerous stress corrosion cracking failures. Additionally, swaged and other cold-worked parts not adequately stress-relieved have sometimes failed.

To preclude crack initiation resulting from part geometry, loading, finishing, environmental exposure, and assembly practices, the following procedures should be implemented:

1. Whenever possible, use design practices specifying generous radii and absence of sharp corners or notches which result in abrupt changes in section modulus.
2. Assess the environmental fluids to which the part will be exposed in manufacturing, test, and use to preclude inadvertent embrittlement or cracking of the part resulting from the stress corrosion or environmental stress cracking phenomena of the process fluid.
3. Structural analysis will include an assessment of the fatigue characteristics, as well as other property considerations, for major structural subassemblies and assemblies. When so directed, tests will be conducted to evaluate conformance to dynamics criteria and to prove that fatigue-type cracking is not a problem.
4. A corrosion control plan will be applied to protect parts during manufacture, storage, test, or use. Proper surface protection will be noted on the engineering drawing, and dissimilar metal corrosion will be assessed. In-process corrosion prevention methods will be exercised as required.
5. Diligence will be exercised in subassembly and assembly buildups to prevent imposition of excessive stresses resulting from improper installation procedures, tooling, or tolerance accumulations. Where noted, inspection and/or manufacturing personnel will work with the design engineer to provide the necessary shim, spacer, etc., to preclude the inducement of high imposed stresses.

2.3 FRACTURE CONTROL METHODS FOR INITIALLY CRACKED STRUCTURES

Structures are designed by one of the following approaches:

1. Safe-life design based on conventional fatigue life considerations
2. Safe-life design based on fracture mechanics considerations
3. Fail-safe design

Safe-life design in which conventional fatigue prevention and analysis methods are used recognizes local stress concentrations due to detail design characteristics such as joints, fittings, and section discontinuities. However, it does not consider the potential of undetected crack-like defects existing in the structure before the start of operational service. The useful life of structural elements determined by fatigue tests consists primarily of the number of cycles required to initiate a visible fatigue crack. To avoid the confusion between these two kinds of structural design approaches (safe-life design using fatigue or fracture mechanics), the following terminologies are adopted:

1. Fatigue life is the life of an unflawed structural element to failure as determined by S-N curve.
2. Safe-life, also called safe-crack-growth life, is the life for initial defects in a structural element to grow to a critical size.

Conventionally, fail-safe design requires that failure of any single structural element not degrade the strength or stiffness of the remaining structure to the extent that the vehicle cannot complete the mission at a specified percentage of limit loads. This type of design is usually achieved by providing structural redundancy and a means for arresting unstable crack growth.

The fatigue life design methods are discussed in Sections 2.1 and 2.2. This section presents the methods for design and analysis of safe-crack-growth and fail-safe structures.

2.3.1 Safe-Crack-Growth and Fail-Safe Structures

The concept of fail-safe design assumes that failure of a structural element can be temporarily tolerated if sufficient residual strength or alternate load paths are provided to avoid catastrophic failure under subsequent exposure to a limited period of service operation. Successful application of this design approach depends on three major factors:

1. The fail-safe structure must be accessible for regular and effective in-service inspection so that a damaged condition will be reliably detected.
2. The residual strength and stiffness after initial failure must provide an acceptably low probability of catastrophic failure under subsequent normal service operation. Limit load is most commonly taken as the required residual strength level.

3. The fatigue life of the remaining structure, after failure of a single principal element, must prevent any significant additional damage from occurring prior to the next regular inspection period.

In actual application, it is necessary to specify the extent and type of damage and the load level to be achieved with the damage present. These basic criteria are assigned on the basis of engineering judgement and are motivated by the desire to ensure that the damage-strength relationship is such that the damage may be readily detectable before the strength is impaired beyond the point of safe flight. Once the basic criteria are defined, the structures must be designed to meet the criteria. Development of detailed design criteria is beyond the scope of the present study. Typical airframe structural design criteria are given in References 15, 16, and 17 for military aircraft, Reference 18 for transport aircraft, and in References 1 and 19, 20, and 21 for Space Shuttle applications. This report presents only the methodologies necessary to help achieve the design goal.

Typical fail-safe design involves multiple element or redundant structural arrangements, with crack arrest provisions in the form of geometric boundaries or stiffening elements. Many of the stiffened or reinforced panels employed in conventional aircraft wing and fuselage structures possess an inherent fail-safe capability of significant magnitude. It is obviously desirable to make use of such inherent fail-safe characteristics and enhance them to the extent required to comply with the fail-safe design requirements to obtain maximum efficiency in applying this design concept.

Typical structural configurations are:

1. Monolithic structure
2. Crack arrest (crack stopper) structure
 - Skin-stringer design (examples, L-1011 wing and fuselage, C5-A fuselage)
 - Integral stiffener design (examples, Electra and C5-A wing box)
3. Multiple element structure
 - Multi-load path dependent (example, multi-plank design, Electra and C5-A wing box)
 - Multi-load path independent (example, multi-laminate, or redundant element design, B-1 wing carry-through structure)

As a reference for discussion, consider that the structures are inspectable in service. Additionally, assume that damage, a_0 (an appropriate crack size parameter, the subscript o stands for initial or original), is initially present which is the size of the largest flaw that could be missed in the initial fabrication inspection or during a regularly scheduled inspection. Fatigue crack propagation characteristics (plots of damage size versus time or mission) for each type of structure are schematically illustrated in Figures 2-10 and 2-11. The mechanics of component failure, or residual strength, under single monotonically increasing loads (plots of load level versus crack size) for each type of structure are schematically shown in Figure 2-12. It is seen that both crack stopper structures and multiple element structures are inherently provided with fail-safe and safe-life (safe-crack-growth) capabilities. Therefore, unlike the conventional definition for fail-safe structure, which primarily refers to residual strength of the multiple element structures, in this report fail-safe will be considered to be the residual strength capability of the structure, while safe-life will be considered to be the safe-crack-growth capability for a given structure.

2.3.2 Classification of Space Shuttle Structural Elements

Reviewing the Space Shuttle structural elements listed in Tables 1-1 to 1-9, it is recognized that these parts can be grouped in four general areas by their product forms and seven subareas by functional considerations. Furthermore, as discussed, each type of structure can be classified in (or designed to) one of three structural configurations: monolithic, crack arrest, or multiple element.

Table 2-1 is a matrix of information regarding the formulation of these general forms of structural elements and the probable corresponding classifications. For each type of the structure, the expected loading condition, type of damage, and the probable method of analysis will also be determined and listed. Note most of the methods of analysis are presented in Volume II, Assessment of Fracture Mechanics Technology for Space Shuttle Applications. Analysis methodology specifically relevant to structural analysis applications is discussed in the following sections.

2.3.3 Monolithic Structure

The basic differences among the three typical classes of structures (monolithic, crack arrest, and multiple elements) are such that the crack extension process would be interrupted (or altered) by an artificial barrier in the crack arrest structure or by a geometric discontinuity in the multiple element structure. When the crack is far away from these geometric discontinuities or barriers, the structure is essentially monolithic. In this section, the problems are confined to cracked sheets or plates subjected to

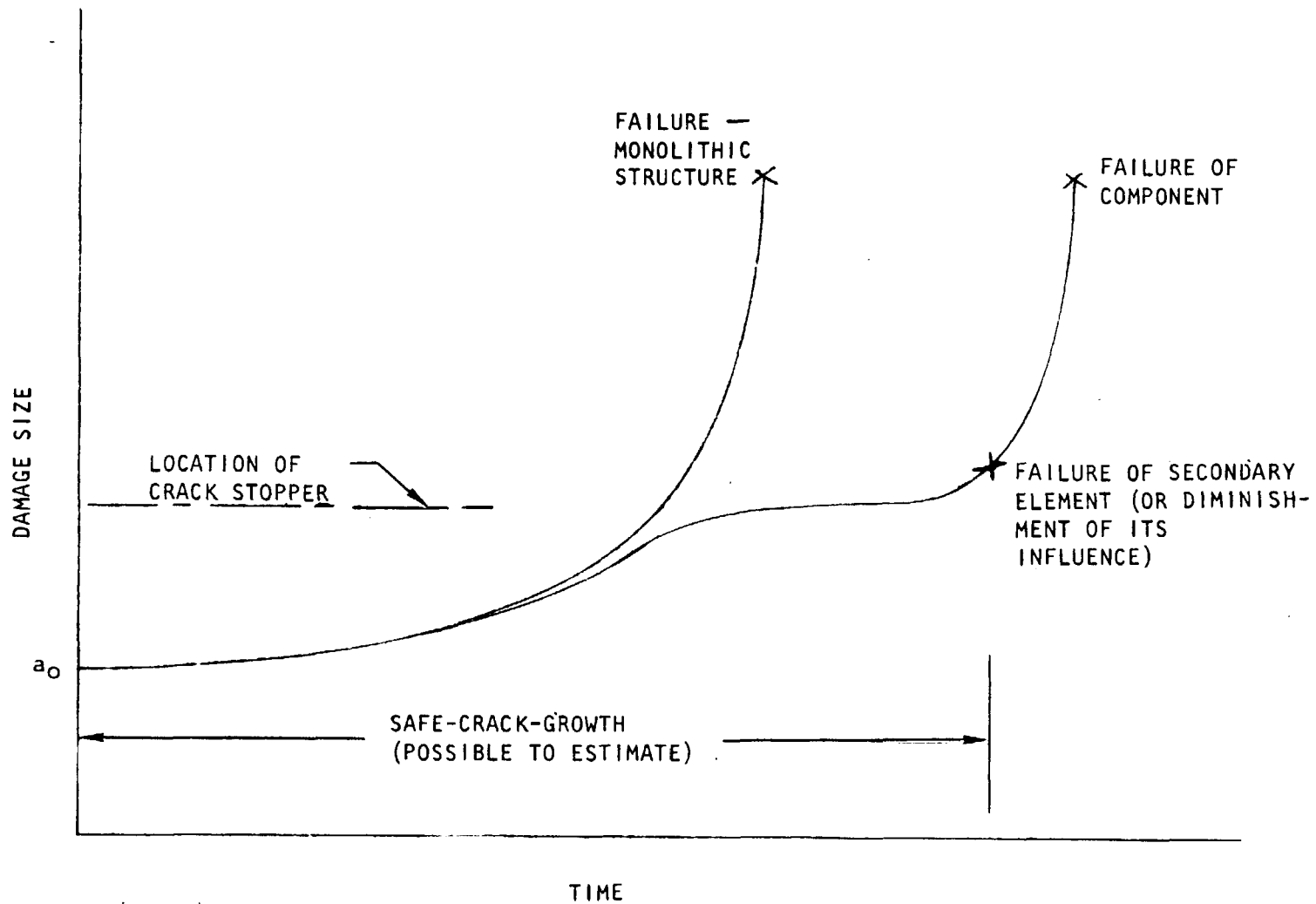


Figure 2-10. Comparison of Fatigue Crack Growth Characteristics for Monolithic Structure and Crack Arrest Structure

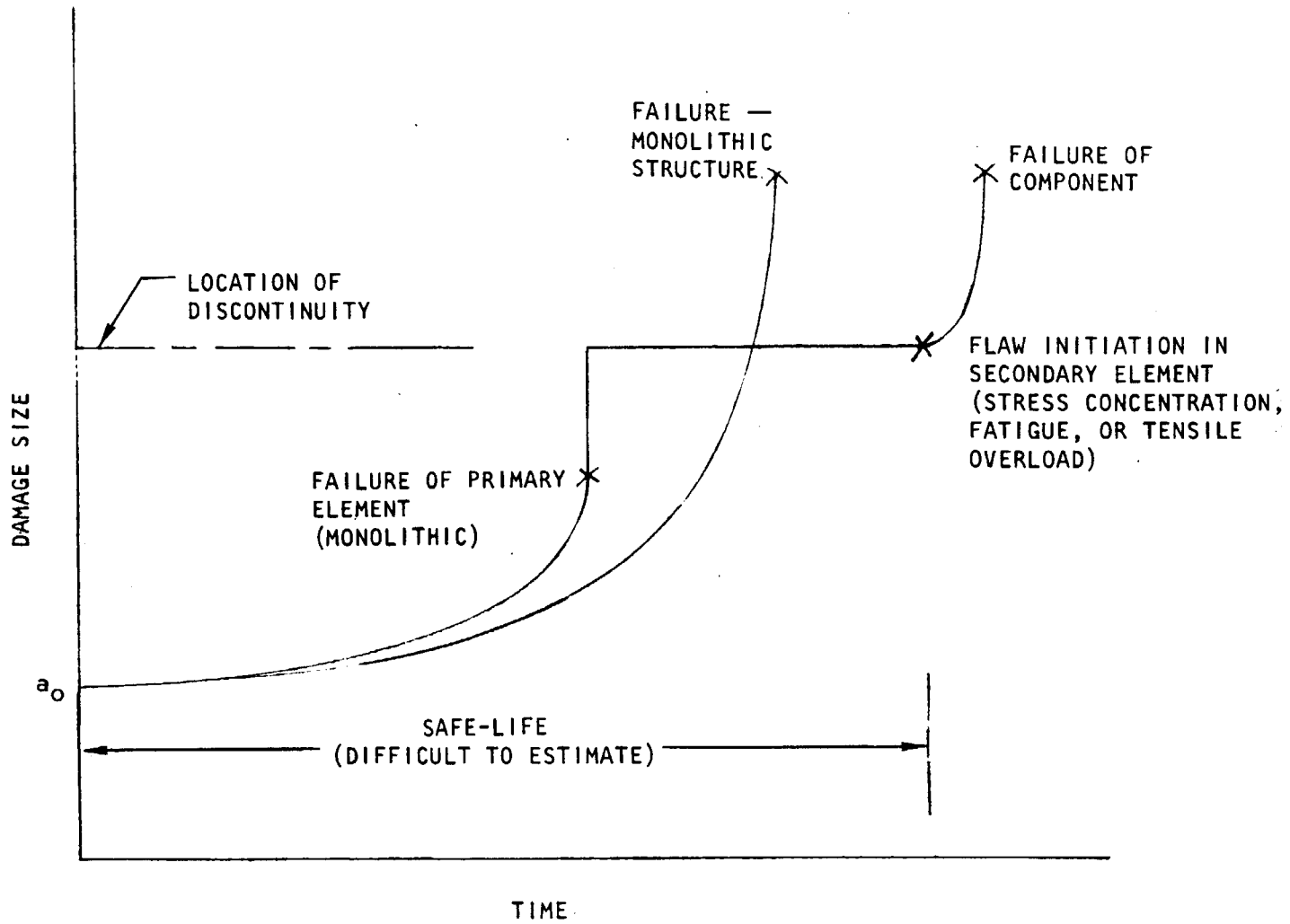
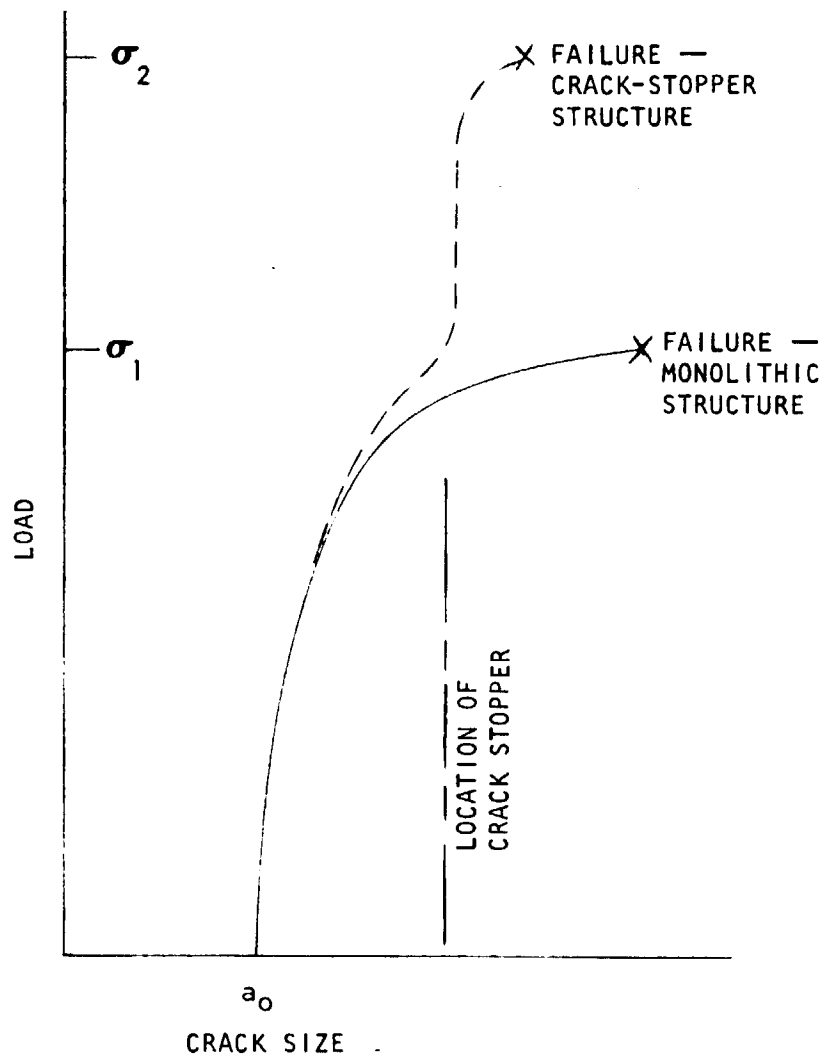


Figure 2-11. Comparison of Fatigue Crack Growth Characteristics for Monolithic Structure and Multiple Element Structure

(a) Comparison of Monolithic Structure and Crack Arrest Structure



(b) Comparison of Monolithic Structure and Multiple Element Structure

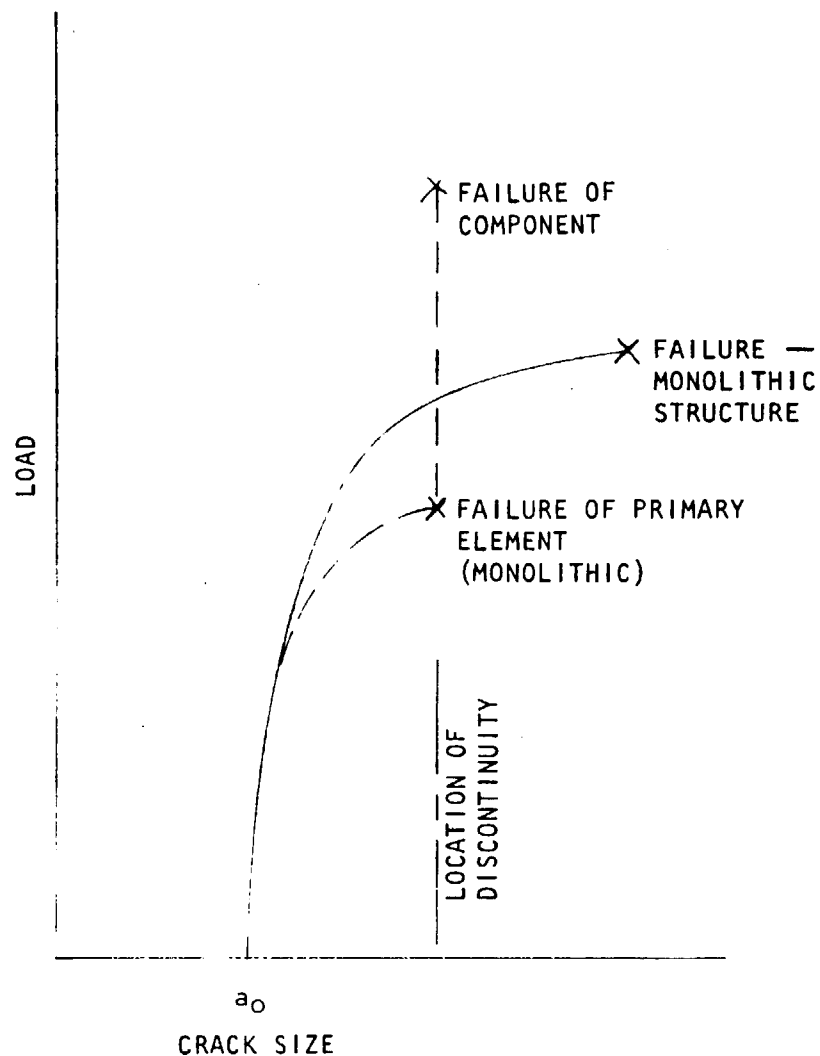


Figure 2-12. Crack Growth Characteristics Under Monotonic Increasing Load

Table 2-1. Classification of Cracked Structure

Type of Structure		Structural Classification	Structural [△] Elements	Expected Loading Condition	Type of Damage	Fracture [△] Mechanics Analysis Methods
Product Form	Typical Examples					
Pressure vessels	Thick wall tankage (SRB, etc.)	Monolithic	544, 569, 205, 579, ABES, 2-5, 2-6, 2-8, 3-2, 3-12, 3-13	Internal pressure	Primary surface flaw	3.3.3, 5.2 of Vol. II
	Thin wall tankage (ET, etc.)	Monolithic	439, 441, 438, 440, 563, 572, 570, 204, 578, 3-1, 3-3, 3-4, 3-5, 3-10, 3-14	Internal pressure	Surface flaw and through-the-thickness crack	3.3.3, 3.3.7, 5.2 of Vol. II
	Thin shell (crew compartment)	Crack arrest and/or multi-element	6-1, 6-2, 6-3, 6-6, 6-7, 6-8	Internal pressure	Primary through-the-thickness crack; crack from hole	3.3.3, 3.3.4, 3.3.5, 3.3.7, 5.2 of Vol. II
Sheet or plate	Wing skin; skin for fuselage sections	Crack arrest and/or multi-element	4-4, 5-1, 5-15, 6-9, 7-1, 7-6, 7-9, 8-1, 8-11	Tension, shear, or both	Primary through-the-thickness crack	3.3.3, 3.3.4, 3.3.5
Extruded parts	Longeron, web-stiffener, spar cap, frame, etc.	Monolithic	4-1, 4-2, 4-8, 4-9, 4-10, 5-10, 6-12, 6-13, 7-3, 7-2, 7-4, 7-5, 7-10, 7-11, 7-14, 7-15, 7-17, 7-18, 8-5, 8-8, 8-13, 8-14	Tension, bending, or both	Corner crack and surface crack; crack from hole	3.3.3
Forging, machined parts, etc.	Landing gear components	Monolithic	9-1 to 9-7, 9-9 to 9-19	Tension, shear, bending, or both	Corner crack and surface crack; crack from hole	3.3.3
	Fitting, lug, hinge, etc.	Monolithic or multi-element	3-15, 3-16, 4-15, 4-18, 4-23, 5-12, 5-13, 5-14, 6-15, 6-16, 6-17, 7-13, 7-16, 7-19	Tension	Corner crack and surface crack; crack from hole	3.3.3, 3.3.5
[△] Number refers to structural elements listed in Tables 2-1 to 2-9. [△] Number refers to section number in the text.						

far field uniform extensional stresses. The effects of curvature and loading conditions such as biaxial tension, bending moment, or shear, will be discussed in later sections.

Effective fracture mechanics analysis on cracked structures requires appropriate stress intensity factors representative of local structural geometries and crack morphologies. This section will present and discuss Mode I stress intensity factors for the crack geometries commonly found in structural components, such as those illustrated in Figure 2-13. Stress intensity factors for other crack geometrics can be obtained from Reference 22.

Generally, for a structural element containing a crack of an appropriate dimension, a , subjected to a uniform far field extensional stress, σ (perpendicular to the crack), the stress intensity factor can be expressed as

$$K = \sigma \sqrt{\pi a} \cdot M_p \cdot \Pi \alpha \quad (3)$$

where M_p is the crack tip plasticity correction factor (refer to Volume II) and $\Pi \alpha$ is the product of a series of parametric factors accounting for the influence of the structural geometry, loading conditions, and crack morphology. In the following cases the emphasis will be on determination of the geometric factors.

2.3.3.1 Through-the-Thickness Crack

Through-the-thickness cracks may be located at the middle region of a plate, called the center crack (Case 1 in Figure 2-13), the edge of a plate (a special case of Case 1 or Case 3 in Figure 2-13), or at the edge of a hole (Case 4 in Figure 2-13). Only the first two types of cracks are discussed in this section. The third type will be discussed in a later section along with other types of cracks emanating from a hole.

The stress intensity factor for the center crack is given by

$$K = \sigma \sqrt{\pi a} \cdot M_p \cdot \phi_1 \quad (4)$$

where the geometric factor, ϕ_1 is a function of the crack length to panel width ratio and the panel length to panel width ratio (Figure 2-14). For a panel length greater than twice the panel width, the curve given in Figure 2-14 can be approximated by the expression (Reference 24).

$$\phi_1 = \sqrt{\text{Sec} \left(\frac{\pi a}{W} \right)} \quad (5)$$

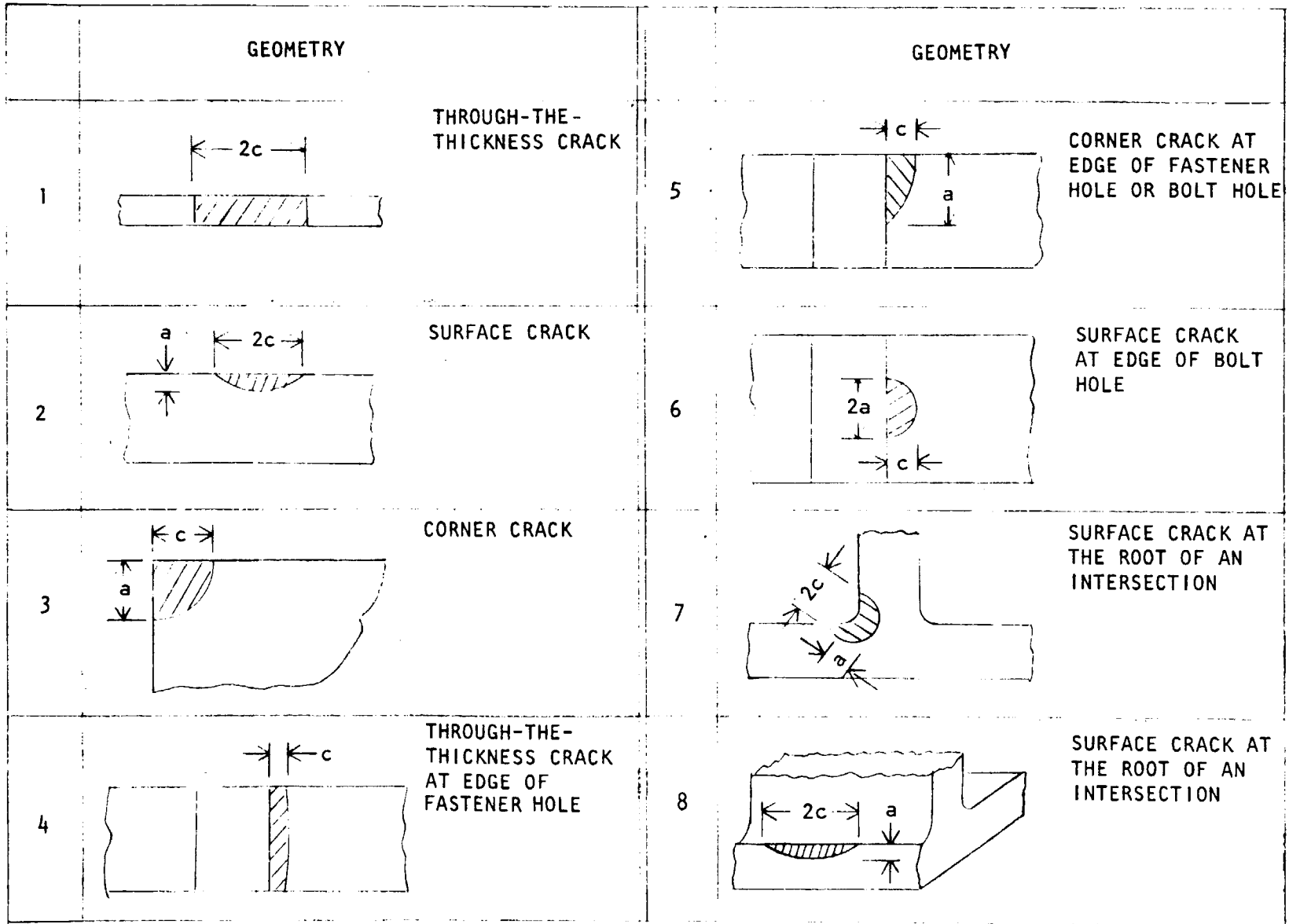


Figure 2-13. Cross-Sectional Views of Common Crack Geometries

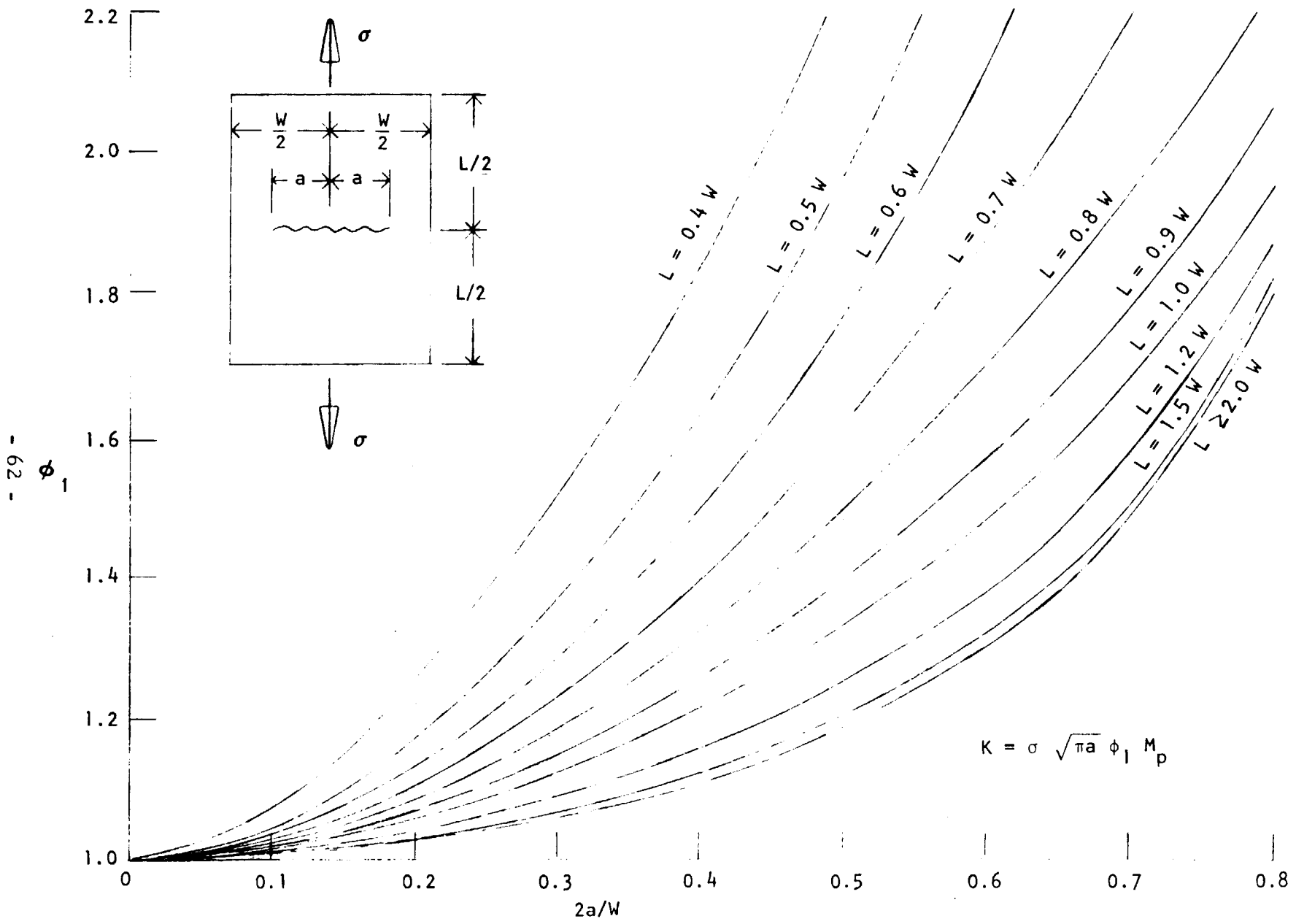


Figure 2-14. Through-the-Thickness Crack Loaded in Tension (Reference 23)

If the crack is located off the center of the plate, another set of curves for the geometric factor, ϕ_1 is given in Figure 2-15. As a limiting case, when the crack is right at the edge of the plate, the ϕ_1 factors are given in Figure 2-16.

The crack tip plastic zone size has been estimated by Irwin (Reference 27) as

$$2r_y = \frac{2}{n\pi} \left(\frac{K}{F_{ty}} \right)^2 \quad (6)$$

which gives the plasticity correction factor

$$M_p = \left[1 - \frac{1}{n} \cdot \phi_1^2 \left(\frac{\sigma}{F_{ty}} \right)^2 \right]^{-1/2} \quad (7)$$

where F_{ty} is the material tensile yield strength and n varies between 2 to 6, depending on the stress state at the crack tip. For plane stress $n = 2$. The value of n increases as the triaxiality of crack tip stress state increases, $n \approx 6.0$ for the limiting case of plane strain. The geometry term (ϕ_1) in Equation (7) only approximately accounts for the interactions between the crack tip plastic zone and the overall (as well as local) geometry of the plate. The exact procedures will be those used by Irwin, published in ASTM Bulletin No. 243 (January, 1960), or the iteration procedures used by Forman (Reference 28). These computational procedures are complicated and will become more complicated for complex structural (and/or crack) geometries such as, surface cracks or cracks emanating from a hole. Therefore it is felt that plasticity term, (M_p), in the form of Equation (7) would be an appropriate compromise.

It has been pointed out by Key (Reference 29) that, for the case of a short crack (say, $2a \leq W/3$ at failure load for the data he used), the crack tip plastic zone size might be excessively large because of the higher stress level required to cause propagation of the short crack. In this case, a larger plasticity correction factor (for plane stress)

$$M_p = \sqrt{\left(\text{Sec } \frac{\pi}{2} \cdot \frac{\sigma}{F_{ty}} \right)^2} \quad (8)$$

offers better correlation with test data. This plasticity correction factor was derived by using $a_e = a + 2r_y$ (instead of $a + r_y$) based on the Dougdale's crack tip plastic zone relationship (Reference 30),

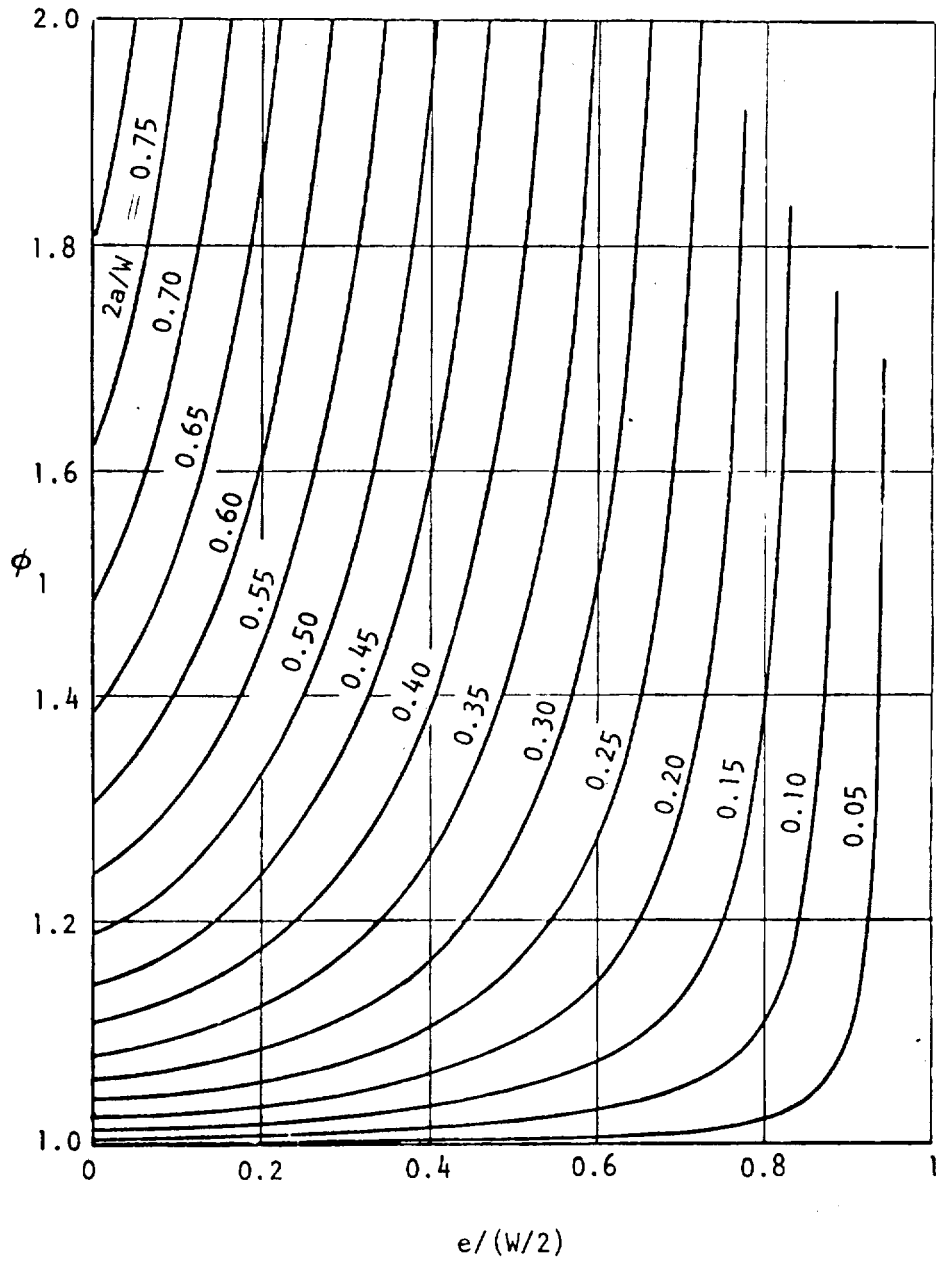
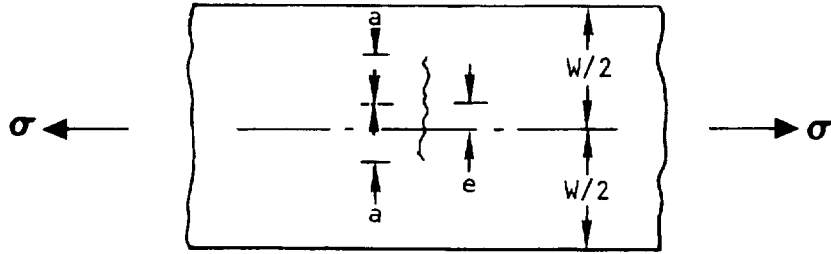


Figure 2-15. Stress Intensity Factors for Eccentrically Cracked Plate (Reference 25)

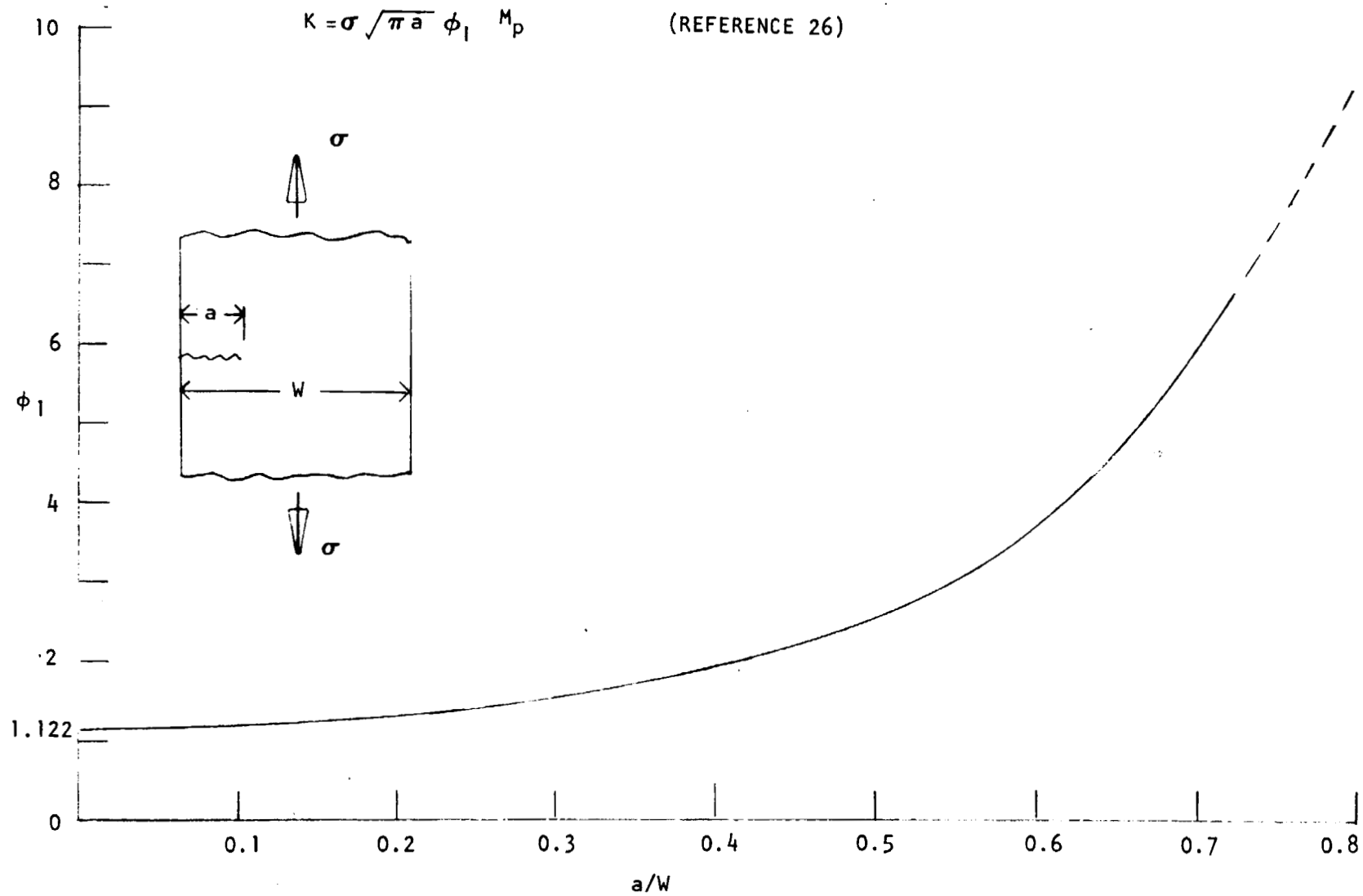


Figure 2-16. Through-the-Thickness Edge Crack in a Plate Loaded in Tension

$$2r_y = a \left[\text{Sec} \left(\frac{\pi}{2} \cdot \frac{\sigma}{F_{ty}} \right) - 1 \right] \quad (9)$$

and neglecting the interactions between the plastic zone and the free edge of the sheet. (This is correct for a short crack.) Many other investigators (e. g., References 31 to 33) have developed different crack tip plastic zone correction factors. Their results showed that the plastic zone sizes for the plane stress condition are within the two boundaries represented by Equations (7) and (8). On the other hand, Newman (Reference 34) has shown that the crack tip plastic zone size is also a function of the material strain hardening exponent and loading rate. His calculations showed that the plastic zone sizes corresponding to a wide range of materials having different strain hardening exponents and specimens subjected to different loading rates also are within the range bounded by Equations (7) and (8).

There is a more serious problem in the development of K_C data of center cracked specimens and the prediction of structural component residual strength for the center crack configuration with use of available K_C data. It is that the K_C value is not a constant. The K_C value for some material and a given thickness is strongly dependent on the size (width) of the panel and, to a lesser degree of severity, is affected by the crack-length-to-panel-width aspect ratio. Such a phenomenon is due in part to the slow stable tear behavior of the material and in part to net section yielding, which sometimes is exhibited in narrow panels (or panels containing a very long crack). The effect in the short-crack cases is further complicated by the excessively larger plastic zone at the crack front.

The effect of slow stable tear is illustrated schematically in Figure 2-17. Here it is shown that superimposing the material R-curve and the calculated K-curve for panels having different geometrics (e. g., different widths, refer to Volume II for the definition of R-curve) results in a different K_C value (the point of tangency). Generally, even if net section yielding is not considered, the narrower the panel width, the lower the K_C values. In Figure 2-17 it can be seen that this effect increases for materials having an R-curve of larger curvature.

If failure of a panel is controlled by a net section yielding mechanism, then the stress intensity factor is limited by the net section stress. A fictitious stress intensity factor, K_{yield} , can be computed by setting the net section stress equal to the tensile yield stress for the material:

$$K_{yield} = F_{ty} \left(1 - \frac{2a}{W} \right) \sqrt{\pi a \cdot \text{Sec} \left(\frac{\pi a}{W} \right)} \quad (10)$$

Here, the criterion for unstable crack growth is the point where this K-curve intersects the R-curve. If the sheet fails by the net section yielding

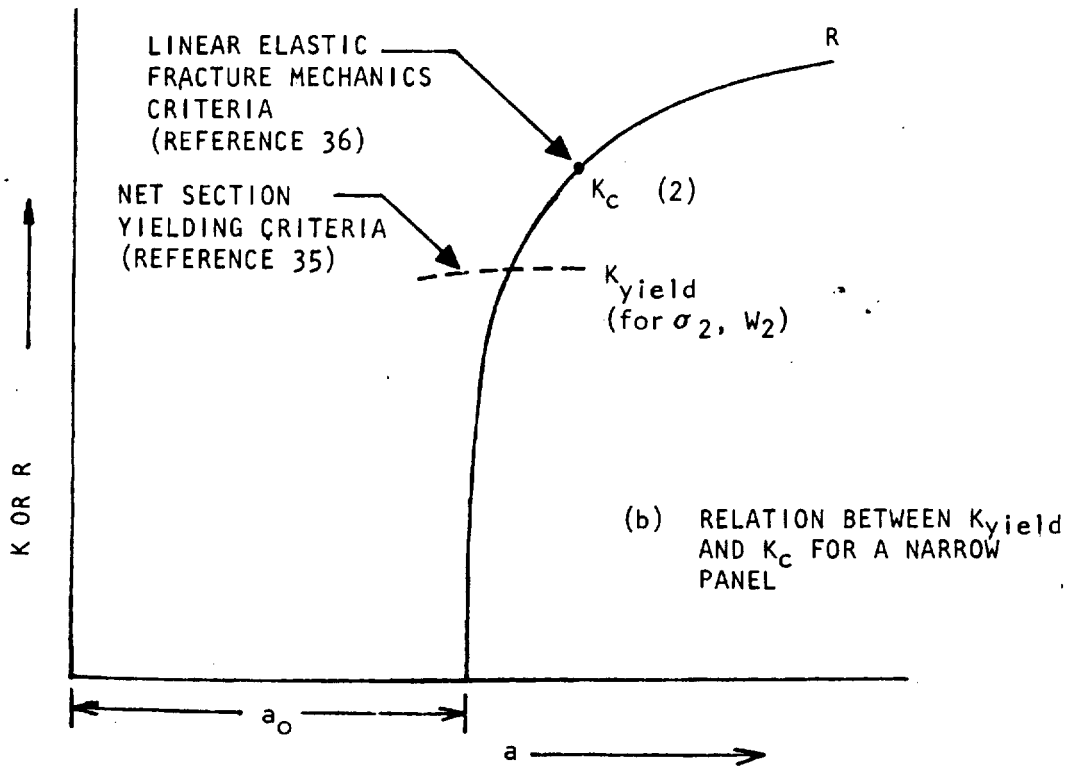
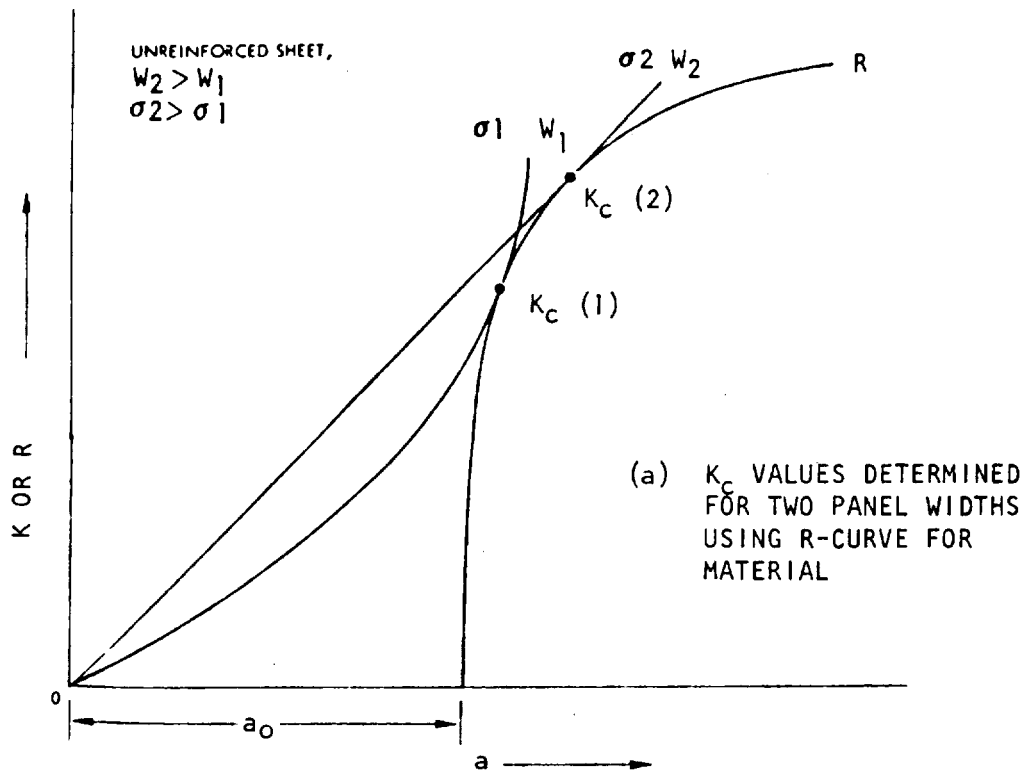


Figure 2-17. Failure Analysis Using an R-Curve

mechanism, the K_{yield} point should occur prior to the point of failure defined by the "tangency" criterion; i. e., $K_{\text{yield}} < K_C$ (Figure 2-17). The K_{yield} parameter is approximately a constant over a narrow range between initial crack length and critical crack length, as illustrated in Figure 2-17.

With the aid of the defined "tangency point criteria" and the proposed " K_{yield} criteria," the fracture behavior of pre-cracked sheets of any size can be assessed by use of the appropriate R-curve for the material. For example, with the R-curves for two different 2024-T3 aluminum alloy sheets, as shown in Figure 2-18, curves that describe the failure phenomena can be synthesized for each of the alloy sheets. The steps given below outline the procedure for obtaining these curves for the case when the ratio of initial crack length to panel width is one-third.*

First a particular width, W , is chosen. The origin of the R-curve is set at $2a_0 = W/3$. A failure, K_C , according to the tangency criteria and the K at the intersection of the K_{yield} and resistance curves are found. The lower of these is taken to be critical stress intensity for that width. The same procedure is repeated for various panel widths. As a result, the curves of Figure 2-19 were obtained. The portions of the curve that reflects the effect of net section yielding are shown as dotted lines in Figure 2-19. (Note that for this illustration problem, plasticity corrections were not included in the R-curves nor were the calculated K_C values.) It is seen that panels of up to 53.3 centimeters (20 inches) wide in one case or up to 76.2 centimeters (30 inches) wide in the other case would result in low K_C values, which can be attributed to the occurrence of net section yielding rather than fracture due to rapid propagation of a crack.

Two related important observations may be made from Figure 2-19. First it should be noted that relatively minor variations in wide panel toughness values can significantly affect the magnitude of the width in which net section yielding ceases to occur. The difference in the wide panel K_C values for these two sets of panels was less than 10 percent and the critical widths varied by a factor of 1.5. Second, and more important, is the observation that the fracture toughness values from narrow panel widths—the dotted lines in Figure 2-19—are in the reverse order of the actual wide panel toughness values. Therefore, even for qualitative comparisons of materials, subsized specimens may lead to invalid conclusions.

Figure 2-20 shows another set of available test data that illustrates the effect of panel width and net section yielding on the K -critical values for the 2024-T3 alloy. The same trends as those shown in Figure 2-19 are evident. Figure 2-20 shows that only the wide panel data exhibited real K_C failure. The

*The net section stress is approximately a minimum for this crack-length-to-panel width ratio.

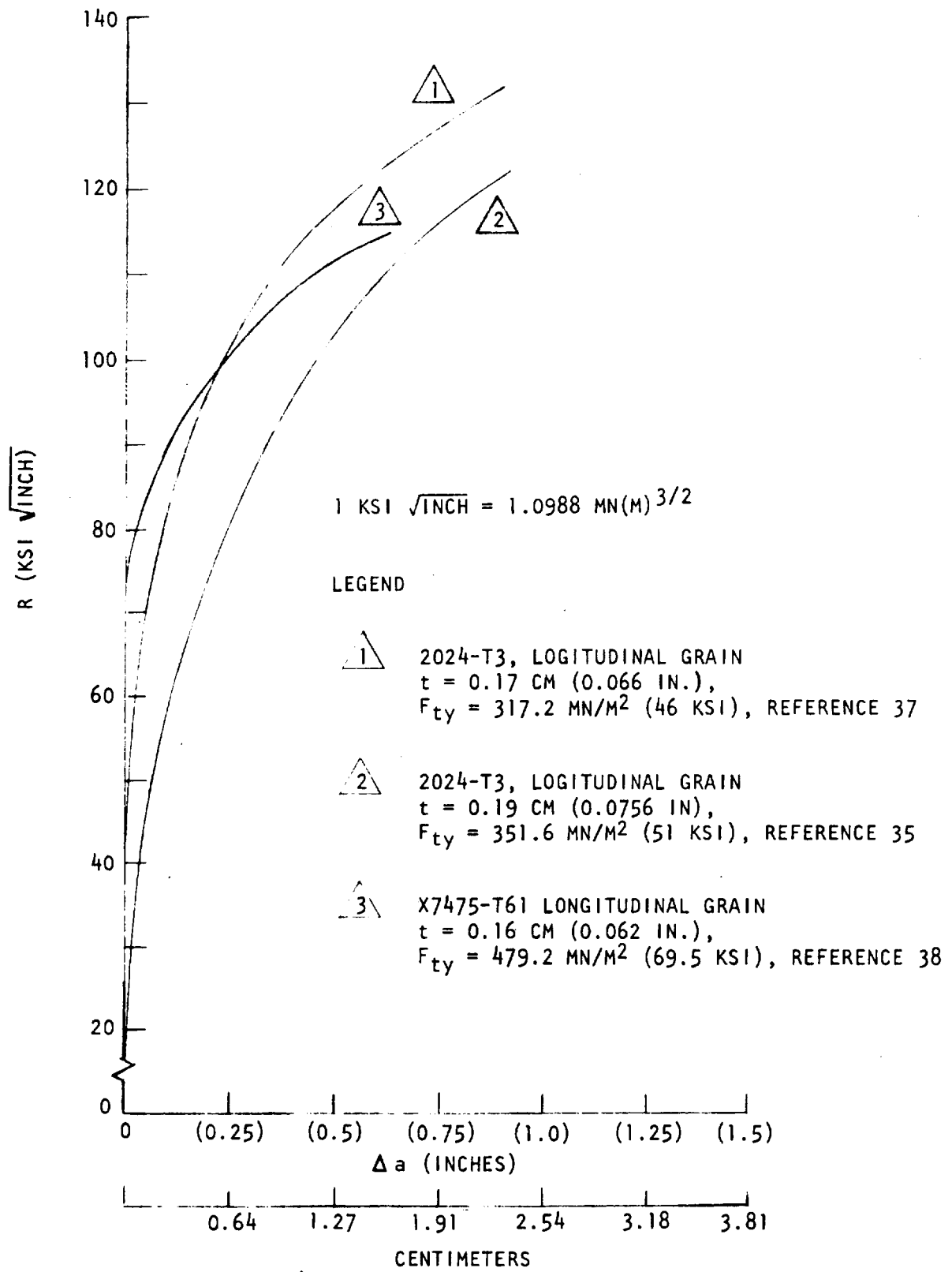


Figure 2-18. R-Curves for Aluminum Alloys

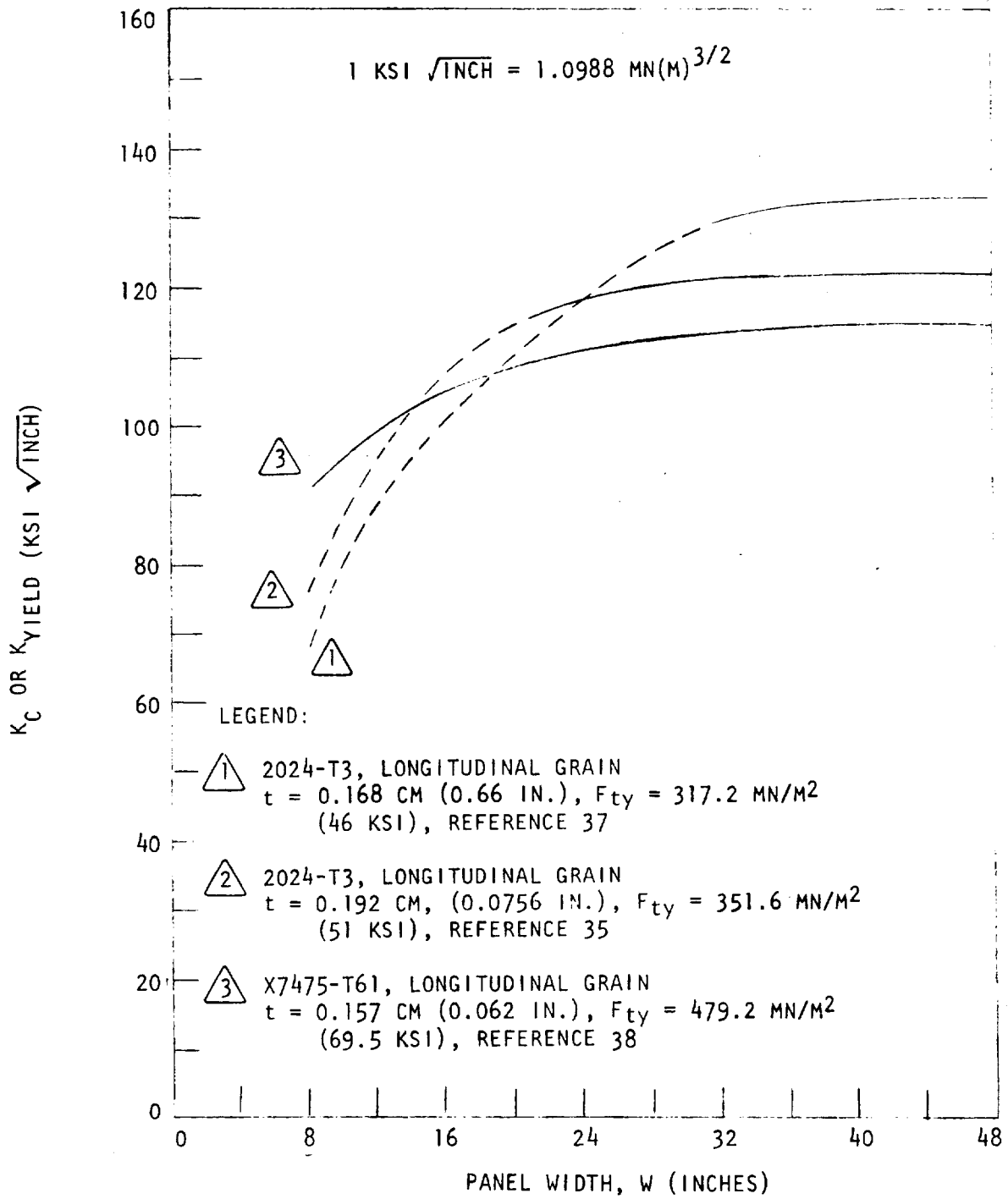


Figure 2-19. Failure of Aluminum Alloy Sheets Predicted From R-Curve

$$1 \text{ KSI } \sqrt{\text{INCH}} = 1.0988 \text{ MN}(\text{M})^{3/2}$$

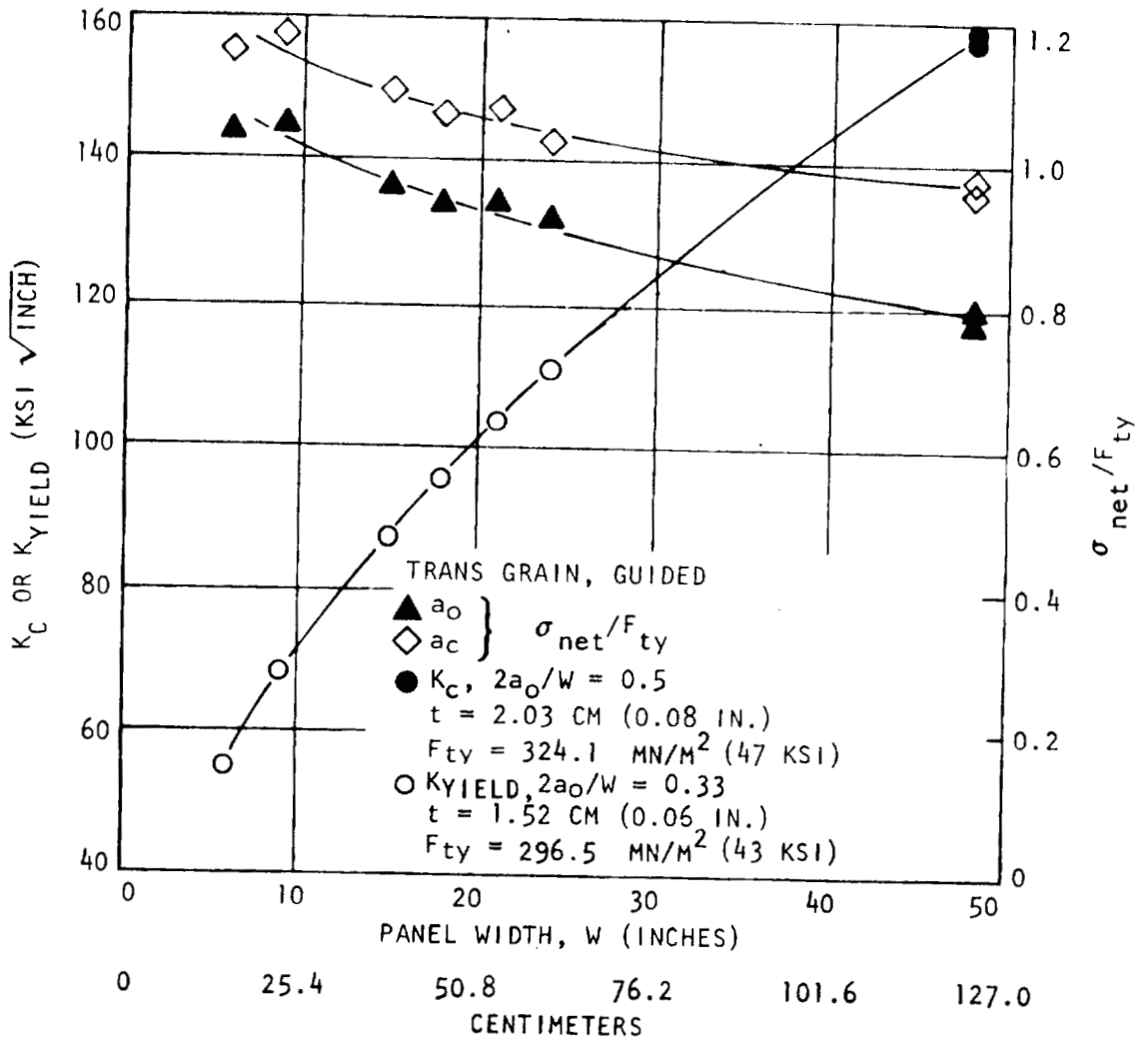


Figure 2-20. Fracture Toughness of Bare 2024-T3 Sheets (Reference 39)

$K_{critical}$ values for the smaller panels could be calculated by utilizing the net section yield (K_{yield}) or actual failure load (K_C). For the smaller panels, these two calculations result in approximately the same numerical K value.

This effect of panel width and net section yielding on fracture toughness is rather pronounced if comparisons are made between materials of different strength categories, e. g., 2024-T3 versus 7075-T6 aluminum alloys. Referring to the foregoing discussions, one can deduce that the reduction in K_C or K_{yield} values of narrower 7075-T6 aluminum panels would be much less than the 2024-T3 aluminum. This is because 7075-T6 aluminum has much higher tensile yield strength and an R-curve with smaller curvature. Such an example is also shown in Figures 2-18 and 2-19. The selected R-curve represents the average values for a group of seven test panels of high purity 7075 aluminum alloy sheet (designated as X7475-T61). It is expected that this alloy will offer a higher fracture toughness property and, meanwhile, maintain a tensile strength nearly as good as the regular 7075 alloy. In Figure 2-19 the K_C values for various panel widths having crack lengths equal to one-third of the particular panel width are calculated with the previously described procedure. It should be noted that all the K_{yield} values calculated for these panel configurations were above the correspondingly calculated K_C values. In other words, the panels will not be failed by the net section mechanism.

Now it is interesting to examine the actual predictive capability of the R-curve technique. Table 2-2 shows the actual test results of the seven X7475-T61 test panels. Also shown in Table 2-2 are the predictions calculated with use of the R-curve given for the material and the actual dimensions for each test panel (initial crack length and panel width). Despite a scatter band of ± 5 ksi $\sqrt{\text{inch}}$ in R levels actually associated with the entire averaged R-curve, the comparisons in Table 2-2 dramatically indicated that, with the typical R-curve, the predicted K_C , σ_C , and a_{cr} values for each test panel (except panel No. 2) agree within ± 5 percent of the actual values obtained from experiments. For test panel No. 2, because the initial crack length was only one-sixth of the panel width, as mentioned before, better correlation could be obtained if a large plasticity factor were employed in the calculations.

2.3.3.2 The Part-Through Crack

The physical aspects and the application of stress intensity factor and crack growth resistance concepts to the analyses of pressure vessel failures have been thoroughly reviewed and presented in Volume II of this report. Summaries and reviews of available analytical surface flaw stress intensity factors also are available (References 40 and 41). The stress intensity factors to be presented here are the engineering approximations most recently proposed by Hsu and Liu (Reference 42). These stress intensity expressions

Table 2-2. Comparison Between the Actual and the Predicted Values
for Fracture Tests of X7475-T61 Aluminum Panels

Panel No.	W cm (in.)	$2a_o$ cm (in.)	K_C $MN(m)^{3/2}$ (ksi $\sqrt{in.}$)		σ_c $N/m^2 \times 10^6$ (ksi)		$2a_{cr}$ cm (in.)	
			Test	Predicted	Test	Predicted	Test	Predicted
1	60.96 (24)	20.44 (8.05)	126.3 (114.9)	121.1 (111.0)	173.0 (25.1)	174.4 (25.3)	72.1 (10.47)	25.1 (9.9)
2	60.96 (24)	10.2 (4.02)	107.6 (97.9)	117.6 (107.0)	230.9 (33.5)	244.0 (35.4)	35.7 (5.18)	13.9 (5.5)
3	60.96 (24)	15.34 (6.04)	126.8 (115.4)	121.1 (111.0)	215.1 (31.2)	206.8 (30.0)	52.9 (7.68)	20.0 (7.9)
4	20.32 (8)	5.08 (2.00)	93.9 (85.5)	98.9 (90.0)	291.6 (42.3)	301.9 (43.8)	16.2 (2.36)	6.0 (2.4)
5	30.48 (12)	5.08 (2.00)	101.1 (92.0)	102.2 (93.0)	308.1 (44.7)	306.8 (44.5)	17.8 (2.59)	6.4 (2.55)
6	30.48 (12)	11.43 (4.50)	104.4 (95.0)	109.9 (100.0)	199.9 (29.0)	206.8 (30.0)	36.8 (5.34)	13.9 (5.5)
7	30.48 (12)	7.74 (3.05)	110.4 (100.5)	107.1 (97.5)	259.2 (37.6)	262.0 (38.0)	27.8 (4.04)	9.6 (3.8)

From Reference 38.

are basically the same as those presented in Volume II, but the scope was enlarged to include a wide variety of crack geometrics (Figure 2-21). These approximate stress intensity expressions were obtained based on the following assumptions.

1. The crack is in a form of an ellipse having a particular aspect ratio, $2b/2b_1$, where $2b$ is the minor axis and $2b_1$ the major axis of the ellipse. Special cases, such as $b = b_1$ (a circle) and b/b_1 equal to zero (a scratch) also are considered.
2. An appropriate method of analysis may be developed from the existing solution for an elliptical crack embedded in an infinite solid. The elastic stress intensity factor, adopted from References 43 and 44, is

$$K^2 = \sigma^2 \pi \left(\frac{b}{b_1} \right) \sqrt{b^2 \sin^2 \beta + b_1^2 \cos^2 \beta} / \Phi^2 \quad (11)$$

or

$$K = \sigma \sqrt{\pi b} \cdot M / \Phi \quad (12)$$

where

$$M = \left[\left(\frac{b}{b_1} \right)^2 \sin^2 \beta + \cos^2 \beta \right]^{1/4} \quad (13)$$

and

$$\Phi = \int_0^{\pi/2} \left[1 - \left(\frac{b_1^2 - b^2}{b_1^2} \right) \sin^2 \beta \right]^{1/2} d\beta \quad (14)$$

Note in Figure 2-21 that both b_1 and b in Equation (11) can be either a or c . The angle β is always measured from the minor axis to a specific point on the periphery of an ellipse. However, for convenience, an angle θ is defined to describe the position of a point with respect to "a" in Figure 2-21 and later in Figure 2-28. Furthermore, Equation (11) implies that the stress intensity varies along the elliptical periphery.

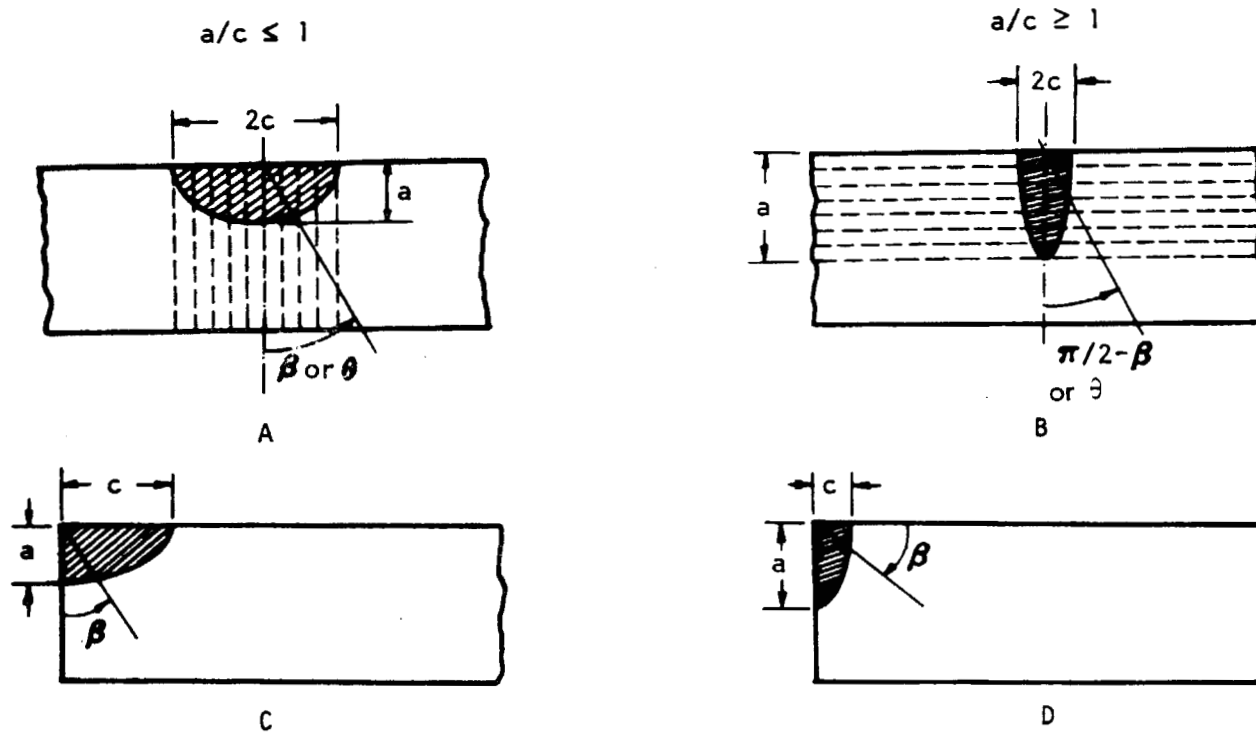


Figure 2-21. Geometries of Truncated Elliptical Cracks

3. The truncation concept of Irwin (Reference 43) is adopted for development of other geometric factors which will account for the free surface exposures; i. e., the infinite solid is truncated into two halves or four quarters, and the truncations are always made right on the major axis of the ellipse (Figure 2-21A) or on the minor axis (Figure 2-21B) or on both axes (Figures 2-21C and 2-21D). These free surface exposure factors will be called the front surface factor, (M_1).
4. The semi-infinite solid and the quarter-infinite solid also can be truncated to have finite dimensions (width and thickness). Therefore, finally, the stress intensity factor for a semi-elliptical crack on one surface of a finite plate or a quarter-elliptical crack at a corner of a finite plate can be expressed as

$$K = \sigma \sqrt{\pi b} \cdot M_1 \cdot M_2 \cdot M_p \cdot \phi_1 \cdot M/\Phi \quad (15)$$

where

M_2 = a factor accounting for the influence of the back free surface

ϕ_1 = the finite width correction factor given in Figure 2-14.

M_p = plasticity correction factor

5. To obtain a front surface factor for the semi-elliptical crack, one may temporarily neglect the effects of the boundary factors ϕ_1 and M_2 and the plasticity correction factor, M_p . Equation (15) then reduces to

$$K = \sigma \sqrt{\pi b} \cdot M_1 \cdot M/\Phi \quad (16)$$

where $b = a$ for Case (a) and $b = c$ for Case (b) in Figure 2-21. For any given flaw shape, a/c ratio, the front surface factor, M_1 , at any point along the crack periphery can be estimated by interpolation of the existing stress intensity factors for the three limiting cases, namely, $a/c = 0$, $c/a = 0$, and $a = c$.

In Figure 2-21A, the extreme case is $a/c = 0$. In this case one can visualize that the plate contains many parallel slices as indicated by the dotted lines. Each slice passing through the crack looks geometrically like a two-dimensional plate having a crack of size "a" at one of the edges. Therefore, from the edge crack analysis given by Reference 45, the front surface factor, M_1 ,

equals 1.122. Similarly, the other extreme case, in Figure 2-21B, would be $a/c = \infty$ or $c/a = 0$. Again the slices between every two adjacent dotted lines are similar to the case of a plate containing a through crack at the center. Therefore, from the stress intensity solution given by Reference 46, $M_1 = 1.0$. These two points were plotted in Figure 2-22 as points A and B, respectively.

The third special case is the transition from a case where $a < c$ to a case where $a > c$, or vice versa, i. e., $a = c$, a semicircle. A numerical solution for this case has been presented by Smith, et al. (Reference 47). Results indicated that the front free surface factor, M_1 , for semicircular case is a function of β (Figure 2-22).

With a linear relationship in a/c (or c/a) assumed, i. e., connecting a straight line from any value of β on $a = c$ axis to either one of the two limiting points A or B in Figure 2-22, then for any given shape of flaw the value of M_1 corresponds to any point on the periphery of the flaw that can be interpolated. Note the M_1 values on the line between points A and C in Figure 2-22 are approximately the same as those M_1 values computed from Equation (30) in Section 2 of Volume II.

The flaw shape factors M and Φ have been defined in Equations (13) and (14), respectively. Defining a combined front surface factor $M'_1 = M \cdot M_1$, we can then rewrite Equation (16) as

$$K = \sigma \sqrt{\pi b} \cdot M'_1 / \Phi \quad (17)$$

The computed M'_1 / Φ values are plotted in Figure 2-23 for $a \leq c$ and in Figure 2-24 for $a \geq c$. It can be seen from these figures that the maximum M'_1 / Φ is at $\theta = 90^\circ$ for a/c greater than 0.78. Conversely, maximum M'_1 / Φ is located at $\theta = 0^\circ$ for a/c less than 0.78.

Also observed in Figure 2-23 is that, at $a/c = 0.78$, the variations on K along the crack periphery are minimum. In other words, without the influences of any other geometrical or physical variables, such as back surface, finite width, or plasticity, the most stable flaw shape would be at $a/c = 0.78$. However, taking another look at Figure 2-23, it is revealed that the constant K point would probably be located at $a/c = 0.9$, where the combined front surface factors for $0^\circ \leq \beta \leq 60^\circ$ converge to one single point. This value agrees with the one previously published by Smith and Alavi, $a/c = 0.84$, (Reference 48). Whether the flaw shape for constant K

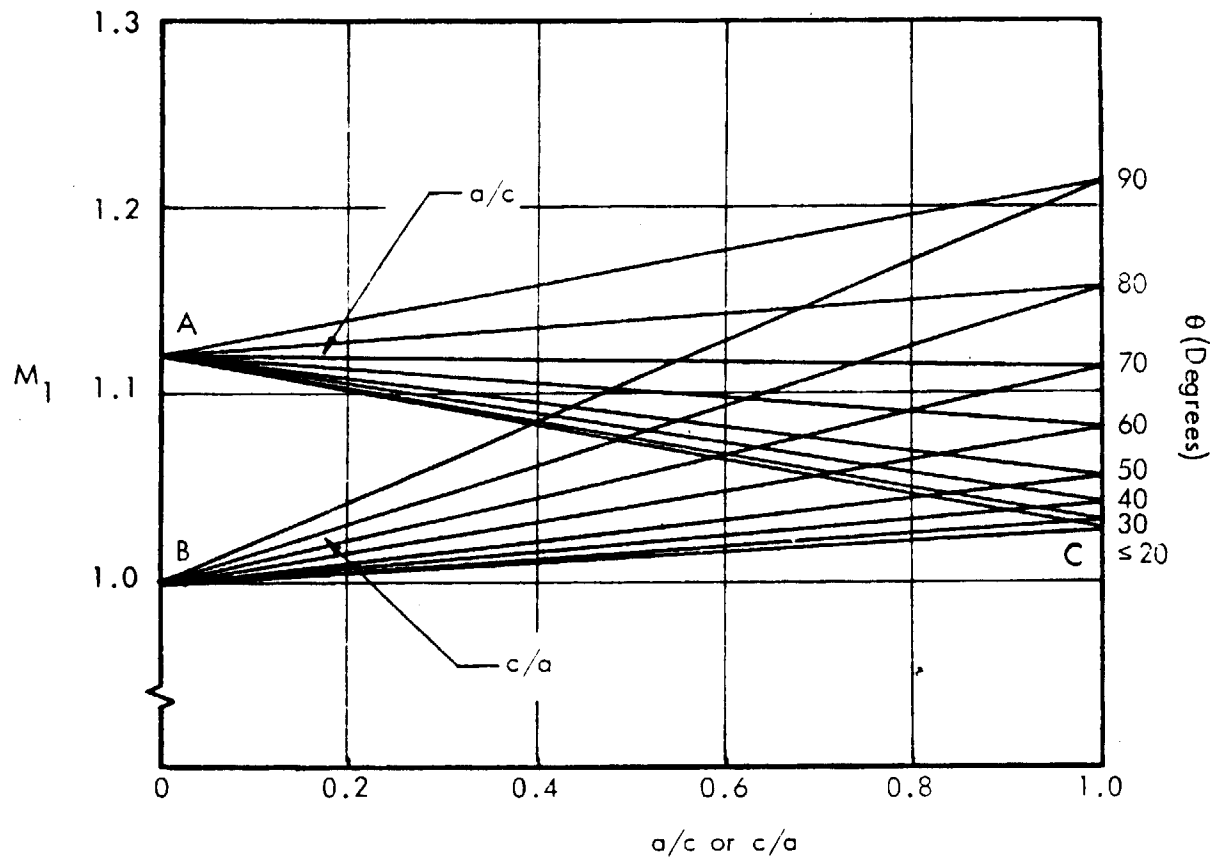
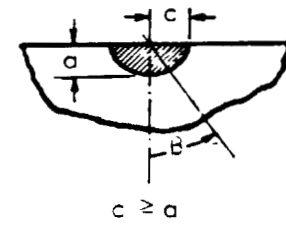
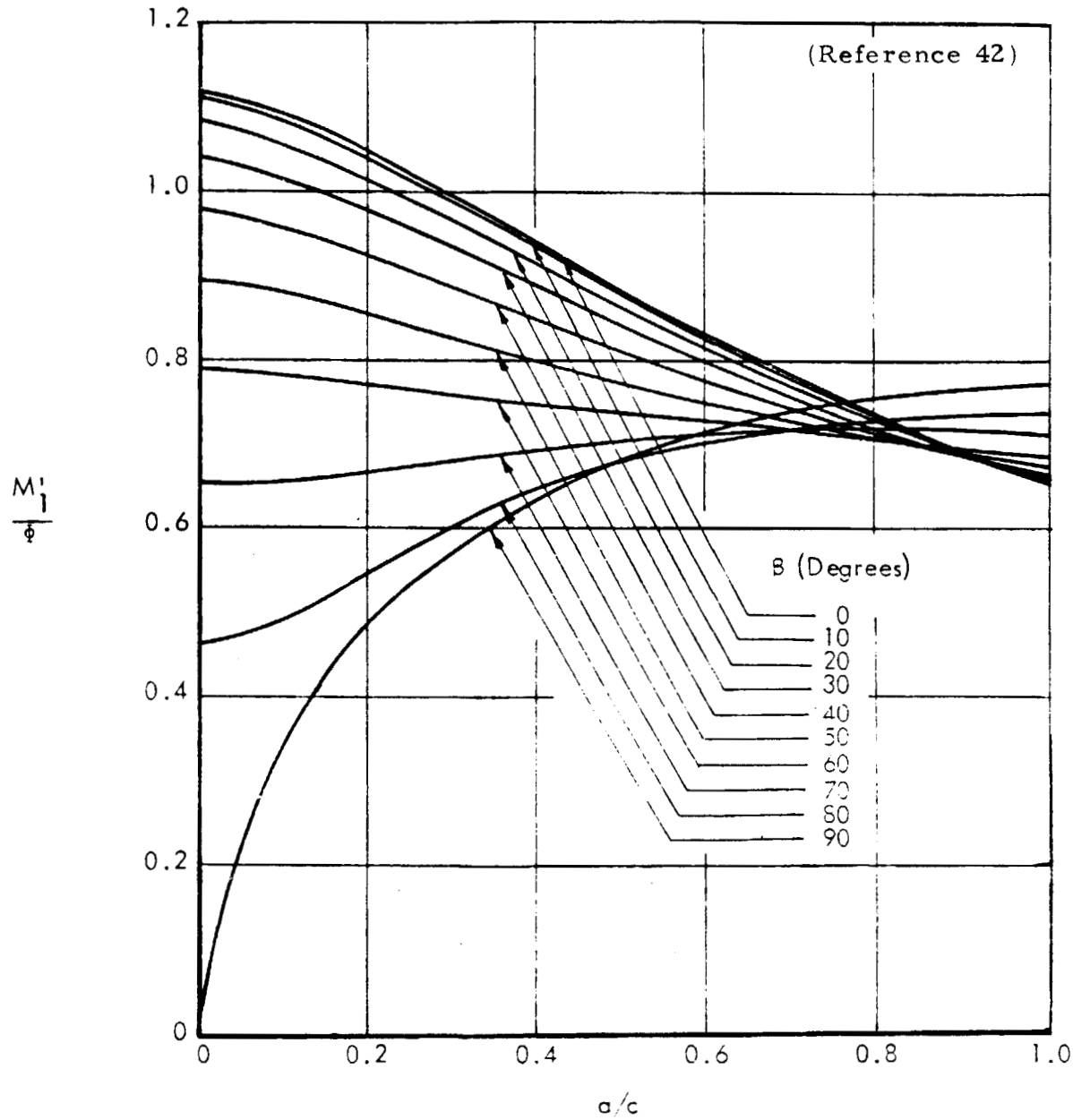
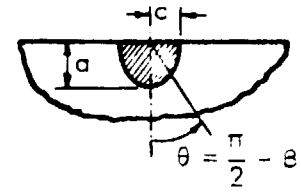
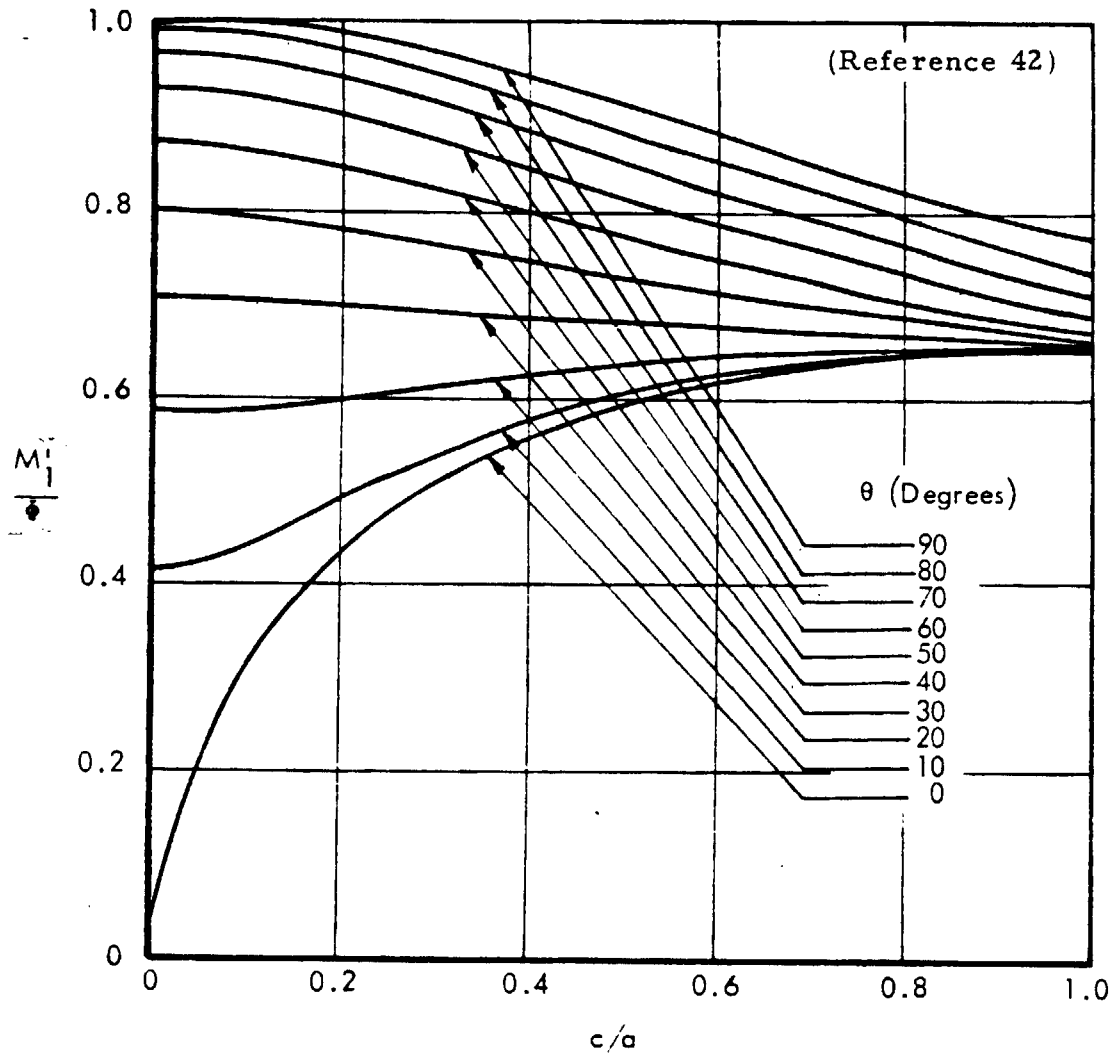


Figure 2-22. Front Free Surface Influence Factor M_1



$$K = \sigma \sqrt{\pi a} \left(\frac{M_1'}{t} \right)$$

Figure 2-23. Front Surface Influence Factor M_1'/ϕ for $a/c \leq 1$



$$c \leq a$$

$$K = \sigma \sqrt{\pi c} \left(\frac{M_1'}{\phi} \right)$$

Figure 2-24. Front Surface Influence Factor M_1'/ϕ for $a/c \geq 1$

should be $a/2c = 0.42$ or 0.39 , these values disagree slightly with the theory of Westmann, who had suggested that the stable flow shape should be $a/c = 1.0$ (Reference 49). The disagreement is mainly attributed to the adoption of Smith's semi-circular flow stress intensity factors in the present analysis procedure.

Experiments have been conducted on ten 7075-T6 aluminum surface flow specimens (Reference 42). These specimens were either 1.27 or 0.635 centimeters (0.5 or 0.25 inch) thick and 7.62 centimeters (3 inches) wide with initial flaw depths approximately 5 to 10 percent of the specimen thickness. The initial flaw shape was $0.262 \leq a/2c \leq 0.533$. The specimens were subjected to constant amplitude cyclic loading with the minimum to maximum applied stress ratio equal to 0.1. The maximum applied stress levels were not the same on every specimen. Despite a wide range of applied stress levels, $13 \leq \sigma_{\max} \leq 50$ ksi, examination of the broken halves of the specimens after testing revealed that nine out of the ten specimens had a stabilized final flow shape of $a/2c = 0.43$, approximately. The last specimen had a flow shape of $a/2c = 0.384$ because the final crack length on the surface ($2c$) was approximately a little longer than one-third of the specimen width and the stress intensity on this specimen might have been significantly affected by the finite width of the specimen.

Perhaps the most significant value of the present analysis procedure is its application to fatigue crack growth analysis. In the past, fatigue crack growth predictions were conducted by assuming that the shape of the surface flaw was unchanged throughout the entire period until the flaw broke through the back surface and became a through-the-thickness crack. Without employing Smith's solution, the point of K_{\max} , for any flaw shape ($a \leq c$), is always located at the center of the flaw periphery. Crack propagation rates were evaluated at this point only. It is now realized that the point of K_{\max} (in the case of a semi-infinite solid) is either at the maximum depth or on the free surface (except for $a = 0.78c$, the transition point having K_{\max} at both locations, Figure 2-23) and that the crack grows faster at these points. However, the other points along the crack periphery also exhibit various amount of growth dependent upon the magnitude of K corresponding to a certain location. This uneven rate of crack growth results in a change of flow shape (a/c ratio) in every single step of crack increment and consequently changes the rate of crack growth in every point along the crack periphery. The previously discussed ten data points, along with the calculated final $a/2c$ ratios, are plotted in Figure 2-25 for comparison. The

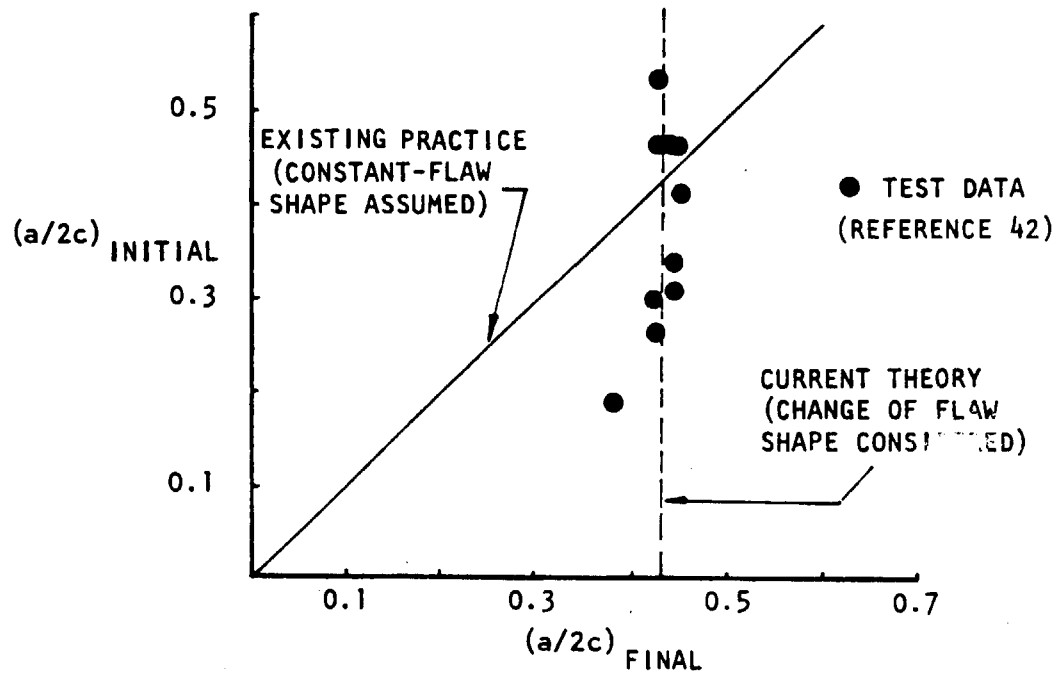


Figure 2-25. Change of Flaw Shape in Propagation of Surface Crack

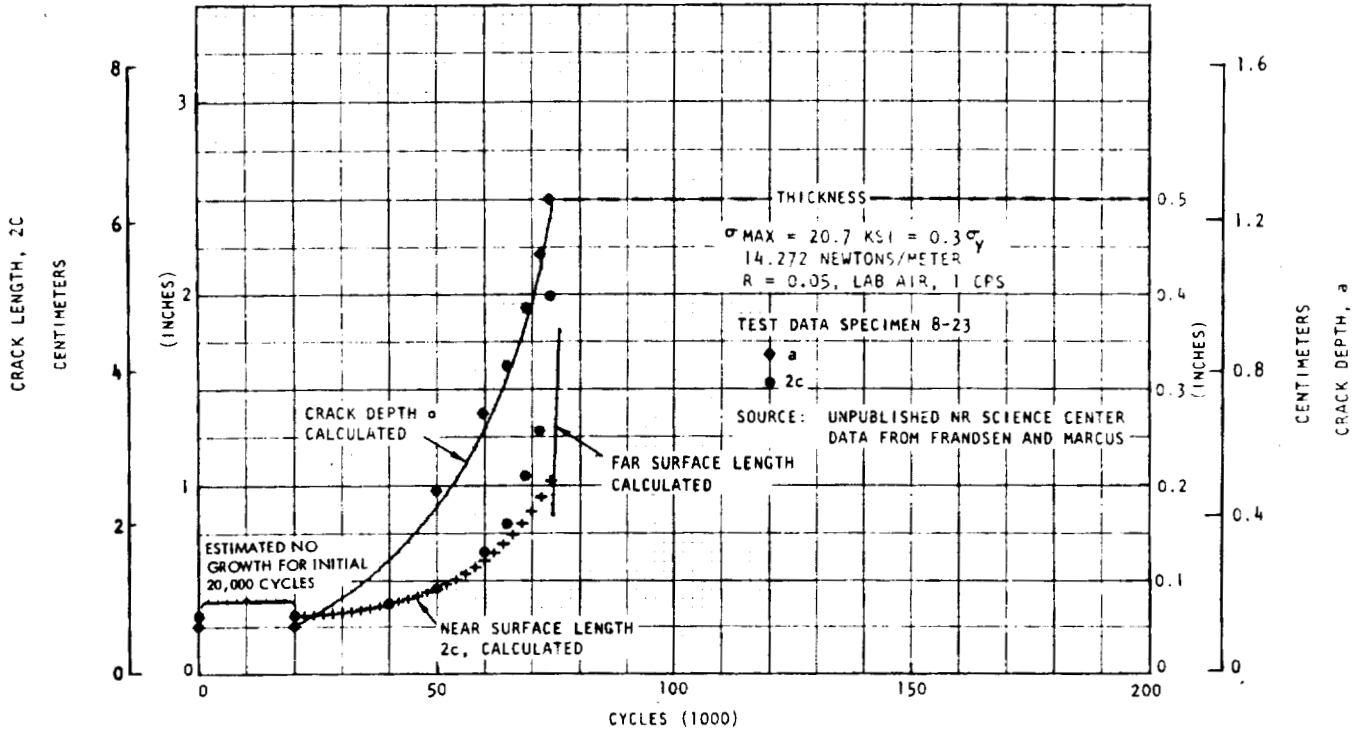
vertical dotted line in the figure represents the final flaw shape value calculated by using the current procedure, whereas the 45-degree solid line indicates what would have happened if the flaw shapes were assumed to be a constant value. Another example taken from Reference 50, is shown in Figure 2-26 where two actual tests are compared with calculations. The figure substantiates the effectiveness of the current approach.

6. So far the geometric factors M , Φ , and M_1 have been discussed. The remaining problems would be the back surface influences and plasticity. These two variables seem to interact with each other. If the flaw is shallow as compared to plate thickness and the applied stress is low as compared to the tensile yield strength of the material, the effects of the back surface and the plasticity at the crack tip are negligible. As the flaw develops and propagates toward the back surface, large scale plastic yielding occurs in front of the crack. When the plastic zone ($2r_y$) in front of the flaw penetrates the thickness of the plate, the effect of this zone is altered. At this point the development of the crack front plastic zone is limited by the fact that the available area in the crack front is bounded by the back surface. As a result, the back surface effect may be truncated when this transition occurs. The mechanics of crack growth in this case are uncertain. One possibility is that fracture will be controlled by the stress intensity at or near the major axis of the semi-ellipse. In other words, the surface flaw would behave like a through-the-thickness crack. As a limiting case, the residual strength for such a specimen configuration or structural component can be estimated by this approach. Consider that the area between the flaw and the back surface is undergoing plastic yielding; the load applied to the gross area is equal to σ times $2ct$, and the maximum load applied to the net area is approximated by F_{ty} times $(2ct - \pi ac/2)$. With a comparison of these two loads, a criterion for the cutoff point can be estimated by

$$a_{et} = \frac{4t}{\pi} \left[1 - \frac{\sigma}{F_{ty}} \right] \quad (18)$$

where a_{et} is defined to be the flaw depth for a flaw equivalent to the through-the-thickness crack. For a crack depth larger than this, the stress intensity may be computed by the through-the-thickness crack formula. Equation (18) was initially derived by G. Vroman as described in Section 4.3 of Volume II. For the fatigue crack propagation case, other transition criteria can be used, such as those proposed in Chapter 4 of Volume II. It can be

(a) 2024 - T851 ALUMINUM



(b) TITANIUM, 6Al - 4V, CONDITION DBA

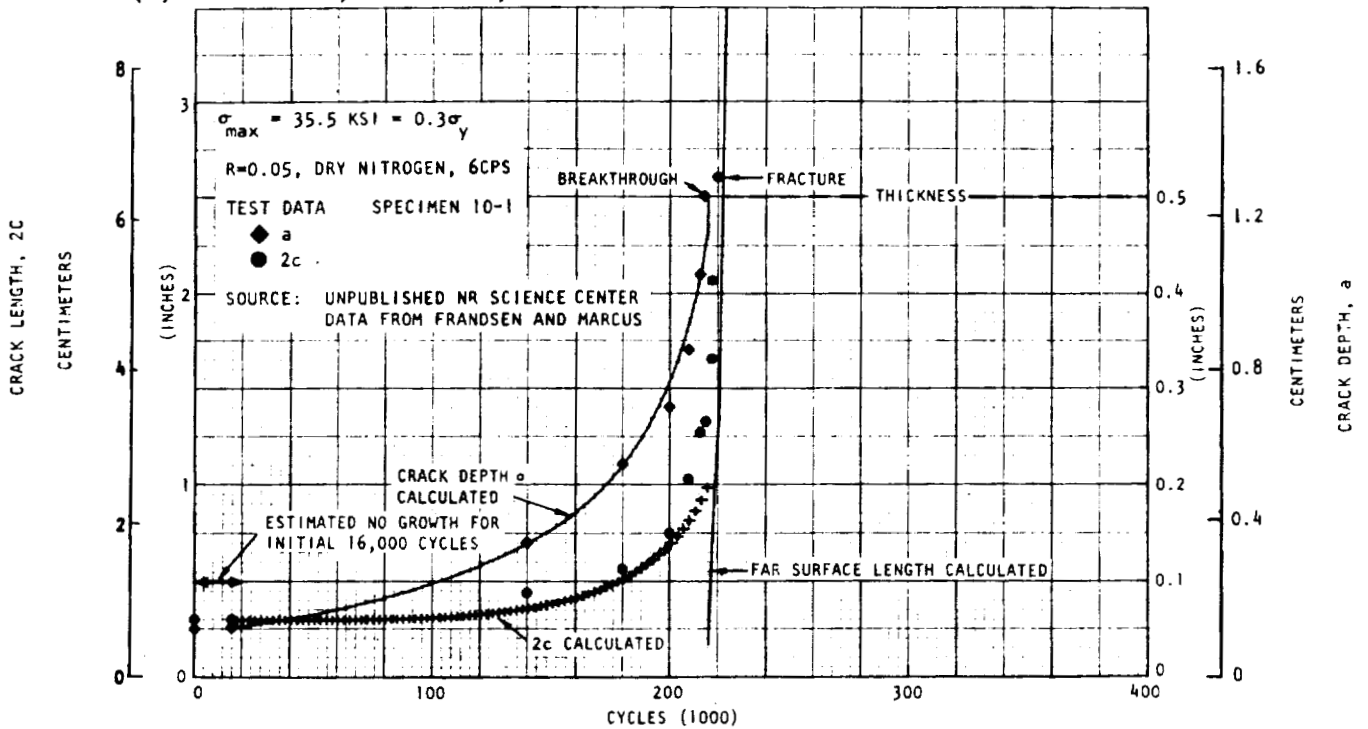


Figure 2-26. Surface Flaw Fatigue Crack Propagation Data (Comparison With Calculations, Reference 50)

expected that the back face yielding behavior would be extremely significant for the thin sheet. Many investigations have been conducted to explore this problem (e. g., References 51, 52, and 53). However, a unified analysis procedure is yet to be developed.

7. For a surface crack in a finite width plate, again with use of the plastic zone size relation of Equation (6) and with $n = 4\sqrt{2}$ for plane strain, the plasticity correction factor, M_p , representing the point of maximum depth in Figure 2-21A is

$$M_p = \left[1 - 0.177 M_2^2 \left(\frac{M_1'}{\Phi} \right)^2 \cdot \left(\frac{\sigma}{F_{ty}} \right)^2 \right]^{-1/2} \quad (19)$$

Similarly, the plasticity correction factor representing the point on the surface (with $n = 2$ for plane stress) in the configuration shown in Figure 2-21B is

$$M_p = \left[1 - 0.5 \phi_1^2 \left(\frac{M_1'}{\Phi} \right)^2 \cdot \left(\frac{\sigma}{F_{ty}} \right)^2 \right]^{-1/2} \quad (20)$$

For the shallow flaw case ($a \leq t/2$), Irwin (Reference 43) has assumed that the combined effects of the front and the back surfaces would be approximately 10 percent. With this assumption, $M_1 \cdot M_2 = 1.1$, Equation (19) reduces to

$$M_p = \left[1 - \frac{0.212}{\Phi^2} \left(\frac{\sigma}{F_{ty}} \right)^2 \right]^{-1/2} \quad (21)$$

or

$$M_p = \Phi \left[\Phi^2 - 0.212 \left(\frac{\sigma}{F_{ty}} \right)^2 \right]^{-1/2} \quad (22)$$

and the quantity inside the square root is the so-called "Q" frequently appearing in the literature.

8. Many back surface factors are available. These back surface factors were developed either by analysis or by experiments (e. g., References 40, 48, 54, 55, and 56). The most representative one is that given in Reference 40. For $0.1 \leq a/2c \leq 0.5$, back surface factor can be expressed by (Reference 50)

$$\begin{aligned}
 M_2 = & 1 + \frac{1}{0.502} \left[0.089 \left(\frac{a}{t} \right) - 0.2315 \left(\frac{a}{t} \right)^2 \right. \\
 & \left. - 0.3873 \left(\frac{a}{t} \right)^3 + 5.28 \left(\frac{a}{t} \right)^4 - 9.11 \left(\frac{a}{t} \right)^5 + 5.233 \left(\frac{a}{t} \right)^6 \right] \\
 & \times \left[1.109 - 9.142 \left(\frac{a}{2c} \right) + 41.56 \left(\frac{a}{2c} \right)^2 - 86.55 \left(\frac{a}{2c} \right)^3 \right. \\
 & \left. + 65.5 \left(\frac{a}{2c} \right)^4 \right]
 \end{aligned} \tag{23}$$

The calculated curves shown in Figure 2-26 are incorporated with this back surface factor. It is seen that this back surface factor, in connection with the current predictive analysis procedure, correlates well with data examined.

9. A crack at one corner of a quarter infinite solid (Type 3 crack in Figure 2-13 or Figures 2-21C and 2-21B without the finite boundaries) can be considered as a surface flaw having two front surfaces, one located at the $\theta = 0^\circ$ position and the other at the $\theta = 90^\circ$ position. Any point on the periphery of the Type c crack corresponds to a reciprocal point on the Type d crack. In other words, the front surface correction factors for both Type c and Type d cracks are identical. At any orientation, β , this factor can be defined as a product of two separate front surface factors, namely $M_1'(\beta)$ and $M_1'(\pi/2 - \beta)$. If $F' = \pi [M_1'(\beta) \cdot M_1'(\pi/2 - \beta)/\Phi]^2$ is defined, Equation (17) becomes

$$K = \sigma \sqrt{F' b} . \tag{24}$$

The values of F' versus a/c ratios are plotted in Figure 2-27.

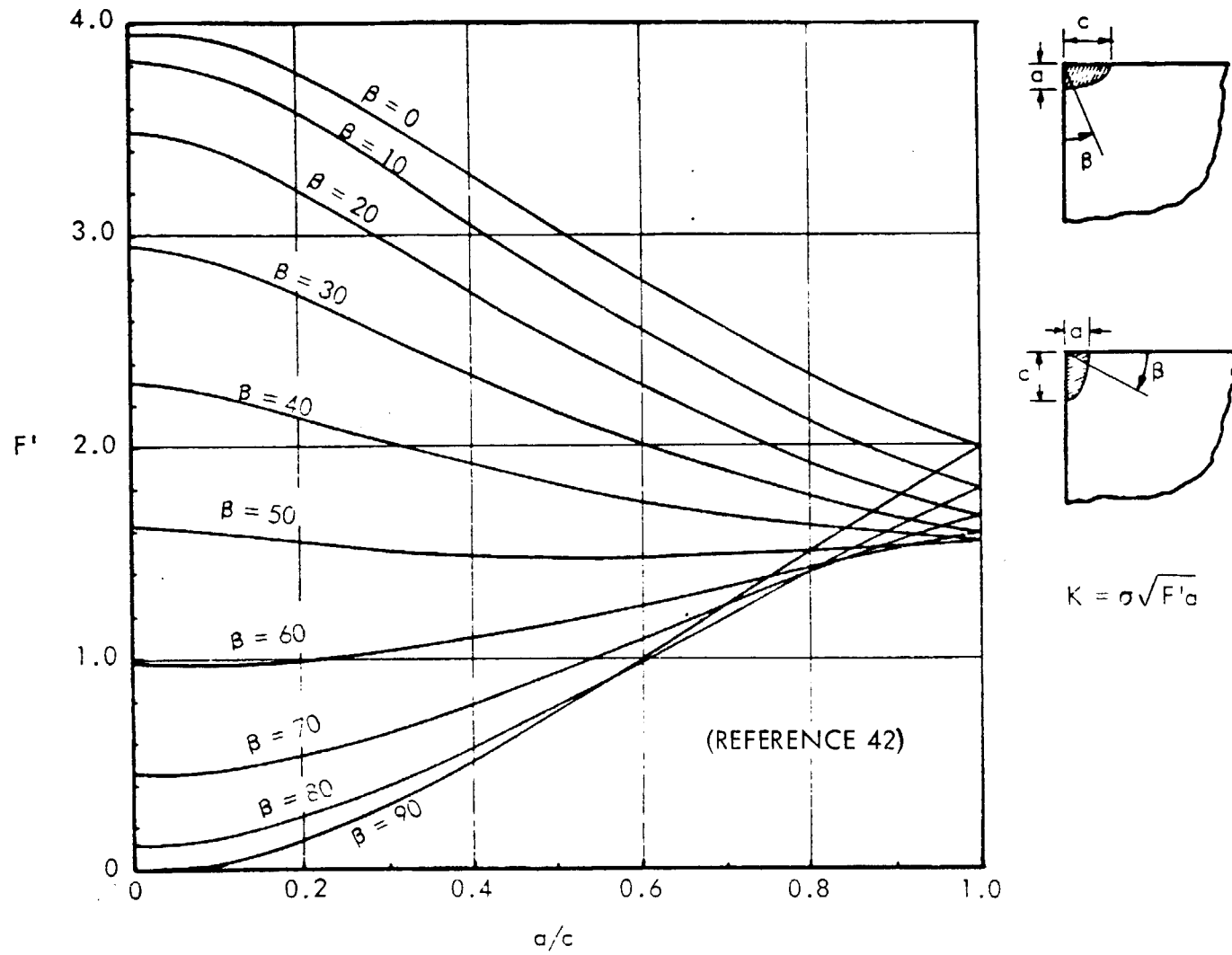


Figure 2-27. Free Surface Correction Factor for Corner Flaw

2.3.3.3 Crack or Cracks Emanating From a Circular Hole

Since B. Kirsch in 1898 showed that the local stress at the edge of a circular hole (in a thin, infinitely wide sheet) was three times that of the applied stress, many investigations have been conducted on stress distributions in the vicinity of the hole. Information is available regarding hole configuration, structural configuration, and loading condition, with or without cracks emanating from a hole, crack propagation approaching a hole, or interaction of cracks at adjacent holes, etc. The crack configurations considered here are those given in Figure 2-28. These crack geometries are similar to those shown in Figure 2-21 and, therefore, it is assumed that some of the previously presented geometric factors are also applicable here. The approximate stress intensity expressions for these crack geometries may be expressed as

$$K = \sigma \sqrt{\pi b} \cdot B \cdot M_p \cdot M_2 \cdot M_1/\Phi \quad (25)$$

for an elliptical corner crack at edge of a hole and

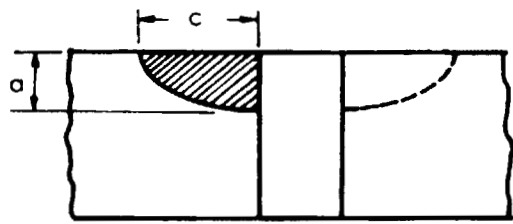
$$K = \sigma \sqrt{\pi b} \cdot B \cdot M_p \cdot M_2 \cdot M/\Phi \quad (26)$$

for an elliptical crack at the edge of a hole. Here parametric curves for M_1/Φ have been given in Figure 2-24. The parametric curves for M/Φ are presented in Figure 2-29. B is the Bowie's factor accounting for the influence of the circular hole (Reference 57, Figure 2-30) and has a factor for the free surface of the hole within it. It is a function of the ratios of the distance from the edge of the hole to the crack tip, L, and the radius of the hole, r. Since L varies between zero and c, the B factor, as well as the stress intensity, varies along the crack periphery.

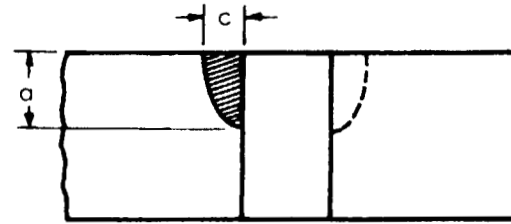
Eventually these cracks will become through-the-thickness cracks (at the edge of a hole) such as those shown as Case 4 in Figure 2-13. Here both M_1/Φ and M/Φ approach unity so that Equations (25) or (26) reduce to

$$K = \sigma \sqrt{\pi c} \cdot B \cdot M_p \quad (27)$$

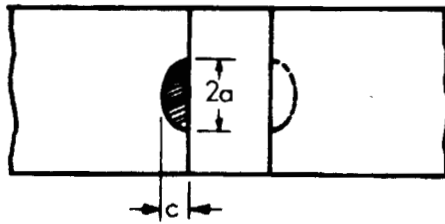
The application of the Bowie's factor is not straightforward. The Bowie's factor is for an elastically loaded open hole in an infinitely wide sheet. It can be considered a special case of the stress concentration factor, K_t . It is commonly known that the values for elastic K_t are affected by the finite dimension of the plate. This finite width effect on K_t of the hole (without a crack) might interact with the finite width effects normally imposed on the crack. Furthermore, if the applied stress exceeds one-third of the



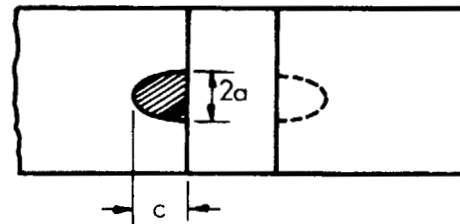
A



B



C



D

Figure 2-28. Crack or Cracks Emanating From a Hole

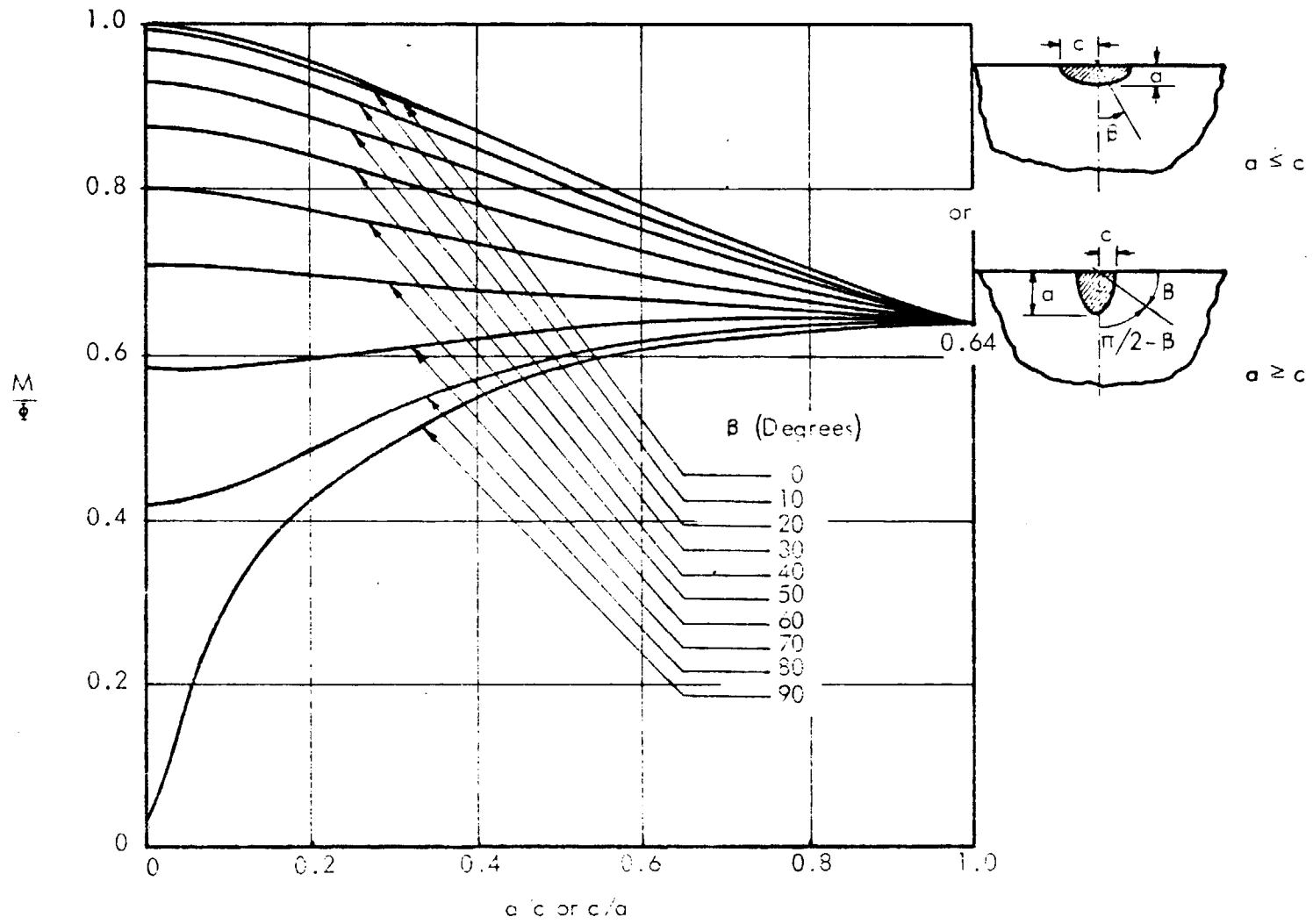


Figure 2-29. Flaw Shape Factor M/ϕ

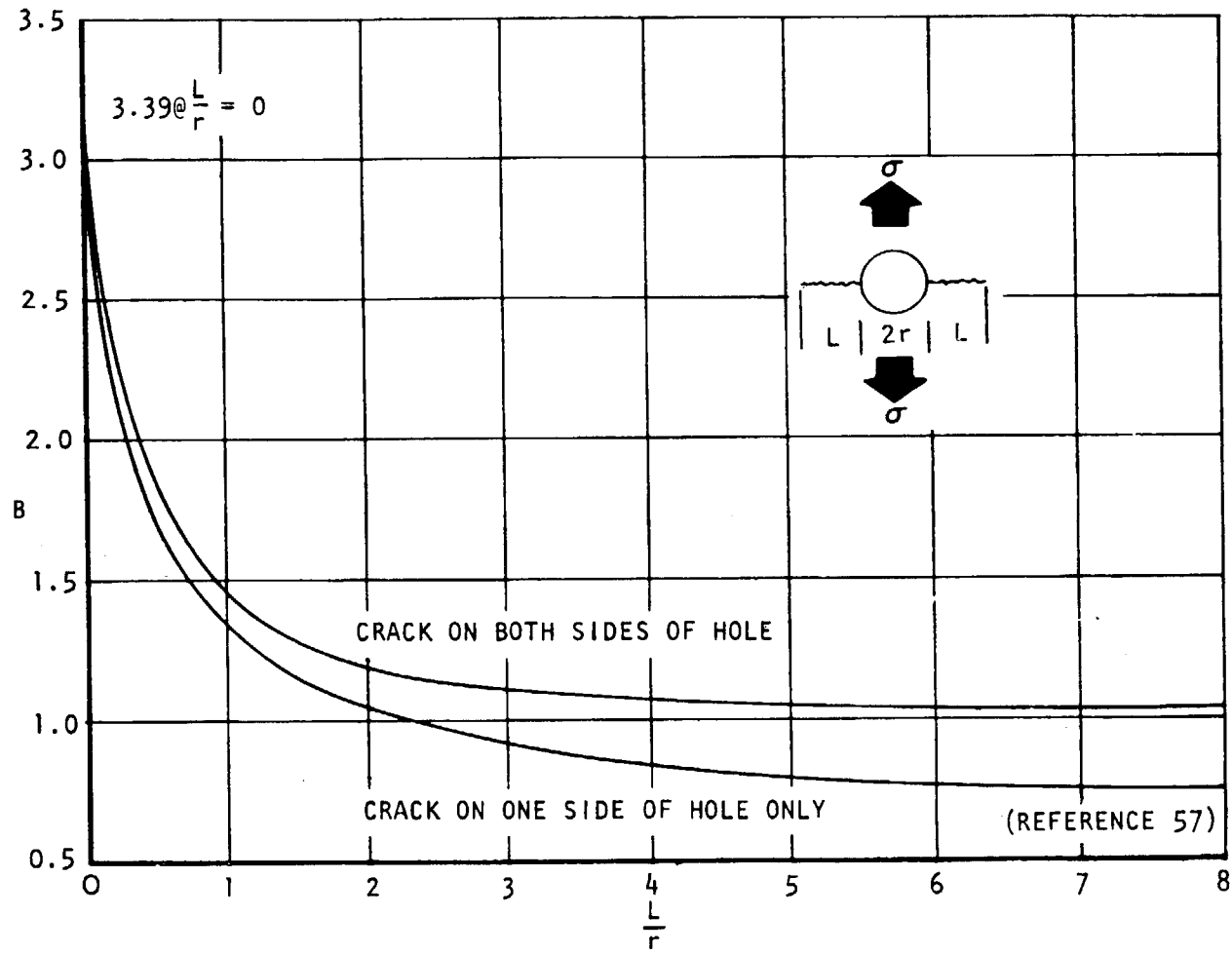


Figure 2-30. Bowie's Factors for Influence of a Hole

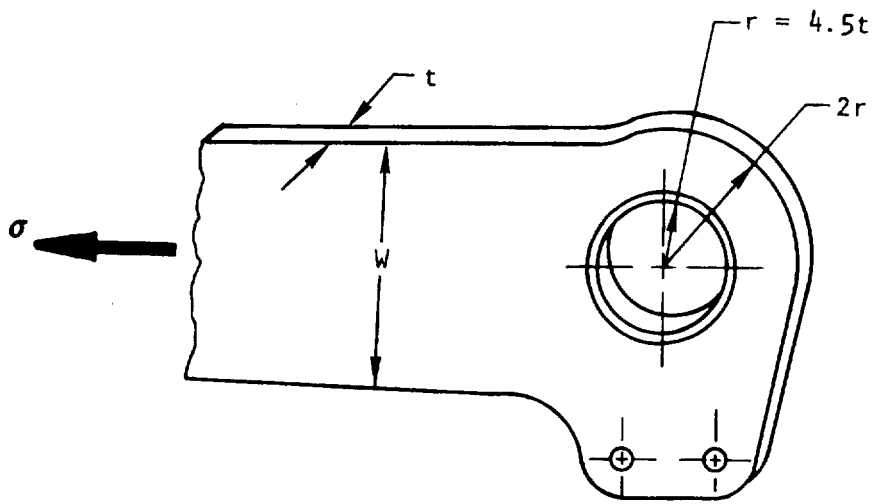
material tensile yield strength, the area adjacent to the edge of the hole deforms plastically. The size of the local yield zone at the edge of the hole increases as the applied stress increases. For a crack smaller than the local plastic zone of a yielded hole, the crack extension behavior would not be the same as predicted by linear elastic fracture mechanics. An analysis procedure has been proposed that uses Neuber's stress and strain concentration factors to account for the plastic behavior on K_t (References 58 and 59) and the J-integral to handle crack tip plasticity (Refer to Volume II for the J-integral concept).

Other important classes of yielded-hole problems are cases that have residual stresses around the hole induced by cold working the hole with an oversized mandrel or by employing an interference fit fastener. Some stress intensity factors for these cases have been developed (References 60 and 61).

2.3.3.4 Special Cases

Two categories of cracks commonly of concern are pin-loaded holes and cracks at the root of an angle (e. g. , at stiffener-sheet intersection). For a pin-loaded hole, consider the rivet load in a sheet and the pin-loaded lug. In either, uniform stress is applied on one side of the hole in the sheet (or in the shank of the lug), and a concentrated force is applied on the opposite side of the hole. This concentrated force causes Mode I as well as Mode II stress intensity factors. Example solutions for particular problems are given in Figures 2-31 and 2-32, respectively. The calculated values for K_{II} in these two cases are very small; therefore, only the K_I component is reported in the figures. Note that these two figures are not general and should not be used for other geometries.

Typical geometrics for cracks at the root of a stiffener are Cases 7 and 8, illustrated in Figure 2-13. A stress intensity solution is not yet available for Case 8. Since the load is usually parallel to this kind of crack surface, it is anticipated that the stress intensity factor would be negligibly small. For Case 7, an engineering approach is to consider that the crack is three-fourths of an ellipse. The stress intensity factor can be obtained by interpolating between a full ellipse and an one-half ellipse. Another special case for a corner crack would be the crack right at the angle of a countersunk fastener. In this case the stress intensity factor can be interpolated between a half-elliptical crack and a 90-degree corner crack.



$$K_I = \sigma \left(\frac{W}{2r} \right) \sqrt{\pi a} \cdot \lambda$$

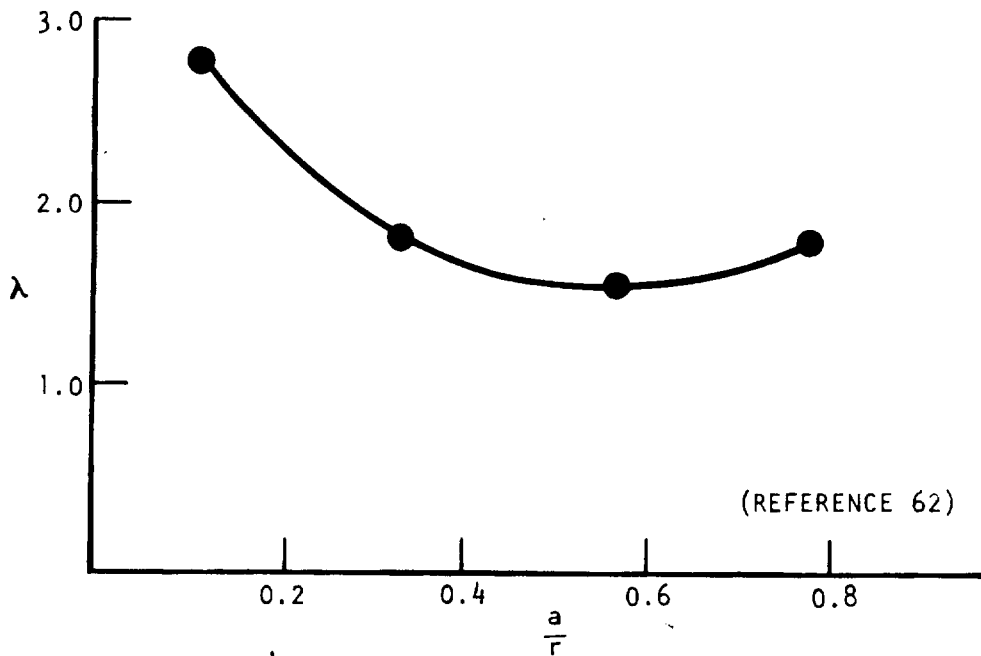


Figure 2-31. Stress Intensity Factor Versus Crack Length for a Lug

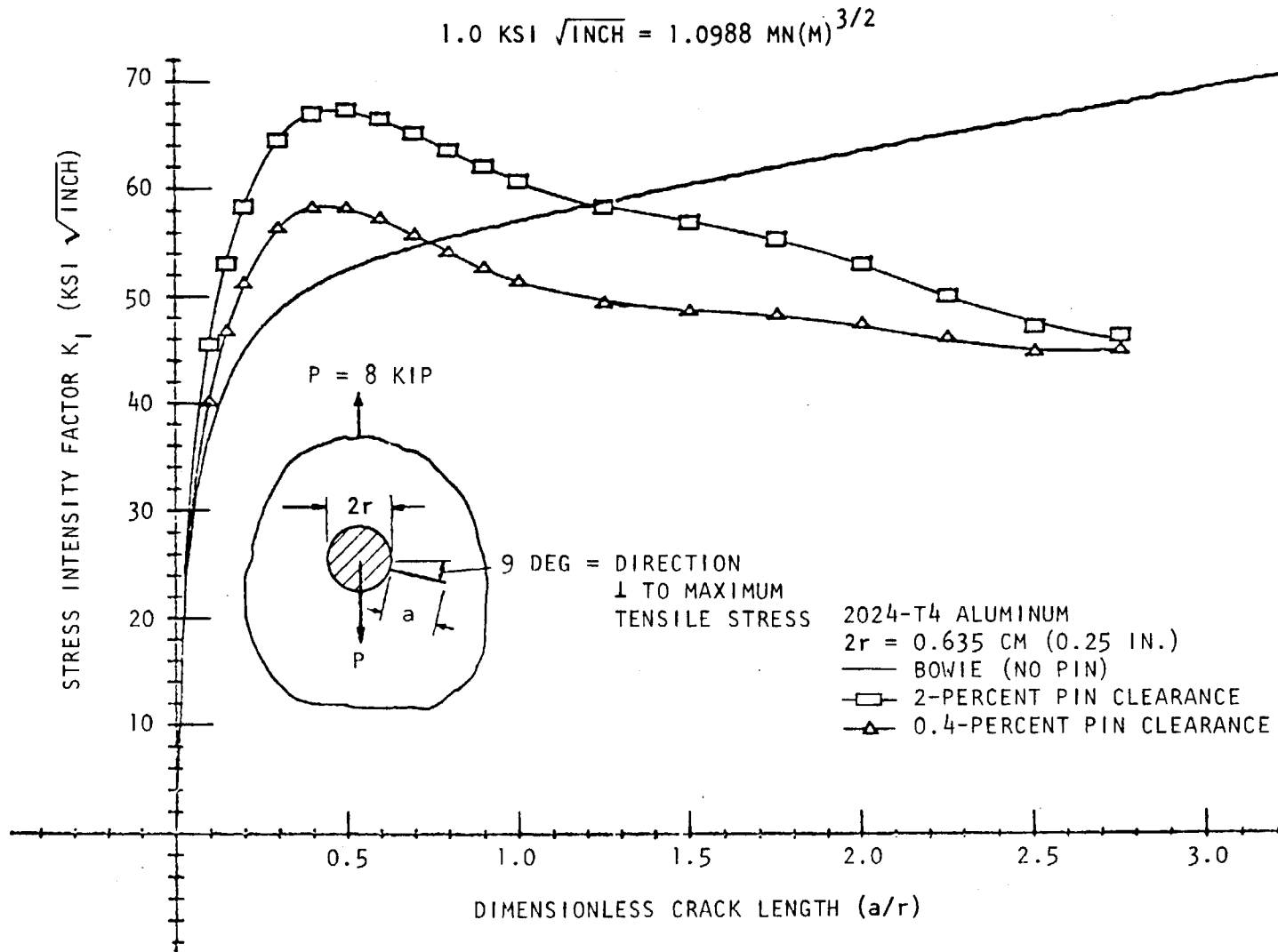


Figure 2-32. Stress Intensity Factor for a Pin-Loaded Hole (Reference 61)

2.3.4 Crack Arrest Structure

The basic techniques for designing this class of structure is to employ an effective barrier to retard fast propagation of a crack under normal operating conditions. These barriers, or reinforcements, redistribute the stress field in the vicinity of the crack tip (i. e., they provide a region of low-stress intensity in the path of the advancing crack front). The barriers can be attached stiffeners or the riser in an integrally stiffened plank. The attached stiffeners are normally stringers or flat straps riveted onto the sheet skin. Flat straps adhesively bonded onto sheet skin (provided that the bond has sufficient flexibility) are also considered to be attached stiffeners. In either one of these cases, the idea is to determine the pattern of crack tip stress intensity at various locations respective to the stiffener position. Fatigue crack growth analysis can be performed by using this pattern to modify the crack tip stress intensity so that the safe-crack-growth period can be estimated from the material fatigue crack propagation rate curve (da/dN versus ΔK curve). The residual strength (can be interpreted in terms of fail-safe load levels) for the stiffened panel can also be estimated by using the same type of crack tip stress intensity analysis. The methods of analysis for either type of the crack arrest structures are discussed in the following paragraphs.

2.3.4.1 Attached Stiffener

Figure 2-33 shows a typical configuration for the attached stiffener structure. For this type of structural arrangement, the stress intensity factor level decreases as the crack approaches the reinforcement and significantly decreases when the crack tip is right at the vicinity of the reinforcement. The K value will increase again as the crack propagates past the region wherein the reinforcement is effective. This temporary reduction of crack tip stress intensity is due to the reaction of the rivet forces (i. e., a portion of skin load is transmitted through the fastener and will be carried by the stiffener). Consequently, the general stress intensity factor for this case will consist of two terms, the term involved with the overall stress acting on the skin (based on uniform stress and crack length only) and the term involved with the transmitted load in the reinforcement. For an infinitely wide panel, the K expression can be written as:

$$K = \left[\sigma - \sum_{j=1}^n f(F_j) \right] \cdot \sqrt{\pi \cdot l/2} \quad (28)$$

Where F_j is the fastener load of the j th fastener, the minus sign refers to the reduced crack tip stress intensity due to the effect of the reinforcement (the rivet forces are acting in the opposite direction respective to the applied load). A typical example of this type of analysis is schematically presented

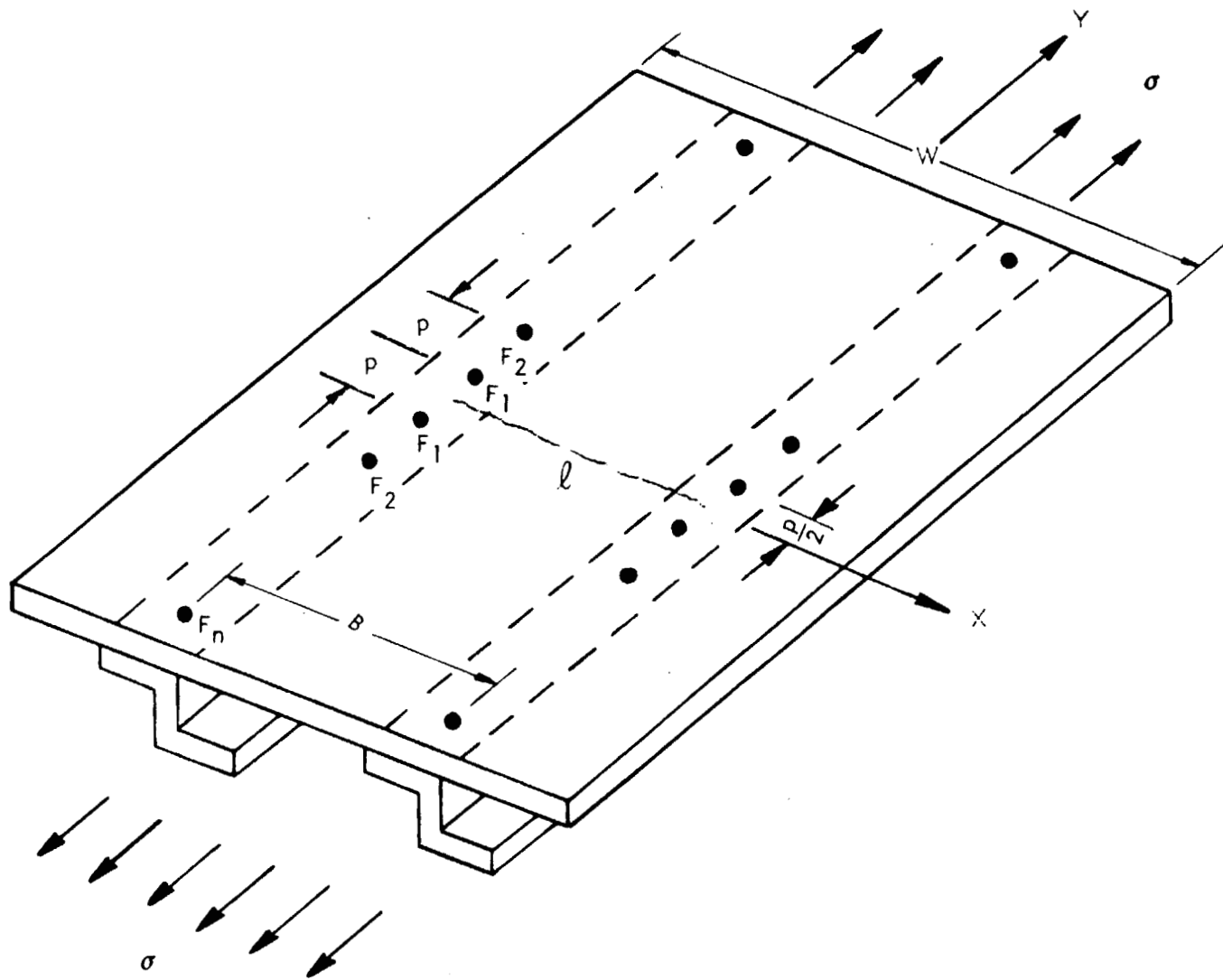


Figure 2-33. Through-the-Thickness Cracks in Skin-Stiffened Panel

in Figure 2-34. Here the variations in K due to the effect of reinforcement (dotted lines) are compared with the normal values of K for the plain sheet alone (solid lines) in two arbitrary chosen stress levels.

2.3.4.2 The Analytical and Physical Aspects of Skin-Stringer Structure

There have been many investigations, both analytical and experimental, involving the damage tolerance of reinforced flat panels. Only a few of these investigations have attempted to systematically study the effect of configuration and material variables. The references listed here (References 63 to 71) are those pertinent to the present study. Three analytical investigations (References 63-66), modeling an infinite linearly elastic cracked plate with linearly elastic reinforcements and rigid attachments, have established the effect of elastic material properties and geometric variables. The result of Poe's analysis (Reference 66) is given in Figures 2-35 and 2-36. In these illustrations, the stress intensity modification factor, C, is essentially the ratio of the stress intensity factor for the stiffened panel (Equation 28) to the stress intensity factor for the plain sheet (without stiffener, the first term in Equation 28). Here the C factor is interpreted to be the function of the following variables:

1. Attachment spacing (rivet pitch), p.
2. Reinforcement spacing, B.
3. A relative stiffness parameter, μ , which is defined as:

$$\mu = \frac{1}{1 + \frac{Bxt}{A_e} \cdot \frac{E}{E_s}} \quad (29)$$

Where E is the Young's modulus for the sheet, E_s is the Young's modulus for the stiffener, t is the sheet thickness and A_e is the effective cross sectional area of the stiffener. For a flat strap, A_e is approximately equal to the actual size (gross area) of the strap. For the case of a stringer, according to Reference 70,

$$A_e = A \left[1 + \left(\frac{y}{\rho} \right)^2 \right]^{-1} \quad (30)$$

Where A is the cross-sectional area of the stringer, y is the distance from the inner surface of the sheet to the centroid of the stringer, and ρ is the radius of gyration of the stringer.

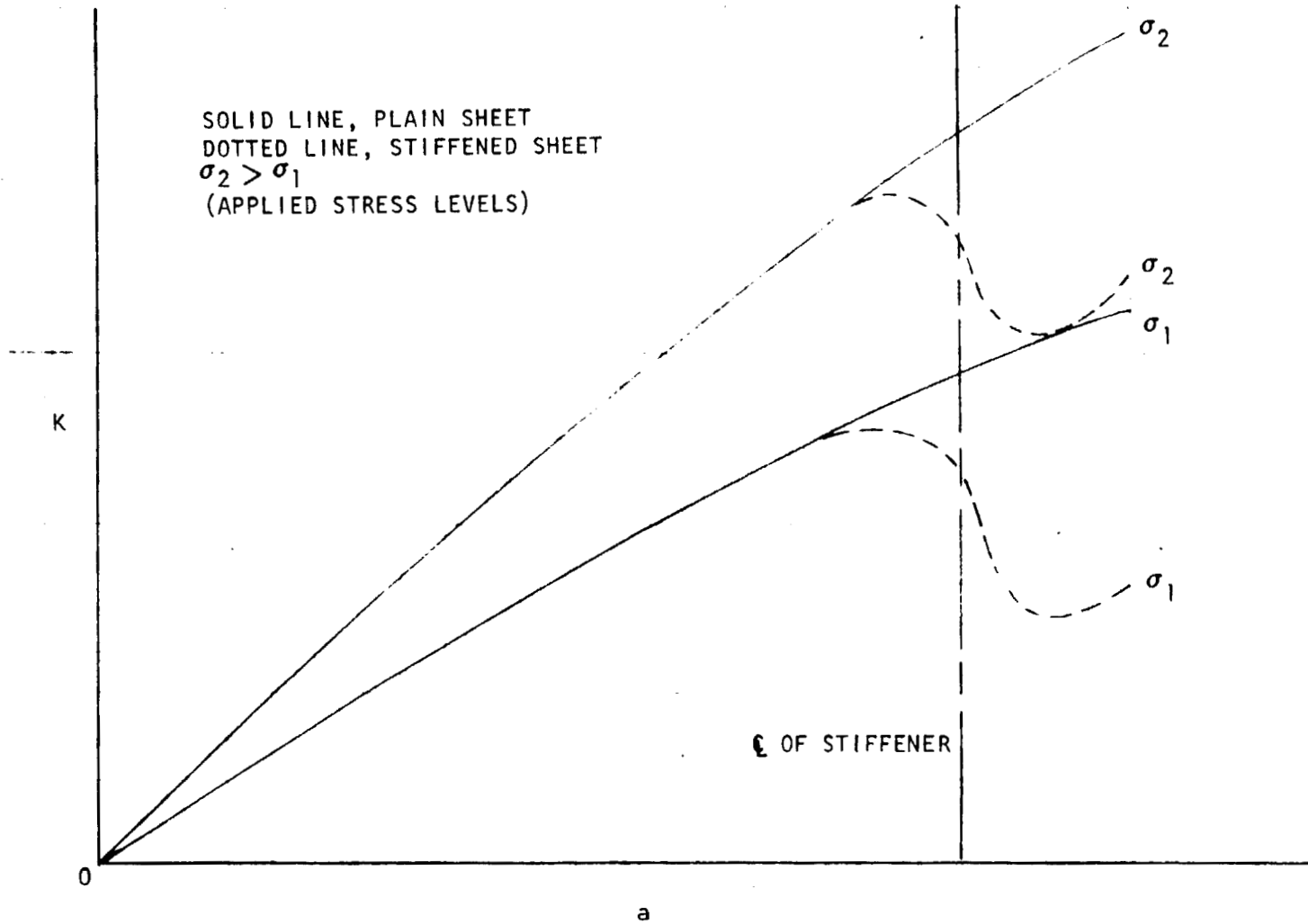


Figure 2-34. Stress Intensity Analysis of Unstiffened and Stiffened Structure

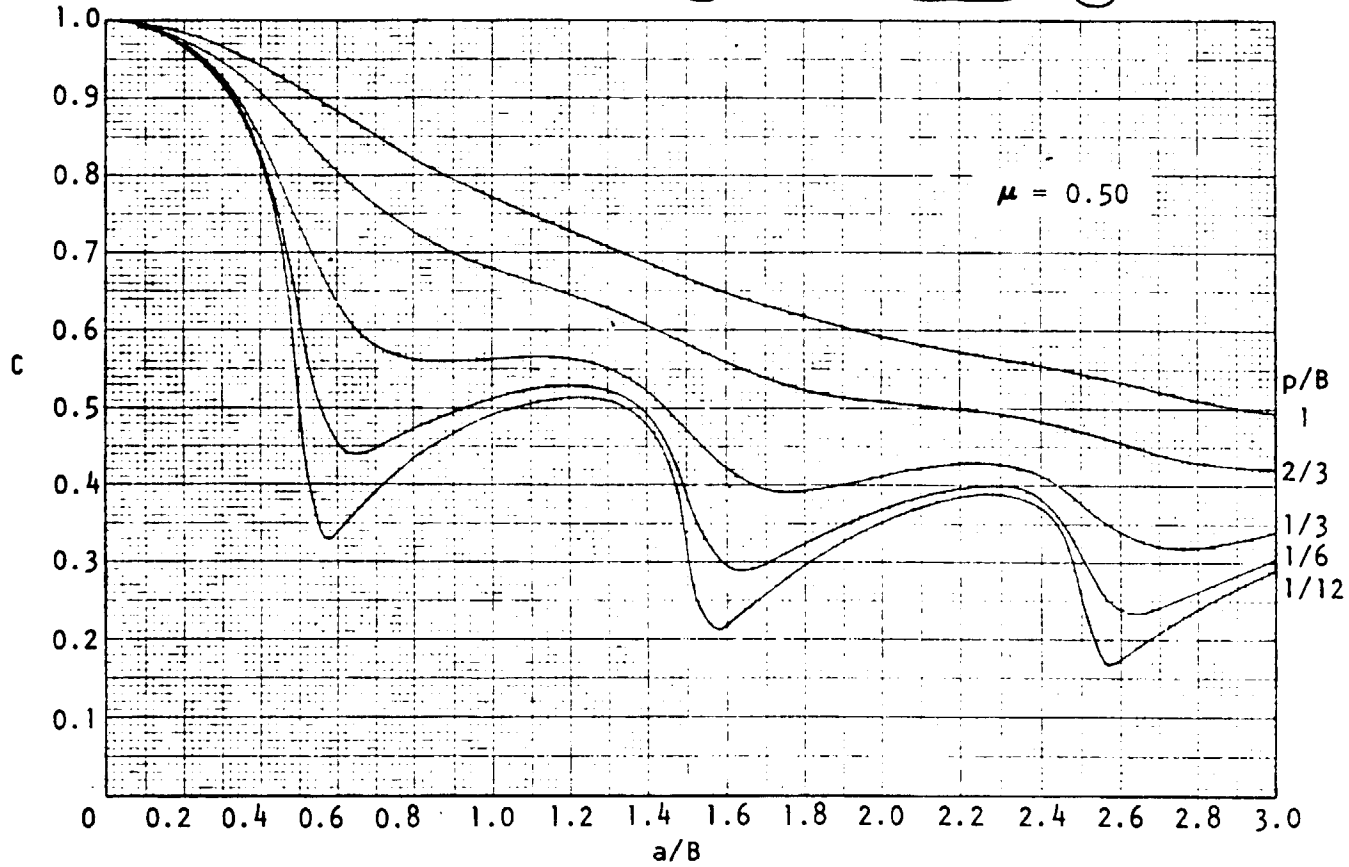
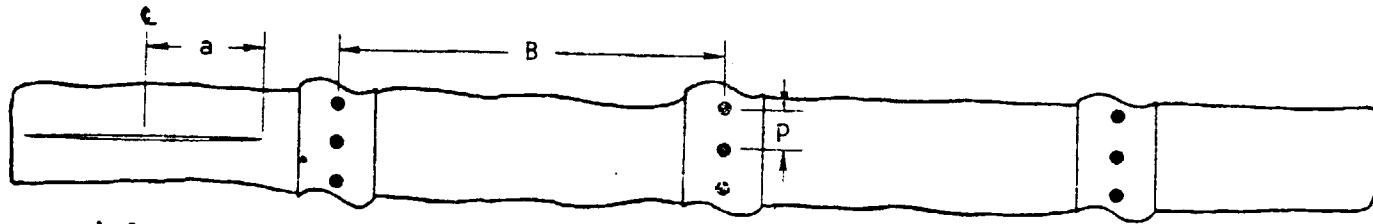


Figure 2-35. Stress Intensity Factor for Crack Extending Equally on Both Sides of Point Midway Between Two Stringers (NASA TR R-358)

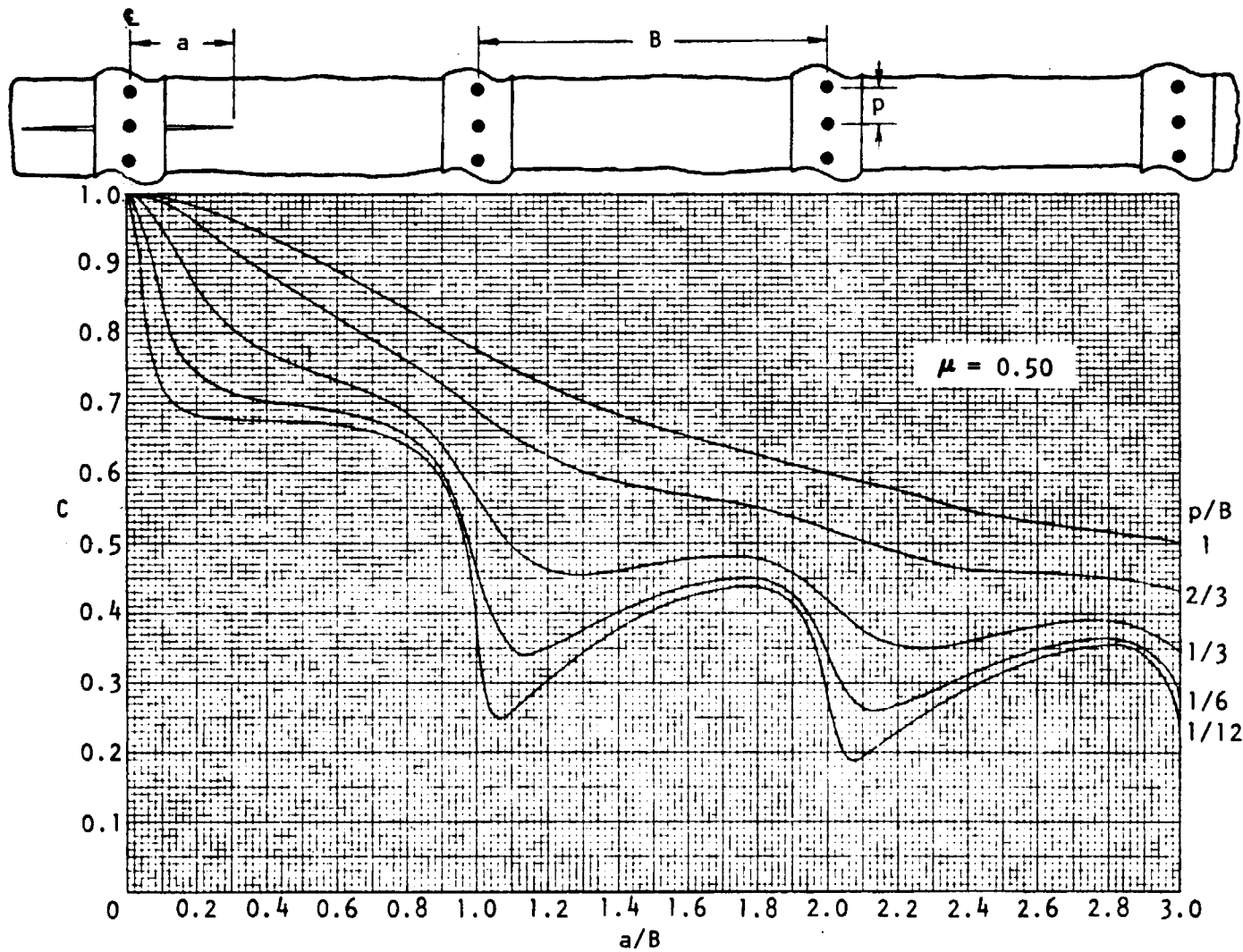


Figure 2-36. Stress Intensity Factor for Crack Extending Equally on Both Sides of Stringer (NASA TR R-358)

A plot of μ as a function of A_e to (Bxt) ratio for several typical skin and stiffener material combinations is presented in Figure 2-37.

In actual applications, the safe-crack growth period can be computed by modifying the crack tip stress intensity factor with a series of appropriate C factors given in Figures 2-35 and 2-36 (interpolation or extrapolation as required). The general stress intensity factor thus has the form:

$$K = \sigma \sqrt{\pi a} \cdot C \cdot Y \alpha \quad (31)$$

Where α is the appropriate factor accounting for the structural geometry and crack morphology.

Fatigue crack propagation tests on skin-stringer panels conducted by Poe (Reference 67) have confirmed the applicability of these stress intensity modification factors. Fatigue crack propagation tests conducted on panels having adhesively bonded flat straps (Reference 68) indicated that the life of the strap was greatly affected by the nonuniform and very high-stress gradient building up on the strap at the advancing crack front (crack on the skin). Therefore, it was suggested that both the low-cycle fatigue property of the stiffener material, and probably the bonding procedure, should be considered to ensure that the reinforcement will be effective for a reasonable length of time.

For estimating the residual strength of a reinforced structure, the mechanism of crack growth and fracture of the reinforced panel, under monotonically increasing load, must be understood. In addition, other variables, that might be significantly affecting the reinforcement efficiency have to be considered and properly accounted for in the stress-intensity calculations.

Referring back to Figures 2-12A and 2-34, for an unreinforced, center cracked panel (monolithic structure), the stress intensity K at the crack tip increases linearly with the value of normal stress component acting on the panel. As the K level increases, some point will be reached at which the crack will start to increase in length. As illustrated in Figure 2-12A, a crack in sheet material with sufficiently high-fracture toughness will extend gradually as the load continues to increase, until reaching the critical size at which rapid fracture occurs. For the reinforced structure (dotted line in both figures), it can be interpreted from Figure 2-34 that the stress intensity level at the vicinity of the reinforcement is drastically reduced so that the crack will not extend until a higher load level is reached. If the crack in a sheet will normally grow to failure at a final stress level σ_1 , a crack of the same size in a reinforced panel will grow (under monotonically increasing load), will slow down (K reduced, see Figure 2-34), and will be capable of

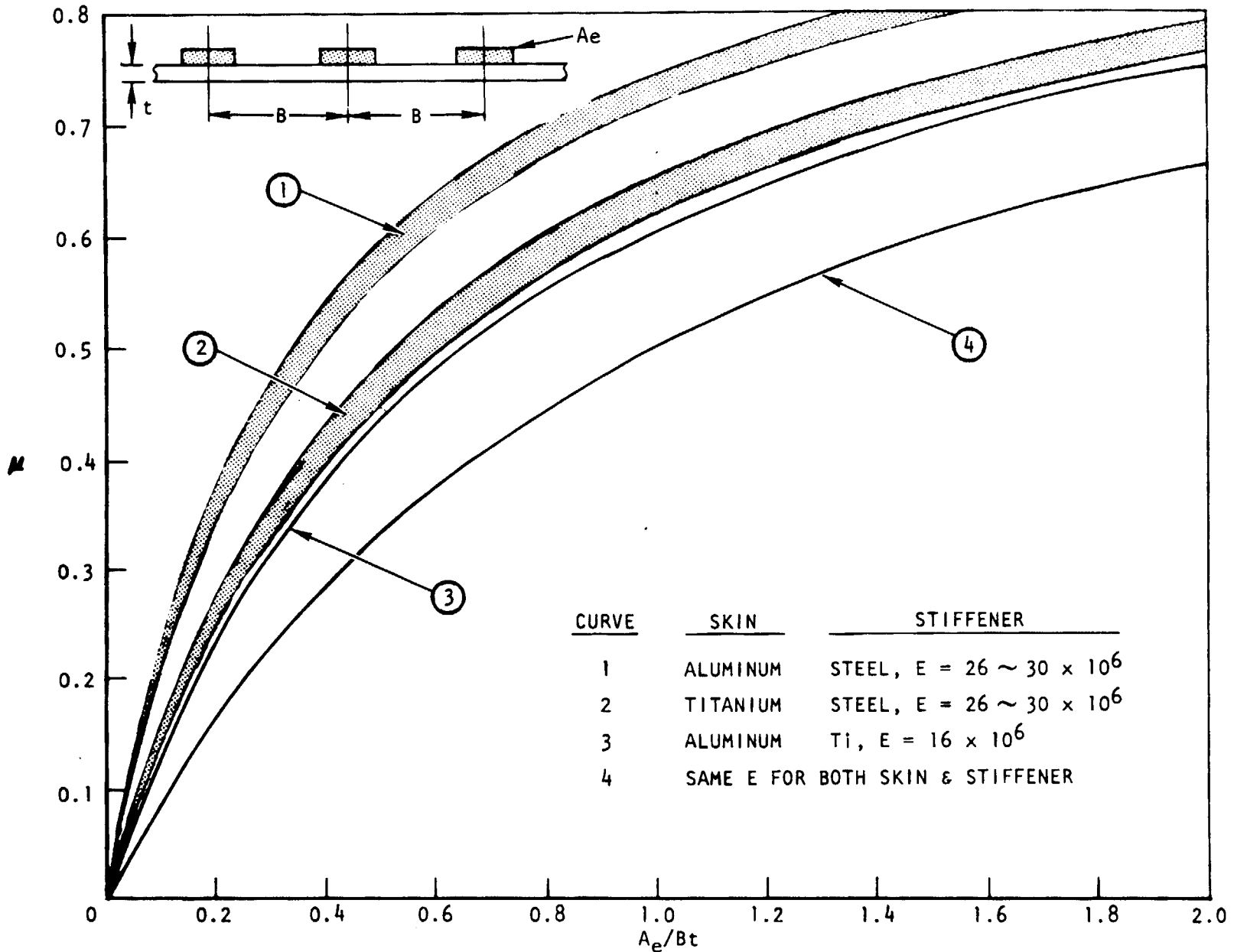


Figure 2-37. Stiffener Stiffness Parameter as a Function of Effective Stiffener Area

taking up more load until the reinforcement has reached its limit of effectiveness (e. g. , may be at a stress level of σ_2); then the crack will extend again, and probably rapid fracture will follow immediately. Therefore, the effect of the reinforcement on the residual strength is to increase the critical failure curve (constant K_c curve, σ_c versus a) for the stiffened panel over the sheet alone. The fail-safe capability (the residual strength) for the stiffened panel can be estimated simply by applying a reinforcement efficiency factor, γ , onto the basic allowable stress, σ_c , for the plain sheet; i. e. , the residual strength for the reinforced panel is:

$$\sigma_s = \sigma_c \cdot \gamma \quad (32)$$

Where $\sigma_c = K_c / \sqrt{\pi l/2}$

For all design purposes the crack length, l , can be taken as the distance between two intact stiffeners.

The value of γ for any type of reinforcement (e. g. , any A_e or μ values) can be developed by experiments, by analysis, or both. For the example just discussed in Figure 2-12A, $\gamma = \sigma_2 / \sigma_1$ and $\sigma_c = \sigma_1$.

In the analytical case (Figures 2-12A, 2-35, and 2-36), the crack is usually arrested at the vicinity of the reinforcement where the K value is reduced to a minimum (the maximum capability for the reinforcement). In order to have failure at the same K_c value in both cases (reinforced and not reinforced, see Figure 2-12A), assuming that the errors attributed to the slow stable tear behavior in these cases are insignificant, it is required that $\sigma_1 = \sigma_2 \cdot C_{min}$, where C_{min} is the C value for the point at the bottom of the valley in the C versus a/B curve.

$$\gamma = \frac{\sigma_2}{\sigma_1} = \frac{1}{C_{min}} \quad (33)$$

As an example, a set of the γ versus μ curves is reduced from Poe's work (Figure 2-35) and is presented in Figure 2-38. Only the γ value for the first pair of stiffeners is presented in the illustration because, in the monotonic increasing loading case, once the crack starts to grow again the second pair of stiffeners are not likely to stop the fast running crack.

For an airframe structure, crack or cracks would most likely initiate from a fastener hole. Initially the crack or cracks would be developed on the skin but not on the stiffener. Then, under normal fatigue loading conditions and assuming the crack will propagate safely and be arrested at the next stiffener, the safe-crack-growth period can be estimated by using the stress intensity modification factors given in Figure 2-36. To estimate the residual

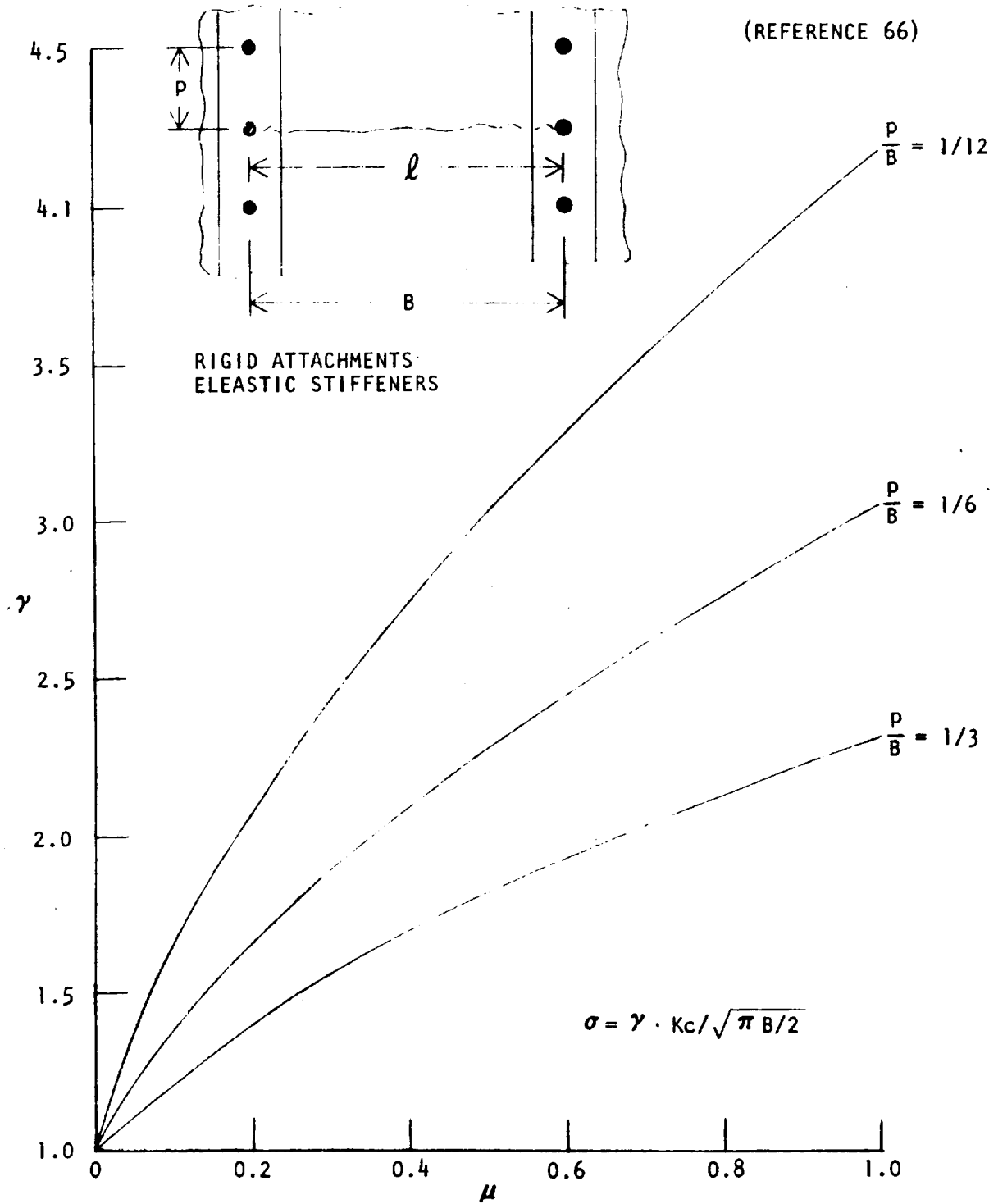


Figure 2-38. Stiffener Efficiency Factor for a One-Bay Crack as a Function of Stiffener Stiffness Parameter

strength for the same reinforced panel, there are two possibilities: (1) At the time the monotonic increasing loads are applied onto the structure, the crack tip is either remote from the second adjacent stiffener (close to the center stiffener); or (2) the crack tip is close to the second stiffener (remote from the center stiffener). From Figure 2-16, it is reasonable that the mid-bay location be chosen as the cutoff point for these two cases, because at the central portion of the bay the stress intensity modification factors are (almost) a constant. The first case is for a crack having a length shorter than one-half of a bay. The reinforcement efficiency factor, Y , can be developed by converting the C factors at the mid-point of the bay given in Figure 2-36. At this location, the efficiency for the center stiffener is maximum, and the efficiency for the second stiffener ahead of the crack is negligible. The Y factors for this case are plotted in Figure 2-39.

For the second situation, since the crack is so long, the center stiffener might be broken while the panel is under load. The loads in the broken stiffener would have to be fed back into the cracked sheet. In addition, experiments conducted on a wide class of stiffener configuration and material variations indicated that for stiffeners having small cross-sectional area, the efficiency of the reinforcement would be limited by the occurrence of reinforcement yielding (Reference 68).

A schematic illustration on the reinforcement yielding effects is presented in Figure 2-40. The reinforcement efficiency, Y , is plotted as a function of the ratio of the gross applied stress (σ) in the panel to the tensile yield strength of the reinforcement material (F_{ty}). The horizontal portion of the curves reflect the simple fact that until the reinforcements actually begin to yield, the yield stress does not play a role. The rapid drop in efficiency, once the reinforcement starts to yield, is clear evidence of the importance of this effect. Although this has not been proven by experiments, stiffener yielding may not be a problem for the short-crack case (the case involved only with the center stiffener) because the Y values are relatively small (i. e., very little extra loads will be transferred to (added onto) the center stiffener).

Therefore at this point, it is important to consider three additional variables which would significantly affect the efficiency of the reinforcement (both the C and the Y values). These variables are:

1. Broken stiffener,
2. Reinforcement yielding, and
3. Stiffness of the attachment.

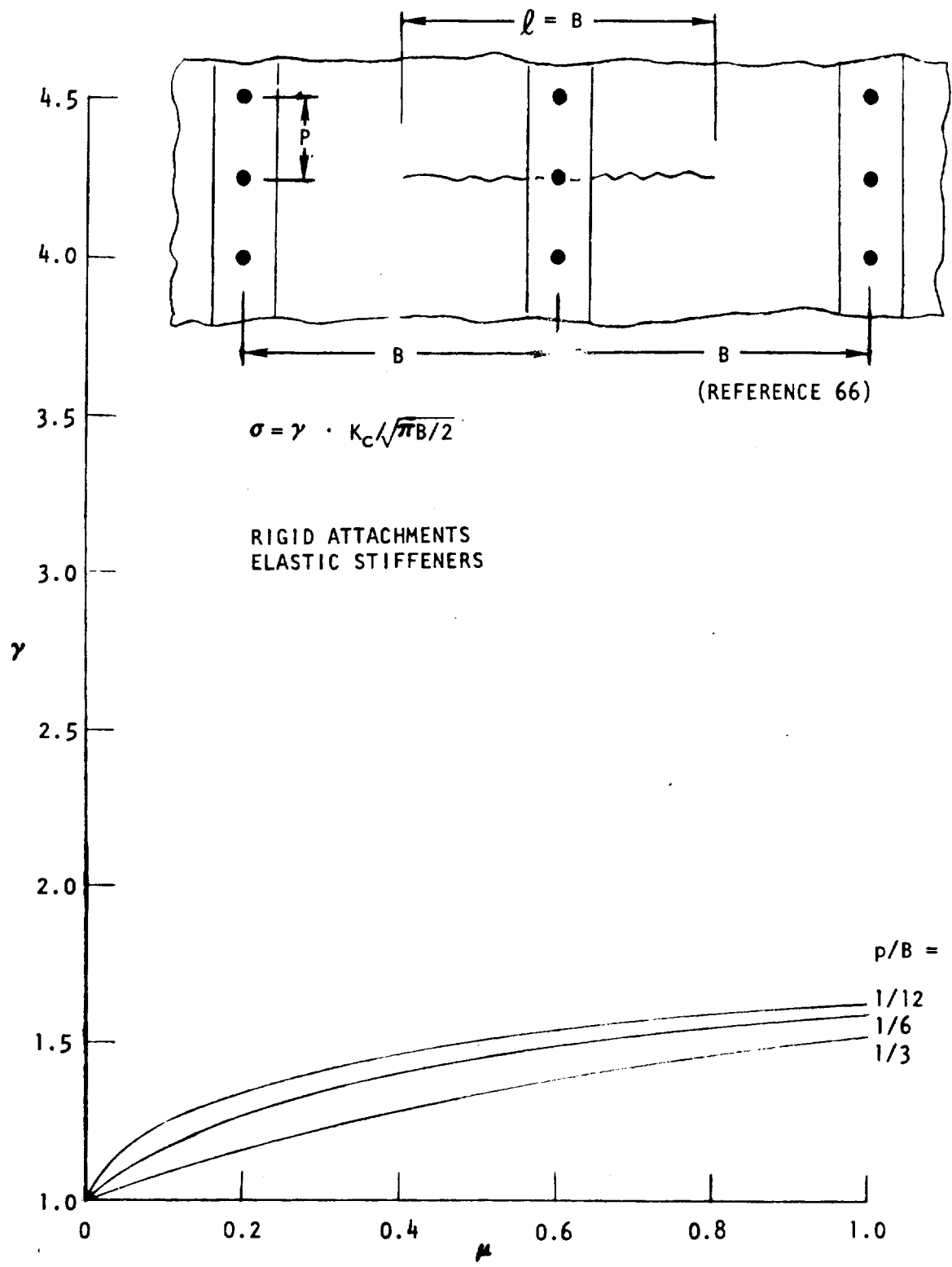


Figure 2-39. Stiffener Efficiency Factor for a Crack Extended Symmetrically on Both Sides of a Stringer

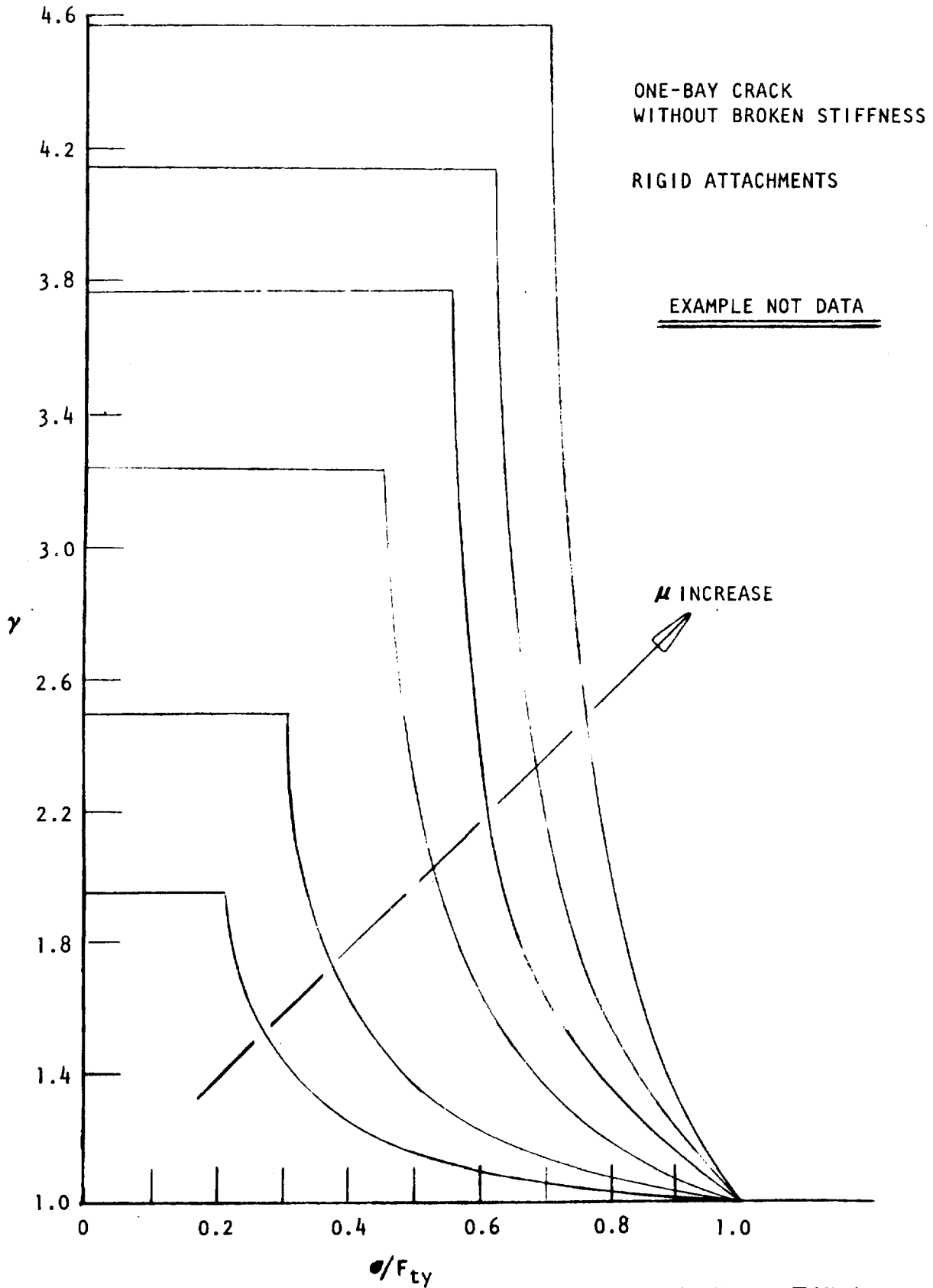


Figure 2-40. Effects of Applied Stress Levels on the Stiffener Efficiency

To discuss these aspects, the problem considered by Creager and Liu (Reference 69) should be studied. The result of their problem is shown in Figure 2-41. They computed the stress intensity factor for the cases described as in the following paragraph.

There are two panels 1.2 meters (48 inches) wide and 2.5 meters (100 inches) long. The panels were reinforced with seven flat straps having one strap located at the centerline of the panel (parallel to loading direction). The remaining straps were placed symmetrically on either side of the centerline strap. The strap spacing was 15.24 centimeters (6 inches). The crack was at the middle length of the panel (between two rivets) with the centerline strap broken ($l = 30.48$ centimeters (12 inches)). The cross-sectional area for each of the straps in one of the panels was two- and one-half times larger than those in the other panel. The thickness of the skin in each case was adjusted to balance the differences in the strap area so that the gross weight and the gross area stress of both panels will be the same.

It was also assumed that flexible rivets were used in the panels (rivet stiffness was approximately equal to 700×10^6 Newtons per meter (4×10^6 pounds per inch) of deflection per inch of sheet thickness). The stress intensity factors in the vicinity of the first pair of intact stiffeners were calculated with the effect of straps yielding, included (dotted lines), and ignored (solid lines). The higher crack tip stress intensity in the reinforced sheet at the center region of the panel was primarily attributed to the damaging effect of the broken center stiffener. The resultant stress intensity modification factor, C , is plotted lines as dotted lines in Figure 2-42. The K calculations in Figure 2-41 also indicate the following:

1. In this particular example, if the effects of reinforcement yielding are ignored and the intact straps are assumed to remain elastic, the effect of strap cross-sectional area on residual strength of the panel is insignificant. The fact that the gain in reduction in K (in the effective region of the intact strap) obtained by increasing the size of the strap is negligible, is due in part to the broken center strap. Increasing the size of the broken strap causes higher loads to be transferred to the crack tip vicinity and, consequently, tends to increase the stress intensity factor. Had a less realistic configuration, without a broken center strap been considered, a greater effect of reinforcement area would be evident (the solid lines shown in Figure 2-42, assumed the center strap did not exist).
2. When the effects of reinforcement yielding are included, it is seen that the difference in reinforcement efficiency between the two sizes of straps studied is very significant.

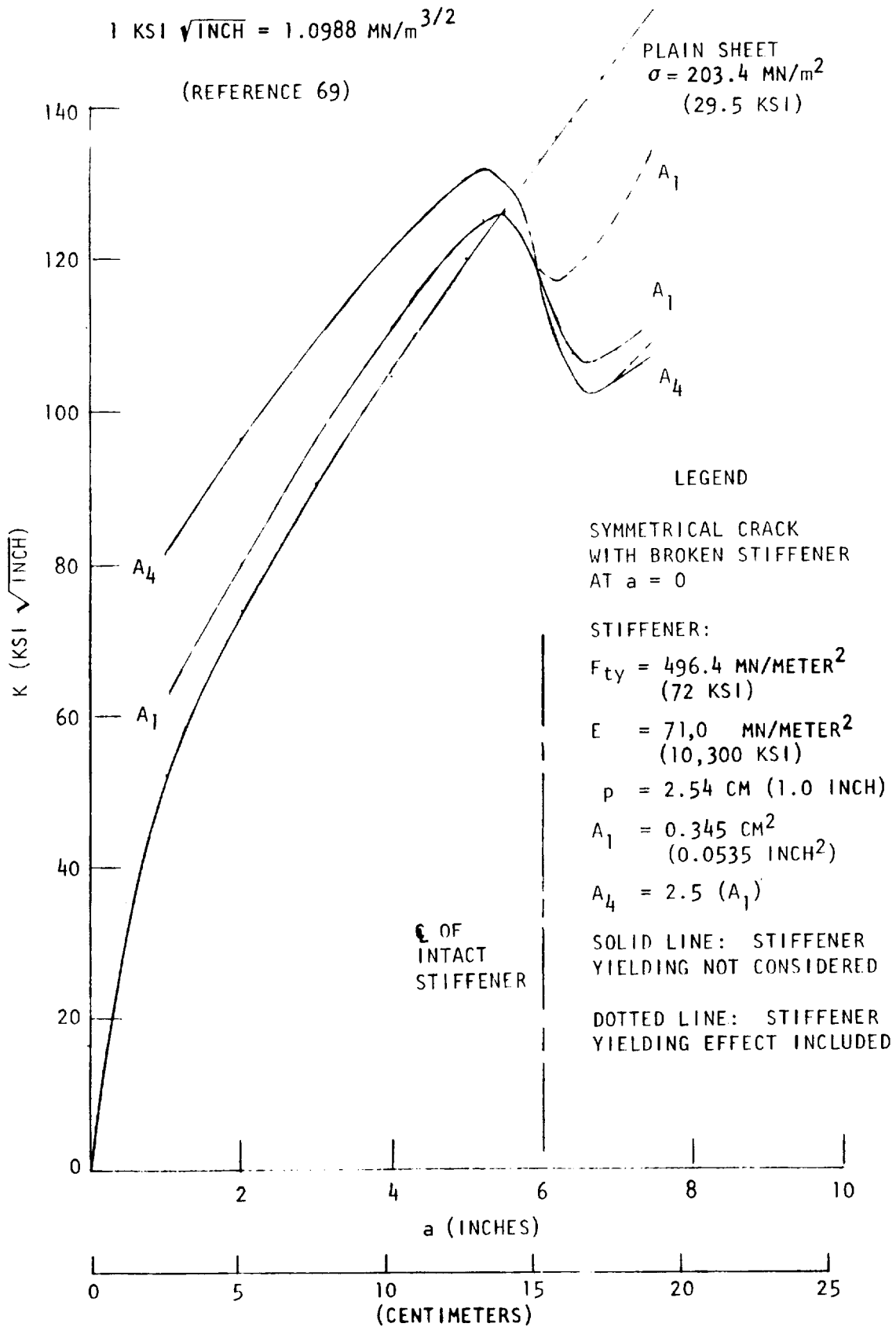


Figure 2-41. The Effects of Broken Stiffener and Stiffener Yielding on Crack Tip Stress Intensity

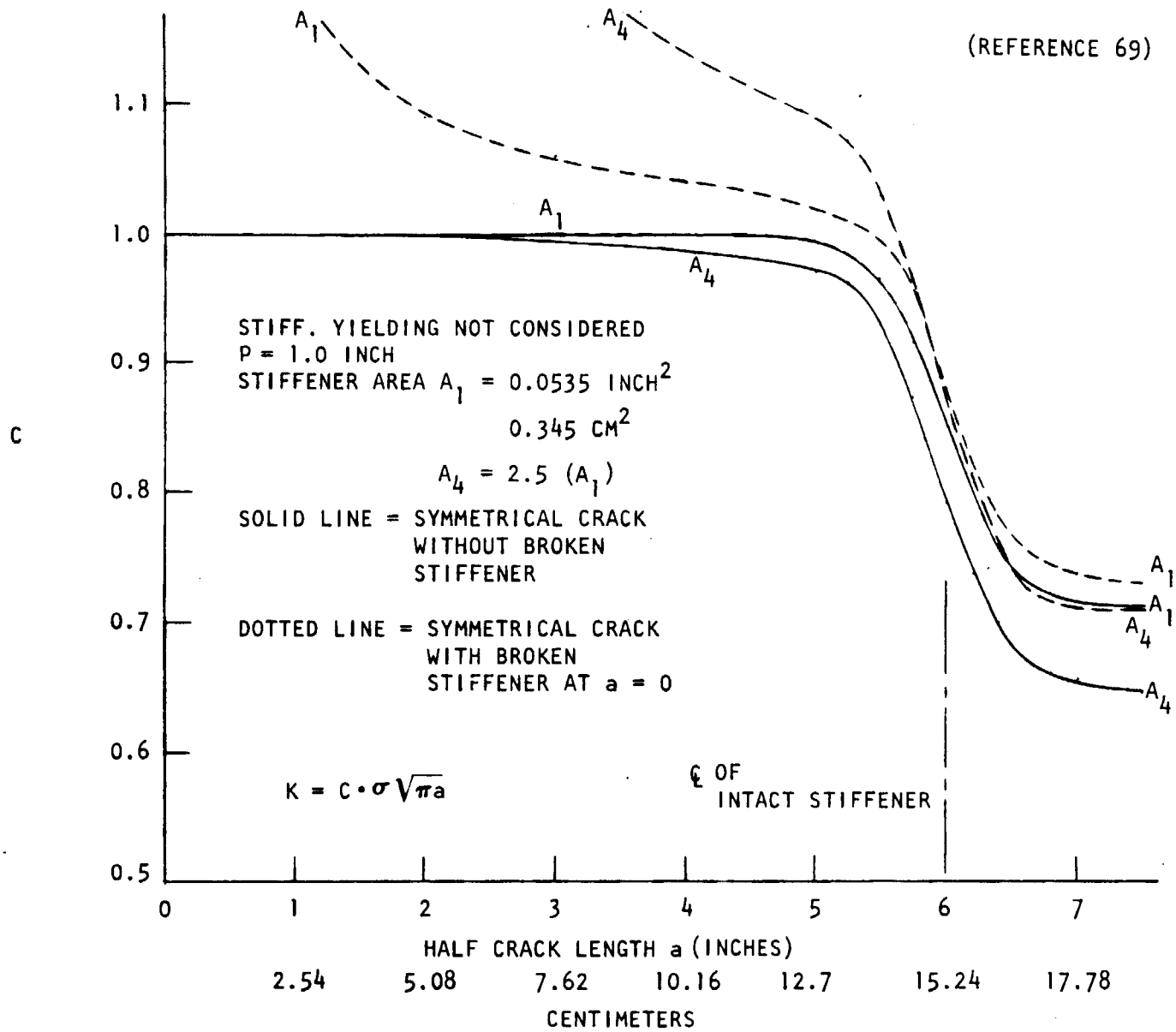


Figure 2-42. The Effect of Broken Stiffener on the Stress Intensity Factor

3. K-curves for the panel having a larger size of strap are almost the same for the elastic and the plastic cases. Therefore, in this particular problem, it is not necessary to design a strap area larger than that size.

The easiest way to construct a set of parametric design curves for the case having a two-bay crack with a center stiffener broken is by superimposition of two separate cases; i. e., the case without a center stiffener (Figure 2-35) and the case involved with a broken stiffener alone. The analytical result for the stress intensity modification factor for the broken stiffener, C_b , taken from Reference 63, is presented in Figure 2-43. An example of the result of such superimpositions is presented in Figure 2-44. It should be noted that since the load carried by a stiffener is proportional to its area, the full stiffener area was used to obtain the C_b values from Figure 2-43.

This type of design curve provides very important information for design consideration. For example, consider the case of $p/B = 1/6$ in Figure 2-44; this curve indicates that a reinforced structure can be designed having the relative stiffness parameter μ equal 0.45 or 0.76 to obtain the same γ value (reinforcement efficiency parameter) of 2.0. (See Figure 2-37.) If the panel is made up of aluminum skin and titanium stiffeners, the required A_e values corresponding to the μ values of 0.45 and 0.76 are 0.41 (Bxt) and 2.05 (Bxt), respectively. If the reinforcements are flat straps (i. e., $A_e = A$), it would mean a total difference of 500 percent in weight for the stiffener material.

The previous examples clearly demonstrated the importance of design considerations and the necessary information for implementing them in regard to structural design optimization, tradeoff, and weight savings.

2.3.4.3 Experimentally Developed Design Curves

Discussions in the previous section have pointed out that the reinforcement efficiencies, especially γ , are dependent upon many variables, both physical and geometrical. It would take a great deal of effort to develop a satisfactory parametric analysis procedure which would properly account for the effects of these variables. After a satisfactory procedure has been developed, successful correlation with actual test data would still be required. At Lockheed (Reference 70), a set of design curves has been constructed based on reinforced flat panel test data available in the late 1950's and early 1960's. This set of design curves, presented in Figure 2-45, correlates the reinforcement efficiency parameter, γ , and a lumped stiffening parameter

$$\Sigma \bar{A}_e/t$$

where t is the skin thickness.

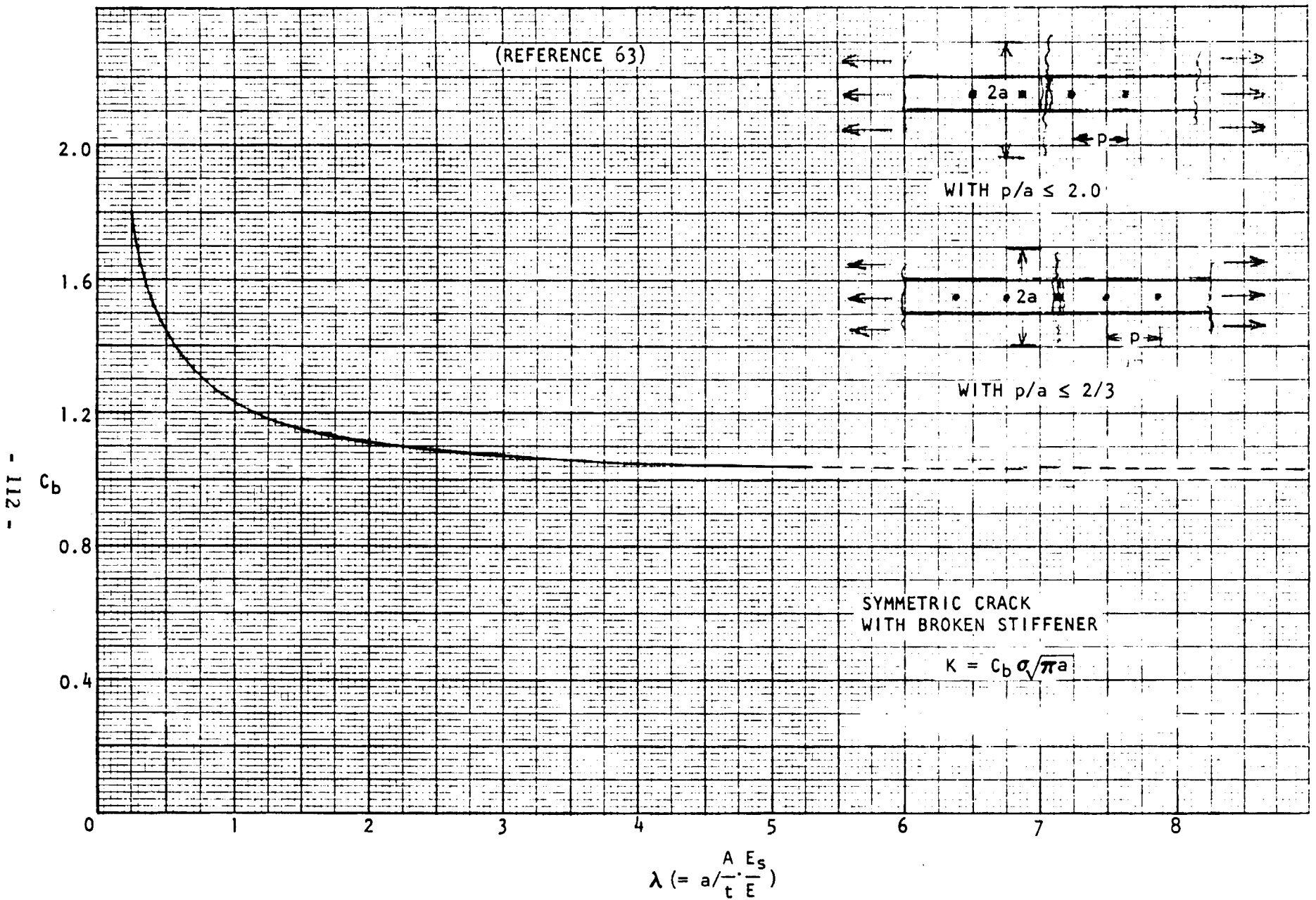


Figure 2-43. The Effect of Broken Stiffener on the Stress Intensity Factor

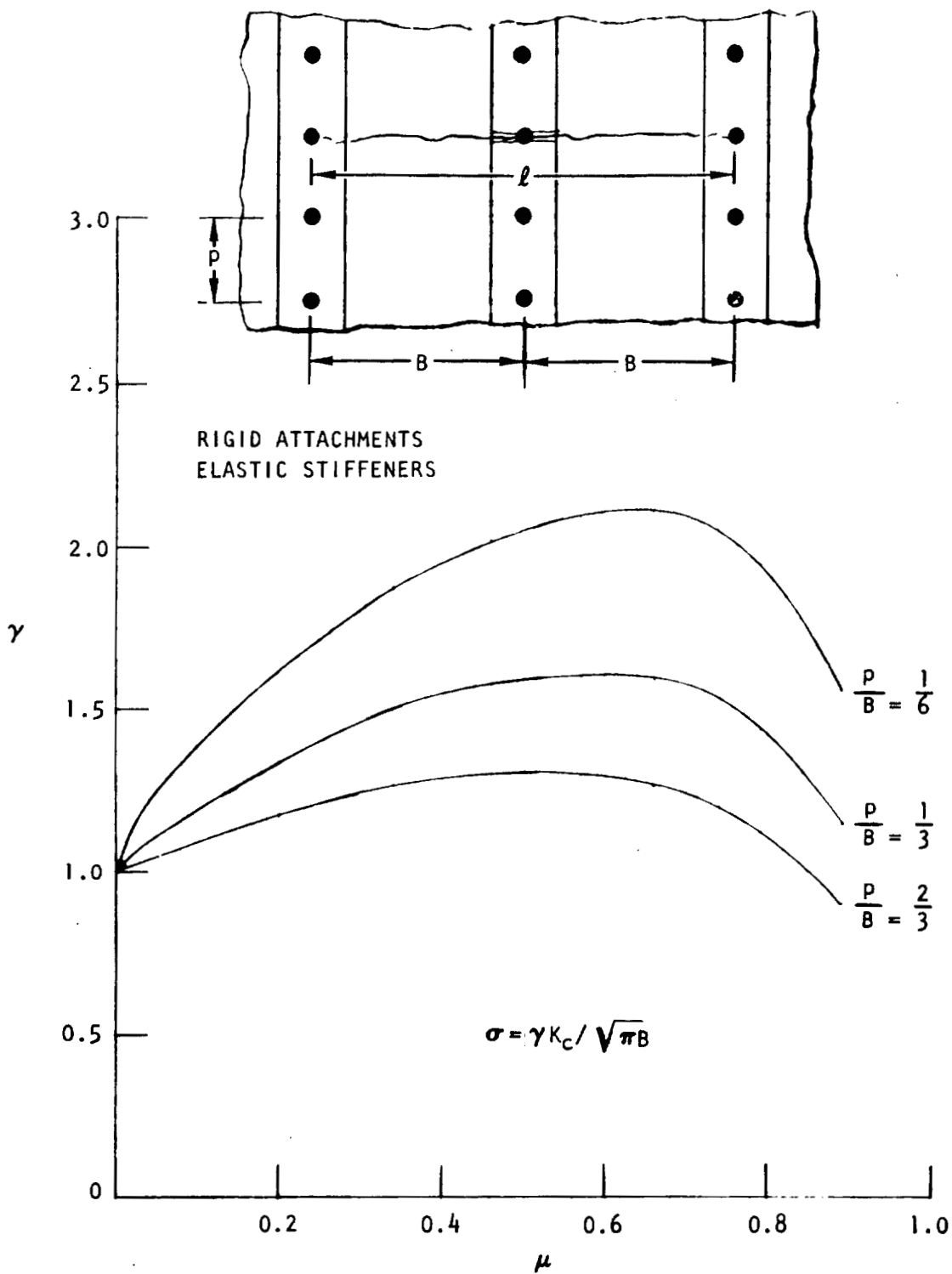


Figure 2-44. Stiffener Efficiency Factor for a Two-Bay Crack With a Center Broken Stiffener

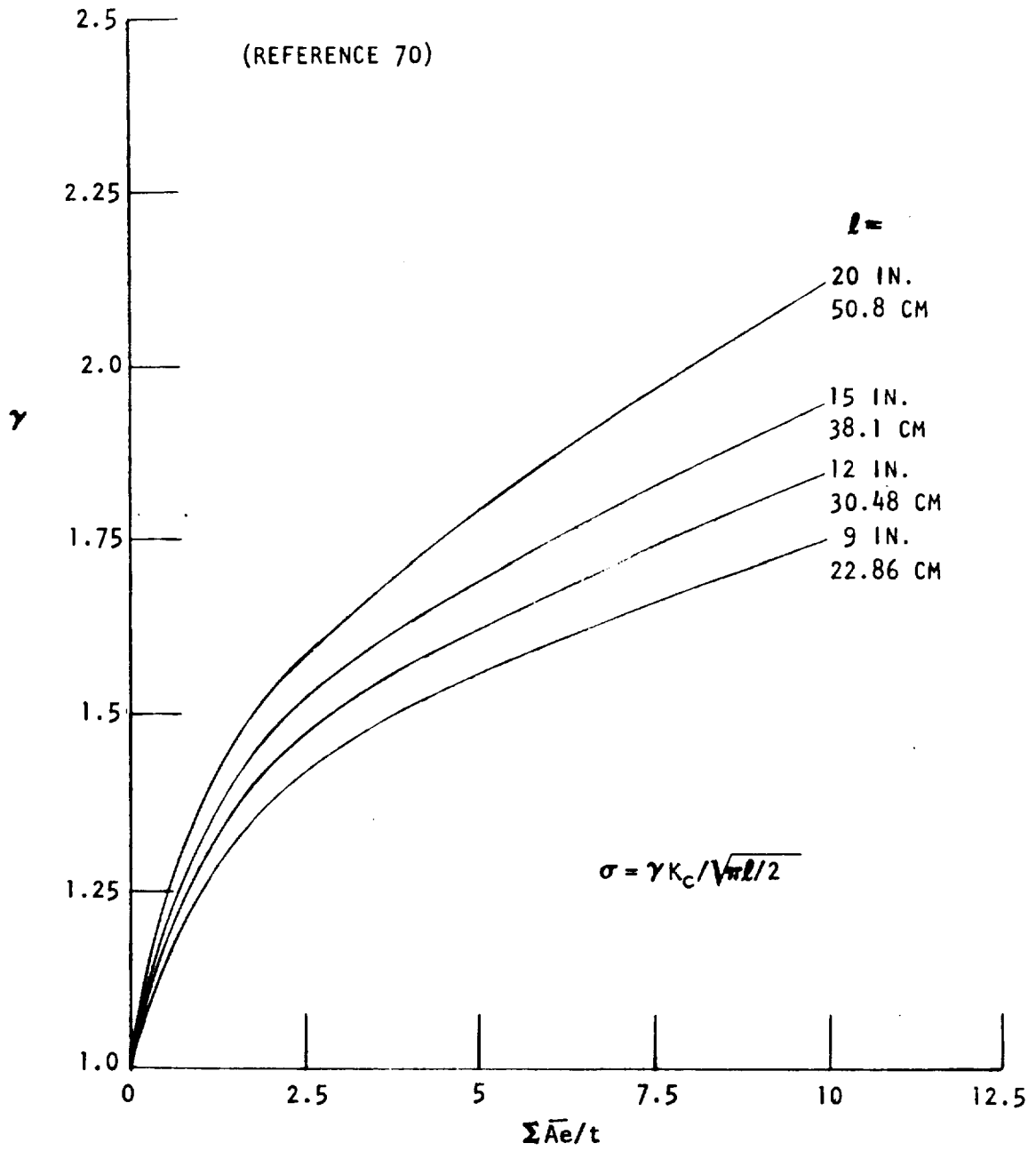


Figure 2-45. Design Curves for Reinforced Flat Panels

According to the reasoning discussed in the previous section (i. e. , if the reinforcement area is small, as in the case of a flat strap), the fracture process will take place in the plastic range of the strap material. If, however, the reinforcement is relatively large (e. g. , a heavy stringer), the reinforcement material might remain in the elastic stress-strain range throughout the entire fracture process. Therefore, the reinforcement effective area can be approximated by the following:

$$\bar{A}_e = A \cdot \left(\frac{F_{tys}}{F_{ty}} \right)$$

for a flat strap where F_{tys} is the tensile yield strength for the strap material and F_{ty} is the tensile yield strength for the skin material.

For the case of a stringer

$$\bar{A}_e = A_e \cdot \left(\frac{E_s}{E} \right)$$

where E_s and E are the Young's modulus for the stringer and skin materials, respectively, A_e is computed by Equation 30. The Σ sign in $\Sigma \bar{A}_e/t$ stands for the sum of the intact stiffeners which contribute the stiffening effects to the cracked area. For example, the Σ will be 1 for the case shown in Figure 2-39 and Σ will be 2 for the case shown in Figure 2-44.

This set of parametric curves can be used for any kind of reinforced panels (attached stiffeners only, riveted or bonded). The analysis for the three cases shown in Figures 2-38, 2-39, and 2-44 will depend on whether: (1) The reinforcement bridges the crack (case in Figure 2-39), reinforcement considered effective if $l \leq B$, assuming $l = B$ for analysis; (2) the ends of the crack are near the reinforcement (cases in Figures 2-38 and 2-44), reinforcement considered effective if $B/2 \leq l \leq B$ for the one-bay crack case and if $B \leq l \leq 2B$ for the two-bay crack case, assuming $l = B$ and $l = 2B$, respectively for analysis; and (3) the crack tips are remote from the reinforcement (case in Figure 2-38 with $l < B/2$), assuming $\Sigma \bar{A}_e = 0$, i. e. , $Y = 1.0$.

Checkout of the above analysis procedure was also reported in Reference 17. The test data used were those recently developed at Lockheed (also reported in Reference 17). Although the majority of the data was developed from panels having thin sheet of 2024-T3 aluminum ($0.15 \text{ cm} \leq t \leq 0.2 \text{ cm}$) ($0.06 \text{ inch} \leq t \leq 0.08 \text{ inch}$), and only one panel of 0.558 centimeter (0.22 inch) thick 7075-T7651 aluminum was tested, a wide range of reinforcement area to sheet thickness ratios ($0.8 < \Sigma \bar{A}_e/t < 11.0$) was included. The test panels

were either 1.01 or 1.2 meters (40 or 48 inches) wide with stringers or flat straps riveted or adhesively bonded onto the skin. The crack sizes were 25.4 to 50.8 centimeters (10 to 20 inches) long with or without broken stiffener at the centerline of the panel (cases shown in Figures 2-38 and 2-44). The correlation between prediction and test results has shown that the errors in the predictions for these 24 tests were less than ± 20 percent.

2.3.4.4 Integrally Stiffened Panel

Although the load transfer behavior for the integrally stiffened panel is similar to that for the skin-stringer-type structure, for the case of a panel with the reinforcement riveted or adhesively bonded onto the skin, the skin crack grows under the stiffener. However, for the case of the panel with integral risers, the crack will advance through the integral stringer as well as the sheet itself. To develop the stress intensity modification factors (the C factors) for this type of structural configuration, the same analytical technique can be used as those used by Poe for the skin-stringer configuration. An example (taken from Reference 67) of the C factors is shown in Figure 2-46 for a stiffness parameter (μ) value of 0.22. As pointed out by Poe, this C versus a/B curve was calculated by assuming a very close attachment spacing and properly accounting for the effects of the partially damaged integral stringer as the crack branches and proceeds simultaneously through the sheet and the integral riser. Fair correlations between analysis and fatigue crack growth test results were also reported (Reference 67). The crack arrest capabilities (under monotonic increasing load) for this type of structure are not well understood and test data of this type are not available. Therefore, a recommendable residual strength analysis procedure cannot be developed at the present time.

2.3.5 Multiple Element Structure

Many structural designs lend themselves to partitioning in the interest of fail-safe damage tolerance with little or no increase in cost, weight, or complications. Examples include longerons made of back-to-back channels in place of I-beams, back-to-back angles in place of T-sections, and panelization of wing surfaces. These multimember redundant structures, any single member of which may be completely severed, require only static strength principles to predict allowable strengths. Fatigue analysis or fatigue tests may be required to determine the safe inspection intervals after one member is broken. A special kind of multiple elements structure is the skin panel made up of several layers of thinner sheets adhesively bonded together to obtain the total desired thickness to carry the design loads.

For back-to-back members, the structure must be able to support fail-safe loading conditions with one member broken. Therefore, for this type of structural arrangement, static strength analysis can be used by considering

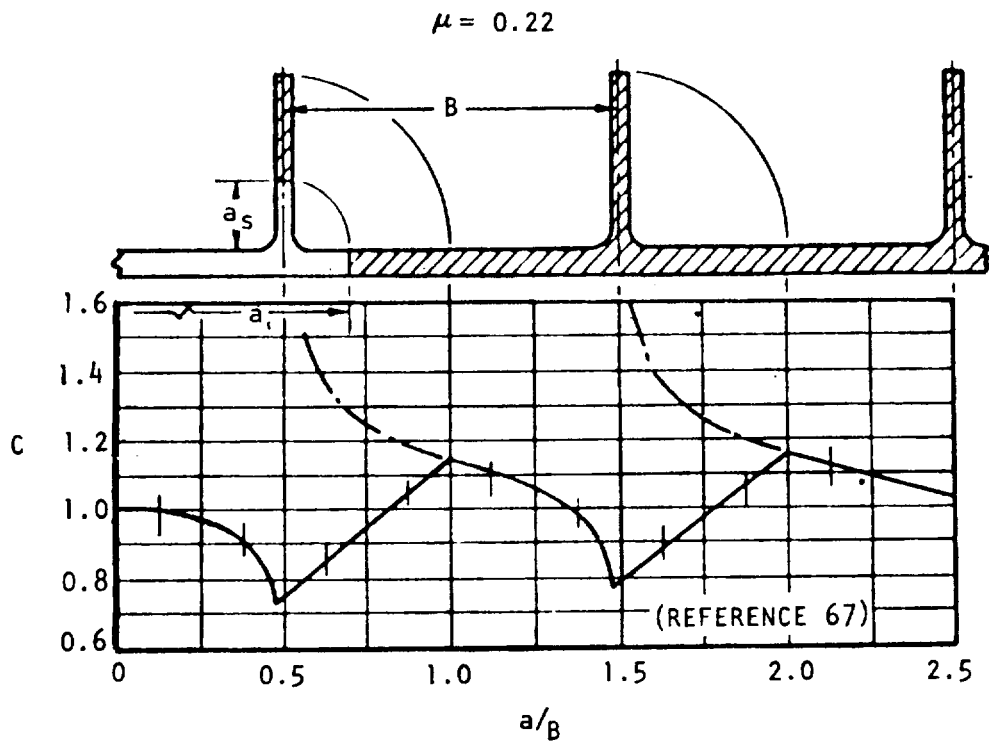


Figure 2-46. Relationship Between Stress Intensity Factor and Crack Length for Panel With Integral Stiffeners

the redistribution of loads due to the broken element. For the multiplank design case, the residual strength of the structure is determined assuming that a crack extends completely across the width of one-skin plank. Because the riveted splice joint provides a geometric discontinuity to serve as an effective means to interrupt crack propagation, it is not necessary to apply fracture mechanics theory to predict residual strengths for the remaining structure. However, the failure of one-skin plank will cause an elastic concentration of loading in the adjacent planks. This is basically a load redistribution or "shear lag" problem. The fatigue crack propagation and monotonic load-carrying characteristics for these two types of structures were previously illustrated in Figures 2-14 and 2-15B. Unlike the crack arrest structures, the propagation of the fatigue crack is a continuous process and its safe-crack-growth period can be estimated by knowing the variations in crack tip stress intensity. However, in the multiple elements structure cases, especially for the case of multiload-path-dependent design (e. g., multiplank skins), the remaining life in the adjacent unbroken member is very difficult to estimate because it involves such problems as reinitiation of the fatigue crack, or pre-existing fatigue cracks in the adjacent elements, etc. Therefore, only the residual strength prediction methods will be discussed here.

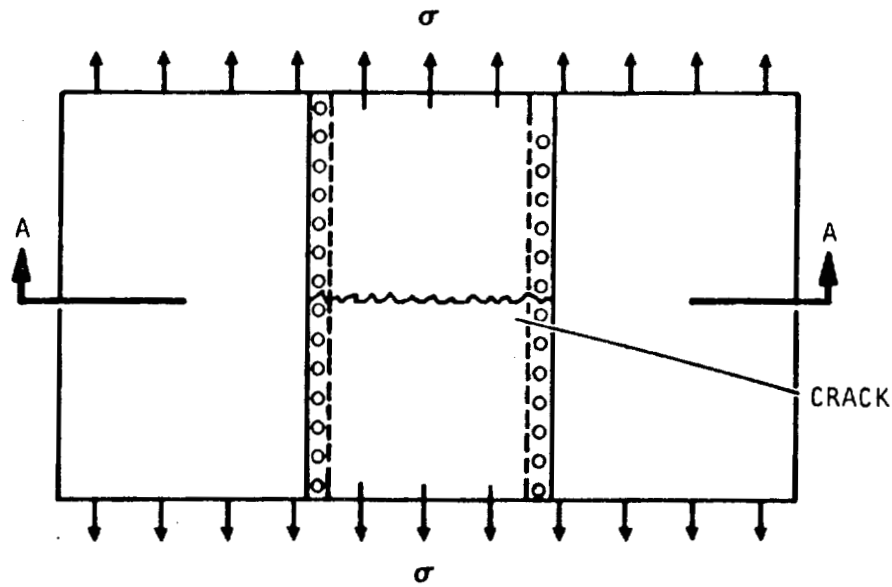
For the multiple-laminated sheets case, it is eventually a monolithic structure if the crack is all the way through all the layers of the sheets, or a multiple-element structure (multiload-path-independent) if the crack is in one of the sheets only.

2.3.5.1 Multiple Plank Structure

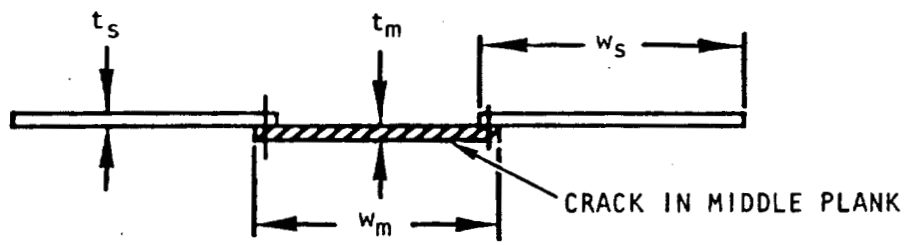
In the multiload-path-dependent design, the fail-safe load-carrying capability in the remaining structure after failure of one major structural element relies on the load-redistribution characteristics of the structural system. One way to handle this type of problem is to adopt the Kuhn's three-stringer model for cutouts (Reference 72). An excellent example problem was given in Reference 1 where this method had been applied to model the broken skin plank in the vertical stabilizer of the B-9U Shuttle booster. In this section, an alternate analysis procedure, called the Crichlow's "effective width" method (Reference 73), is discussed in the following paragraphs.

Suppose a spliced panel is made up of three planks as shown in Figure 2-47, and assume that the middle plank has completely severed, the fail-safe criterion for this configuration is:

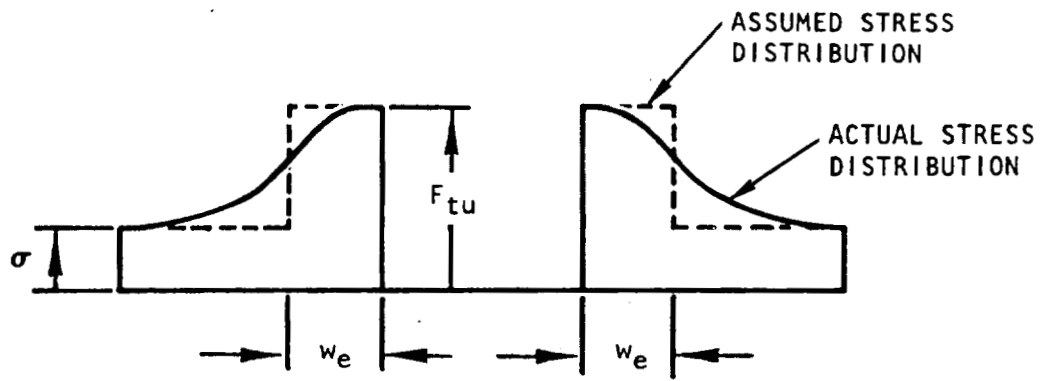
$$\begin{aligned}
 (\sigma + f_{we}) &< F_{tu}, \text{ fail-safe} \\
 &\geq F_{tu}, \text{ not fail-safe}
 \end{aligned}
 \tag{34}$$



a. TEST PANEL CONFIGURATION



b. SECTION A-A



c. STRESS DISTRIBUTION ACROSS SECTION A-A

(REFERENCE 73)

Figure 2-47. Stress Distribution Across a Three-Plank Fail-Safe Test Panel With the Middle Plank Broken

F_{tu} is the tensile ultimate strength of the side planks, σ is the applied stress, and f_{we} is the additional stress picked up by the side planks due to failure of the middle plank. Its magnitude is essentially equivalent to the cut load, P_{cut} , divided by the total effective sheet area of the adjacent planks which is capable of picking up the additional load, i. e. ,

$$f_{we} = P_{cut} / 2A_1 \quad (35)$$

where $P_{cut} = \sigma \cdot W_m \cdot t_m$

$A_1 = w_e \cdot t_s$, and

A_1 is the effective sheet area on each side of the adjacent planks; its value has to be determined experimentally. Since the sheet thickness, t_s , is a known value, only the value for the effective width, w_e , has to be developed. Figure 2-48 shows that the effective width, w_e , is a function of the sheet materials, the attachment shear strength, the attachment spacing and the attachment load-deflection characteristics. It should be noted that the w_e values in Figure 2-48 were empirically generated from test data of structure and fasteners typical of the Lockheed Electra aircraft, thin aluminum sheets with $0.101 \text{ cm} \leq (t_s = t_m) \leq 0.203 \text{ cm}$ ($0.04 \text{ inch} \leq (t_s = t_m) \leq 0.08 \text{ inch}$), and P_A values ranging from 4450.0 to 8900.0 Newtons (1000 to 2000 pounds). Extrapolations to other sheet materials or the same material having considerably thicker gages and/or different attachment systems should be done with care. In addition, it should be realized that at the incipient of the sudden failure of a nearly primary element, it would have created a considerable magnitude of dynamic effects onto the adjacent secondary element. Present Federal Aviation Agency requirements include a factor of 15 percent on the overall static load (i. e. , 1.15σ). However, in Reference 17, after going through a lengthy exercise and discussion, including the consideration of load redistribution and local yielding, they have concluded that a factor of 1.1 on the cut load alone would be adequate for design purposes, except where a dynamic factor may be particularly intense. In other words, the fail-safe criterion expressed in Equation (34) may be rewritten as

$$(\sigma + 1.1 f_{we}) = F_{tu} \quad (36)$$

for the marginal case, if insertion of a dynamic factor is so desired.

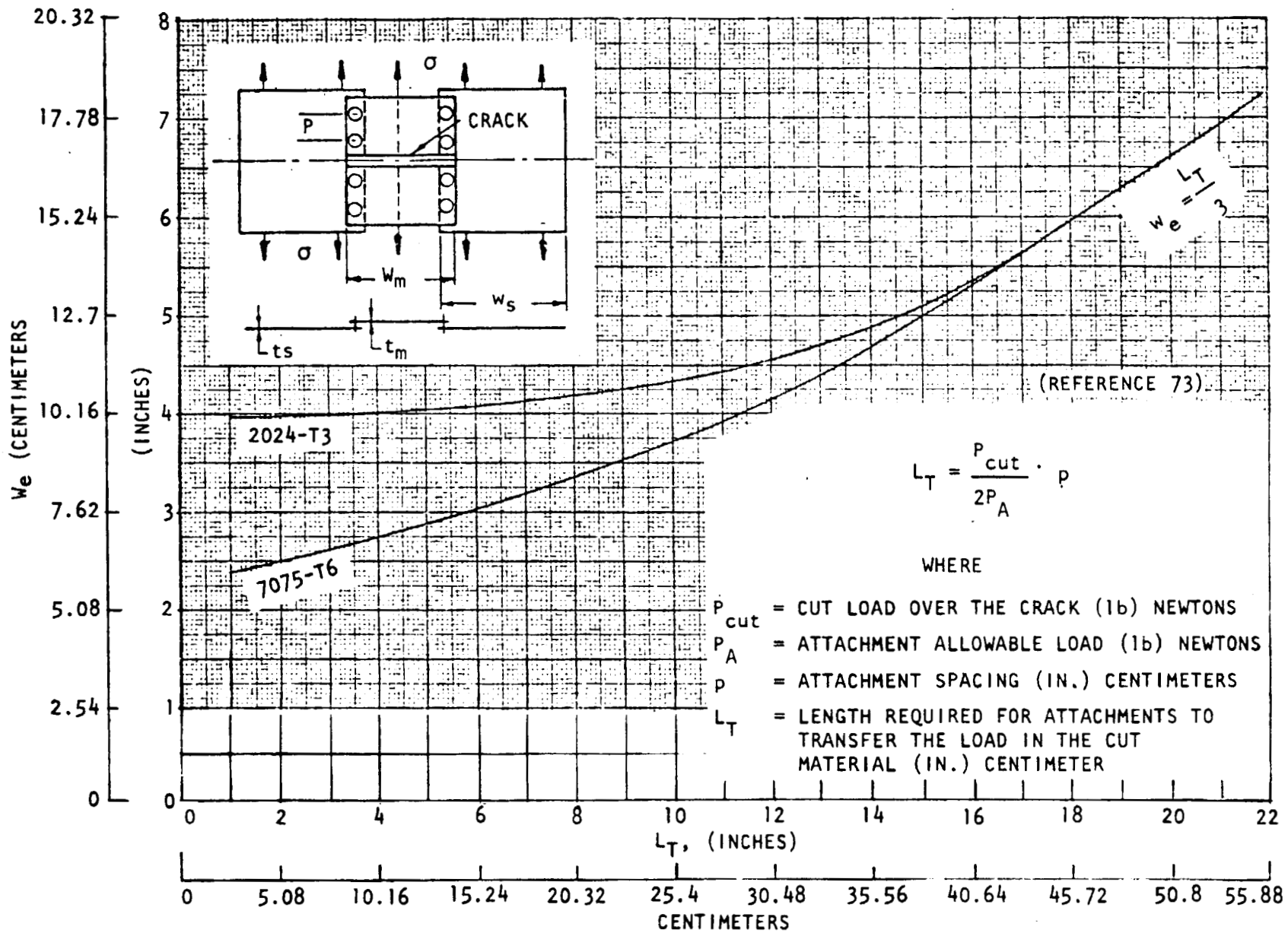


Figure 2-48. Effective Width in Side Planks for Flat Panels with Longitudinal Splices

2.3.5.2 Multiple Laminated Sheets

A laminated panel made up of several plies of sheets or plates can be classified in either one of the following categories:

1. A monolithic structure if it contains a through-the-total-thickness crack,
2. A multi-element (multiload-path-independent) structure if it contains a crack or cracks in only one (may be more than one but not all) of the plies.

In either case, the advantage for lamination is that the fatigue crack growth and fracture behavior for any cracked plies in the panel would be determined by the fatigue crack growth and fracture toughness properties for the individual sheet alone. An effect which is rather familiar is that both the fatigue crack growth rate and fracture toughness are a function of material thicknesses. For example, if a wing skin plank is sized to have a thickness of 1.27 centimeters (1/2 inch) in order to meet the static strength and fatigue requirements. Utilizing the difference in K_{IC} values between a 0.25-centimeter (0.1 inch) thick sheet and a 1.27-centimeter (0.5 inch) thick plate, the wing skin plank can be designed by making up of five plies of 0.254-centimeter (0.1-inch) thick sheet (in the fracture mechanics point of view only). In this design, a substantially larger crack can be tolerated because the fracture toughness in the 0.254-centimeter (0.1-inch) thick sheet is much higher than the fracture toughness in the 1.27-centimeter (1/2-inch) thick plate. Furthermore, the laminated sheet design would exhibit a much longer fatigue crack growth life because the fatigue crack growth rate is lower in the thinner sheet (usually), and the critical crack length is larger (takes more cycles to grow the crack to a larger crack size) as determined by K_{IC} .

2.3.6 Failure Under Complex Loading Conditions

This section discusses what must be done to analyze situations where uniaxial tensile loading conditions are not predominant. Although tensile loadings are by far the most usual and most damaging case, it is not the only case that must be considered. Therefore, available information to analyze for shear, bending, and biaxial loadings will be discussed.

2.3.6.1 Shear

For a through-crack in a plate-like structure subjected to combined tension and shear loadings, both Mode I and Mode II stress intensity factors arise at the crack tip. This problem is discussed in some detail in Section 1 of Volume II. (Note tension means loads perpendicular to the plane of crack and shear means loads parallel to the crack.) Loads at an angle to the

crack plane will also cause Mode I and Mode II stress intensity factors as discussed in Volume II. Failure load predictions are made by using Mode I - Mode II interaction curve as shown in Figure 2-49 and described in Volume II. The interaction curve is generated from combined load tests. For fatigue crack growth calculations, a reasonable assumption (Reference 74) is that the crack turns and propagates perpendicular to the principal stress direction. Under this assumption, fatigue crack propagation analysis is carried out in the normal manner, although it may be difficult to estimate the stress intensity factors for this case.

The case of part-through cracks under combined loading is more complex since Mode I, Mode II, and Mode III stress intensity factors are present. Interaction curves may be used for this case also. Presently, no test data are available in the technical literature. Stress intensity factors are available in References 75 and 76.

2.3.6.2 Bending

Little experimental data and analysis exist for the problem of a through-crack in a structure subjected to out-of-plane bending loads. Out-of-plane bending means loads that have a moment vector component perpendicular to the crack front. The analytic problems are large for a problem of this type for many reasons. First, under bending, portions of the crack surface may come into contact and the extent of that contact is unknown. For the case of a through-crack in a plate, this results in an elastic three-dimensional contact problem which is beyond the current state of the art of analysis capability. If it is assumed that sufficient tension loadings are applied to keep the crack open at all points, the contact aspect of the problem is removed and a much simpler problem results. However, to accurately analyze this simpler problem, the use of a sixth-order bending theory (such as a Reissner theory) is required. The simpler fourth-order Kirckoff theory gives an incorrect answer for the strength of the elastic singularity (i. e., the stress intensity factor). Furthermore, the solution is dependent on the thickness; and the thickness dependency is different for different planar geometries. Only a few simple geometries have been analyzed. (Reference 77)

From some experimental work on fatigue crack propagation, Roberts (Reference 78) concluded that for thin plates, modification of the stress intensity factor developed from the simpler Kirckoff theory (for which many solutions exist) by a factor λ equal to 1/2 gave consistent fatigue crack propagation predictions. This factor of 1/2 is also consistent with the work of Hartranft and Sih (Reference 77) where the factor for thin plates varies approximately between 0.4 and 0.6. According to their work, a plate will be sufficiently thin for Roberts' approximation if the thickness divided by "a" is less than 1. Their analysis indicates that for a thick plate (thickness divided by "a" is greater than 10) λ should be 1.0. This is all predicated on the fact

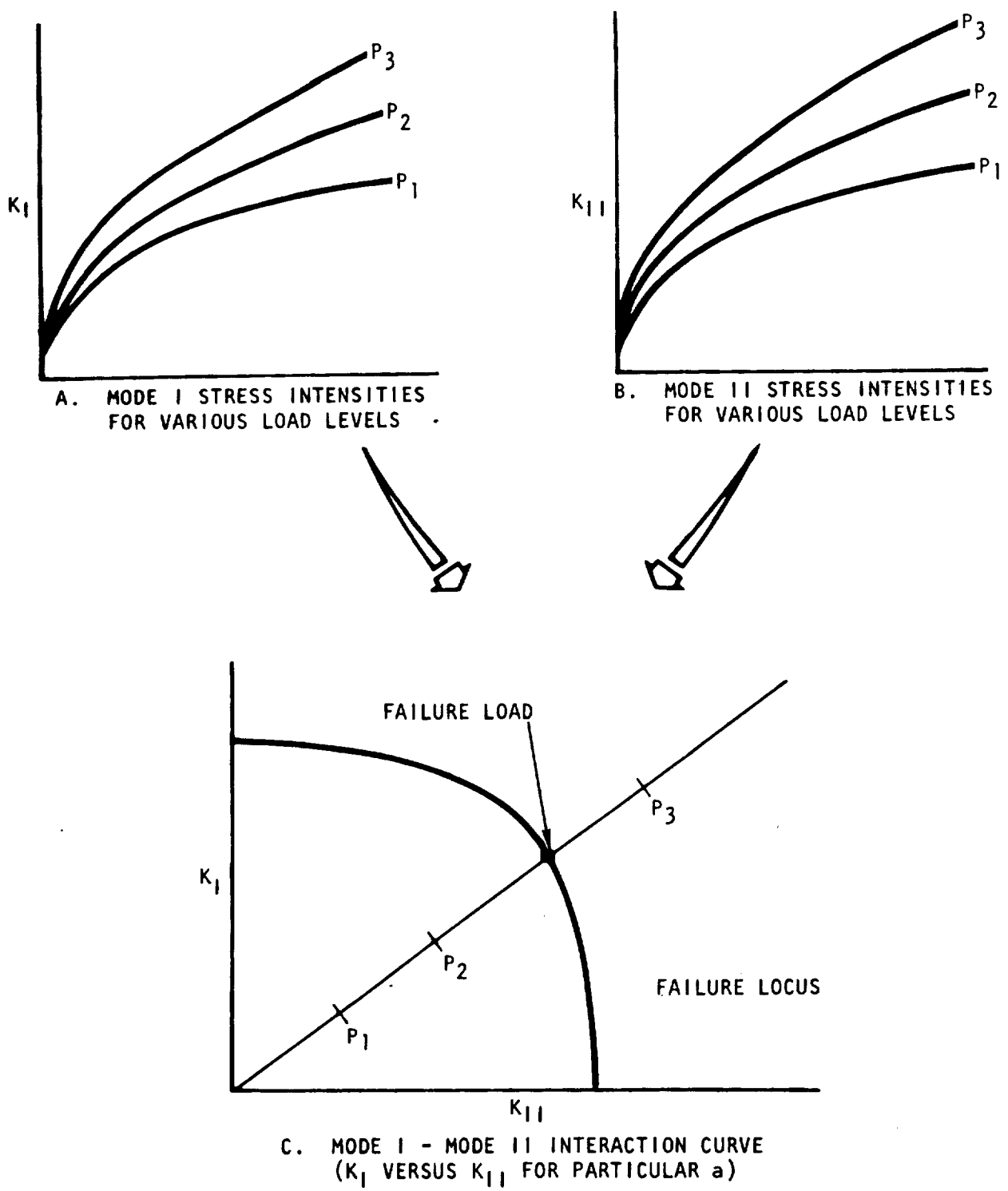


Figure 2-49. Failure Under Combined Tension and Shear

that the crack remains open. Reference 79 shows experimental correlation with the Sih-Hartranft work for the prediction of catastrophic fracture when the crack remains open at fracture.

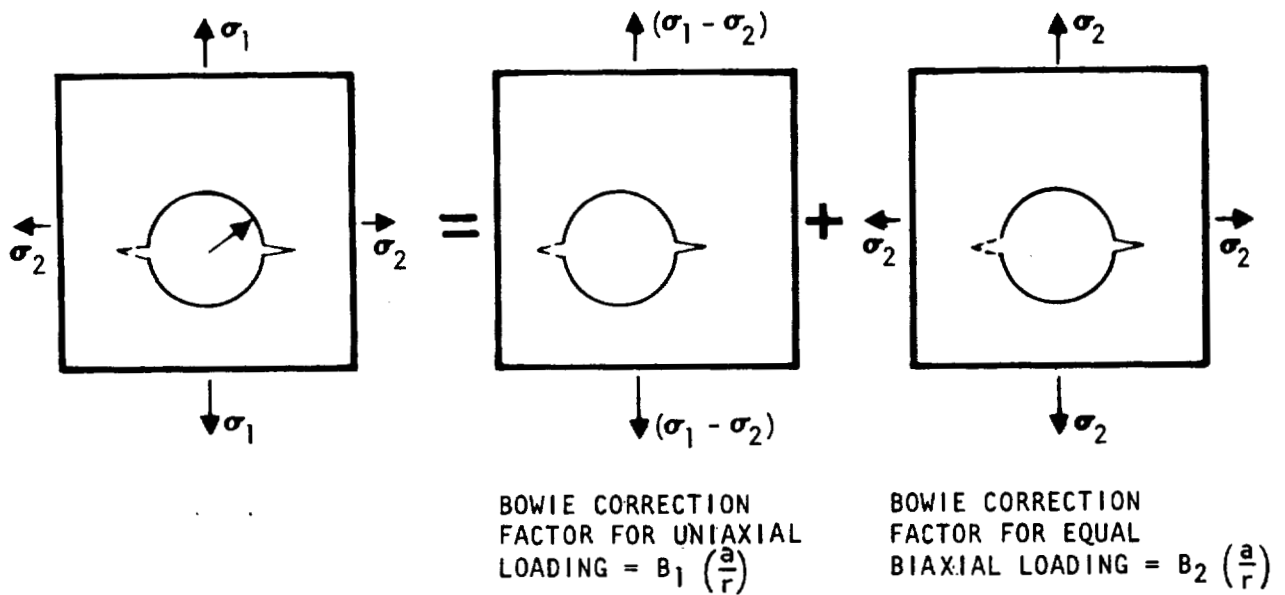
The bending of structures with part-through cracks can be handled using the analysis of Shah and Kobayashi which is presented in Figure 2-22 in Section 2 of Volume II. This analysis has been confirmed by experimental work performed by Schroedl and Smith (Reference 80).

2.3.6.3 Biaxiality

The effect of biaxial loadings on fatigue crack propagation rates has been investigated in Reference 81. When the stress parallel to the crack was 0.78 times the stress perpendicular to the crack, the crack growth rate was observed to be less than half that of the uniaxial rate. However, the authors state "... the existing data are not sufficiently exhaustive and the differences observed are not sufficiently large to draw any quantitative conclusions." Therefore, for the analysis of a central crack in a sheet, the effect of biaxiality can be ignored. However, it should be noted that if a crack is coming out of a hole in a plate, compressive loading parallel to the crack can cause tensile Mode I stress intensity factors. The value of this stress intensity factor can be developed from the uniaxial and biaxial solutions of Bowie (Reference 57) as shown in Figure 2-50.

2.3.7 Failure of Pressure Vessels and Shells

The mechanism of pressure vessel failures and the current fracture mechanics technology for handling this problem have been discussed in Reference 19 and also in Volume II of this report (Assessment of Fracture Mechanics Technology for Space Shuttle Applications). In these discussions, only one problem has been considered. It concerns the case of a part-through crack emanating from one side (surface) of the pressure vessel wall. In this case, if the crack length on the surface, $2c$, is small compared to the mean radius of curvature, R , of the vessel, and the crack depth is also small compared to the wall thickness of the vessel, plastic yielding would be restricted to the close neighborhood of the crack periphery, and the state of stresses around the leading edge of the crack is approximately plane strain. The residual strength and the fatigue crack propagation rate behavior can be estimated by applying stress intensity factors such as those developed by Irwin (Reference 43) for the elliptical cracks. Although some uncertainties arise concerning the problem such as back surface yielding (or break through) in the case of a deep flaw and the slow stable crack growth phenomenon exhibited in relatively high toughness materials, correlation between experimental data and analysis has been successful.



$$K = [(\sigma_1 - \sigma_2) B_1 + \sigma_2 B_2] \sqrt{\pi a}$$

IF $\lambda = \frac{\sigma_2}{\sigma_1}$, THIS IS CONVENIENTLY WRITTEN AS

$$K = \begin{cases} \sigma_1 \sqrt{\pi a} [(1-\lambda) B_1 + \lambda B_2], & |\lambda| \leq 1 \\ \sigma_2 \sqrt{\pi a} \left[\left(\frac{1}{\lambda} - 1\right) B_1 + B_2 \right], & |\lambda| \geq 1 \end{cases}$$

Figure 2-50. Evaluation of Bowie Factor for Biaxial Loading

For the case of a through-the-thickness crack in a relatively thin-walled shell, the problem is rather complicated. A well-recognized fact is that the crack tip stress intensity is drastically increased (as compared to a flat plate containing a crack of the same size) so that the cracked shell might fail at a substantially lower load or exhibit a considerably higher fatigue crack growth rate. It is commonly agreed that such increases in stress intensity or decreases in burst strength are partly attributed to interaction of the structural geometry (crack size, thickness, curvature, etc.), with the inherent properties of the material and the effect of bulging at the crack tip, which is caused by internal pressure. In typical applications, the shells or cylinders might be an airplane fuselage, a submarine hull, a pressure vessel, a pressure tube in a nuclear reactor, or natural gas pipelines. These structures cover a wide range of combinations in structural geometries, size, and materials. Consequently, a variety of failure modes is possible and it might be quite different for each class of geometry-material combinations. Theories (References 82 and 83) have been proposed to classify the possibility of failure modes in cylindrical shells containing an axial crack and to develop failure criteria suitable to each class of failure mode. In these theories, the geometry variables considered were crack length ($2c$) and a geometry parameter a/\sqrt{Rt} where R and t are the radius and the thickness of the shell, respectively. The material variables considered were the flow stress ($\bar{\sigma}$), the plastic zone, and the fracture toughness indices either measured by crack length and failure load (K_C), or by crack opening displacement (COD).

The Paris criterion (Figure 2-51) states that for a cracked shell having a certain geometry, (say, a/\sqrt{Rt}), if the material critical plastic zone size (determined by K_C and $\bar{\sigma}$) is large as compared to \sqrt{Rt} the shell will fail by a "plastic zone instability" mechanism so that the linear fracture mechanics type of failure analysis will not be applicable. However, as depicted in Figure 2-51, if the crack size is large (for the same geometry and material combination); i. e., a/\sqrt{Rt} increases, the crack might undergo a K_C -type of failure mechanism.

The Paris criteria can be described by an example as follows: Consider a typical fuselage having a radius of 2.2 meters (90 inches) and sheet thickness of 0.254 centimeter (0.1 inch). The material is 2024-T3 aluminum alloy which normally exhibits a K_C over yield (or $K_C/\bar{\sigma}$) ratio of 2.0 (approximately). Therefore, a value of 0.213 is obtained for the parameter on the ordinate. This value corresponds to an a/\sqrt{Rt} value of approximately 0.33 on the dividing line in Figure 2-51. Substituting values for R and t indicates the requirement for a K_C -type failure in this case would be $2a \geq 5.08$ centimeters (2.0 inches).

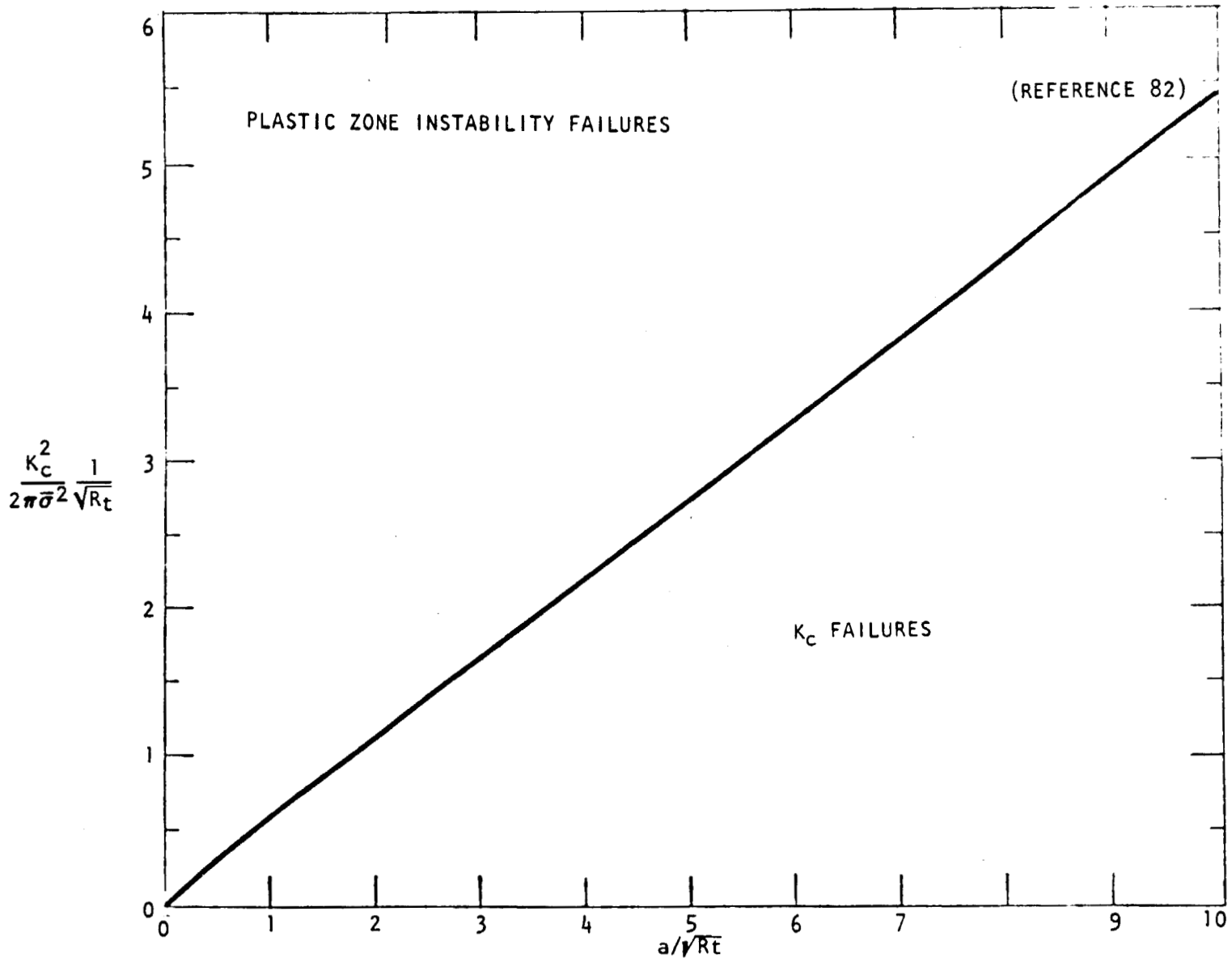


Figure 2-51. Paris Failure Criteria for Cylindrical Pressure Vessels With Axial Through-the-Thickness Crack

Hahn's theory (Figure 2-52) is similar to that proposed by Paris. In Figure 2-52, Hahn hypothesizes three categories of failure modes. They are:

Category 1 - linear elastic behavior

Category 2 - nonlinear elastic behavior

Category 3 - plastic instability behavior.

The dividing criterion between these categories is in terms of the parameter $(K_C/F_{ty})^2/a$. (Note, here he compares the critical plastic zone size with the crack length instead of the shell geometry.) They are $(K_C/F_{ty})^2 \leq 1.2(a)$ for Category 1, $(K_C/F_{ty})^2$ between $1.2(a)$ and $7(a)$ for Category 2, and $(K_C/F_{ty})^2 > 7(a)$ for Category 3.

Generally, the cracked shells that undergo Category 1 failure mode can be handled by a linear elastic-fracture-mechanics-type of analysis whereas for shells that belong in Category 2 failure modes a plastic-zone corrected analysis procedure would be required. For very tough material combined with short cracks (Category 3), the failure mechanism would be controlled by the flow stress ($F_{ty} < \bar{\sigma} < F_{tu}$) of the material.

The applications of Figure 2-52 can be illustrated with the same airplane fuselage examples problem. Here, based on Figure 2-52, the crack length ($2a$) has to be larger than 2.89 centimeters (1.14 inches) to avoid the flow stress controlled mode of failure. Now consider an airplane fuselage containing a 20.32-centimeter (8-inch) crack. The $(K_C/F_{ty})^2/a$ parameter approximately equals to 1.0. Therefore, the crack should exhibit a Category 1 failure and thus linear elastic fracture mechanics analysis is applicable. However, a supplementary requirement outlined in Figure 2-52 indicates that a crack opening displacement (COD) type of fracture index (see Reference 83 for COD definition) would be preferred for carrying out the calculations because K_C/F_{ty} is greater than 1.5 for 2024-T3 aluminum.

Now if the crack is only 10.16 centimeters (4 inches) in total length, this configuration would be Category 2 in Figure 2-52. On the other hand, according to Figure 2-51, this configuration would also be a K_C -type failure. It should be noted here that in Paris's criteria there is no such thing as Category 1. The dividing line in Figure 2-51 simply divides the failure mechanisms into two failure modes - either flow-stress controlled or K controlled. In the K -controlled area, plasticity corrections are always preferred in all the calculations.

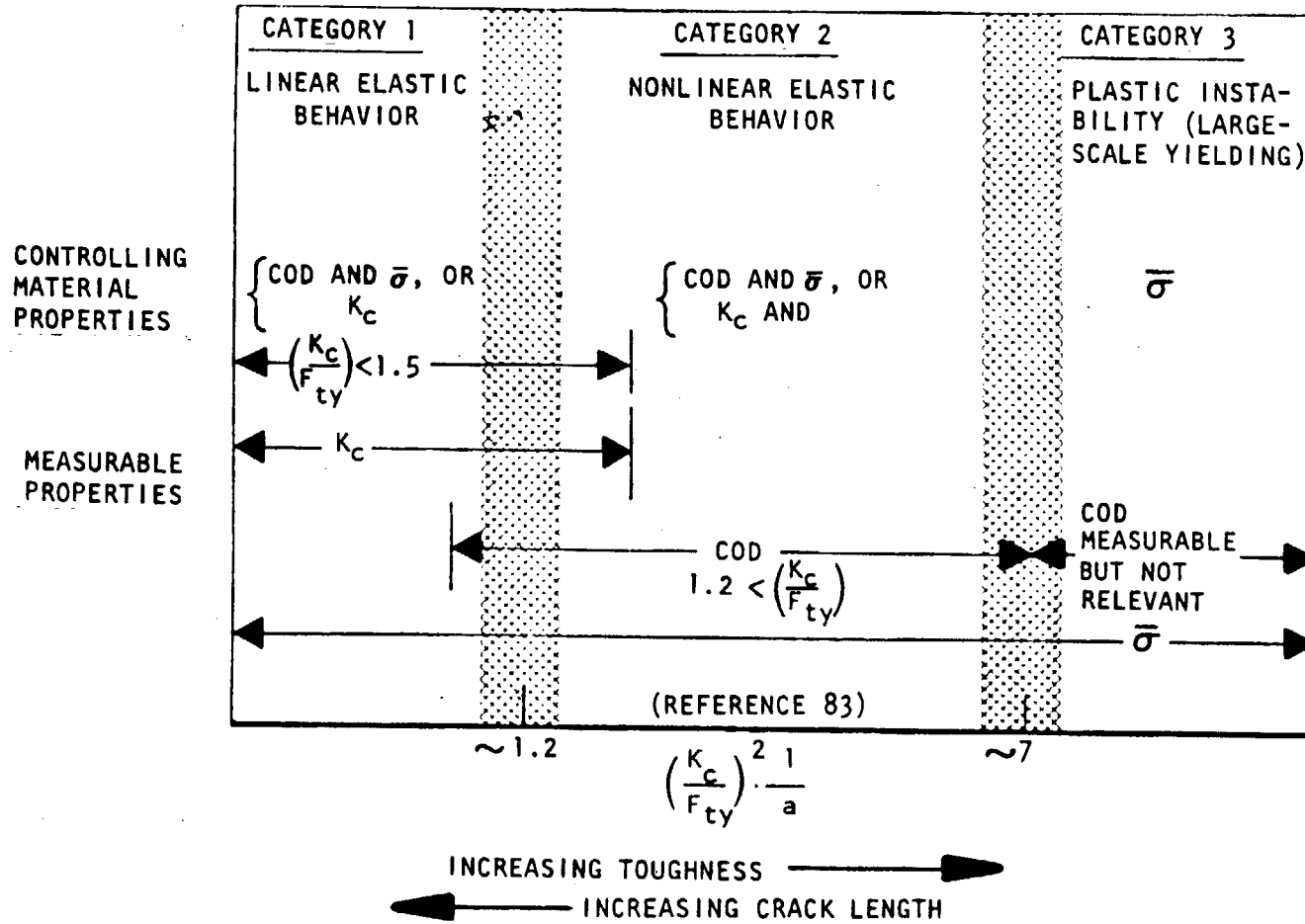


Figure 2-52. Hahn's Failure Criteria for Cylindrical Pressure Vessels With Axial Through-the-Thickness Crack

In summary, it is recommended that in any attempt to conduct a failure analysis in shells one should always check the anticipated failure mode for the shell under consideration. The method is simple and outlined in the following:

1. Establish the values of all shell parameters. The geometry, the material, the variables R , t , K_C , K_{IE} , F_{ty} , F_{tu} , and the applied stress level (refer to Section 2.3.8 for definition of K_{IE}).
2. Calculate a_{et} and a_{cr} for a surface flaw using K_{IE} .
3. If $a_{cr} \geq a_{et}$, recalculate $2a_{cr}$ for a through-the-thickness crack, using K_C .
4. Calculate a_{cr}/\sqrt{Rt} where a_{cr} is obtained from step No. 3.
5. Calculate $(K_C/\bar{\sigma})^2/2\pi\sqrt{Rt}$ where $\bar{\sigma} = (F_{ty} + F_{tu})/2$.
6. Check the possible failure mode using Figure 2-51. The Paris criterion is preferred because it accounts for all the geometric variables, R , t , and $2a$. (Note the Hahn's criteria only account for $2a$.)

After the failure mode is determined, the residual burst strength for the shell can be estimated by using the available values of K_C or $\bar{\sigma}$, whichever is appropriate. For fatigue crack propagation, since the applied K level is usually low and thus the corresponding plastic zone size is small, it can be assumed that the crack extension mechanism is always controlled by the current crack tip stress intensity factor, which is only a function of applied stress level and geometry (including crack length). The methods for calculating the residual burst strength and the fatigue crack propagation rates in shells will be discussed in the subsequent sections. For the cases which involve surface flaw failures, the basic fracture mechanics technology has been discussed in Volume II in detail. A summarized discussion concerning generalized design procedures will be given in Section 2.3.7.4.

2.3.7.1 Stress Intensity Factors for Curved Plates or Shells

For a through-the-thickness crack in a shallow shell, the external loads applied to the cracked shell cause two types of stress singularities at the crack tip. The crack tip stress intensity factor in the shell is thus made up of two components: One accounts for the local crack tip membrane stress and the other accounts for the local crack tip bending stress; i. e.,

$$K_{IS} = K_I \left[A_m - \frac{2Z}{t} \cdot A_b \right] \quad (37)$$

for the crack opening displacement mode (Mode I) and

$$K_{2S} = K_2 \left[B_m - \frac{2Z}{t} \cdot B_b \right] \quad (38)$$

for the crack sliding mode (Mode II). Here t is the thickness of the curved sheet, Z is measured from the neutral axis of the sheet with the positive direction toward the inside of the shell, and subscripts m and b , respectively, refer to the membrane and the bending components in the local crack tip stress field. K_1 and K_2 are as defined in Figure 1-5 of Volume II for Mode I and Mode II stress intensity factors, respectively, in flat sheets or plates; i. e.,

$$K_1 = \sigma \sqrt{\pi a} \cdot \Pi \alpha,$$

$$K_2 = \tau \sqrt{\pi a} \cdot \Pi \alpha,$$

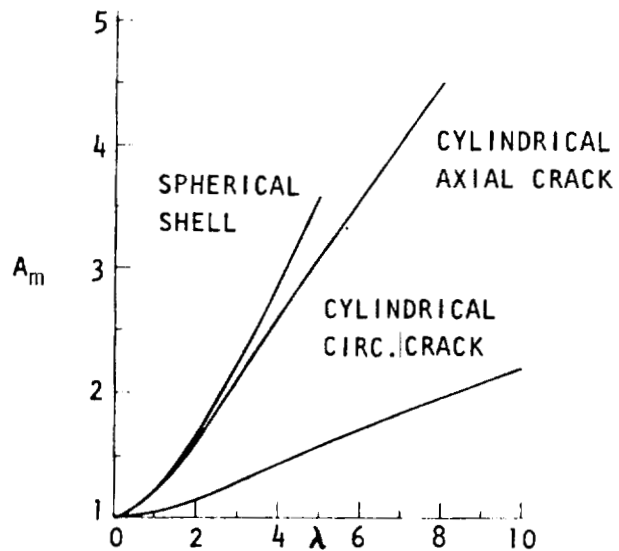
where σ and τ are the applied far field tensional and shear stresses, respectively. In the shell, the applied tensional stress could either be the axial stress, N_0 (e. g., the pR/t or the $pR/2t$ stresses), or the Mc/I stress, whichever is appropriate.

Consequently, if the coefficients A_m and A_b (for tension) and B_m and B_b (for shear) can be determined, the stress intensity factor in the shell (or curved sheet) can be estimated in terms of the stress intensity factor available for the flat plate. In other words the fatigue crack growth rate behavior and the residual strength for the shell can be estimated by using the material properties determined for the flat plate.

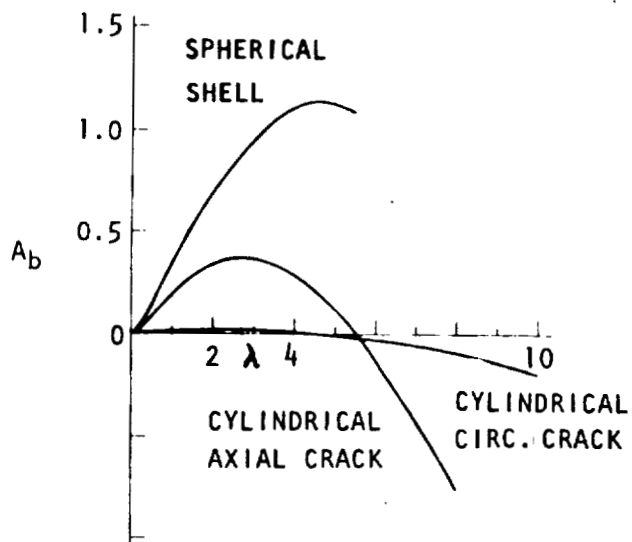
Much analytical work has been conducted in an attempt to obtain these curvature effect coefficients for various combinations in structural configurations and loading conditions (References 84 to 100). The structural configurations considered were:

1. An axial crack in a cylindrical shell
2. A circumferential crack in a cylindrical shell
3. A meridional crack in a spherical shell

The Mode I curvature effect coefficients (A_m and A_b) for these cracks under tension load only ($N_0 \neq 0$, $M = 0$) and under bending moment only ($N_0 = 0$, $M \neq 0$), taken from References 84, 87, and 88, are presented in Figures 2-53 and 2-54. The Mode II curvature effect coefficients B_m and B_b

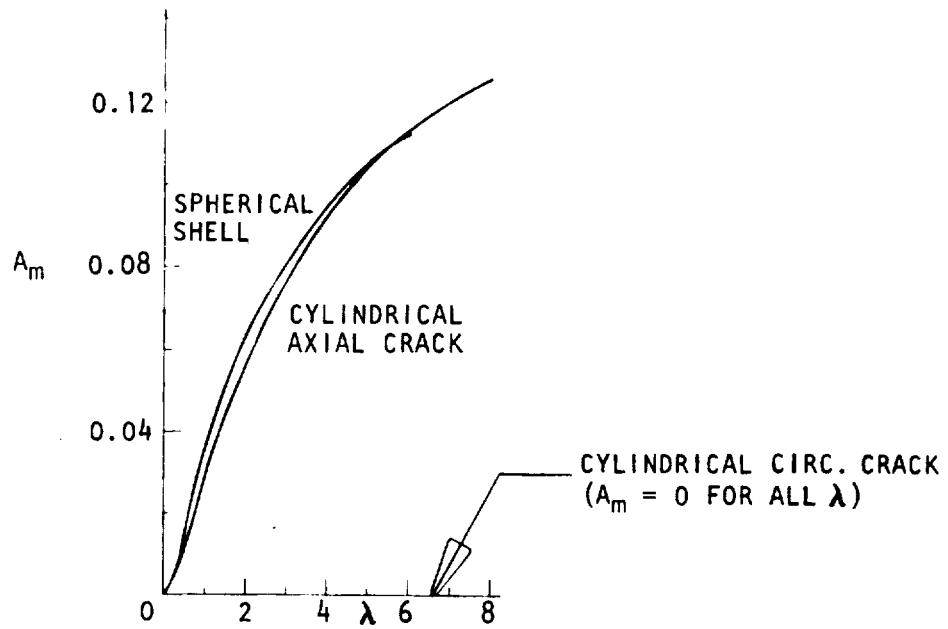


(a) MEMBRANE COMPONENT

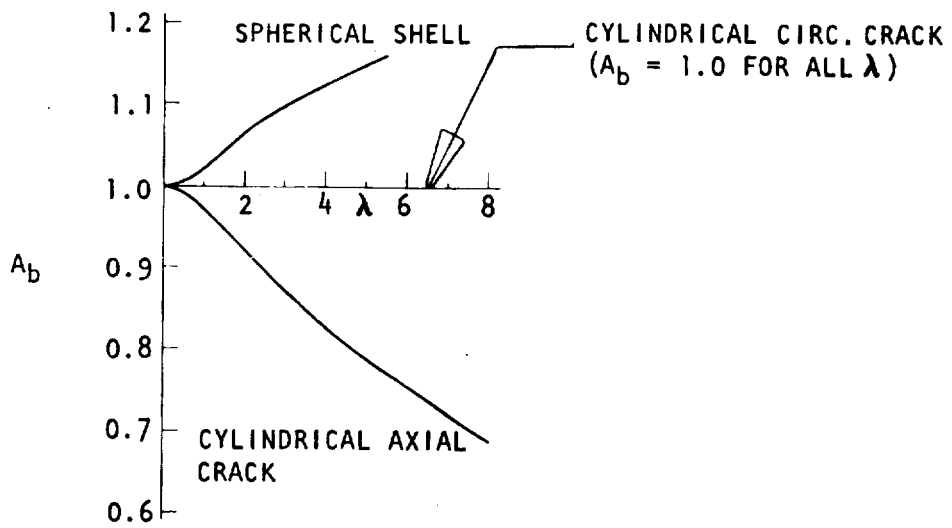


(b) BENDING COMPONENT

Figure 2-53. Curvature Effect Coefficients in Symmetrically Loaded Shells ($N_o \neq 0, M = 0$, Reference 84)



(a) MEMBRANE COMPONENT



(b) BENDING COMPONENT

Figure 2-54. Curvature Effect Coefficients in Symmetrically Loaded Shells
 $(N_o = 0, M \neq 0, \text{ Reference 84})$

for these cracks (taken from References 84, 85, and 90) are given in Figure 2-55. These curvature effect coefficients are plotted as the function of a geometric parameter, λ , where $\lambda = [12(1 - \nu^2)]^{1/4} \cdot (a/\sqrt{Rt})$. For $\nu = 0.33$, $\lambda = 0.905(2a/\sqrt{Rt})$.

Note the curvature effect coefficients determined by other investigators are much similar to those derived by Erdogan et al. As an example, the A_m factors for an axial crack in a cylindrical shell derived by Copley and Sanders (Reference 97) and Folias (Reference 94) and Erdogan and Kibler (Reference 88) published in three different sources of references are compared in Figure 2-56. It is seen that the results of Folias are identical to those reported in Figure 2-53. In the range having a higher value of λ , the A_m values derived by Copley and Sanders are somewhat higher.

One can define a stress intensity ratio parameter

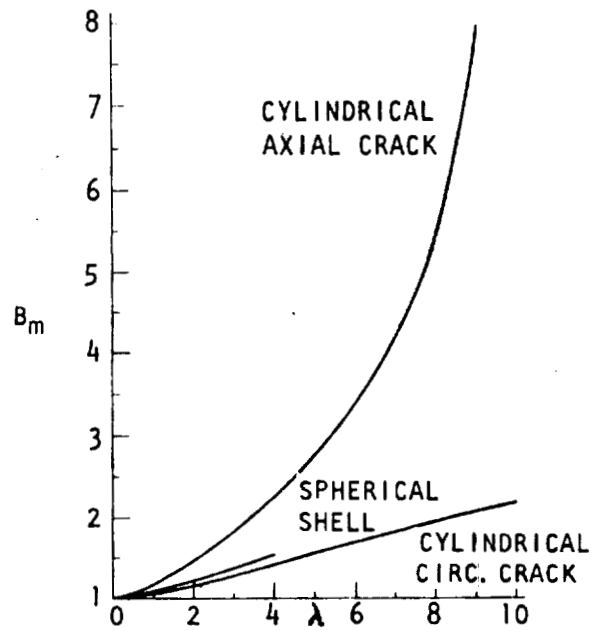
$$\alpha_s = K_{IS}/K_I, \quad (39)$$

which, from Equation 37, results in $\alpha_s = [A_m - 2Z/t \cdot A_b]$. If α_s is plotted versus the geometry parameter, $2a/\sqrt{Rt}$, then since R and t are constants for each individual case, α_s works just like a stress intensity modification factor for calculating the fatigue crack propagation rate (as a function of crack length) as the crack progresses. Similarly,

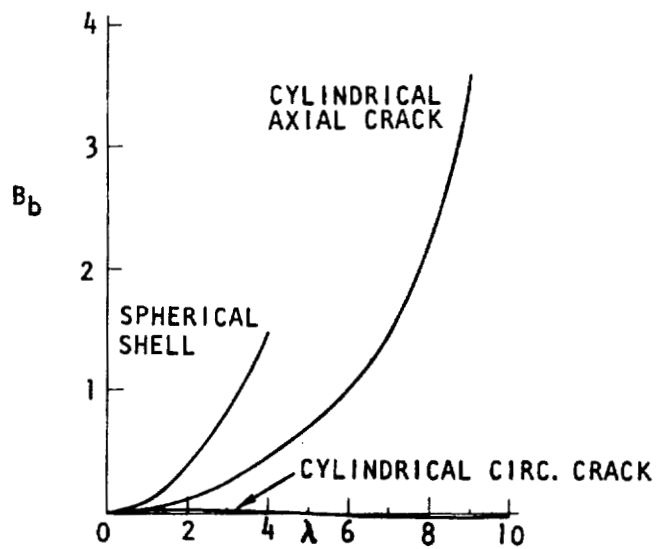
$$\frac{1}{\alpha_s} = \frac{\sigma_{\text{shell, critical}}}{\sigma_c} \quad (40)$$

correlates the burst strength for the shell, $\sigma_{\text{shell, critical}}$, and the flat plate allowable stress, (σ_c) predicted by the predetermined material property (K_c).

Figure 2-57 presents a plot of the theoretical α_s values for the case of cylindrical shell containing an axial crack subjected to internal pressure. Available experimental data on the burst strength of aluminum curved panels and titanium cylinders and curved panels are plotted in the same figure for comparison. It is seen in Figure 2-57 that the relationship between the critical stress intensity factor for a flat sheet and the critical stress in pressurized shells is strongly dependent upon materials. It should be noted that the calculated plastic zone parameter, $(K_c/\bar{\sigma})^2/2\pi\sqrt{Rt}$, is equal or less than 0.25 for all the 2024-T3 aluminum panels. A check using Paris criteria defined in Figure 2-51 revealed that the minimum required structural shape parameter, a/\sqrt{Rt} , would be 0.5. The shape parameter for the aluminum panels was 2.25 or larger (Figure 2-57). Moreover, it can also be shown that these panels satisfy Hahn's Category 1 requirement. The relative plastic zone index, $K_c/\bar{\sigma}$, for the 2024-T3 aluminum is approximately equal to 2.0.



(a) MEMBRANE COMPONENT



(b) BENDING COMPONENT

Figure 2-55. Curvature Effect Coefficients in Shells Under Torsion (Reference 84)

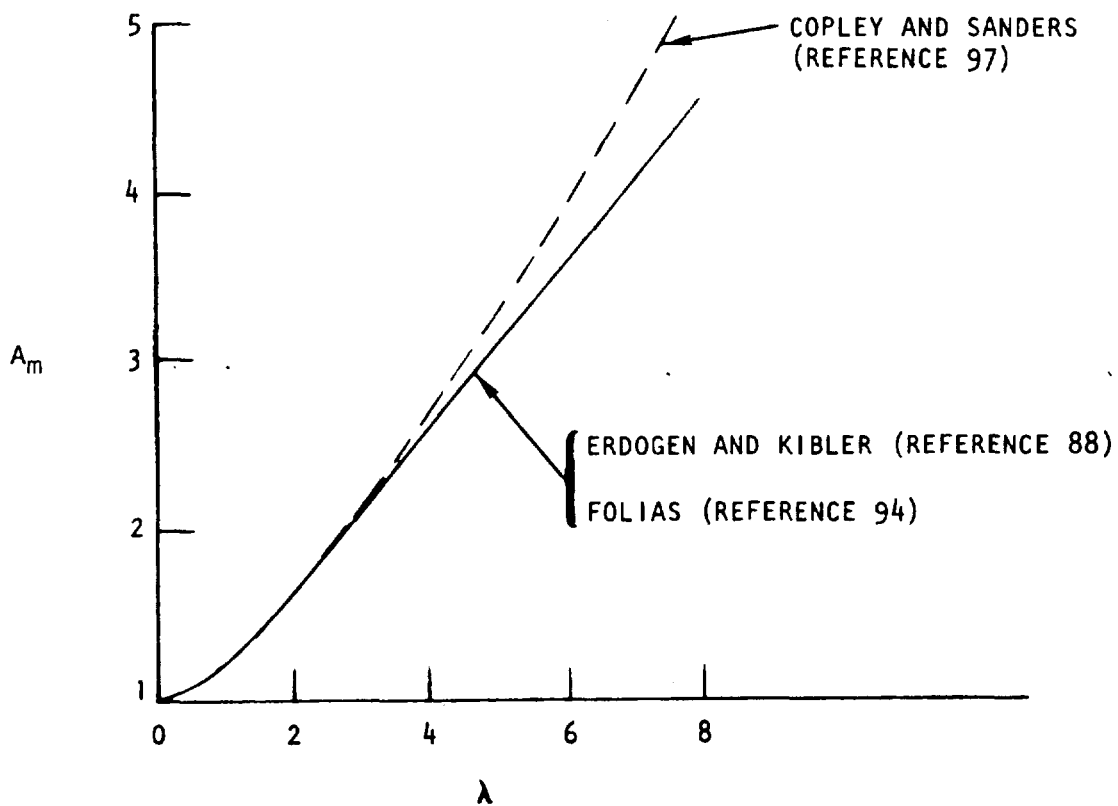


Figure 2-56. The Membrane Stress Singularities for a Cylindrical Shell Containing an Axial Crack ($N_0 \neq 0$, $M = 0$), Comparison of Three Analytical Results

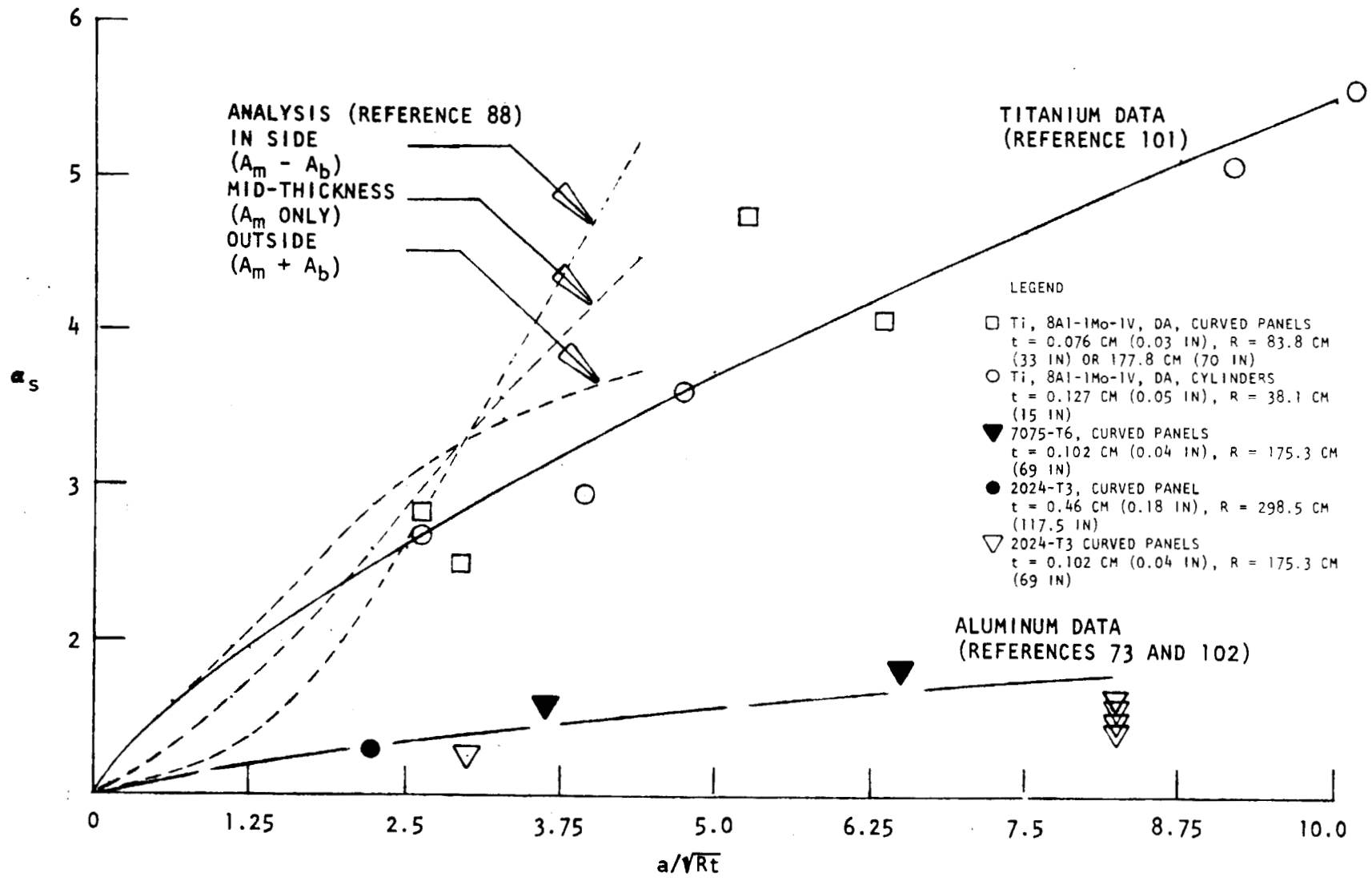


Figure 2-57. Stress Intensity Multiplication Factor for Axially Cracked Cylindrical Shell

The $K_C/\bar{\sigma}$ values for titanium and 7075-T6 aluminum are both approximately equal to 1.0, and, therefore, it can be concluded that K_C failures were attended in all the tests, and the corresponding α_s values were apparently valid.

Figure 2-58 presents comparisons of the analytical results for circumferential crack and fatigue crack propagation test data on 2014-T4 cylinders under uniform axial tension stresses. It is seen that the actual increase of crack tip stress intensity in the cylinder tests is also less severe than those predicted by analysis.

2.3.7.2 Plastic Zone Instability Failure of Pressure Vessels

When the residual burst strength of the pressure vessel is expected to be controlled by the plastic zone instability failure mechanism. The failure stress would simply be, according to Hahn (Reference 83),

$$\sigma_{pi} = \bar{\sigma} \left(\frac{1}{\alpha_s} \right) \quad (41)$$

where α_s could be the analytical A_m value taken from Figure 2-57 and $\bar{\sigma}$ might be the average of the material tensile yield strength and ultimate strength. In a particular case, Hahn has determined the $\bar{\sigma}$ value for the low-strength structural steels to be 1.04 F_{ty} plus 6.9 MN/m² (10 ksi).

On the other hand, an equation has been derived by Paris for calculating the plastic zone instability strength in shells. The Paris equation is

$$\sigma_{pi} = \bar{\sigma} \sqrt{2} \left\{ \alpha_s \cdot \left(\frac{a_{eff}}{\sqrt{Rt}} \right)^2 \cdot \left[\alpha_s + 2 \alpha_s' \left(\frac{a_{eff}}{\sqrt{Rt}} \right) \right] \right\}^{-1/2} \quad (42)$$

when α_s is the slope at the appropriate point on the α_s versus a/\sqrt{Rt} curve (Figure 2-57). Using the analytical A_m values of Erdogan and Kibler, Paris has plotted Equation (42) in a curve (Figure 2-59). This kind of parametric curve can be used for quick calculation of the σ_{pi} values for any shell configurations. The σ_{pi} values developed based on Equation (41) with use of the analytical values and the data for aluminum curved test panels are also shown in Figure 2-59. Figure 2-59 indicates that the Paris Equation is conservative as compared to Equation (41). It is anticipated that a reasonable estimate of the σ_{pi} values can be attained with use of Equation (42) in cooperation with the α_s values determined by experimental results for a specific material (i. e., obtain a curve for each material).

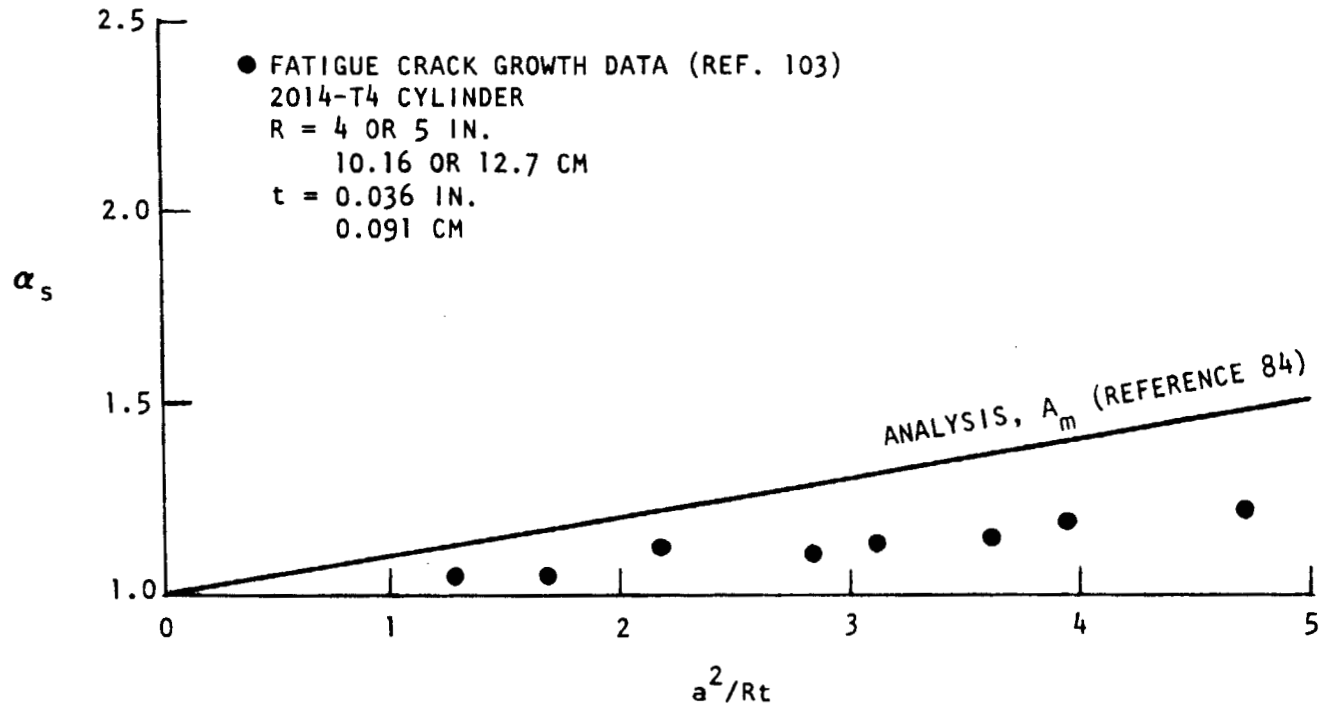


Figure 2-58. Stress Intensity Multiplication Factor for Circumferentially Cracked Shell

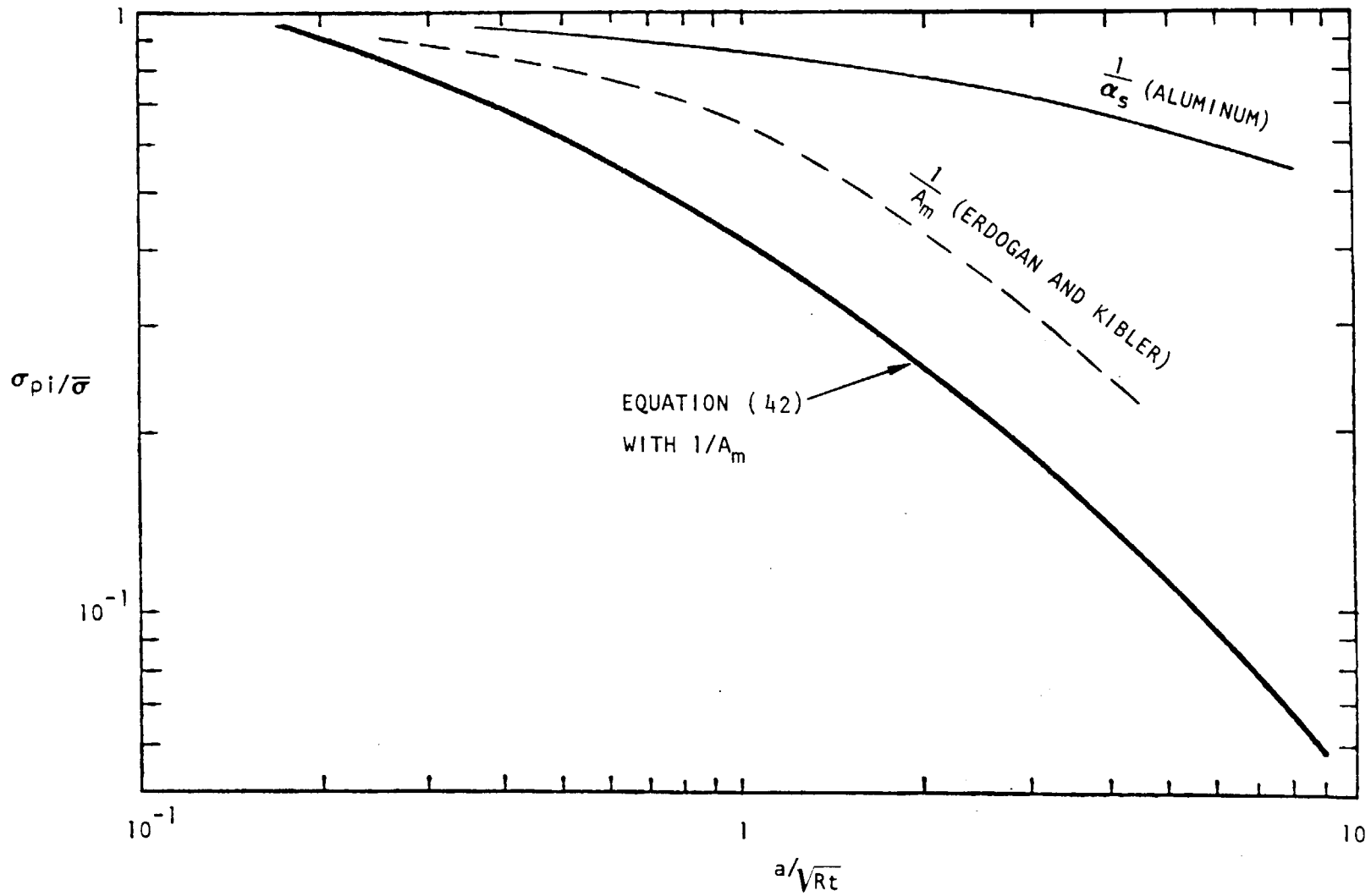


Figure 2-59. Plastic Zone Instability Failure Strength of Pressure Vessels

2.3.7.3 Failure of Reinforced Shells

The reinforcements in a shell are frames and longitudinal stringers either parallel or perpendicular to the crack depending on the direction the crack is oriented. For a circumferential crack, the horizontal stringers might act as crack stoppers. For a longitudinal crack, the frames might act as crack stoppers. Only one paper (Reference 99) has treated the reinforced shell by analysis. At present it is anticipated that the reinforcement analysis for flat sheet (discussed in Section 2.3.4) can also be applied here.

When the reinforcements are parallel to the crack, the reinforcements help reduce the crack bending intensity. They help in such a way that the reinforcements resist bending by the load applied perpendicular to it and thus help the crack remain closed (or open up to a less degree). Since this is not a load transfer problem, pure analysis would be difficult. Certainly, semi-empirical curves can be developed with test data available from References 73, 101, and 102. However, the scope of this effort is outside of the bounds of the present study.

2.3.7.4 Damage Tolerance Analysis for Pressure Vessels

It is possible to use fracture mechanics to design a pressure vessel initially. For example, design curves relating wall thickness to desired life such as depicted in Figure 2-60 could be constructed with the use of fracture mechanics and appropriate damage tolerant design criteria. However, most structures will be initially sized on the basis of arbitrary design factors for fatigue and static strength, and fracture mechanics and damage-tolerant requirements are usually applied only to verify the design by providing an acceptable or nonacceptable decision criteria. The incorporation of fracture mechanics concepts into design methodology has not progressed to the stage of providing a rational means for selection of static strength and fatigue margins on the basis of material toughness and crack propagation characteristics. Accordingly, fracture criteria are not currently introduced into preliminary design trade studies, and parametric analyses are not conducted over wide ranges of stress levels and structural configurations. The primary role of fracture mechanics is to utilize information regarding proof loads, NDE capability, design stresses, and material properties to validate or reject a given design on the basis of a safe-crack-growth life requirement.

In general there are a number of rationale paths that may be followed to meet a safe-crack-growth life requirement for a pressure vessel. Basically the differences depend upon whether the responsibility for initial flaw size is placed on NDE or a proof test (or both) and whether the responsibility for determining critical crack size is based upon complete catastrophic failure or upon leakage. A variety of combinations is possible. The following is a brief outline of the procedures for utilizing state-of-the-art fracture mechanics to analyze the damage tolerance of a pressure vessel.

In Section 5 of Volume II, proof-test logic is discussed in great depth. Included in that section are descriptions of important phenomena associated with NDE, proof testing, and life calculations. It is pointed out that current state of the art cannot exactly account for all these phenomena. Therefore at present it is necessary to build some arbitrariness in the overall life calculations. These assumptions follow those made in the example on page 5-19 of Volume II. These assumptions are:

- 1.(a) Use of a flaw survival stress intensity, K_S , when proof testing is considered.
- 1.(b) Use of approximate size limitations on NDE capability.
2. Use of a particular crack growth model (with or without retardation).
3. Use of the approximate-breakthrough criterion.
4. Use of a critical stress intensity factor for catastrophic failure.

Item 1 (a and b) is concerned with determination of the initial flaw size to be used in the analysis. In general, in a design situation, there are four ways the initial flaw to be considered can be established:

1. NDE
2. Proof test
3. By definition
4. Combinations of the first three.

In Figure 5-1 of Volume II are examples of the relationships that may be established between surface flaw length and surface flaw depth when NDE establishes the initial flaw size. A similar relationship is established through the use of Equation 29 in Section 2 of Volume II, when K_S is used to establish the flaws screened out by proof testing. When a pressure vessel is to be proof-tested and inspected by NDE procedures, a composite figure such as Figure 2-61 should be used to establish the values of the flaws that may remain in the vessel. Note that in the example presented NDE serves to set initial flaw sizes for the shallow flaws, and proof stress sets the initial flaw sizes for the deeper flaws. Note also that $a = t$ is a natural limit to the extent of possible flaw depth, but that there is no natural limit on possible flaw length. For practical reasons and for additional reasons discussed in Section 5 of Volume II, the life analyses are considered within the limits $a/2c = 0.1$, $a/2c = 0.5$ or $a = t$. As also pointed out, it is never clear at the outset which of these limits will be the critical limit (i. e. which

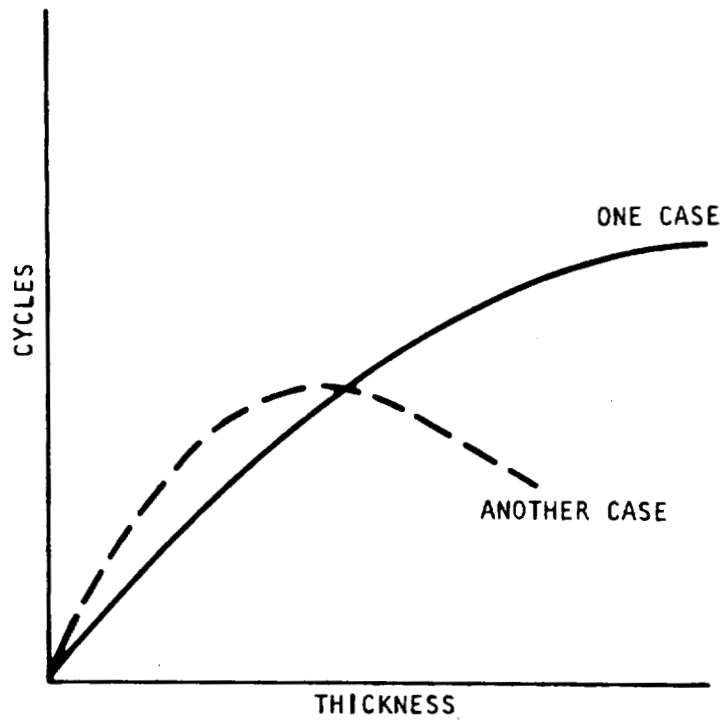


Figure 2-60. Thickness Versus Design Life
(Generalized Illustration)

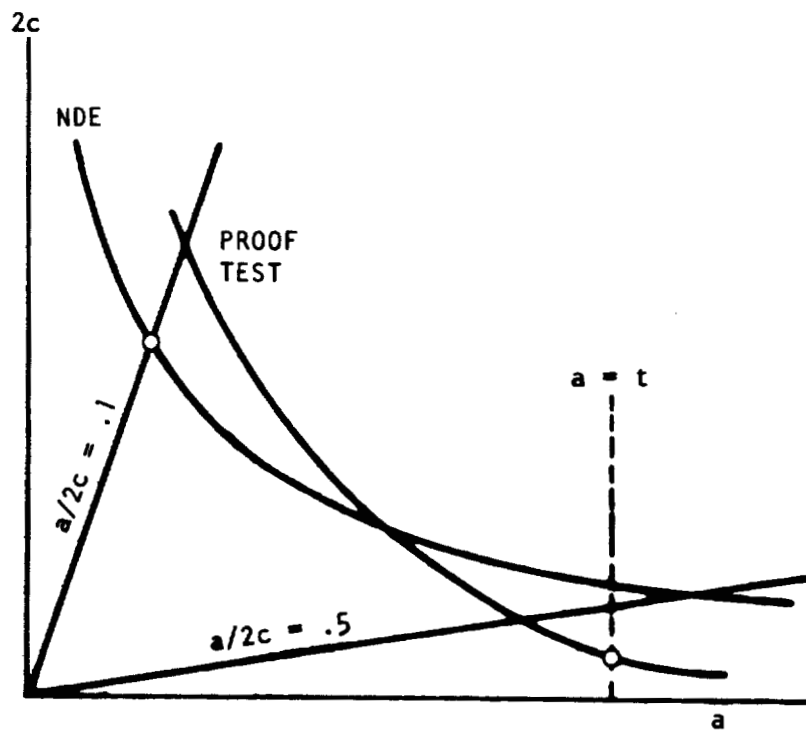


Figure 2-61. Initial Flaw Size Determination

initial flaw shape will have the shortest life). It is therefore necessary to perform the analysis for the two most extreme flaw shapes. These are indicated by the circles in Figure 2-61. Occasionally, depending upon the combination of stress, material, and thickness, the worst case may be the one having an intermediate initial flaw shape; in this case, a complete survey should be conducted.

Before the life is calculated, the end point of that calculation must be established (or a method of deciding when the end of life has been reached). A particular load is used to establish the flaw size at the end of life. For constant amplitude loading, it is usually taken to be the constant amplitude load. For spectrum loads, it is usually taken to be the maximum spectrum load or some higher load specified by a contractual agreement. In any event, use of that load and a critical value of the stress intensity factor establishes a relationship between surface flaw length and depth of a part-through crack, as in Figure 2-62. In addition, the crack length for failure as a through crack must be established. This is illustrated schematically by the X in Figure 2-62. Note that if the flaw size is at 1 when the part fails as a part-through crack, then the surface length will be sufficient to cause failure as a through crack. However, if the flaw size is at 2 when it fails as a part-through crack, additional life will be left as the crack grows out to the length required for failure as a through crack.

Before the life calculation is made, the applied stress intensity factor as a function of crack length and shape must be established. Note that for a part-through crack it is necessary to do this at the depth and at the surface. Expressions for these stress intensity factors are given in Section 2.3.3 and in Volume II. A subject similar to this is the transition criteria, since a transition criterion (how a crack grows from a part-through crack to a through crack) can be thought of as a relationship between the applied stress intensity factors and geometry. For example, the simple transition criterion of assuming that when $a + 2r_y = t$, or $a_{et} \geq t$, whichever case is appropriate, the surface length $2c$ of the part-through crack becomes the length of a through crack and can be thought of as the stress intensity relations given in Figure 2-63. Similar curves could represent the relationships for $K_{backside}$ (which is actually a transition criterion) given in Section 4 of Volume II.

One must now establish the fatigue crack propagation rate relationship that is to be used. It is appropriate to use one of the equation forms given in Section 3 of Volume II, with the correct material constants. Equally acceptable is the use of points that represent the rate data and interpolation between these points (Figure 2-64).

Now, for each initial flaw to be examined, an integration of da/dN (and dc/dN) is performed, taking into account changes in a and c which affect

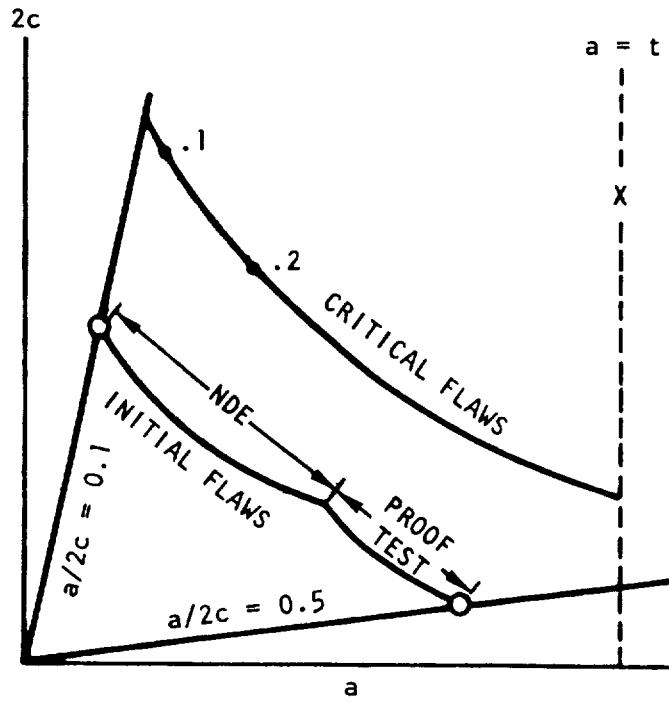


Figure 2-62. Initial and Critical Flaws

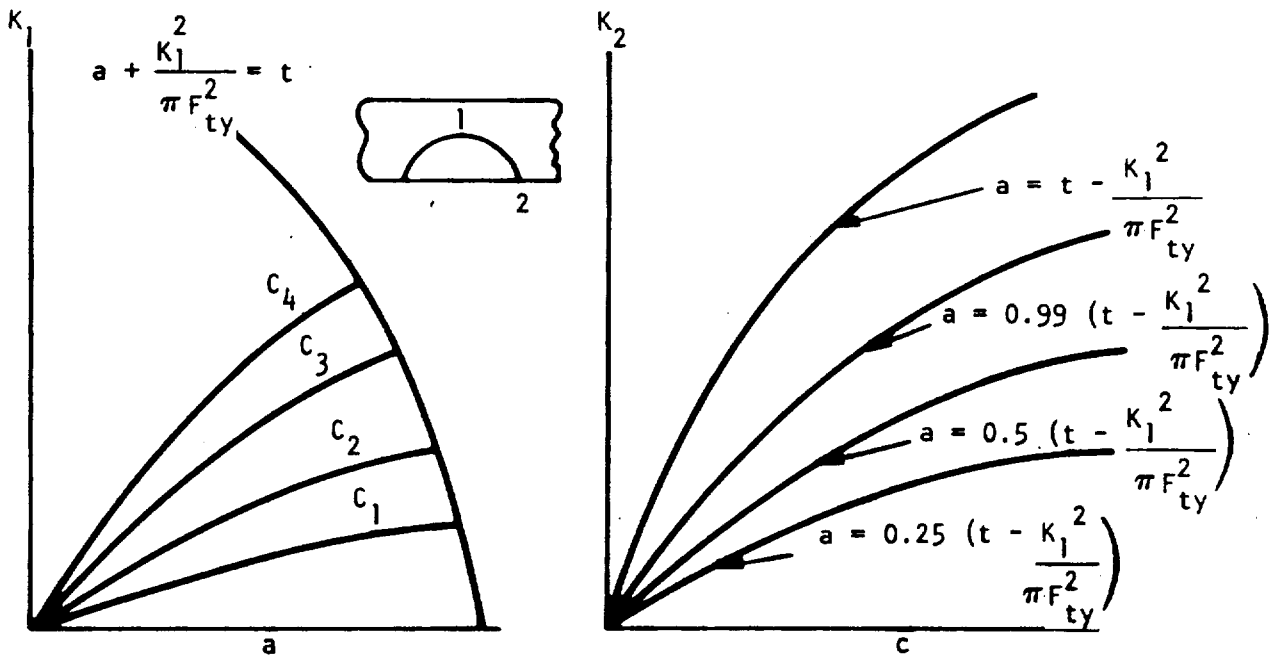


Figure 2-63. Typical Transition Criteria

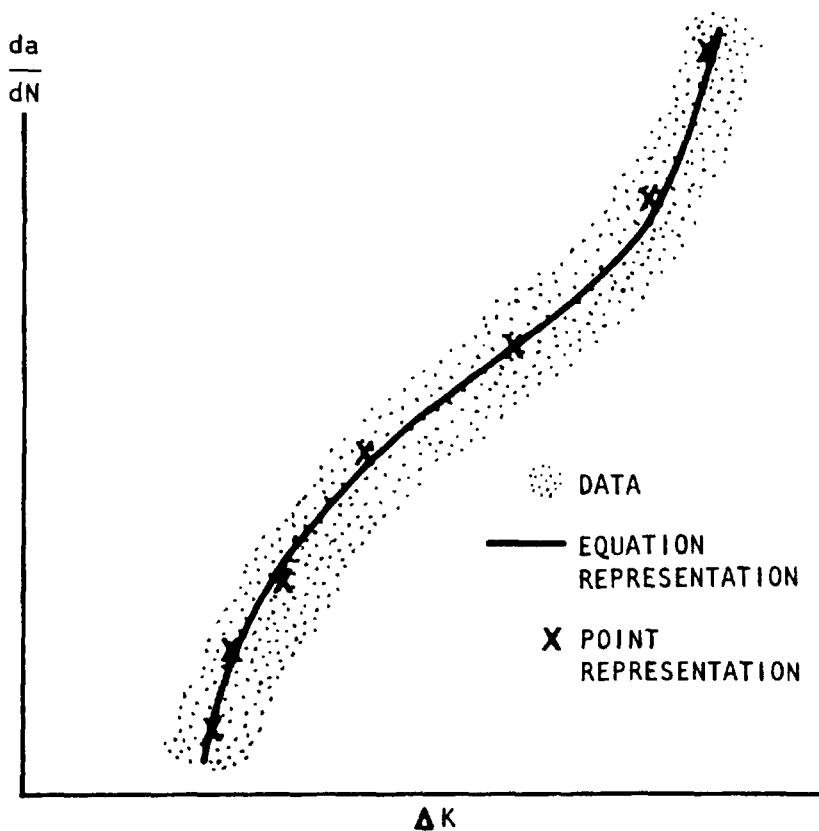


Figure 2-64. Fatigue Crack Propagation Rate Representations

the stress intensity factor as the crack grows. This is illustrated in Figure 2-65 where:

- Block 1: The initial crack dimensions are set. This is done by selecting the points defined in Figure 2-62.
- Block 2: The stress intensity relationships (and transition criteria) are used to get ΔK_1 and ΔK_2 (e. g., Figure 2-63).
- Block 3: The fatigue crack propagation rate law is used to get the appropriate rates (e. g., Figure 2-64).

- Block 4: An increment of cycles ΔN is chosen, and increments of Δa and Δc are calculated for that number of cycles. Note that for a spectrum of loads ΔN could be all the loads applied at a particular level in the spectrum. It is important that ΔN must be chosen sufficiently small such that a and c do not cause the new stress intensity factor (calculated on the next pass through the loop) to change significantly (say ~ 1 percent).
- Block 5: The new values of a , c , and N are calculated.
- Block 6: A comparison of the new crack size and the critical crack size is made. If the new crack is equal to or exceeds the critical crack size, the crack growth calculation is complete, and the cycles attained thus far are the life. If the critical crack size is not exceeded, the entire procedure (loop) is repeated for another cycle increment. Note that for spectrum loading a new stress level may be used at this point.

It should be noted that there are many other ways to compute the increment of crack lengths and cycles (Blocks 4 and 5). For instance, the required ΔN may be calculated for a selected value of Δa and then Δc may be computed, which corresponds to the same ΔN . It is also noteworthy that the flow diagram of Figure 2-65 is, for the most part, generally applicable for all crack growth calculations and with minor modifications could be used in conjunction with structures other than pressure vessels.

For each of the two cases considered (the circled points of Figure 2-62), a life (cycles) is established. The shortest of these is the life that must be compared to the minimum life specified in the safe-crack-growth life requirement. If the calculated life is greater than that required, then the pressure vessel is deemed acceptable, and the damage tolerance analysis task is complete. If the calculated life is less than that required, then one of the remedies described in Section 5 of Volume II must be taken and a new analysis performed.

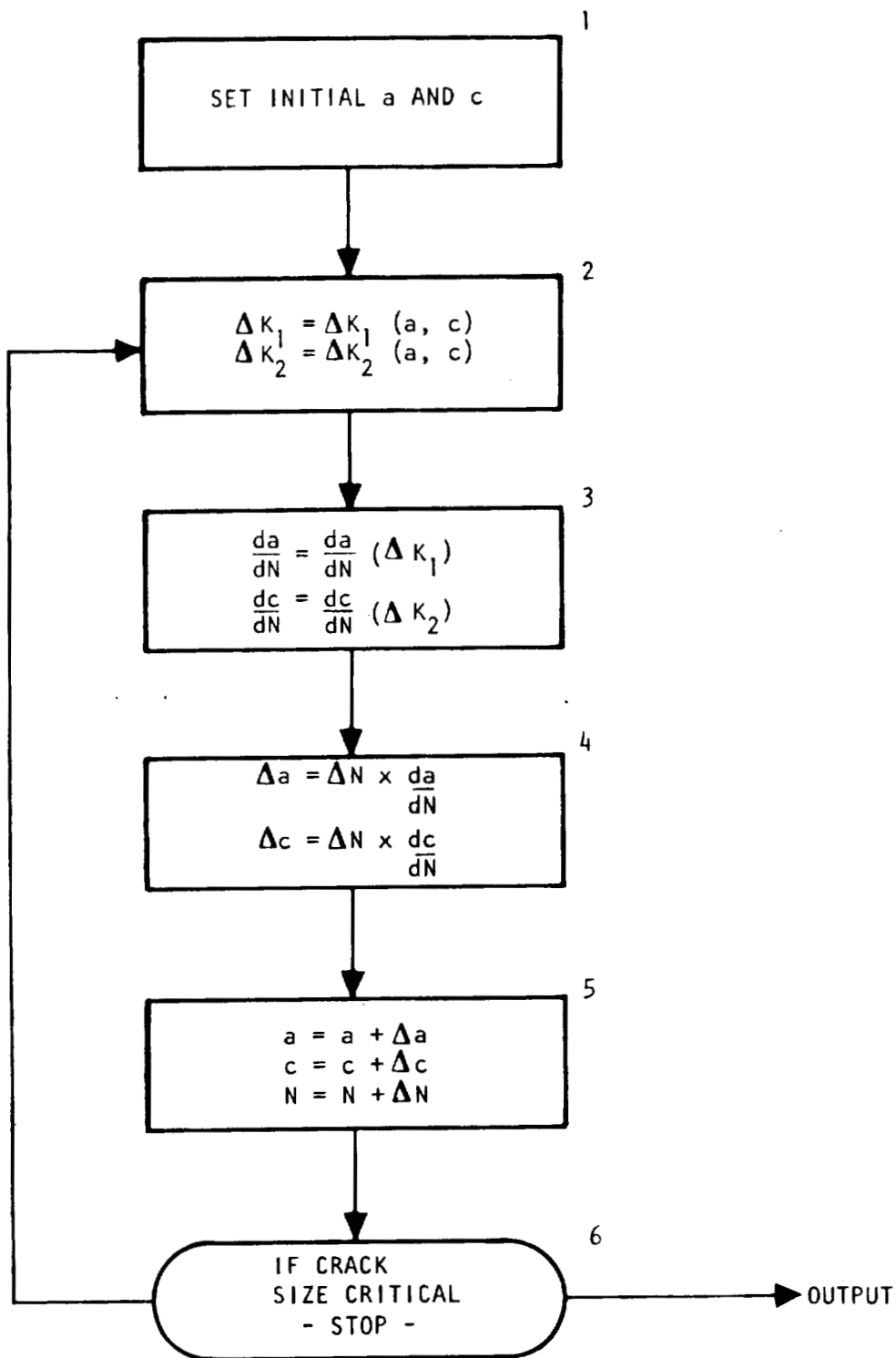


Figure 2-65. Crack Growth Calculation

2.3.8 Required Material Property Data for Space Vehicle Fracture Mechanics Analysis

Material property data for linear elastic fracture mechanics analysis can be separated into three general classifications: those used for predictive analysis of fatigue crack growth, those used in proof test logic, and those used for static analysis to predict the residual strength of a structure containing a flaw.

2.3.8.1 Predictive Analysis of Fatigue Crack Growth.

Fatigue crack growth rates are most conveniently represented by some functional expression relating crack growth rate, da/dN , to the applied stress intensity excursion, ΔK . As discussed in detail in Volume II, several mathematical relationships are available that adequately represent measured crack growth rate behavior. For Space Shuttle applications, it is intended that fatigue crack growth rates be described by the Collipriest equation (refer to Volume II), which requires four "material parameters" plus the maximum and minimum applied stress intensities to predict the attendant crack growth rate. These parameters are:

- K_C - the critical value of the maximum applied stress intensity corresponding to an infinite fatigue crack growth rate resulting in fracture
- ΔK_0 - the applied threshold stress intensity range below which fatigue crack growth is presumed not to occur
- n - the growth rate exponent corresponding to the mid range of a log-log plot of da/dN vs. ΔK (maximum stress intensity minus minimum stress intensity)
- C - The growth rate coefficient corresponding to the mid-range crack growth rate slope extrapolated to a unity value of ΔK

Where a special dependency upon load ratio (the minimum load/the maximum load) has been identified, additional growth rate shaping parameters may be required.

Presently there is no published standard for measuring fatigue crack growth rates, and the environmental and geometric effects on the growth rate "material parameters" have not been rigorously identified. Therefore, for Space Shuttle applications, crack growth rate data (and the corresponding material parameters) will be published as nominal values corresponding to

each alloy system, temper, product form, environment, and loading direction. Dependency upon thickness and temperature will be expressed by variation of a minimum number of the material parameters. For example variation of growth rate with thickness may sometime be accommodated by identifying a thickness dependency with K_C without requiring changing the values of the remaining material parameters. Also, distinctions must be made between published values for critical stress intensities for surface flaws and through-cracks due to the different stress states associated with the two defect geometries and/or anisotropy.

Since nominal values of crack growth rates material parameters will be used in safe-life analysis, confidence in the analysis results will be secured by application of an appropriate scatter factor to the safe-life analysis results.

2.3.8.2 Proof Test Logic Data

Some measure of material toughness is required to predict the maximum defect size that could possibly survive a proof load. As discussed in Volume II, use of lower bound K_{Ic} -type toughness values in proof test logic calculations can lead to an underestimate of the flaw size that might be screened by a proof test, which could lead to an unconservative safe-life analysis. Therefore, for proof test logic applications, a survival toughness value (K_S) will be published that will accommodate stable crack growth prior to fracture. K_S is a measure of the stress intensity at the failure stress calculated by using the flaw size at fracture. This value can alternately be determined by calculations that use crack growth resistance curves (if available for the material being analyzed) and the stress intensity analysis of the structure and defect geometry of concern.

The survival toughness value will also be published as a nominal value until a statistical data base becomes available and sensitivity studies concerning the exact effects of using upper bound values for maximum initial flaw size predictions have been completed.

2.3.8.3 Static Analysis Data

A measure of fracture toughness is required to evaluate the flaw size that will precipitate fracture at design or limit load conditions. The size of the structure and the type of constraint anticipated at the crack tip will dictate the type of material property data to be utilized. In any case, however, statistically treated lower bound numbers are appropriate for static fracture toughness numbers used in residual strength analysis.

Plane strain fracture toughness values will be measured to the ASTM standard E-399-72. Where ideal plane strain conditions will not prevail, other measures of toughness must be utilized. Surface flaw toughness values calculated from initial flaw size and failure stress (K_{IE}) are also appropriate for determination of the critical flaw size that might cause failure on the next load cycle. Thin sheet fracture properties may be generated in the form of K_C values with specimens of size nearly equivalent to the structure being analyzed or, more generalized, in the form of a crack growth resistance curve. The K_C data (computed from the final flaw size and the failure stress) should include a measure of the apparent toughness (computed from the initial flaw size and the failure stress) to facilitate analysis of the critical initial flaw size that might cause fracture.

Situations in which aggressive environments reduce the fracture stress will require assessment of an environmental threshold stress intensity, K_{th} , above which significant crack extension will occur without a corresponding increase in stress intensity. Special care, however, must be taken to avoid the use of artificially low threshold values that simply reflect the stable flaw growth experienced during monotonic loading.

For the Space Shuttle Program, it will be presumed that accommodation of sustained load crack growth, da/dt , which occurs at stress intensity levels above K_{th} , is beyond the current state of the art of fracture mechanics data acquisition and analysis techniques. With such a presumption, K_{th} must then correspond to the critical stress intensity which may not be exceeded under static loading during the service life of the structure.

2.3.9 Recommendations on Fracture Mechanics Research and Development

Based upon the preceding discussions, a number of fracture mechanics areas which should be developed is evident. The following is a listing of suggested topics for development of fracture mechanics analysis procedures.

1. Develop data and analysis procedures to handle the back surface magnification factor, back surface yielding, and local eccentric bending phenomena in the part-through-crack problem.
2. Develop data and analysis procedures which adequately account for the effects of local yielding at a hole.
3. Develop stress intensity factors and fatigue crack growth rate data for pin-loaded lugs.

4. Develop analysis procedures for skin-stringer structure which adequately account for the effects of reinforcement yielding, broken stringers, and the stiffness of the fastener system.
5. Develop data and adequate analysis procedure for integrally stiffened structure.
6. Develop data to establish failure criteria for combined tension and shear.
7. Develop data to establish failure criteria for combined bending and tension.
8. Develop fatigue crack growth rate and residual strength data for shells.
9. Develop data and analysis methods to account for the interaction effects of load sequence, environment, and hold time.
10. Although many investigations have been conducted to determine the size and shape of the crack tip plastic zone, none of these investigations (except Reference 82) attempts to define the role of the crack tip plastic zone in structural component failures. Research in this area is urged.

2.4 NONDESTRUCTIVE EVALUATION

The impact of applying fracture mechanics to the design and analysis of fail-safe and safe-life structures has led to a recognition of the need for a knowledge of crack detection. Consequently, the capability of various nondestructive evaluation techniques might impose a restriction on performing the linear elastic fracture mechanics analysis. Fracture control design method further recognizes that there are specific limitations for the implementation of nondestructive evaluation flaw detection methods with sensitivities capable of reliably ascertaining crack-like flaws and preventing structural damage associated with the initiation or propagation of these flaws. The reliable detection of damage before actual occurrence is of considerable importance, and the approach becomes one of deciding how, when, and where the nondestructive evaluation shall be performed.

The NDE techniques selected for fracture control design include surface examination methods capable of detecting surface-connected or near-surface flaws and penetration radiation methods for internal flaws. The liquid fluorescent method detects surface-connected flaws and performs well on both magnetic and nonmagnetic metallic materials. The magnetic particle inspection method is used exclusively on magnetic metallic materials for

detecting surface-connected flaws. Another applicable surface examination technique is the eddy current method, which is capable of flaw detection in metallic electrical conductive material. To detect internal flaws, any source of radiation capable of penetrating the volume of metallic material can be used. Ultrasonic and X-ray methods can be used to perform the necessary detection of internal flaws. The principles and technologies associated with these NDE techniques are described in Chapter 5 of Volume II.

As a starting point, the present state-of-the-art NDE techniques were considered, and Rockwell International Corporation, Space Division, Quality Control Specification MQ0501-008, Revision C, Nondestructive Inspection Requirements for Materials and Processed Parts, provided a basic rationale for the NDE application during material procurement and production line operations for the selected candidate structural elements. Essentially, the applicable NDE techniques determine that raw materials conform to Engineering requirements and that reliable data are provided with respect to the size, location, and character of the flaw type induced during a particular fabrication operation, including forming, machining, and thermal processing. The raw material product forms, such as forging plate, tubing, and extrusions, considered for reference structural elements fabrication, are without limitations all 100-percent inspectable items by appropriate NDE methods. However, after significant machining, forming, welding, diffusion bonding, adhesive bonding, brazing, or mechanical fastening, the changes in material geometry and surface condition may reduce the sensitivity of the nondestructive evaluation techniques. NDE flaw detection capabilities are further reduced or limited after the structural assembly is completed and the vehicle structure is in-service. Therefore, the following five phases are considered for application of nondestructive inspections:

1. Raw material inspection
2. Inspection on a finished part
3. Inspection after assembly
4. Inspection after proof test (when applicable)
5. In-service inspection

First, the configurations of flaws or cracks commonly found in structural components are considered. These flaw geometries are those shown in Figure 2-13. They are identified by an assigned number, e. g., a Type 4 crack corresponds to a crack from a fastener hole through the thickness. Then, the most probable types of flaws or cracks that might be

present in a given structural element are considered, e. g. , an integrally stiffened skin (thin sheet) might have cracks at the root of the integral stiffener (types 7 and 8), cracks at the edge of a fastener hole (types 4 and 5), and cracks on the sheet (types 1 and 2). The most appropriate NDE method (or methods) for detecting these kinds of cracks are determined. Tables 2-3 to 2-11 are listings of the selected structural elements, the probable crack geometries in each part, and the crack detection techniques applicable to these local geometries, material, and product form. The NDE methods are determined separately for each phase of inspection.




The flaw size detectabilities for each type of the NDE techniques are listed in Table 2-12. The values given in Table 2-12 for radiographic, penetrant, ultrasonic, and eddy current techniques were developed under two study contracts (NAS9-12276 and NAS9-12326, Report SD 73-SH-0219). Data analysis emphasized the statistical approach and the specific flaw parameters, such as lengths, depth, or area, characterized by each particular NDE technique. The probability of detection was expressed as 90 percent probability of detection with 95 percent confidence level. These values are considered most appropriate for the fabrication phases of inspection. "Fabrication" refers to the finished part and, to some extent, the assembled part, depending on the complexity of the structural configuration. Data relevant to NDE sensitivities in other phases of inspection are not available at this time; this is a continuing effort of the Space Division Quality Assurance organization.


Accessibility for in-service inspection is dependent upon the thorough review of prospective design to include provisions for making necessary nondestructive inspection of selected structural elements. Information pertaining to structural access was obtained by the review of drawing VL72-000071A, Shuttle-Maintenance Access and Penetrations—Baseline (MCR 0200, Revision 1, dated 16 May 1973), which disclosed that doors, panels, hatches, and void open apertures generally provide some exposure of the reference structural elements. The accesses for inspection of the selected structural elements are identified from these drawings (Figures 1.10.1 to 1.10.5 in Volume III) and also are listed in Tables 2-3 to 2-11.

Table 2-3. Orbiter Reusable Tankage Structural Elements and Applicable NDE Methods

I. D. No.	Raw Material Inspection	Applicable NDE Methods/Minimum Flaw Size Detectability/Phase					Access		
		Type of Flaw	Finished Part	After Assembly	Post-Proof	In-Service	Zone	Number	Type
438	NA	2C, 2R	P ₁	NA	P ₁	P ₁	Accessible, removable		
439		2C(W)	X ₂		X ₂	X ₂			
440		1C, 1R	P ₁		P ₁	P ₁			
441		1C(W)	X ₂		X ₂	X ₂			
205		3R, 5R, 4R	E ₅		E ₅	u ₅ , E ₆			
579									
204	NA	2C, 2L	P ₁		P ₁	P ₁			
570		2C(W), 2L(W)	X ₂		X ₂	X ₂			
572		1C, 1L	P ₁		P ₁	P ₁			
578		1C(W) 1L(W)	X ₂		X ₂	X ₂			
		3R, 5R, 4R	E ₅		E ₅	u ₅ , E ₆			
544	u	2C, 2R	P ₁		P ₁	P ₁			
569		2C(W)	X ₂		X ₂	X ₂			
		1C, 1R	NA		P ₁	P ₁			
		1C(W)	NA		X ₂	X ₂			
		3R, 5R	E ₅		E ₅	u ₅ , E ₆			
ABES tanks	u	2C, 2L	P ₁	NA	P ₁	P ₁	Accessible, removable		
		2C(W), 2L(W)	X ₂		X ₂	X ₂			
		1C, 1L	NA		P ₁	P ₁			
		1C(W), 1L(W)	NA		X ₂	X ₂			
		3R, 5R	E ₅		E ₅	u ₅ , E ₆			

Table 2-3. Orbiter Reusable Tankage Structural Elements and Applicable NDE Methods (Cont)

I. D. No.	Raw Material Inspection	Applicable NDE Methods/Minimum Flaw Size Detectability/Phase					Access		
		Type of Flaw	Finished Part	After Assembly	Post-Proof	In-Service	Zone	Number	Type
413	NA	2C, 2R	P ₁	NA	P ₁	P ₁	Accessible, removable		
414		2C(W)	X ₂		X ₂	X ₂			
415		1C, 1R	P ₁		P ₁	P ₁			
416		1C(W)	X ₂		X ₂	X ₂			
Metal		3R, 4R, 5R	E ₅		E ₅	u ₅ , E ₆			
413	NA	2C, 2R	u ₁	NA	u ₁	u ₁	Accessible, removable		
414		2C, 2R	u ₁		u ₁	u ₁			
415		1C, 1R	u ₁		u ₁	u ₁			
416		3R, 4R, 5R	E ₅ 		E ₅ 	u ₅ , E ₆ 			
Glass epoxy									

 Eddy current evaluation of metallic bosses.

LEGEND

A. Flaw Geometry

Arabic numbers correspond to type of flaw illustrated in Figure 2-13.

Alphabet refers to orientation of the crack as related to overall geometry of the component:

- C = Circumferential
- R = Radial
- T = Transverse
- L = Longitudinal
- W = Crack at the weld

B. NDE Methods

- P = Penetrant
- X = X-ray
- E = Eddy current
- u = Ultrasonic
- m = Magnetic particle

C. NDE Subscript

- 1 = 100 percent
- 2 = Class 1 welds
- 3 = Class 2 welds
- 4 = Fracture critical area
- 5 = Critical fastener holes
- 6 = Critical fastener holes (if fastener can be removed)
- 7 = Diffusion bonds
- 8 = Boron-epoxy bond, 100 percent
- 9 = Boron-epoxy bond, sample

Table 2-4. Solid Rocket Booster Structural Elements and Applicable NDE Methods

I. D. No.	Raw Material Inspection	Applicable NDE Methods/Minimum Flaw Size Detectability/Phase					Access		
		Type of Flaw	Finished Part	After Assembly	Post-Proof	In-Service \triangle	Zone	Number	Type
2-3	NA	1L, 1C	P ₁	NA	NA	u ₄	Outside, open access		
		2L, 2C	P ₁	NA	NA	u ₄			
		4R, 5R	P ₁ , E ₅	NA	NA	u ₅ , E ₆			
2-4	u,m	2T, 2L	m ₁	NA	NA	m ₁			
		3R, 5R	m ₁	NA	NA	m ₁			
2-5	u,m	2L, 2C	m ₁	NA	NA	m ₁			
		5R, 3R	m ₁	NA	NA	m ₁			
		1L, 1C	NA	NA	NA	m ₁			
2-6	u	1L, 1C	NA	NA	NA	m ₁			
		2L(W)	m ₁ , X ₂	NA	NA	m ₁ , X ₂			
		5R	m ₁	NA	NA	m ₁			
		2L, 2C	m ₁	NA	NA	m ₁			
2-7	u,m	3R, 5R	m ₁	NA	NA	m ₁			
2-8	u,m	2L,2C	m ₁	NA	NA	m ₁			
		5R, 3R	m ₁	NA	NA	m ₁			
		1L, 1C	NA	NA	NA	m ₁			
\triangle Reuse cycle									

Table 2-4. Solid Rocket Booster Structural Elements and Applicable NDE Methods (Cont)

LEGEND		
A. Flaw Geometry	B. NDE Methods	C. NDE Subscript
Arabic numbers correspond to type of flaw illustrated in Figure 2-13.	P = Penetrant	1 = 100 percent
Alphabet refers to orientation of the crack as related to overall geometry of the component:	X = X-ray	2 = Class 1 welds
C = Circumferential	E = Eddy current	3 = Class 2 welds
R = Radial	u = Ultrasonic	4 = Fracture critical area
T = Transverse	m = Magnetic particle	5 = Critical fastener holes
L = Longitudinal		6 = Critical fastener holes (if fastener can be removed)
W = Crack at the weld		7 = Diffusion bonds
		8 = Boron-epoxy bond, 100 percent
		9 = Boron-epoxy bond, sample

Table 2-5. External Tank Structural Elements and Applicable NDE Methods

I. D. No.	Raw Material Inspection	Applicable NDE Methods/Minimum Flaw Size Detectability/Phase					Access		
		Type of Flaw	Finished Part	After Assembly	Post-Proof	In-Service	Zone	Number	Type
3-1	NA	2L, 2C 1C, 1C 2L(W) 4R, 5R	P ₁ P ₁ X ₂ E ₅	NA	P ₁ P ₁ X ₂ E ₅	NA		NA	
3-2	NA	2L, 2C 1L, 1C 2L(W)	P ₁ P ₁ X ₂		P ₁ P ₁ X ₂				
3-3	u	2L, 2C 1L, 1C 2C(W), 2L(W) 4R, 5R 8L 1C(W), 1L(W)	P ₁ P ₁ X ₂ E ₅ P ₁ X ₂		P ₁ P ₁ X ₂ E ₅ P ₁ X ₂				
3-4	NA	2C, 2R 1C, 1R 1C(W), 1R(W) 2C(W), 2R(W)	P ₁ P ₁ X ₂ X ₂		P ₁ P ₁ X ₂ X ₂				
3-5	NA	2C(W) 1C(W) 8L	X ₂ X ₂ P ₁	NA	X ₂ X ₂ P ₁	NA		NA	

Table 2-5. External Tank Structural Elements and Applicable NDE Methods (Cont)

I. D. No.	Raw Material Inspection	Applicable NDE Methods/Minimum Flaw Size Detectability/Phase					Access		
		Type of Flaw	Finished Part	After Assembly	Post-Proof	In-Service	Zone	Number	Type
3-6	NA	2C(W),2L(W)	X ₂	NA ↑	X ₂	NA ↑			NA ↑
		1C(W),1L(W)	X ₂		X ₂				
		2C, 2L	P ₁		P ₁				
		1C, 1L	P ₁		P ₁				
		8L	P ₁		P ₁				
		4R, 5R	E ₅		E ₅				
3-8	u	2T	P ₁		P ₁				
		1T	P ₁		P ₁				
		8L	P ₁		P ₁				
		4R, 5R	E ₅		E ₅				
3-9	u	1T	P ₁		P ₁				
		2T	P ₁		P ₁				
		8L	P ₁		P ₁				
		5R	E ₅		E ₅				
3-10	NA	2C, 2R	P ₁	NA ↓	P ₁	NA ↓		NA ↓	
		1C, 1R	P ₁		P ₁				
		1C(W),1R(W)	X ₂		X ₂				
		2C(W),2R(W)	X ₂		X ₂				

Table 2-5. External Tank Structural Elements and Applicable NDE Methods (Cont)

I. D. No.	Raw Material Inspection	Applicable NDE Methods/Minimum Flow Size Detectability/Phase					Access		
		Type of Flaw	Finished Part	After Assembly	Post-Proof	In-Service	Zone	Number	Type
3-11	NA	2L, 2C 1L, 1C 2C(W) 1C(W) 4R, 5R 8L	P ₁ P ₁ X ₂ X ₂ E ₅ P ₁	NA ↑	P ₁ P ₁ X ₂ X ₂ E ₅ P ₁	NA ↑		NA ↑	
3-12	u	2C, 2L 2C(W), 2L(W)	P ₁ X ₂		P ₁ X ₂				
3-14	NA	2C, 2R 1L, 1R 2C(W), 2R(W) 1C(W), 1R(W)	P ₁ P ₁ X ₂ X ₂		P ₁ P ₁ X ₂ X ₂				
3-15	u	3R, 5R	P ₁ , E ₅		P ₁ , E ₅				
3-16	u	2L, 2C 1L, 1C 2C(W) 1C(W) 4R, 5R 8L	P ₁ P ₁ X ₂ X ₂ E ₅ P ₁	NA ↓	P ₁ P ₁ X ₂ X ₂ E ₅ P ₁	NA ↓		NA ↓	

Table 2-5. External Tank Structural Elements and Applicable NDE Methods (Cont)

LEGEND		
A. Flaw Geometry	B. NDE Methods	C. NDE Subscript
Arabic numbers correspond to type of flaw illustrated in Figure 2-13.	P = Penetrant	1 = 100 percent
Alphabet refers to orientation of the crack as related to overall geometry of the component:	X = X-ray	2 = Class 1 welds
C = Circumferential	E = Eddy current	3 = Class 2 welds
R = Radial	u = Ultrasonic	4 = Fracture critical area
T = Transverse	m = Magnetic particle	5 = Critical fastener holes
L = Longitudinal		6 = Critical fastener holes (if fastener can be removed)
W = Crack at the weld		7 = Diffusion bonds
		8 = Boron-epoxy bond, 100 percent
		9 = Boron-epoxy bond, sample

Table 2-6. Mid Fuselage Structural Elements and Applicable NDE Methods



I. D. No.	Raw Material Inspection	Applicable NDE Methods/Minimum Flaw Size Detectability/Phase					Access 		
		Type of Flaw	Finished Part	After Assembly	Post-Proof	In-Service	Zone	Number	Type
4-3	NA	7T	P ₁	NA	NA	u ₄	4	42-1,2,3,4	Door
		8L	P ₁			u ₄		43-1,2,3,4	Door
		4R,5R	E ₅			u ₅ ,E ₆			
		1L,1T	P ₁			u ₄			
		2L,2T	P ₁			u ₄			
4-4	NA	7T	P ₁			u ₄	4	44,45	Door
		8L	P ₁			u ₄		50-3	Door
		4R,5R	E ₅			u ₅ ,E ₆		44-6	Void opening
		1L,1T	P ₁			u ₄			
		2L,2T	P ₁			u ₄			
4-5	u	7T	P ₁			u ₄	4	47-1,2	Panel
		8L	P ₁			u ₄		47-7	Void opening
		4R,5R,6R	E ₅			u ₅ ,E ₆			
		1L,1T	NA			u ₄			
		2L,2T	P ₁			u ₄			
4-8	NA	7T	P ₁			u ₄	4	48-0,9	Void opening
		8L	P ₁			u ₄			
		4R,5R	E ₅			u ₅ ,E ₆			
4-9	u	7T	P ₁	NA	NA	u ₄	4	48-0,9	Void opening
		8L	P ₁			u ₄			
		4R,5R	E ₅			u ₅ ,E ₆			

Table 2-6. Mid Fuselage Structural Elements and Applicable NDE Methods (Cont)

I. D. No.	Raw Material Inspection	Applicable NDE Methods/Minimum Flaw Size Detectability/Phase					Access 		
		Type of Flaw	Finished Part	After Assembly	Post-Proof	In-Service	Zone	Number	Type
4-10	u	7T	P ₁	NA ↑	NA ↑	u ₄	4	48-0,9	Void opening
		8L	P ₁			u ₄			
		4R,5R,6R	E ₅			u ₅ ,E ₆			
		2L,2T	P ₁			u ₄			
4-15	u	7T	P ₁			u ₄	4	48-0,9	Void opening
		8L	P ₁			u ₄			
		3R,5R,6R	E ₅			u ₅ ,E ₆			
4-18	u	7T	P ₁			u ₄	4	46-1,2	Panel
		8L	P ₁			u ₄	6	63-1,2	Panel
		3R,5R,6R	E ₅			u ₅ ,E ₆			
		2L,2T	P ₁			u ₄			
4-23	NA	7T	P ₁	NA ↓	NA ↓	u ₄	4	42-1,2,3,4	Door
		8L	P ₁			u ₄			
		4R,5R	E ₅			u ₅ ,E ₆			


 Figures 1.10.1 to 1.10.5 in Vol. III

Table 2-6. Mid Fuselage Structural Elements and Applicable
NDE Methods (Cont)

LEGEND		
A. Flaw Geometry	B. NDE Methods	C. NDE Subscript
Arabic numbers correspond to type of flaw illustrated in Figure 2-13.	P = Penetrant	1 = 100 percent
Alphabet refers to orientation of the crack as related to overall geometry of the component:	X = X-ray	2 = Class 1 welds
	E = Eddy current	3 = Class 2 welds
	u = Ultrasonic	4 = Fracture critical area
	m = Magnetic particle	5 = Critical fastener holes
C = Circumferential		6 = Critical fastener holes (if fastener can be removed)
R = Radial		7 = Diffusion bonds
T = Transverse		8 = Boron-epoxy bond, 100 percent
L = Longitudinal		9 = Boron-epoxy bond, sample
W = Crack at the weld		

Table 2-7. Wing Structural Elements and Applicable NDE Methods

I. D. No.	Raw Material Inspection	Applicable NDE Methods/Minimum Flaw Size Detectability/Phase					Access \triangle		
		Type of Flaw	Finished Part	After Assembly	Post-Proof	In-Service	Zone	Number	Type
5-1	NA	4R, 5R 1L, 1T 2L, 2T	P ₁ , E ₅ P ₁ P ₁	NA ↑	NA ↑	u ₅ , E ₆ u ₄ u ₄	6	62-1,2 63-1,2 64-9 to 15 66-1 to 4	Door Panel Panel Panel
5-10	NA	4R, 5R 7T 8L	P ₁ , E ₅ P ₁ P ₁			u ₅ , E ₆ u ₄ u ₄	6	60-1 60-1	Panel Panel
5-12	u	3R, 5R, 6R	P ₁ , E ₅			u ₅ , E ₆	4 6	47-1,2 63-1,2	Panel Panel
5-13	u	3R, 5R, 6R	P ₁ , E ₅			u ₅ , E ₆	6	60-2 61-2	Panel Panel
5-14	u	3R, 5R, 6R	P ₁ , E ₅			u ₅ , E ₆	6	60-3 61-3	Panel Panel
5-15	NA	1L, 1T *	u ₁ X ₁ , u ₁	NA ↓	NA ↓	u ₄ u ₄ , X ₄	6	60-1 61-1	Panel Panel

\triangle Figures 1.10.1 to 1.10.5 in Vol. III.

*Other flaws considered are:

- (1) Facesheet buckling
- (2) Detached core - voids, fillet failure
- (3) Core node separation
- (4) Crushed core
- (5) Core cracking


Table 2-7. Wing Structural Elements and Applicable NDE Methods (Cont)

LEGEND		
A. Flaw Geometry	B. NDE Methods	C. NDE Subscript
Arabic numbers correspond to type of flaw illustrated in Figure 2-13.	P = Penetrant	1 = 100 percent
Alphabet refers to orientation of the crack as related to overall geometry of the component:	X = X-ray	2 = Class 1 welds
	E = Eddy current	3 = Class 2 welds
	u = Ultrasonic	4 = Fracture critical area
	m = Magnetic particle	5 = Critical fastener holes
C = Circumferential		6 = Critical fastener holes (if fastener can be removed)
R = Radial		7 = Diffusion bonds
T = Transverse		8 = Boron-epoxy bond, 100 percent
L = Longitudinal		9 = Boron-epoxy bond, sample
W = Crack at the weld		

Table 2-8. Crew Cabin and Forward Fuselage Structural Elements and Applicable NDE Methods

I. D. No.	Raw Material Inspection	Applicable NDE Methods/Minimum Flaw Size Detectability/Phase					Access \triangle		
		Type of Flaw	Finished Part	After Assembly	Post-Proof	In-Service	Zone	Number	Type
6-1	NA	2L,2T	P ₁	NA	P ₁	u ₄	2	22,23	Door
		2L(W),2T(W)	P ₁ ,X ₂		P ₁ ,X ₂	u ₄ ,X ₂	4	42-1	Door
		1L,1T	P ₁		P ₁	u ₄			
		1L(W),1T(W)	P ₁ ,X ₂		P ₁ ,X ₂	u ₄ ,X ₂			
6-2	u	4R,5R	P ₁ ,E ₅		NA	u ₅ ,E ₆	2	24	Hatch
							3	30	Void opening
6-3	NA	2L,2T	P ₁		P ₁	u ₄	1	14	Hatch
		7T	P ₁		P ₁	u ₄	3	30	Void opening
		8L	P ₁		P ₁	u ₄			
		1L,1T	P ₁		P ₁	u ₄			
		1L(W),1T(W)	P ₁ ,X ₂		P ₁ ,X ₂	u ₄ ,X ₂			
		2L(W),2T(W)	P ₁ ,X ₂		P ₁ ,X ₂	u ₄ ,X ₂			
		4R,5R	P ₁ ,E ₅		NA	u ₅ ,E ₆			
6-6	u	4R,5R	P ₁ ,E ₅		NA	u ₅ ,E ₆	1	15	Panel
							2	25	Panel
6-7	u	1L,1T	P ₁	NA	P ₁	u ₄	1	14	Hatch
		1L(W),1T(W)	P ₁ ,X ₂		P ₁ ,X ₂	u ₄ ,X ₂	1	24	Hatch
		2L,2T	P ₁		P ₁	u ₄			
		2L(W),2T(W)	P ₁ ,X ₂		P ₁ ,X ₂	u ₄ ,X ₂			

Table 2-8. Crew Cabin and Forward Fuselage Structural Elements and Applicable NDE Methods (Cont)

I. D. No.	Raw Material Inspection	Applicable NDE Methods/Minimum Flaw Size Detectability/Phase					Access 		
		Type of Flaw	Finished Part	After Assembly	Post-Proof	In-Service	Zone	Number	Type
6-8	NA	1L,1T	P ₁	NA	P ₁	u ₄	4	42-1	Door
		1L(W),1T(W)	P ₁ ,X ₂		P ₁ ,X ₂	u ₄ ,X ₂			
		2L,2T	P ₁		P ₁	u ₄			
		2L(W),2T(W)	P ₁ ,X ₂		P ₁ ,X ₂	u ₄ ,X ₂			
6-9	NA	4R,5R	P ₁ ,E ₅		NA	u ₅ ,E ₆	1	14	Hatch
		1L,1T	P ₁			u ₄	2	24	Hatch
							3	30	Void opening
6-13	u	2L,2T	P ₁			u ₄	1	14	Hatch
		8L	P ₁			u ₄	2	24	Hatch
		7T	P ₁			u ₄	3	30	Void opening
		4R,5R	P ₁ ,E ₅			u ₅ ,E ₆			
6-15	u	3R,4R,5R	P ₁ ,E ₅			u ₅ ,E ₆	1	14	Hatch
							2	24	Hatch
							3	30	Void opening
6-16	u	3R,4R,5R	P ₁ ,E ₅			u ₅ ,E ₆	1	14	Hatch
							2	24	Hatch
							3	30	Void opening
6-17	u	3R,4R,5R	P ₁ ,E ₅	NA	NA	u ₅ ,E ₆	1	14	Hatch
							2	24	Hatch
							3	30	Void opening


 Figures 1.10.1 to 1.10.5 in Vol. III

Table 2-8. Crew Cabin and Forward Fuselage Structural Elements and
Applicable NDE Methods (Cont)

LEGEND		
A. Flaw Geometry	B. NDE Methods	C. NDE Subscript
Arabic numbers correspond to type of flaw illustrated in Figure 2-13.	P = Penetrant	1 = 100 percent
Alphabet refers to orientation of the crack as related to overall geometry of the component:	X = X-ray	2 = Class 1 welds
	E = Eddy current	3 = Class 2 welds
	u = Ultrasonic	4 = Fracture critical area
	m = Magnetic particle	5 = Critical fastener holes
C = Circumferential		6 = Critical fastener holes (if fastener can be removed)
R = Radial		7 = Diffusion bonds
T = Transverse		8 = Boron-epoxy bond, 100 percent
L = Longitudinal		9 = Boron-epoxy bond, sample
W = Crack at the weld		

Table 2-9. Aft Fuselage Structural Elements and Applicable NDE Methods

I. D. No.	Raw Material Inspection	Applicable NDE Methods/Minimum Flaw Size Detectability/Phase					Access Δ		
		Type of Flaw	Finished Part	After Assembly	Post-Proof	In-Service	Zone	Number	Type
7-1	u	1L, 1T 2L, 2T 7T, 8L	P ₁ P ₁ P ₁	NA ↑	NA ↑	u ₄ u ₄ u ₄	5	50-1,2,4	Door
7-2	u	2L, 2T 7T, 8L	P ₁ P ₁			u ₄ u ₄	5	50-1,2	Door
7-3	u	2L, 2T 7T, 8L	P ₁ P ₁			u ₄ u ₄	5	54, 55 56-1,2	Door Panel
7-4	NA	2L, 2T 7T, 8L	P ₁ P ₁			u ₄ u ₄	5	54,55,57	Door
7-5	u	1L, 1T 2L, 2T 7T, 8L	P ₁ P ₁ P ₁			u ₄ u ₄ u ₄	5	50-1,2	Door
7-6	u	1L, 1T 2L, 2T 7T, 8L	P ₁ P ₁ P ₁			u ₄ u ₄ u ₄	5	50-1,2	Door
7-9	NA	1L, 1T 4R	u ₁ E ₅			u ₄ E ₆	5	57	Door
7-10	u	2L, 2T 7T, 8L 5R	P ₁ P ₁ E ₅	NA ↓	NA ↓	u ₄ u ₄ E ₆	5	50-1,2	Door

Table 2-9. Aft Fuselage Structural Elements and Applicable NDE Methods (Cont)

I. D. No.	Raw Material Inspection	Applicable NDE Methods/Minimum Flaw Size Detectability/Phase					Access \triangle		
		Type of Flaw	Finished Part	After Assembly	Post-Proof	In-Service	Zone	Number	Type
7-11	u	2L, 2T 7T, 8L 5R	P ₁ P ₁ E ₅	NA ↑	NA ↑	u ₄ u ₄ E ₆	5	50-1,2	Door
7-13	u	3R	P ₁			u ₄	5	50-1,2 54, 55	Door Door
7-14	u	2L, 2T 5R 7T, 8L	P ₁ E ₅ P ₁			u ₄ E ₆ u ₄	5	50-1,2 54, 55	Door Door
7-15	u	1L, 1T 2L, 2T 7T, 8L	P ₁ , u _{7,8} P ₁ , u _{7,8} P ₁ , u _{7,8}			u _{4,9} u _{4,9} u _{4,9}	5	50-1,2 54,55	Door Door
7-16	u	3R 5R 7T, 8L	P ₁ E ₅ P ₁			u ₄ E ₆ u ₄	5	50-1,2 54, 55	Door Door
7-17	NA	1L, 1T 2L, 2T 4R 5R	P ₁ P ₁ E ₅ E ₅	NA ↓	NA ↓	u ₄ u ₄ E ₆ E ₆	5	50-1,2 54, 55	Door Door

Table 2-9. Aft Fuselage Structural Elements and Applicable NDE Methods (Cont)

I. D. No.	Raw Material Inspection	Applicable NDE Methods/Minimum Flaw Size Detectability/Phase					Access \triangle		
		Type of Flaw	Finished Part	After Assembly	Post-Proof	In-Service	Zone	Number	Type
7-18	u	4R	E ₅	NA ↑	NA ↑	E ₆	5	50-1,2	Door
		5R	E ₅			E ₆		54, 55	Door
		7T, 8L	P ₁			u ₄			
7-19	u	3R	P ₁	NA ↓	NA ↓	u ₄	5	57	Door
		6R	E ₅			E ₆			
		7T, 8L	P ₁			u ₄			

\triangle Figures 1.10.1 to 1.10.5 in Vol. III

LEGEND

A. Flaw Geometry

Arabic numbers correspond to type of flaw illustrated in Figure 2-13.

Alphabet refers to orientation of the crack as related to overall geometry of the component:

- C = Circumferential
- R = Radial
- T = Transverse
- L = Longitudinal
- W = Crack at the weld

B. NDE Methods

- P = Penetrant
- X = X-ray
- E = Eddy current
- u = Ultrasonic
- m = Magnetic particle

C. NDE Subscript

- 1 = 100 percent
- 2 = Class 1 welds
- 3 = Class 2 welds
- 4 = Fracture critical area
- 5 = Critical fastener holes
- 6 = Critical fastener holes (if fastener can be removed)
- 7 = Diffusion bonds
- 8 = Boron-epoxy bond, 100 percent
- 9 = Boron-epoxy bond, sample

Table 2-10. Vertical Stabilizer and Rudder Structural Elements and Applicable NDE Methods

I. D. No.	Raw Material Inspection	Applicable NDE Methods/Minimum Flaw Size Detectability/Phase					Access Δ		
		Type of Flaw	Finished Part	After Assembly	Post-Proof	In-Service	Zone	Number	Type
8-1	NA	2L, 2T	P ₁	NA	NA	u ₄	6	70, 71	Panel
		4R, 5R	P ₁ , E ₅			u ₅ , E ₆	7	73-1,2,3	Door
		1L, 1T	P ₁			u ₄	7	76	Void opening
8-5	P	4R, 5R	P ₁ , E ₅			u ₅ , E ₆	6	70, 71	Panel
		7T	P ₁			u ₄			
		8L	P ₁			u ₄			
8-7	u	3R, 4R, 5R, 6R	P ₁ , E ₅			u _{4,5} , E ₆	6	71	Panel
8-8	u	2L, 2T	P ₁			u ₄	6	71	Panel
		1L, 1T	NA			u ₄			
		4R, 5R	P ₁ , E ₅			u ₅ , E ₆			
8-10	u	2L, 2T	P ₁			u ₄	7	73-1,2,3	Door
		1L, 1T	P ₁			u ₄			
		4R, 5R	P ₁ , E ₅			u ₅ , E ₆			
8-11	NA	1L, 1T	u ₁	NA	NA	u ₄	6	70, 71	Panel
		4R, 5R	u ₁ , E ₅			u ₅ , E ₆			
		Honeycomb	u ₁			X _{4,5}			

Table 2-10. Vertical Stabilizer and Rudder Structural Elements and Applicable NDE Methods (Cont)

I.D. No.	Raw Material Inspection	Applicable NDE Methods/Minimum Flaw Size Detectability/Phase					Access \triangle		
		Type of Flaw	Finished Part	After Assembly	Post-Proof	In-Service	Zone	Number	Type
8-12	NA	4R, 5R	P ₁ , E ₅	NA	NA	u ₅ , E ₆	6	70	Panel
		8L	P ₁			u ₄			
		7T	P ₁			u ₄			
8-13	NA	4R, 5R	P ₁ , E ₅			u ₅ , E ₆	6	70, 71	Panel
		8L	P ₁			u ₄			
		7T	P ₁			u ₄			
8-14	NA	4R, 5R	P ₁ , E ₅	NA	NA	u ₅ , E ₆	6	70, 71	Panel
		8L	P ₁			u ₄			
		7T	P ₁			u ₄			

\triangle Figures 1.10.1 to 1.10.5 in Vol. III

LEGEND

A. Flaw Geometry

Arabic numbers correspond to type of flaw illustrated in Figure 2-13.

Alphabet refers to orientation of the crack as related to overall geometry of the component:

- C = Circumferential
- R = Radial
- T = Transverse
- L = Longitudinal
- W = Crack at the weld

B. NDE Methods

- P = Penetrant
- X = X-ray
- E = Eddy current
- u = Ultrasonic
- m = Magnetic particle

C. NDE Subscript

- 1 = 100 percent
- 2 = Class 1 welds
- 3 = Class 2 welds
- 4 = Fracture critical area
- 5 = Critical fastener holes
- 6 = Critical fastener holes (if fastener can be removed)
- 7 = Diffusion bonds
- 8 = Boron-epoxy bond, 100 percent
- 9 = Boron-epoxy bond, sample

Table 2-11. Main and Nose Landing Gears Structural Elements and Applicable NDE Methods

I. D. No.	Raw Material Inspection	Applicable NDE Methods/Minimum Flaw Size Detectability/Phase					Access		
		Type of Flaw	Finished Part	After Assembly	Post-Proof	In-Service Δ	Zone	Number	Type
9-1, 9-2 300M Tubing	u,m	2L,2C 2L(W),2C(W) 4R,5R 6R	m ₁ m ₁ ,X ₂ E ₅ E ₅	NA ↑	NA ↑	m ₄ m ₄ ,X ₄ m ₅ ,E ₆ m ₅ ,E ₆	Fully extended position ↑		
9-1, 9-2, 9-3, 9-5, 9-6, 9-7, 9-10, 300M Forging	u,m	8L 4R,5R,6R 7T 2L,2T	m ₁ E ₅ m ₁ m ₁			m ₄ m ₅ ,E ₆ m ₄ m ₄			
9-4, 9-9 300M Forging	u,m	2L,2C	m ₁			m ₄			
9-6 Al. Forging	u,P	8L 4R,5R 7T	P ₁ E ₅ P ₁	NA ↓	NA ↓	u ₄ u ₅ ,E ₆ u ₄	Fully extended position ↓		

Table 2-11. Main and Nose Landing Gears Structural Elements and Applicable NDE Methods (Cont)

I. D. No.	Raw Material Inspection	Applicable NDE Methods/Minimum Flaw Size Detectability/Phase					Access		
		Type of Flaw	Finished Part	After Assembly	Post-Proof	In-Service Δ	Zone	Number	Type
9-11, 9-12 300M Tubing	m,u	2L,2C 2L(W),2C(W) 4R,5R	m ₁ X ₂ ,m ₁ E ₅	NA ↑	NA ↑	m ₄ m ₄ ,X ₂ m ₅ ,E ₆	Fully extended position ↑		
9-11, 9-12, 9-16, 9-17, 9-19 300M Forging	m,u	2L,2T 8L 4R,5R 7T	m ₁ m ₁ E ₅ m ₁			m ₄ m ₄ m ₅ ,E ₆ m ₄			
9-13 9-14 9-15 300M Forging	m,u	8C 2L,2C 7T	m ₁ m ₁ m ₁	NA ↓	NA ↓	m ₄ m ₄ m ₄	Fully extended position ↓		

Table 2-11. Main and Nose Landing Gears Structural Elements and Applicable NDE Methods (Cont)

I. D. No.	Raw Material Inspection	Applicable NDE Methods/Minimum Flaw Size Detectability/Phase					Access		
		Type of Flaw	Finished Part	After Assembly	Post-Proof	In-Service Δ	Zone	Number	Type
9-18	m,u	8L	m ₁	NA	NA	m ₄	Fully extended position		
9-19		4R,5R	E ₅			m ₅ ,E ₆			
Al. Forging		7T	m ₁			m ₄			

Δ Use ultrasonic instead of magnetic particual if desired.

LEGEND

A. Flaw Geometry

Arabic numbers correspond to type of flow illustrated in Figure 2-13.

Alphabet refers to orientation of the crack as related to overall geometry of the component:

- C = Circumferential
- R = Radial
- T = Transverse
- L = Longitudinal
- W = Crack at the weld

B. NDE Methods

- P = Penetrant
- X = X-ray
- E = Eddy current
- u = Ultrasonic
- m = Magnetic particle

C. NDE Subscript

- 1 = 100 percent
- 2 = Class 1 welds
- 3 = Class 2 welds
- 4 = Fracture critical area
- 5 = Critical fastener holes
- 6 = Critical fastener holes (if fastener can be removed)
- 7 = Diffusion bonds
- 8 = Boron-epoxy bond, 100 percent
- 9 = Boron-epoxy bond, sample

Table 2-12. Crack Detection Capabilities

Technique	Expressed In	Detectable Size ^{△1}	
		Fabrication	In-Service
Radiography (X-ray)	Crack depth, percent of material thickness	70%	--
Penetrant	Crack area ^{△2}	0.0619 cm ² (0.0096 in. ²)	--
Ultrasonic	Crack area ^{△2}	0.0458 cm ² (0.0071 in. ²)	--
Eddy current	Crack depth	0.096 cm (0.038 in)	--
Magnetic particle	Crack length	0.190 cm (0.075 in.) ^{△3}	0.381 cm ^{△3} (0.15 in)
Visual	Crack length	0.635 cm (0.25 in.) ^{△3}	1.27 cm ^{△3} (0.5 in)
^{△1} 90-percent probability of detection with 95-percent reliability ^{△2} $0.1 \leq a/2c \leq 0.6$ ^{△3} B-1 NDT Demonstration Program (Air Force)			

3.0 FRACTURE CONTROL PROCEDURES

Fracture control methods have been classified and discussed under two general conceptual approaches:

1. Fatigue oriented (Sections 2.1 and 2.2).
2. Fracture mechanics oriented (Sections 2.3 and 2.4).

Since fatigue-oriented fracture control methods are relatively routine procedures in design and manufacture of aircraft and space vehicles, emphasis has been placed on the use of fracture mechanics analysis methodologies.

3.1 FRACTURE MECHANICS PROCEDURE

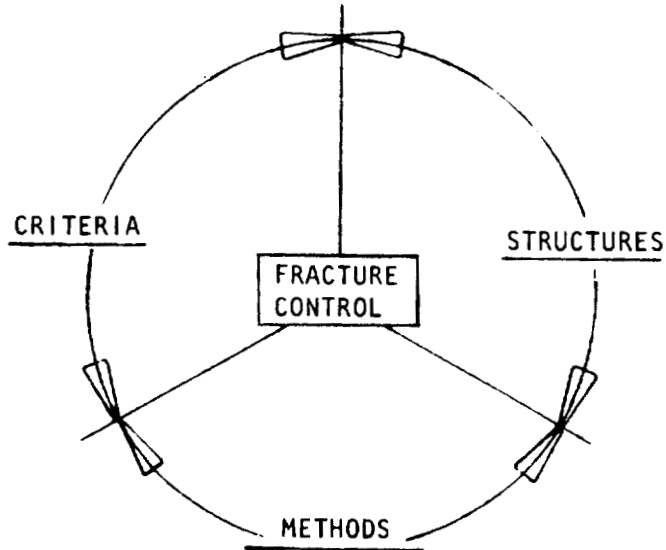
A fracture mechanics oriented fracture control procedure

1. Establishes design criteria suitable to the expected operational usage of the vehicle
2. Identifies structural elements and the expected loading conditions, magnitude, and environments
3. Develops a systematic means of identifying the criticality of these structural elements
4. Utilizes the best available fracture mechanics methodology to check the actual criticality of the questionable structural elements and to perform trade studies regarding safety and weight. (The fracture mechanics analysis also helps to establish reliable in-service inspection intervals.)

These objectives constitute an interaction circle as shown in Figure 3-1. This circle simply implies that there are three major areas in fracture control. Fracture control requires a knowledge of what kind of a structure is going to be built. At the same time, a criteria to establish a design goal is required. Furthermore, all the appropriate design, analysis, and manufacturing methods must be available.

Criteria are involved with overall system reliability and contractual requirements and are a management decision.

The current trend in development and design of a damage tolerant vehicle is to employ a safe-crack-growth approach. The structural requirement is described in terms of longevity. It is assumed that the structural element originally contains a certain flaw at a critical location (e. g., corner crack emanating from fastener hole, etc.). The assumed initial crack size usually relies on the known nondestructive-evaluation capability or the result of proof testing. Sometimes this crack size can be determined by gathering



• CRITERIA

- ULTIMATE STRENGTH
- FATIGUE
- SAFE-LIFE
- FAIL-SAFE

• STRUCTURE

- (A CRITICAL PART???)
- CONFIGURATION
- LOADING & ENVIRONMENT
- MATERIAL
- PROBABLE FLAW GEOMETRIES AND LOCATIONS

• METHODS

- FATIGUE
- DESIGN, M&P, AND MANUFACTURING
- FRACTURE MECHANICS
- NONDESTRUCTIVE EVALUATION

Figure 3-1. Fracture Control Functions

nondestructive-inspection data from periodic in-service inspections or inspection during full-scale testing. If none of these techniques are applicable, a reasonable initial crack size has to be selected.

In preliminary design (or sometimes, in redesign), it is often convenient to conduct a parametric analysis involving the design stress level and the allowable number of missions as a function of initial flaw size. A schematic example of this type of parametric investigation is given in Figure 3-2. Here the calculated allowable number of missions is plotted against the operating stress levels which are interpreted as fractions of the baseline design stress level. These parametric data can be converted into a display of structural weight increase as a function of initial flaw size or operating stress level for various service life requirements; this use is illustrated in Figure 3-3. A reference value for initial flaw size may be selected, based on expected detection capability; and the effect on structural weight of applying a safety factor either to the initial flaw size or on the required service life may be quickly determined.

A more thorough analysis, such as those presented in Reference 17, can be performed. In Reference 17, several criteria were selected. These criteria are the requirements of static strength, fatigue strength, durability, inspectability, and in-service inspection intervals. Several candidate design configurations and materials were studied. Each structural configuration and material combination was analyzed to check and determine if any one of the combinations would satisfy all the criteria. In case more than one of the designs satisfy the criteria, the structures will be further compared on the basis of weight and cost.

It has been proposed in Section 1.0 that the first logical step in exercising fracture control, by means of fracture mechanics, is to identify the potentially fracture-critical parts using a "selection logic" flow diagram. Fracture mechanics analysis would then be conducted on the potential fracture-critical parts to determine actual criticality of the part by checking the analysis results against the design criteria. At the same time, trade studies can be conducted on the same structural part to attain an optimized design.

It is realized that analytical results are sensitive to many input variables. The following are some of the most important ones:

1. Fracture mechanics methodology
2. Structural geometry
3. Crack geometry
4. Initial crack length

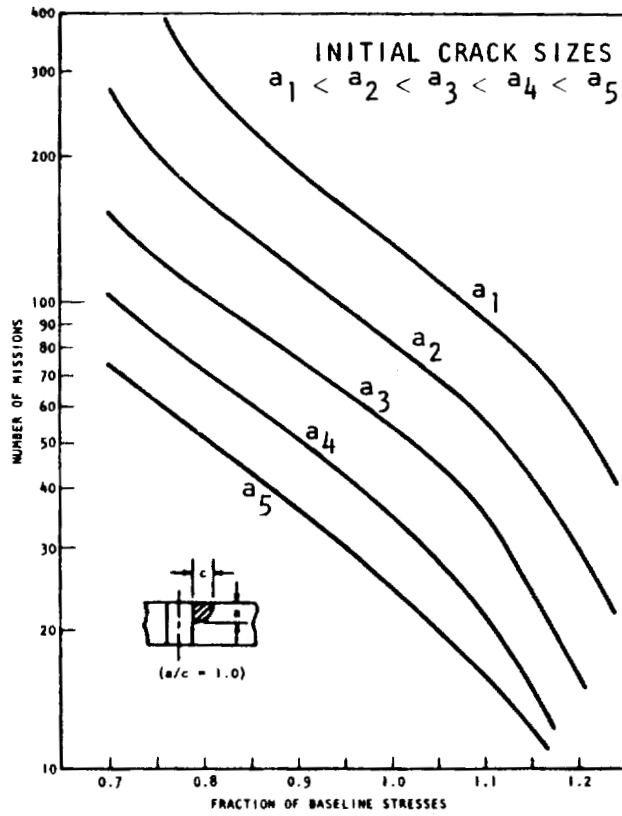


Figure 3-2. Missions to Failure as a Function of Applied Stress Levels and Crack Geometry (A Schematic Illustration)

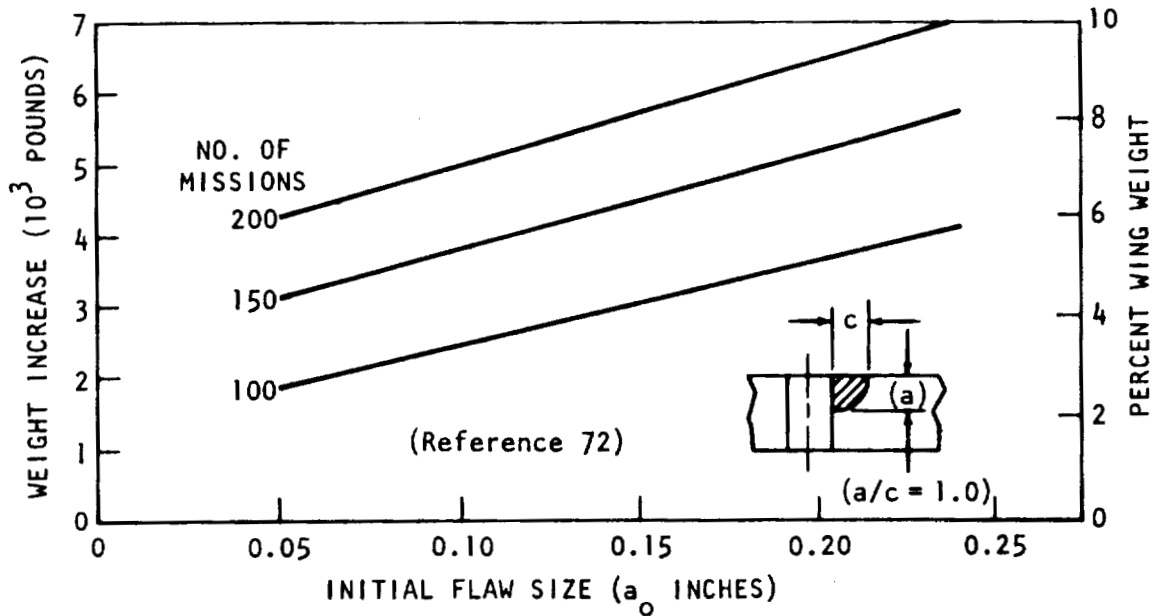


Figure 3-3. Effect of Initial Flaw Size on Wing Weight for Safe-Life (B-9U Booster)

5. Stress levels
6. Material properties

These variables interact with each other, and it is difficult to separately pinpoint the significance of the sensitivity attributed to each of the variables. However, the sensitivity of most of these variables lies in their effect on the stress intensity factor. For example, when the initial stress intensity factor in one case is below or slightly above the threshold value in the da/dN curve and the initial stress intensity factor in another case is relatively higher, the difference in calculated life will be substantial.

3.2 AN EXAMPLE PROBLEM

In the following paragraphs, an example is given to illustrate how a fracture mechanics analysis is conducted. The structural assembly under consideration is the crew compartment. To estimate the safe-crack-growth life for the crew compartment, one must first consider Figure 3-4 and determine the general structural arrangement at the location under consideration. The "selection logic" flow diagram (Figure 1-1) indicates that the cabin skin (Item 6-3 in Table 1-6) is a potential fracture-critical area. For this illustrative example, the cabin skin on the opposite side of the cutout (i. e., no cutout) is analyzed.

The kind of information necessary to conduct the analysis is the next consideration. These variables are discussed in the following paragraphs.

3.2.1 Design Stress Level, Material and Structural Dimensions

The primary stresses acting on the cabin skin are the hoop stress (pR/t , from the internal pressure) and the axial stress which is the $pR/2t$ stress combined with some axial stress coming from the flight load. The expected maximum difference in cabin pressure during an orbital flight, ΔP , is 0.11 MN/m^2 (16 psi) and the design limit stress is set at 213.7 MN/m^2 (31 ksi).

Two locations on the cabin skin will be considered. One location is near the front of the cabin, at X_{410} ; and the other is located close to the back of the cabin, at X_{542} . The radius of curvature at these two locations are 1.7 and 2.5 meters (70 and 100 inches), respectively. The required skin thicknesses at those two locations are $t_{410} = 0.091$ centimeter (0.0361 inch) and $t_{542} = 0.130$ centimeter (0.0515 inch), based on static strength and fatigue considerations.

The material is 2219-T851 aluminum alloy. The properties for this alloy are as follows:

$$F_{ty} = 317.15 \text{ MN/m}^2 \text{ (46 ksi)}$$

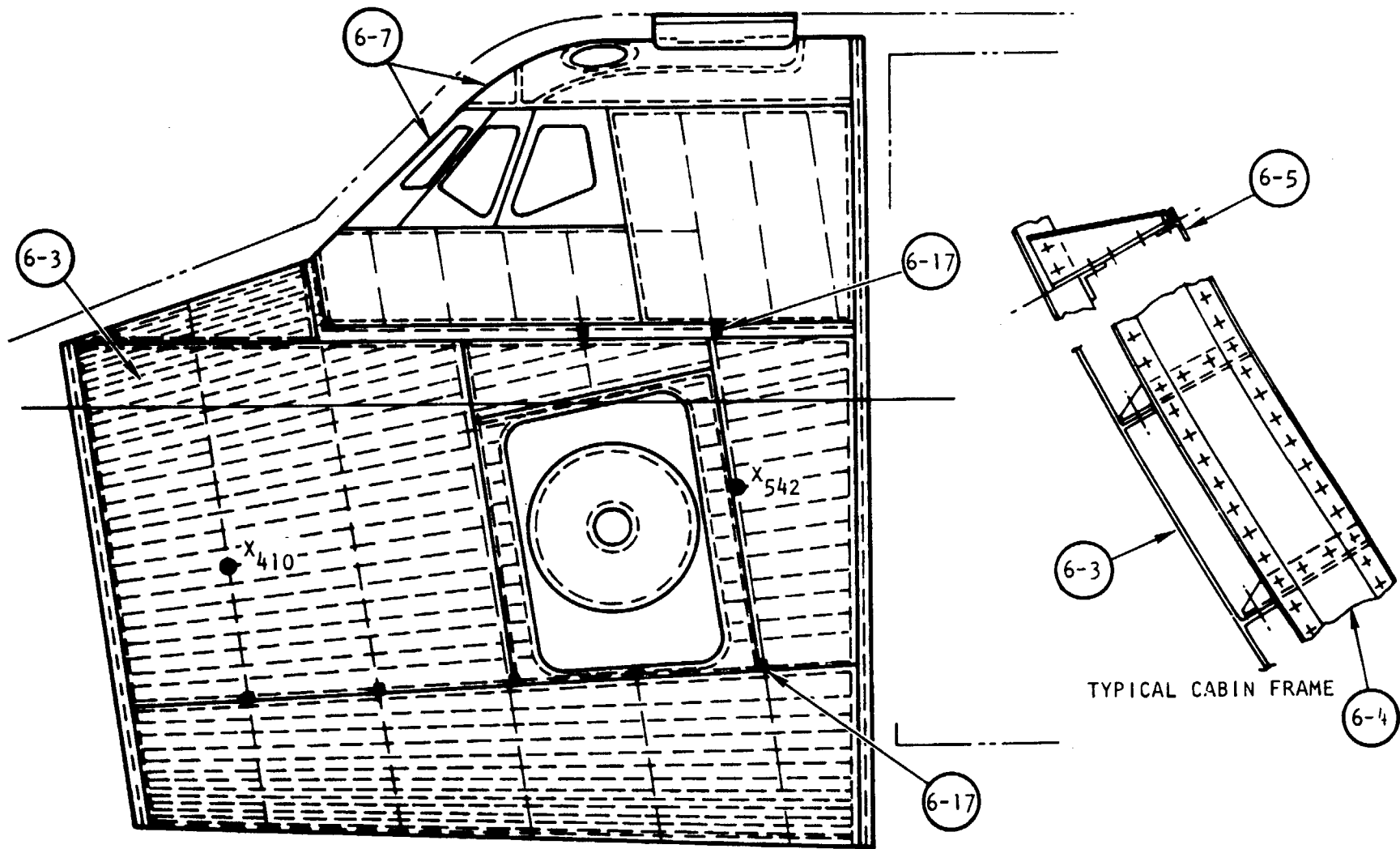


Figure 3-4. Crew Compartment Configuration

$$K_{IE} = 38.5 \text{ MN/m}^{3/2} (35 \text{ ksi} \sqrt{\text{inch}})$$

$$K_c = 68.1 \text{ MN/m}^{3/2} (62 \text{ ksi} \sqrt{\text{inch}})$$

Parameters in Collipriest's fatigue-crack-growth rate equation:

$$C = 27.6 \times 10^{-20}$$

$$n = 3.3$$

$$\Delta K_o = 3.85 \text{ MN/m}^{3/2} (3.5 \text{ ksi} \sqrt{\text{inch}})$$

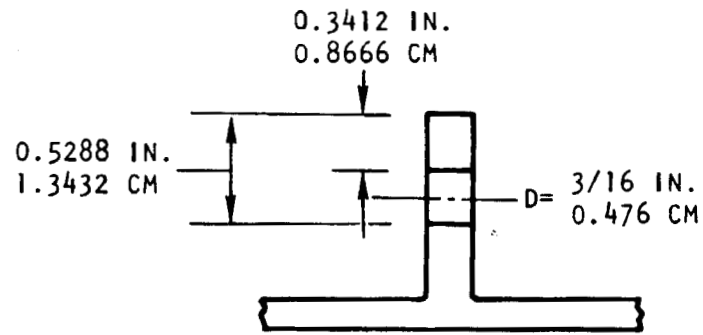
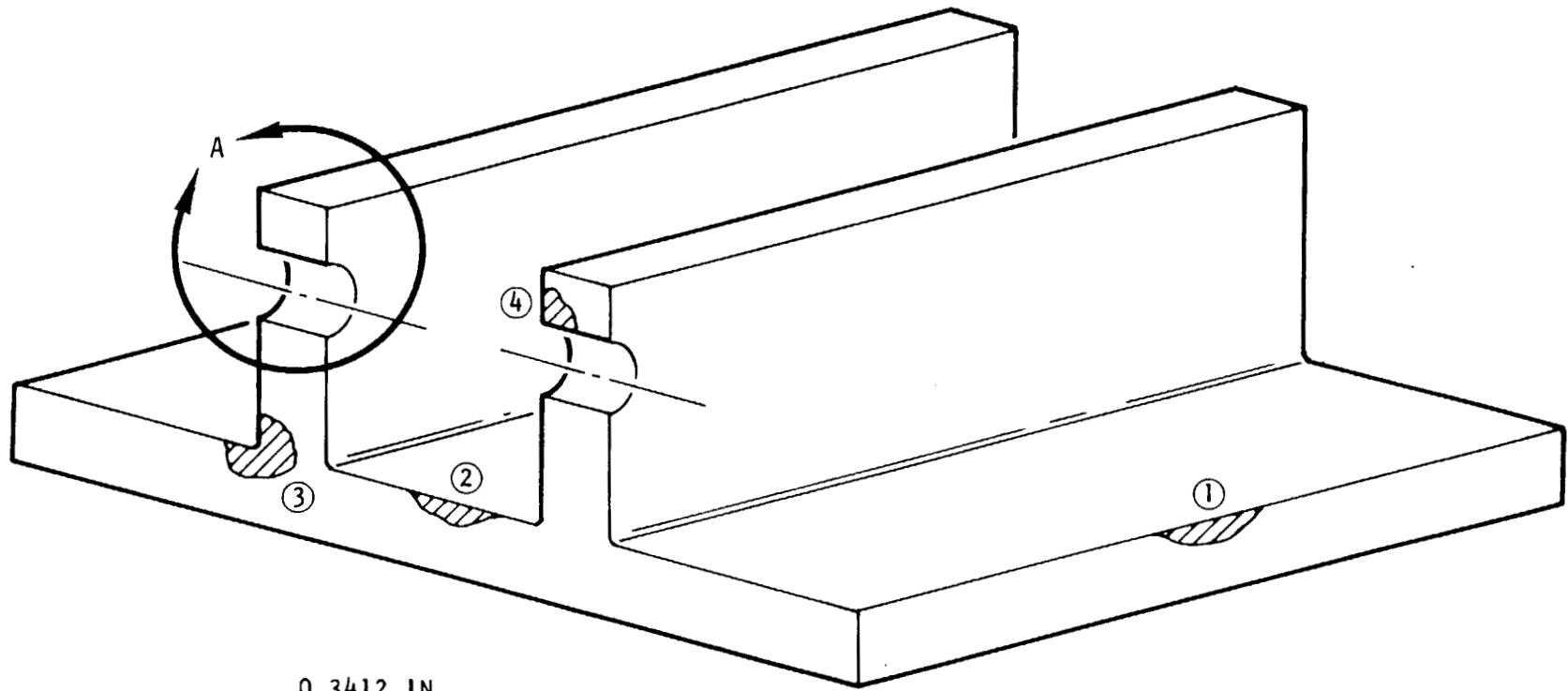
$$K_c = 68.1 \text{ MN/m}^{3/2} (62 \text{ ksi} \sqrt{\text{inch}})$$

It is anticipated that there will be six ferry missions after each orbital mission. The operating ΔP for the orbital mission is 0.101 MN/m^2 (14.7 psi) and the operating ΔP for the ferry mission is 0.069 MN/m^2 (10 psi). The corresponding PR/t stress for these ΔP 's are 196.5 MN/m^2 (28.5 ksi) and 133.75 MN/m^2 (19.4 ksi), respectively. Since cracks can occur in both longitudinal and circumferential directions, it is required to have separate load spectra for the longitudinal and the circumferential cracks.

The load spectra for the longitudinal crack will be the hoop stresses, i. e., 196.5 MN/m^2 (28.5 ksi) for one cycle plus 133.75 MN/m^2 (19.4 ksi) for six cycles. The load spectra for the circumferential crack is the $PR/2t$ stresses, i. e., 98.25 MN/m^2 (14.25 ksi) for orbital flight and 66.87 MN/m^2 (9.7 ksi) for each ferry mission. In addition, there are flight loads, which usually come from axial bending, which are superimposed on the internal pressure. Since the load spectra for the flight loads are not available at the present time, assumptions are made, for the purpose of this example, of an additional 68.9 MN/m^2 (10 ksi) of axial stress for the orbital mission and an additional 34.47 MN/m^2 (5 ksi) of axial stress for the ferry mission. Consequently, the final load spectra for the circumferential crack will be 167.19 MN/m^2 (24.25 ksi) for one cycle and 101.35 MN/m^2 (14.7 ksi) for six cycles.

3.2.2 Crack Geometry

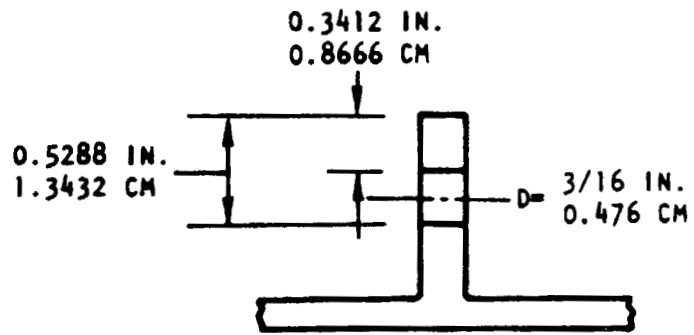
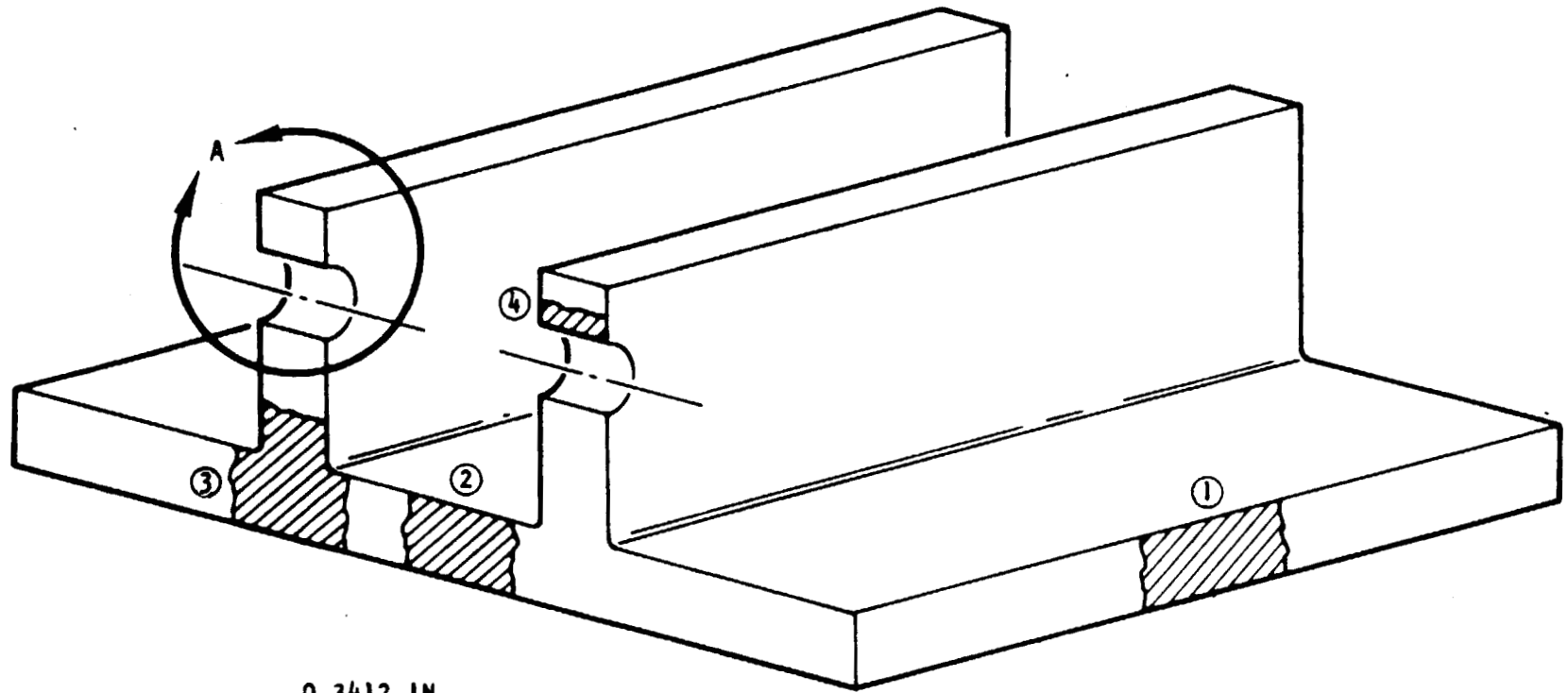
Figure 3-5A shows four cases of the most probable types of damage and their locations. These cracks would eventually develop to be through-the-thickness cracks. Since the sheet thickness is thin, it would take a short time for these cracks to grow through the thickness. Therefore, in the



DETAIL A

(a) PART-THROUGH CRACKS

Figure 3-5. Crack Geometries (Sheet 1 of 2)



DETAIL A

(b) THROUGH CRACKS

Figure 3-5. Crack Geometries (Sheet 2 of 2)

analysis, it can be assumed that all these cracks are initially through-the-thickness cracks as shown in Figure 3-5B.

Particularly, reference is made to Cases 3 and 4. In Case 3, it is assumed that the crack is located at the root of the stiffener. The crack lengths in all three directions are the same and the crack growth rates in all are also the same. In Case 4, it is assumed that initially only one crack exists at the edge of the rivet hole, as shown. When the crack breaks through the small ligament in the stiffener, another crack will shortly be formed at the other side of the rivet hole. In other words, it becomes an edge crack, and it will propagate toward the sheet. When the edge crack propagates through the entire stiffener and the sheet thickness, the stiffener is considered to be completely broken, and the crack will be a circumferential through-the-thickness crack on the skin. In this case, the criterion for break-through of the small ligament due to the crack emanating from the rivet hole and the criterion for the edge crack breaking through the wall are that the total plastic zone ($2 r_y$) in front of the crack has penetrated through the free boundaries.

3.2.3 Stress Intensity Factors

To develop an appropriate stress intensity expression for each of these damage cases, it is necessary to determine the detail dimensions of the horizontal stiffener and the frame. Assuming a design in which the stiffener spacing (B) is 10.16 centimeters (4 inches) for the X_{542} location and 5.08 centimeters (2 inches) for the X_{410} location and the thickness of the stiffeners is the same as the thickness of the sheet at each location. The height of the stiffeners is set equal to $B/2$ at each location. The size and the location of the rivet hole at the stiffener are presumed to be as shown in Detail A of Figure 3-5. Since the frame is not directly attached to the sheet, its crack arrest capability is negligible. Therefore, its size and spacing are not of concern (the typical frame spacings for the current design configuration are 38.1 centimeters (15 inches) at X_{410} and 43.18 centimeters (17 inches) at X_{542}).

3.2.3.1 Case 1, Longitudinal Crack

The geometric factors involved in this configuration are the stress intensity modification factors for the frame (perpendicular to crack) and the horizontal stiffener (parallel to crack). Since the load is perpendicular to the crack, it can be assumed that the stress intensity factors are approximately the same whether the crack is at the middle of the bay (between two integral stiffeners) or right at the root of the skin-stiffener intersection.

As mentioned in Section 2.3.7.3, the stress intensity modification factor for the horizontal stiffeners is still under development. Based on past experience, it is reasonable to assume that the total contribution in reduction of crack tip stress intensity from the combined effects of the horizontal stiffener and the frame is approximately 15 percent. In other words, the geometric factor in Equation (3)

$$\Pi\alpha = 0.85 \cdot \phi_1 \cdot \alpha_s$$

with $\phi_1 = 1.0$ for an infinitely wide sheet. The α_s values, given in Figure 2-57, obtained from testing of aluminum curved panels, are selected for the analysis.

3.2.3.2 Case 2, Circumferential Crack

A through-the-thickness crack symmetrically located at the middle of the bay as shown in Figure 3-5 will be considered. As the crack propagates past the stiffener, the stiffener is also cracked, and the stiffener crack propagates at the same rate as the skin crack. Using the same technique as described in Section 2.3.4, a set of curves which describes the variations in K at positions relative to the stiffener location is constructed and presented in Figure 3-6. Thus the geometric factor for this case will be

$$\Pi\alpha = C \cdot \phi_1 \cdot \alpha_s$$

with $\phi_1 = 1.0$ for infinitely wide sheet. C is the stress intensity modification factor for the integrally stiffened panel presented in Figure 3-6; α_s are the experimental values given in Figure 2-58 for aluminum alloy cylinders.

3.2.3.3 Case 3, Circumferential Crack at Root of Integral Stiffener

This case is essentially the same as Case 2 except that the crack is initially started at the bottom of the integral stiffener and simultaneously grows up the stiffener and in the skin. The expression for $\Pi\alpha$ is the same as for Case 2 but a different set of C curves given in Figure 3-7 is used.

3.2.3.4 Case 4, Crack Emanating from Rivet Hole

As discussed before, this case could result in three separate steps of crack propagation: the crack propagates from one side of the rivet hole, the edge crack propagates from the opposite side of the rivet hole, and the skin crack propagates away from a broken stiffener. The geometric factors for these cracks are $\Pi\alpha = B$ for the crack from a rivet hole, $\Pi\alpha = 1.122$ for the edge crack, and $\Pi\alpha = C \cdot \alpha_s$ for the skin crack. Here B is the Bowie's

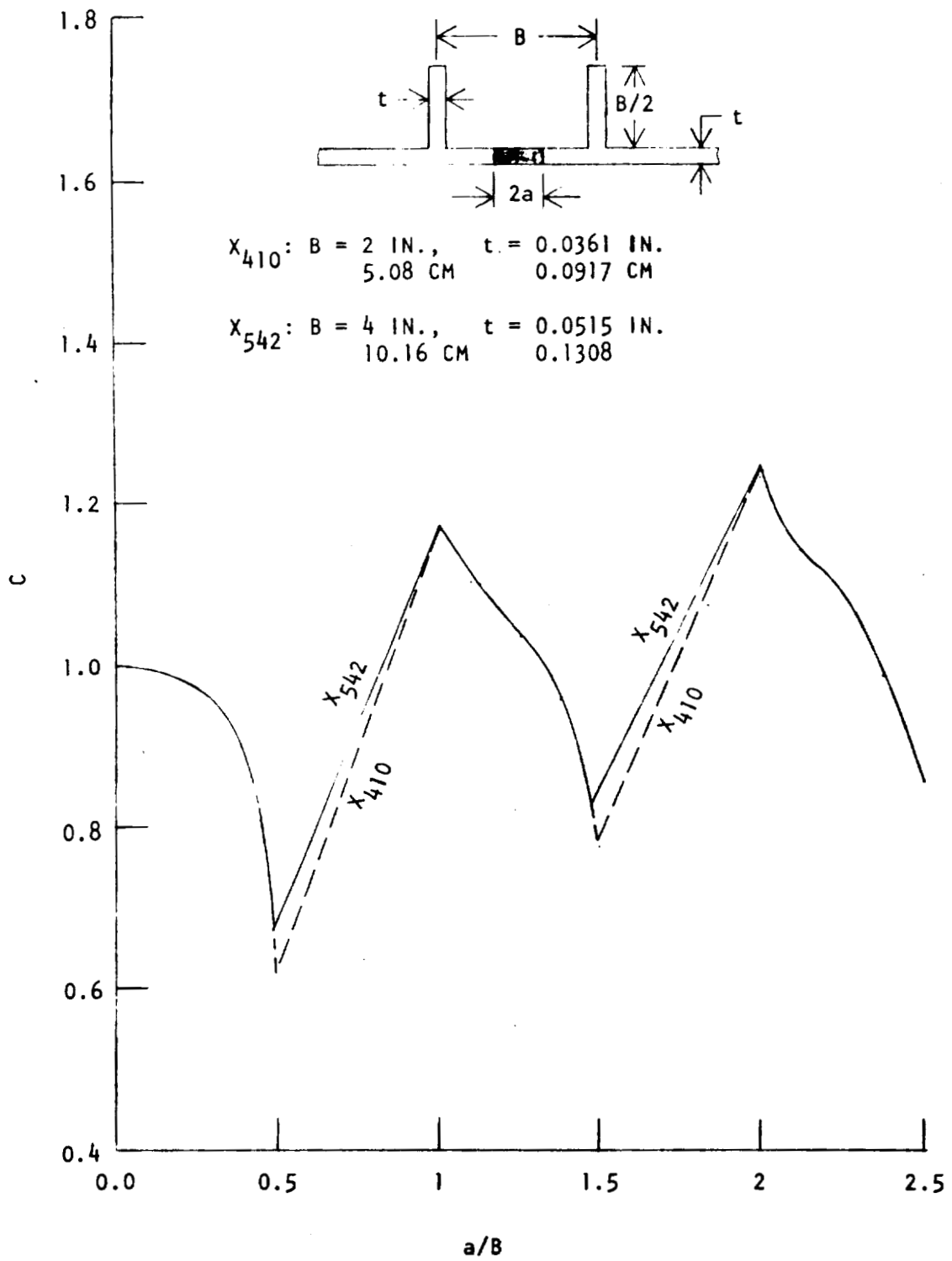


Figure 3-6. Stress Intensity Factor for Integrally Stiffened Skin

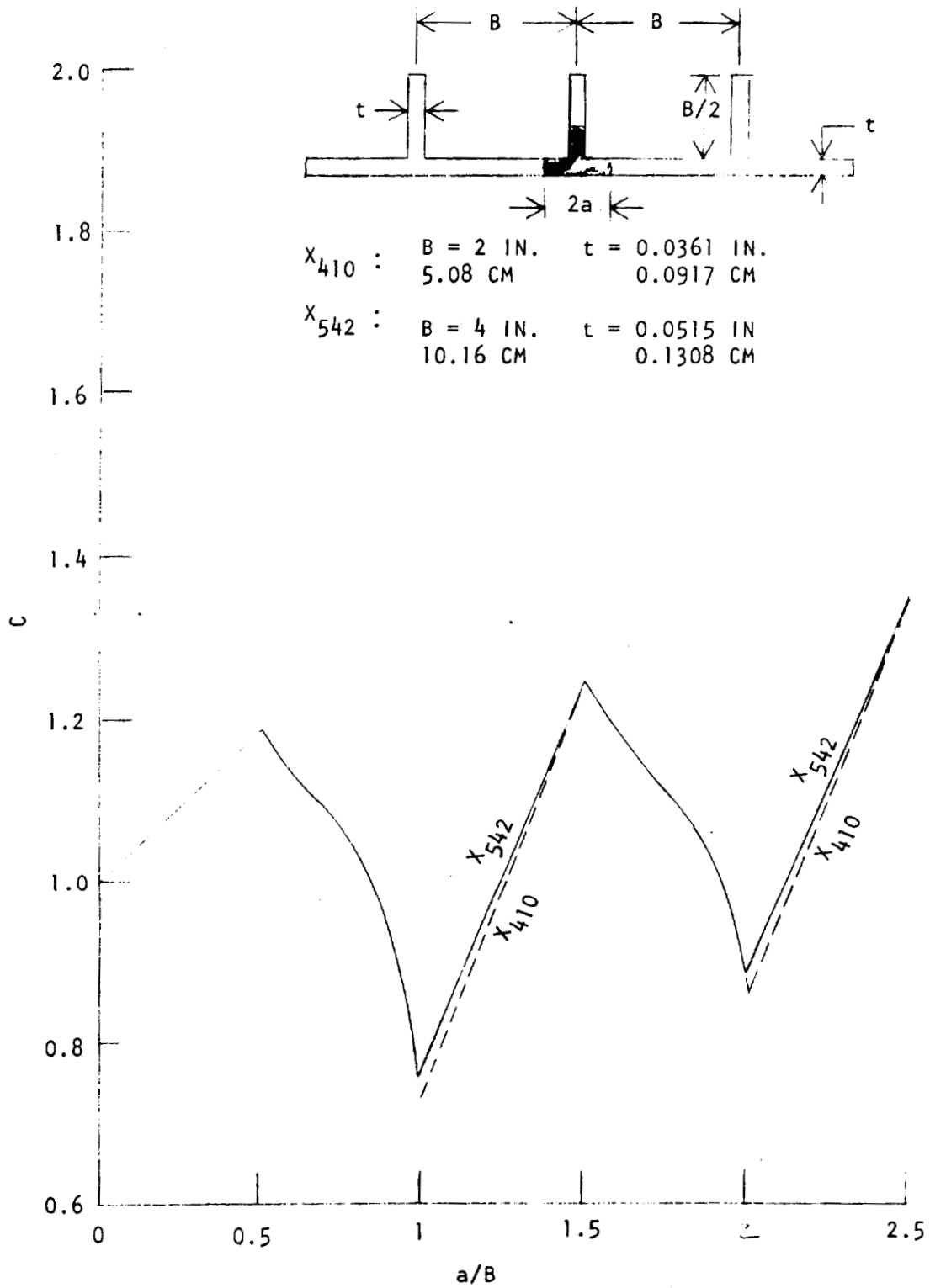


Figure 3-7. Stress Intensity Factor for Integrally Stiffened Skin

factor (Figure 2-30); α_s is the experimental curvature corrections factor for circumferential crack (see Figure 2-58); and C is the integral stiffener influence factor given in Figure 3-8. The angle and the frame (see Figure 3-4) connect with the integral stiffener and provide load paths adjacent to the riveted stiffener; similarly, the sheet skin also provides load-path continuity on the other side of the stiffener. Therefore finite width correction factors are not applied to the edge crack and the crack emanating from the rivet hole.

3.2.4 Initial Crack Lengths

For this example, it is reasonable to assume a nondestructive evaluation (NDE) capability for through-the-thickness cracks to be 0.38 centimeter (0.15 inch) (total crack length) and the NDE capability for a crack emanating from a rivet hole to be 0.127 centimeter (0.05 inch). The initial crack length for Cases 1, 2 and 3, therefore, is 0.38 centimeter (0.15 inch) ($a_0 = 0.19$ centimeter (0.075 inch)). And for Case 4, the initial crack length at the edge of the fastener hole is 0.127 centimeter (0.05 inch).

For Case 4, the crack growth calculations will stop at a crack length equal to $(0.3412 - 2r_y)$. This crack length is estimated to be 0.698 centimeter (0.275 inch). The second step is to assume a 1.34-centimeters (0.5288-inch) edge crack growing toward the skin. The calculations for the second step will stop at a crack length equal to $(\frac{B}{Z} + t - 2r_y)$. This crack length is estimated to be 1.94 centimeters (0.767 inch) for X₄₁₀ and 3.86 centimeters (1.52 inches) for X₅₄₂. The initial crack length for the skin crack in the third step, after breaking the integral stiffener, is uncertain. In the example case, it is assumed that this crack length equals the plastic zone size at break-through i. e., $2a_0 = 2r_y$, where $2r_y$ is 0.68 centimeters (0.268 inch) for X₄₁₀ and 1.35 centimeters (0.5315 inch) for X₅₄₂.

3.2.5 Crack Growth Predictions

Since the current crew compartment configuration only consists of welded integrally stiffened skins, the residual strength or fail-safe capability for the crew compartment skin cannot be increased by taking advantage of load transfer in any form (e. g. , divided planks or attached stiffener); therefore, the residual strength analysis in this case is combined with the fatigue crack propagation analysis. This is done by computing the K value at each crack length using the design limit stress (213.7 MN/m² (31 ksi)). When the K value at any crack length reaches K_c , final failure of the panel is assumed.

The predicted crack growth histories of Cases 1 to 3 are presented in Figures 3-9 to 3-11. The crack growth curves in these figures show that the

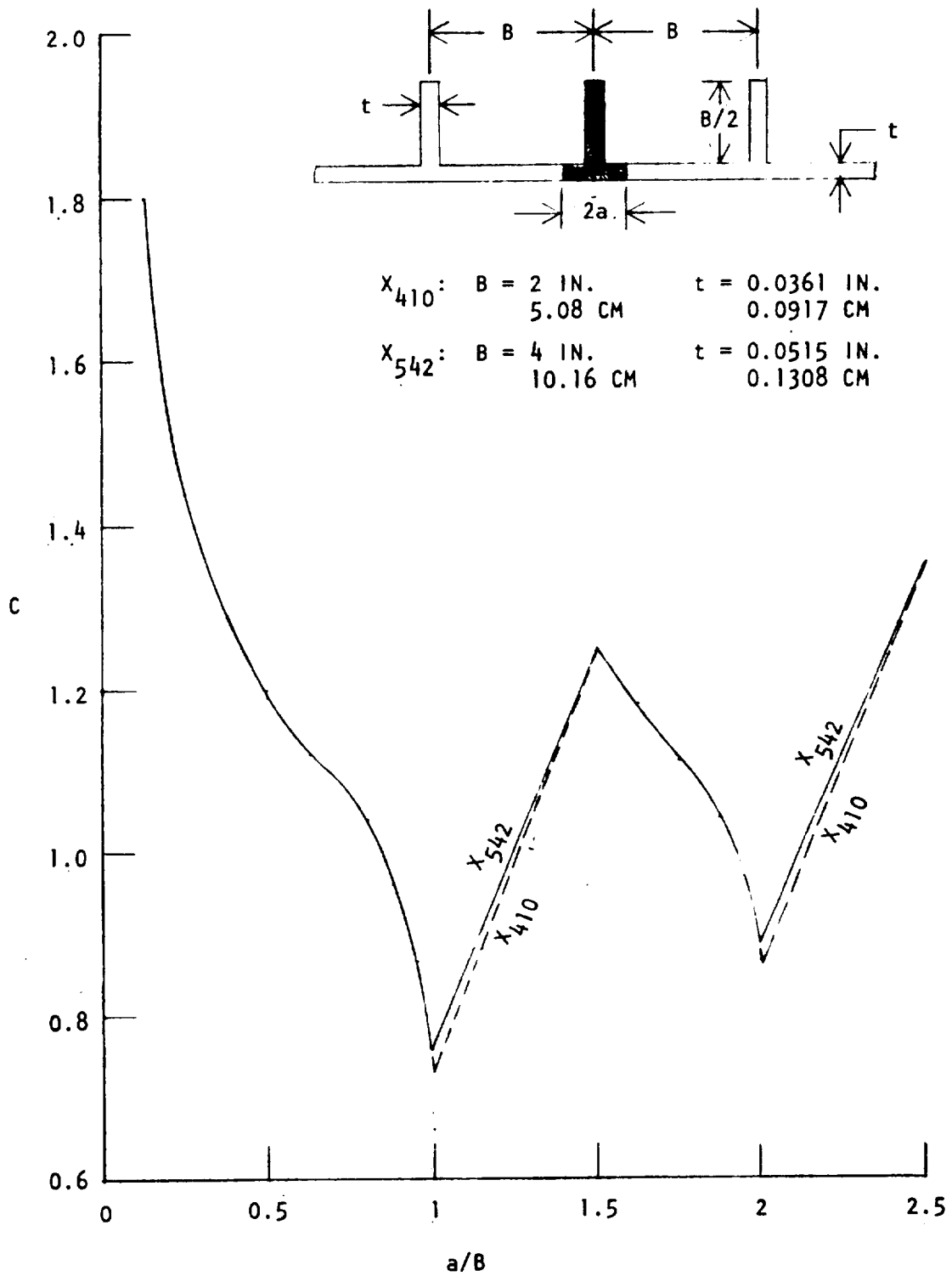


Figure 3-8. Stress Intensity Factor for Integrally Stiffened Skin

safe-crack-growth life in either location, X_{410} or X_{542} , is approximately the same for each case of assumed crack geometrics. Case 1, longitudinal crack, exhibits the shortest life (approximately 4000 loading blocks). Case 2, a circumferential crack initiated at mid-bay between two integral stiffeners, exhibits the longest life (approximately 6000 loading blocks). The predicted results for Case 4 are presented in Figure 3-12. Here it is shown that it will take 2800 loading blocks to grow the 0.127-centimeter (0.05-inch) crack at one side of the hole to break-through of the small ligament adjacent to the hole, and then it will take another 350 loading blocks for the crack, at X_{410} , to break up the entire stiffener. After that, it takes an additional 290 loading blocks to completely fail the skin. As for the crack at X_{542} , complete failure of the whole panel occurs while the edge crack (Step 2) is propagating toward the skin. Nevertheless, the total safe-crack-growth life at either location for the Case 4 crack is approximately 3400 loading blocks regardless of where the final failure points occur.

A summary of the analysis results is shown in Table 3-1. It is seen that the most severe case is 4. If the design life is 500 orbital missions (500 loading blocks) and a factor of six on predicted life is the requirement specified in the design criteria, then the subject structural element (the crew compartment skin) is a fracture-controlled part as described in the selection logic flow diagram in Section 1.2.

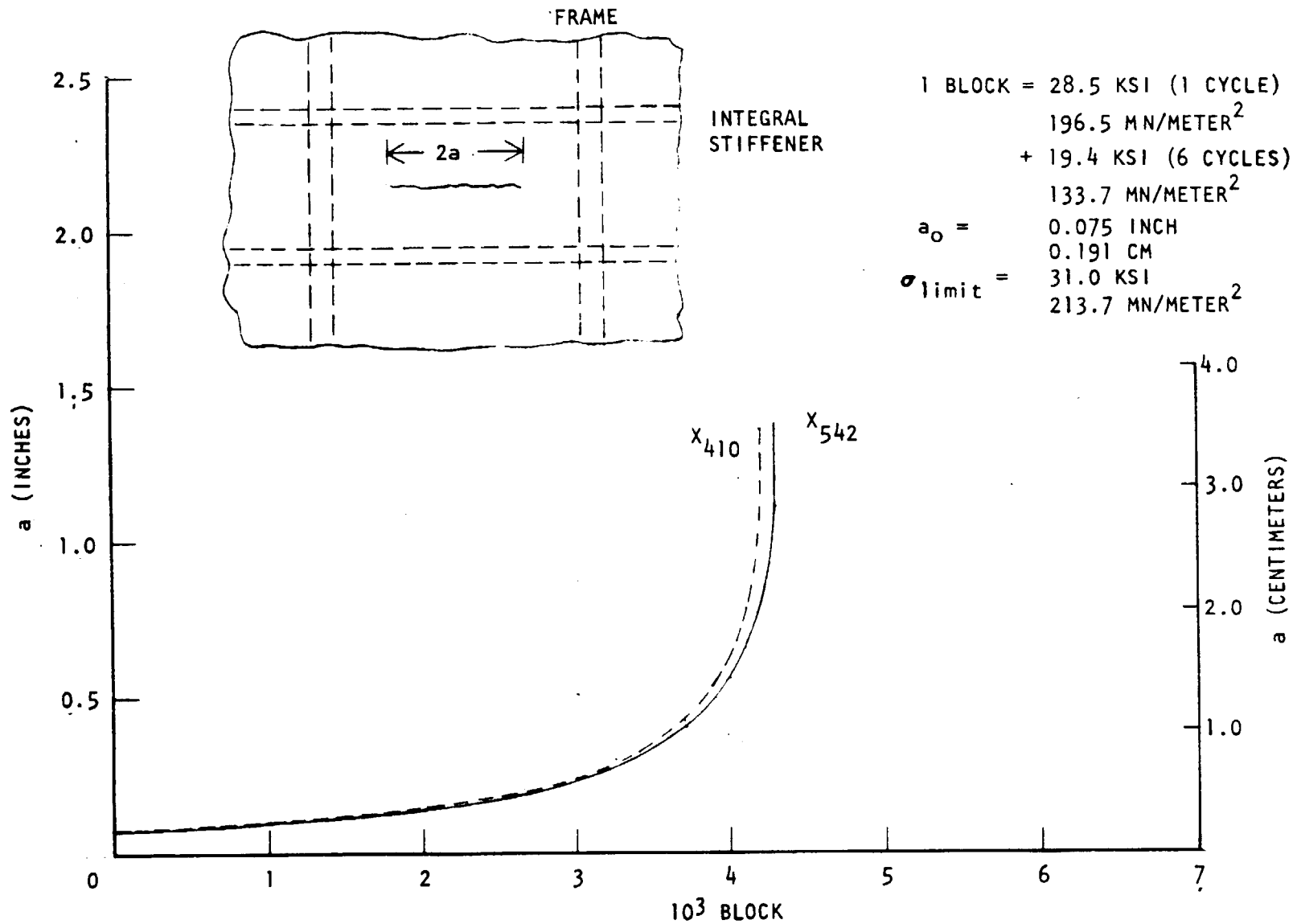


Figure 3-9. Predicted Fatigue Crack Growth History for a Longitudinal Crack in the Crew Compartment Skin

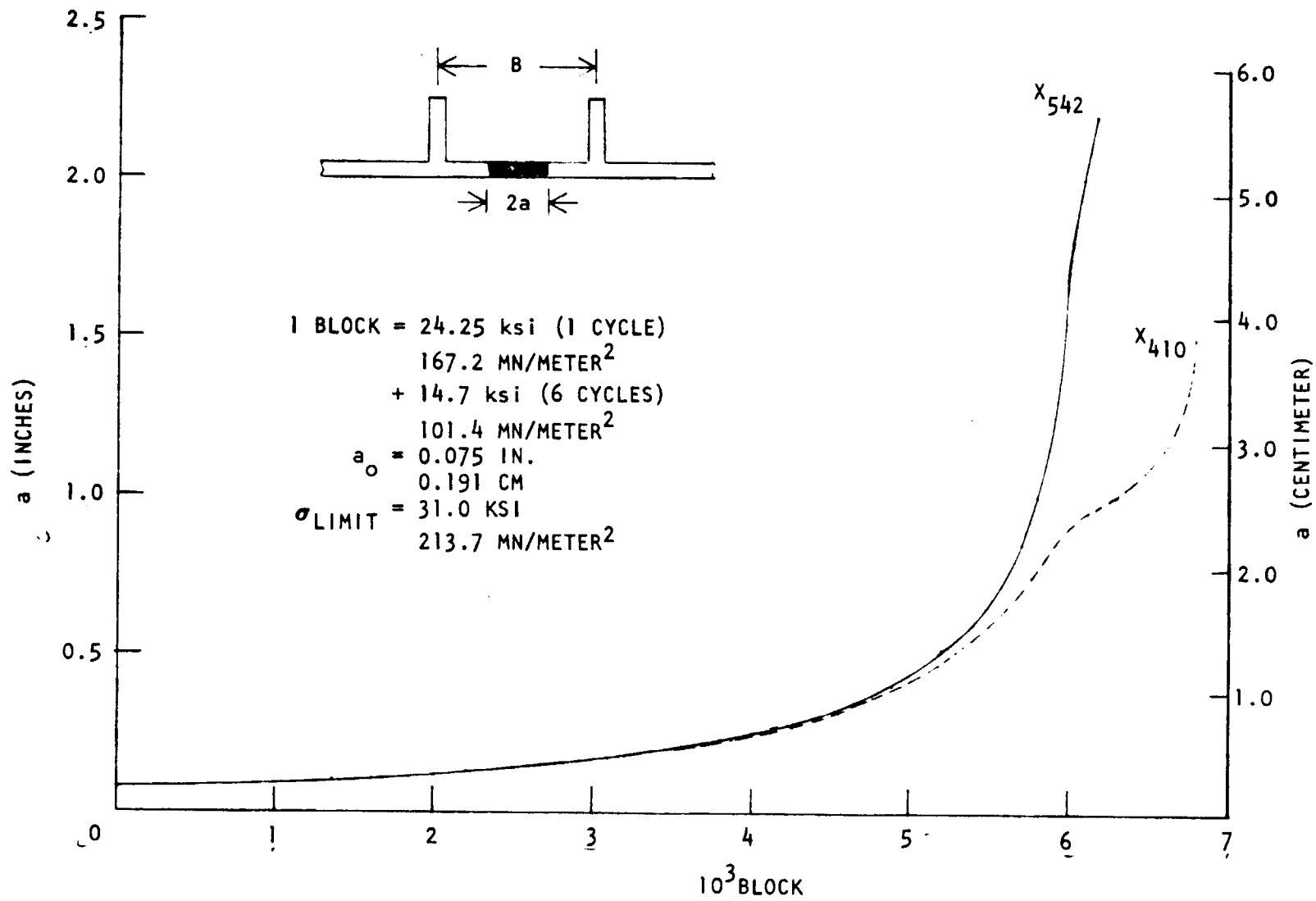


Figure 3-10. Predicted Fatigue Crack Growth History for a Circumferential Crack in the Crew Compartment Skin

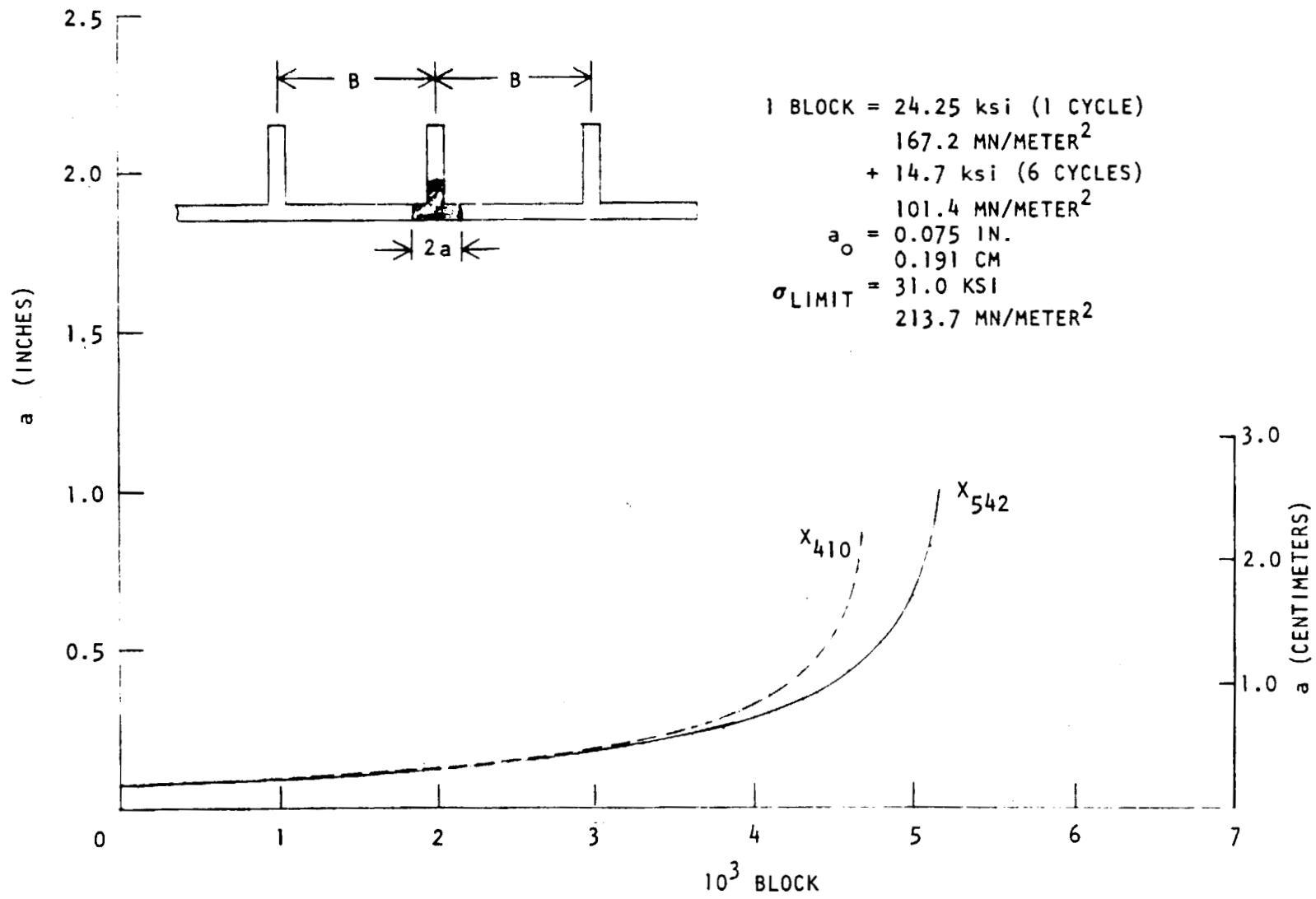


Figure 3-11. Predicted Fatigue Crack Growth History for a Circumferential Crack at Bottom of an Integral Stiffener in the Crew Compartment Skin

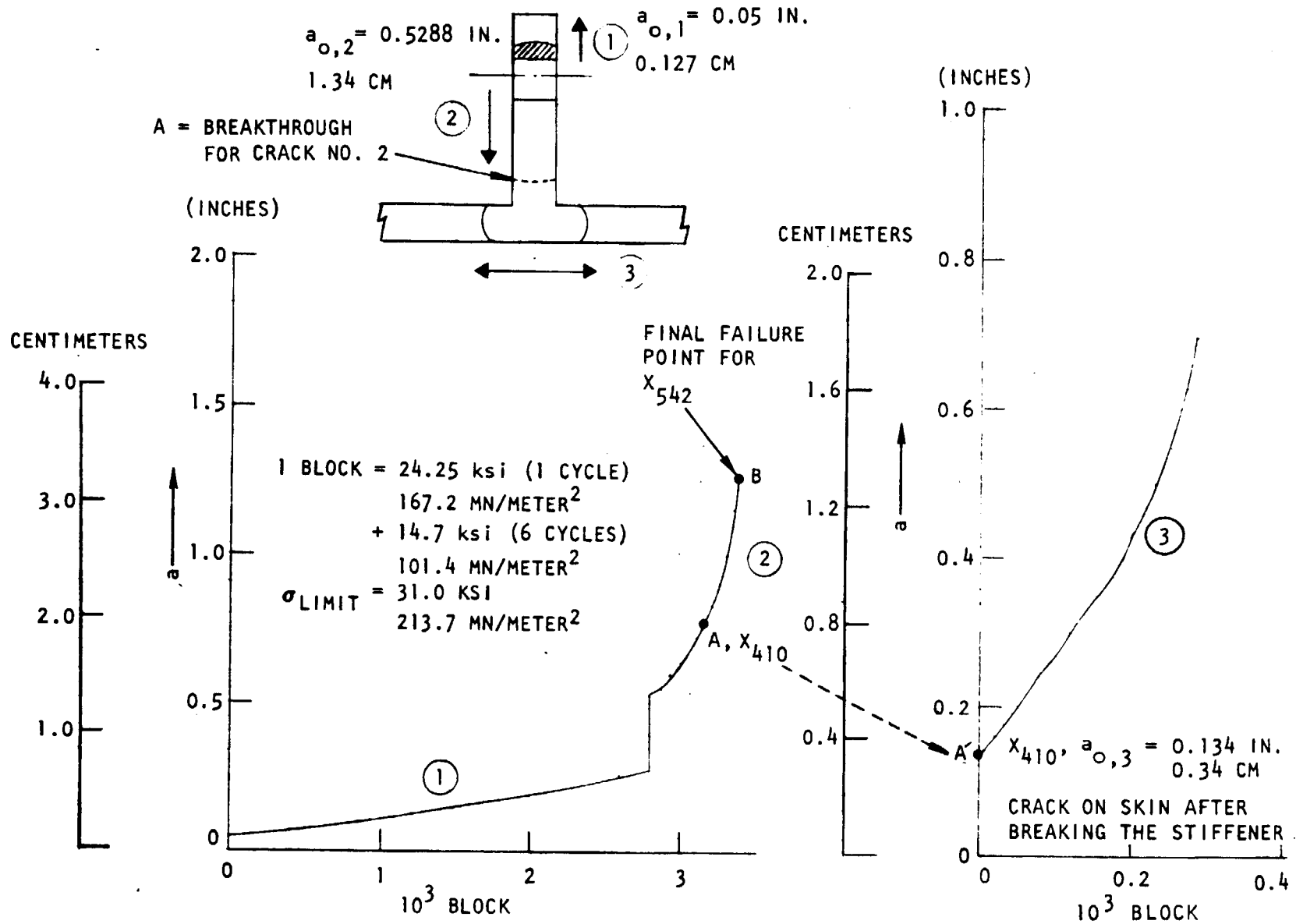


Figure 3-12. Predicted Fatigue Crack Growth History for Crack Emanating From Rivet Hole

Table 3-1. Safe-Crack-Growth Predictions for Crew Compartment Skin

Case	Initial Crack Configuration △	Loads Spectra	Stress Intensity Factors ($\Pi\alpha$) △	Total Number of Loading Blocks to Failure
1	Longitudinal skin crack $a_0 = 0.190$ cm (0.075 in.)	196.5 MN/m ² (28.5 ksi) (1 cycle) +133.7 MN/m ² (19.4 ksi) (6 cycles)	$C \cdot \phi_1 \cdot \alpha_s$ with $\phi_1 = 1.0$, $C = 0.85$ and α_s given in Figure 2-57.	$X_{410} = 4,200$ $X_{542} = 4,300$
2	Circumferential skin crack $a_0 = 0.190$ cm (0.075 in.)	167.19 MN/m ² (24.25 ksi) (1 cycle) +101.35 MN/m ² (14.7 ksi) (6 cycles)	$C \cdot \phi_1 \cdot \alpha_s$ with $\phi_1 = 1.0$, C and α_s given in Figures 3-6 and 2-58.	$X_{410} = 6,750$ $X_{542} = 6,200$
3	Circumferential crack at bottom of integral stiffener $a_0 = 0.190$ cm (0.075 in.)	167.19 MN/m ² (24.25 ksi) (1 cycle) +101.35 MN/m ² (14.7 ksi) (6 cycles)	$C \cdot \phi_1 \cdot \alpha_s$ with $\phi_1 = 1.0$, C and α_s given in Figures 3-7 and 2-58	$X_{410} = 4,700$ $X_{542} = 5,150$
4	Crack emanating from rivet hole $a_0 = 0.127$ cm (0.05 in.)	167.19 MN/m ² (24.25 ksi) (1 cycle) +101.35 MN/m ² (14.7 ksi) (6 cycles)	Growth step No. 1: B (given in Figure 2-30) Growth step No. 2: $C (=1.122)$ Growth step No. 3: $C \cdot \alpha_s$ with C and α_s given in Figures 3-8 and 2-58.	$X_{410} = 3,440$ $X_{542} = 3,350$
<p>△ All through-the-thickness cracks △ Equation (3)</p>				

4.0 SUMMARY AND RECOMMENDATIONS

This study provided an insight into the realistic aspects of accomplishing fracture control on a vehicle system required to perform in a space environment as well as in the atmosphere. The prominent features identified in a functioning fracture control program include the necessary interaction of the technical disciplines involved with design, structural analysis, materials and processes, and quality assurance. These disciplines address: (1) the design features that minimize stress concentrations; (2) the fatigue analysis to prevent the incidence of cracking in service; (3) the fracture mechanics analysis to assure adequate life of components with existing crack-like flaws; (4) the control of materials and processes to maintain favorable material characteristics and to prevent cracking during fabrication; and (5) the incorporation of suitable inspection procedures to detect crack-like flaws after fabrication and, when required, during the operational phase of the vehicle.

A procedure is presented which provides a logical sequence in the identification of critical components and an indication of the kinds of controls necessary to assure an adequate analytical safe-crack-growth life for the component. Critical steps in the procedure include:

1. Definition of the types of loads, the environment, and the level of stress acting on a structural element
2. Identification of fracture-critical parts by use of a selection logic flow diagram
3. Performance of a predictive analysis to evaluate the safe-crack-growth life of the component
4. Application of either corrective action or the controls necessary to achieve the desired safe-crack-growth life

This document applies particular emphasis on the functional aspects relating to safe-crack-growth life analysis as affected by fracture mechanics analytical methods. Performance of the analytical tasks requires that a number of assumptions and approximations be incorporated into the procedure employed. A concerted effort has been exerted by analysts to achieve a balance of factors which recognize conservative and nonconservative behavior in crack growth; however, uncertainties persist in the understanding of crack growth behavior modes.

The most crucial assumption taken in fracture mechanics analysis is that all structures contain cracks of sizes significant to the analysis, independent of the method of metalworking employed or the process control imposed on the component. It appears that this assumption ignores the benefits of closely controlled procedures used in producing certain product forms and the achievement of substantially defect-free components by imposition of an active materials and process control system. It is recommended that studies be initiated which address the statistical probability of flaw existence dependent upon product form and process control. Further, the study should be concerned with size, shape, and orientation of these flaws in components when assessment dictates a high probability of occurrence.

A continuing effort to assess the sensitivity of baseline assumptions and approximations in fracture mechanics analysis on component sizing and configuration is required. Until such time as more suitable assessment is available, it is mandatory to develop firm policies and uniform analysis procedures with regard to the assumptions and approximations employed, so that all participants to a control program recognize the potential optimistic (or pessimistic) conditions which prevail.

5.0 REFERENCES

1. Westrup, R. W.; Establishment of Design Criteria for Acceptable Failure Modes and Fail-Safe Considerations for the Space Shuttle Structural System; Report SD 72-SH-0046, Space Division, Rockwell International Corporation, Downey, California (1 June 1972).
2. Grover, H. J., S. A. Gordon, and L. R. Jackson; Fatigue of Metals and Structures; NAVWEPS 00-25-534, Government Printing Office (Revised 1 June 1960).
3. Grover, H. J.; Fatigue of Aircraft Structures; NAVAIR 01-1A-13, U. S. Government Printing Office (1966).
4. Heywood, R. B.; Designing Against Fatigue of Metals; Reinhold Publishing Corp., New York, N. Y. (1962).
5. Anderson, W. E.; Fatigue of Aircraft Structures; International Metallurgical Reviews, Vol. 17 (1972) pp. 240-263.
6. Schijve, J.; The Accumulation of Fatigue Damage in Aircraft Materials and Structures; AGARDograph AGARD-AG-157 (1972).
7. Metal Fatigue: Theory and Design; A. F. Madayag, editor; John Wiley & Sons, Inc., New York, N. Y. (1969).
8. Metal Fatigue; G. Sines and J. L. Waisman, editors; McGraw-Hill Book Company, New York, N. Y. (1959).
9. Hartmann, E. G., M. Holt, and I. D. Eaton; Static and Fatigue Strengths of High Strength Aluminum Alloy Bolted Joints; NACA TN-2276 (1951).
10. Hartmann, E. C., M. Holt, and I. D. Eaton; Additional Static and Fatigue Tests of High Strength Aluminum Alloy Bolted Joints; NACA TN-3269 (1954).
11. Jarfall, L. E.; Optimum Design of Joints: Stress Severity Factor Concepts; Fifth ICA Symposium, Melbourne, Australia (May 1967).
12. Raphael, C.; "Variable-Adhesive Bonded Joints;" in Applied Polymer Symposia No. 3 (1966) pp. 99-108.

13. Dowling, N. E. ; Fatigue Failure Predictions for Complicated Stress-Strain Histories; T&AM Report 337, Department of Theoretical and Applied Mechanics, University of Illinois, Urbana, Illinois, (January 1971).
14. Crichlow, W. J. , et al; An Engineering Evaluation of Methods for the Prediction of Fatigue Life in Airframe Structures; ASD-TDR-61-434, Wright Patterson Air Force Base, Ohio (1962).
15. Aircraft Structural Integrity Program, Airplane Requirements; MIL-STD-1530 (USAF) (September 1972).
16. Military Specifications on Aircraft Damage Tolerance Requirements; MIL SPEC A-83444 (June 1974).
17. Ekvall, J. C. , T. R. Brussat, A. F. Liu, and M. Creager; Engineering Criteria and Analysis Methodology for the Appraisal of Potential Fracture Resistant Primary Aircraft Structure; AFFDL-TR-72-80, Air Force Flight Dynamics Laboratories, Wright Patterson Air Force Base, Ohio (September 1972).
18. Airworthiness Standards: Transport Category Airplanes; Federal Aviation Regulations Part 25, Federal Aviation Agency.
19. Fracture Control of Metallic Pressure Vessels; NASA SP-8040 (May 1970).
20. Preliminary Criteria for the Fracture Control of Space Shuttle Structures; prepared by NASA/Industry Working Group, Langley Research Center (June 1971).
21. Structural Design Criteria Applicable to a Space Shuttle; NASA SP-8057 (Revised March 1972).
22. Tada, H. , P. C. Paris, and G. R. Irwin; The Stress Analysis of Cracks Handbook; Del Research Corporation, Hellertown, Pennsylvania (1973).
23. Isida, M; Effect of Width and Length on Stress Intensity Factors of Internally Cracked Plate Under Various Boundary Conditions; International Journal of Fracture Mechanics, Vol. 7 (1971).
24. Feddersen, C. E. ; Discussion to: Plane Strain Crack Toughness Testing; ASTM STP No. 410 (1966) p. 77.

25. Isida, M; Stress-Intensity Factors for the Tension of an Eccentrically Cracked Strip; Trans. ASME, Series E, Journal of Applied Mechanics, Vol. 33 (1965).
26. Hayes, D. J.; A Practical Application of Buekner's Formulation for Determining Stress Intensity Factors for Cracked Bodies; International Journal of Fracture Mechanics, Vol. 8 (1972) pp. 157 to 165.
27. Irwin, G. R.; Plastic Zone Near a Crack and Fracture Toughness; in Proceedings, Seventh Sagamore Ordnance Materials Conference, Syracuse University Research Institute (1960) pp. IV-63 to IV-78.
28. Forman, R. G.; Effect of Plastic Deformation on the Strain Energy Release Rate in a Centrally Notched Plate Subjected to Uniaxial Tension; Journal of Basic Engineering, Transactions of ASME, Series D, Vol. 88 (1966) p. 82.
29. Key, P. L.; The Effect of Local Yielding on the Strain Energy Release Rate, Journal of Basic Engineering, Transaction of ASME (December 1969) pp. 852 to 854.
30. Dugdale, D. S.; Yielding of Steel Sheets Containing Slits; Journal of Mechanics and Physics of Solids, Vol. 8 (1960) pp. 100 to 104.
31. Vitvitski, P. M., and M. Ya. Leonov; Slip Bands at Nonuniform Deformation of a Plate; VMRTT, Izdat. An USSR, No. 1, Kiev (1962) pp. 13 to 28.
32. Hussain, M. A., and S. L. Pu; Variational Method for Crack Intensity Factors and Plastic Regions of Dugdale Model; Engineering Fracture Mechanics, Vol. 4 (1972) pp. 119 to 128.
33. Head, P. T., G. M. Spink, and P. J. Worthington; Post Yield Fracture Mechanics; Materials Science and Engineering, Vol. 10 (1972) pp. 129 to 138.
34. Newman, J. C. Jr.; Fracture of Cracked Plates Under Plane Stress; Engineering Fracture Mechanics, Vol. 1 (1968) pp. 137 to 154.
35. Liu, A. F., and M. Creager; On the Slow Stable Crack Growth Behavior of Thin Aluminum Sheet; in Mechanical Behavior of Materials, Vol. 1, The Society of Materials Science, Kyoto, Japan (1972) pp. 558 to 568.

36. Krafft, J. M., A. M. Sullivan, and R. W. Boyle; Effects of Dimensions on Fast Fracture Instability of Notched Sheets; in Proceedings, Crack Propagation Symposium, Vol. I, College of Aeronautics, Cranfield, England (1961).
37. Heyer, R. H., and D. E. McCabe; Plane Stress Fracture Toughness Testing Using a Crack-Line Loaded Specimen; presented at the 3rd National Symposium on Fracture Mechanics, Lehigh University (August 1969).
38. Van Orden, J. M., and A. F. Liu; Evaluation of X7475-T61 Clad Sheet; Report LR24951, Lockheed-California Company, Burbank, California (February 1972).
39. Liu, A. F.; Statistical Variation in Fracture Toughness Data of Airframe Materials, Proceedings of the Air Force Conference on Fatigue and Fracture of Aircraft Structures and Materials, AFFDL-TR-70-144 (1970) pp. 323 to 341.
40. Shah, R. C., and A. S. Kobayashi; On the Surface Flaw Problem; presented at ASME 93rd Annual (Winter) Meeting, New York, N. Y. (26 to 30 November 1972).
41. Merkle, J. G.; A Review of Some of the Existing Stress Intensity Factor Solutions for Part-Through Surface Cracks; Report ORNL-TM-3983, Oak Ridge National Laboratory, Oak Ridge, Tennessee (January 1973).
42. Hsu, T. M., and A. F. Liu; Stress Intensity Factor for Truncated Elliptical Cracks; presented at the Seventh National Symposium on Fracture Mechanics, University of Maryland, College Park, Maryland (27 to 29 August 1973).
43. Irwin, G. R.; Crack-Extension Force for a Part-Through Crack in a Plate; Transactions of ASME, Series E, Journal of Applied Mechanics, Vol. 84, No. 4 (December 1962) pp. 651 to 654.
44. Green, A. E., and I. N. Sneddon; The Distribution of Stress in the Neighborhood of a Flat Elliptical Crack in an Elastic Solid; Proceedings of Cambridge Philosophical Society, Vol. 46 (1950) pp. 159 to 164.
45. Wigglesworth, L. A.; Stress Distribution in a Notched Plate; Mathematika, Vol. 4 (1957) pp. 76 to 96.
46. Irwin, G. R.; Fracture Mechanics; in Structural Mechanics, Pergamon Press, London, England (1960) pp. 560 to 574.

47. Smith, F. W., A. F. Emery, and A. S. Kokayaski; Stress Intensity Factors for Semicircular Cracks (Part II – Semi-Infinite Solid); Transaction of ASME, Series E, Journal of Applied Mechanics (December 1967) pp. 953 to 959.
48. Smith, F. W., and M. J. Alavi; Stress-Intensity Factors for a Part-Circular Surface Flaw; ASME, Proceedings of the First International Conference on Pressure Vessel Technology (1969) pp. 793 to 800.
49. Westmann, R. A.; Note on Estimating Critical Stress for Irregularly Shaped Planar Cracks; International Journal of Fracture Mechanics, Vol. 2 (1966) pp. 561 to 563.
50. Collipriest, J. E. Jr., and R. M. Ehret; Computer Modeling of Part-Through-Crack Growth; Report SD 72-CE-0015B, Space Division, Rockwell International Corp., Downey, California (July 1972, revised October 1973).
51. Orange, T. W., T. L. Sullivan, and F. D. Calfo; Fracture of Thin Sections Containing Through and Part-Through Cracks; NASA TN D-6305 (1971).
52. Bonesteel, R. M.; Fracture of Thin Sections Containing Surface Cracks; Engineering Fracture Mechanics, Vol. 5 (1973) pp. 541 to 554.
53. Newman, J. C. Jr.; Fracture Analysis of Surface-Cracked Sheet and Plates; Engineering Fracture Mechanics, Vol. 5 (1973) pp. 667 to 690.
54. Kobayashi, A.S., and W.L. Moss; Stress Intensity Magnification Factors for Surface-Flawed Tension Plate and Notched Round Tension Bar; Fracture 1969, Chapman and Hall, Ltd., London (1969).
55. Rice, J. R., and N. Levy; The Part-Through Surface Crack in an Elastic Plate; Transactions of ASME, Series E, Journal of Applied Mechanics (March 1972) pp. 185 to 194.
56. Masters, J. N., W. P. Haese, and R. W. Finger; Investigation of Deep Flaws in Thin Walled Tanks; NASA CR-72606, Report on Contract NAS3-10290, The Boeing Company, Seattle, Washington (March 1969).
57. Bowie, O. L.; Analysis of an Infinite Plate Containing Radial Cracks Originating at the Boundary of an Internal Circular Hole; Journal of Mathematics and Physics, Vol. 35 (1956) pp. 60 to 71.

58. Begley, J. A., J. D. Landes, and W. K. Wilson; An Estimation Model for the Application of the J-Integral; presented at the Seventh Symposium on Fracture Mechanics, University of Maryland, (27 to 29 August 1973).
59. Neuber, H.; Theoretical Determination of Fatigue Strength at Stress Concentrations; Report AFML-TR-68-20, U. S. Air Force, Wright Patterson Air Force Base, Ohio (1968).
60. Grandt, A. F., Jr., and J. P. Gallagher; An Infinite Life Fracture Mechanics Criteria for Mechanical Fasteners; presented at the Seventh Symposium on Fracture Mechanics, University of Maryland, (27 to 29 August 1973).
61. Grandt, A. F., Jr.; A General Stress Intensity Factor Solution for Fastener Holes; Technical Memorandum AFML/LLP 73-7, Air Force Materials Laboratory, Wright Patterson Air Force Base, Ohio (June 1973).
62. Aberson, J. A.; Cracked Finite Element Development at Lockheed-Georgia Company; Report No. LG73ER0007, Lockheed-Georgia Company, Marietta, Georgia (17 September 1973).
63. Bloom, J. M., and J. L. Sanders, Jr.; The Effect of a Riveted Stringer on the Stress in a Cracked Sheet; Journal of Applied Mechanics, Transactions of ASME, Series E, Vol. 33 (1966) pp. 561 to 570.
64. Grief, R., and J. L. Sanders, Jr.; The Effect of a Stringer on the Stress in a Cracked Sheet; Journal of Applied Mechanics, Transaction of ASME, Series E. Vol. 32 (1965) pp. 59 to 66.
65. Poe, C. C., Jr.; The Effect of Broken Stringers on the Stress Intensity Factor for a Uniformly Stiffened Sheet Containing a Crack; presented at the Tenth Anniversary Meeting of the Society of Engineering Science, Raleigh, N. C. (5 to 7 November 1973).
66. Poe, C. C. Jr.; Stress Intensity Factor for a Cracked Sheet with Riveted and Uniformly Spaced Stringers; NASA TR R-358 (May 1971).
67. Poe, C. C. Jr.; Fatigue Crack Propagation in Stiffened Panels; in Damage Tolerance in Aircraft Structures, ASTM STP 486 (1971) pp. 79 to 97.
68. Liu, A. F., and J. C. Ekvall; Material Toughness and Residual Strength of Damage Tolerant Aircraft Structures; in Damage Tolerance in Aircraft Structures, ASTM STP 486 (1971) pp. 98 to 121.

69. Creager, M., and A. F. Liu; The Effect of Reinforcements on the Slow Stable Tear and Catastrophic Failure of Thin Metal Sheet; presented at AIAA Ninth Aerospace Sciences Meeting, New York, N. Y. (25 to 27 January 1971).
70. Crichlow, W. J.; The Optimum Design of Shell Structure for Static Strength, Stiffness, Fatigue and Damage Tolerance Strength; presented at AGARD Symposium on Structural Optimization, Istanbul, Turkey (6 to 8 October 1969).
71. Romualdi, J. P., J. T. Frasier, and G. R. Irwin; Crack Extension Force Near a Riveted Stringer; Report 4956, Naval Research Laboratories, Washington, D. C., (May 1957).
72. Kuhn, P.; Stresses in Aircraft and Shell Structures; McGraw-Hill Book Company, New York, N. Y. (1956).
73. Crichlow, W. J.; The Ultimate Strength of Damaged Structure — Analysis Methods with Correlating Test Data; in Full-Scale Fatigue Testing of Aircraft Structures, Pergamaron Press, New York, N. Y. (1960) pp. 149 to 209.
74. Iida, S., and A. S. Kobayashi; Crack Propagation Rate in 7075-T6 Plates Under Cyclic Tensile and Transverse Shear Loadings; ASME Paper 69-Met-I (1969).
75. Kassir, M. K., and G. C. Sih; Three-Dimensional Stress Distribution Around an Elliptical Crack Under Arbitrary Loadings; Journal of Applied Mechanics, Transaction of ASME, Series E, Vol. 33, No. 3 (September 1966) pp. 601 to 611.
76. Smith, F. W., and D. R. Sorensen; The Elliptical Crack Subjected to Nonuniform Shear Loading; ASME Paper APMW-42 (1973).
77. Hartranft, R. J., and G. C. Sih; Effect of Plate Thickness on the Bending Stress Distribution Around Through Cracks; Journal of Mathematics and Physics, Vol. 47, No. 3 (1968) pp. 276 to 291.
78. Roberts, R., and F. Erdogan; The Effect of Mean Stress on Fatigue Crack Propagation in Plates Under Extension and Bending; Journal of Basic Engineering, Transaction of ASME, Series D, Vol. 84 (1967).

79. Wynn, R. H., and C. W. Smith; An Experimental Investigation of Fracture Criteria for Combined Extension and Bending; Journal of Basic Engineering, Transaction of ASME, Series D, (December 1969) pp. 841 to 849.
80. Schroedl, M. A., and C. W. Smith; Load Stresses Near Deep Surface Flaws Under Cylindrical Bending Fields; in Progress in Flaw Growth and Fracture Toughness Testing, ASTM STP 536 (1973) pp. 45 to 63.
81. Erdogan, F., J. J. Kibler, and R. Roberts; Fatigue and Fracture of Thin Walled Tubes Containing Cracks; Lehigh University Institute Report, (March 1969).
82. Vazquez, J. A., and P. C. Paris; The Application of the Plastic Zone Instability Criterion to Pressure Vessel Failure; presented at the Fourth National Symposium on Fracture Mechanics, Carnegie-Mellon University, Pittsburgh, Pa (24 to 26 August 1970).
83. Hahn, G. T., and M. Sarrate; Failure Criteria for Through-Cracked Vessels; in Practical Fracture Mechanics for Structural Steel, R. W. Nichols, editor (1969).
84. Erdogan, F., and M. Ratwani; Fracture of Cylindrical and Spherical Shells Containing a Crack; presented at the First International Conference on Structural Mechanics in Reactor Technology, Berlin, Germany, (20 to 24 September 1971).
85. Erdogan, F., and M. Ratwani; A Circumferential Crack in a Cylindrical Shell Under Torsion; International Journal of Fracture Mechanics, Vol. 8 (1972) pp. 87 to 95.
86. Erdogan, F. and M. Ratwani; Plasticity and Crack Opening Displacement in Shells; International Journal of Fracture Mechanics, Vol. 8 (1972) pp. 413 to 426.
87. Erdogan, F., and M. Ratwani; Fatigue and Fracture of Cylindrical Shells Containing a Circumferential Crack; International Journal of Fracture Mechanics, Vol. 6 (1970) pp. 379 to 392.
88. Erdogan, F., and J. J. Kibler; Cylindrical and Spherical Shells with Cracks; International Journal of Fracture Mechanics, Vol. 5 (1969) pp. 229 to 237.

89. Erdogan, F., and M. Ratwani; Fracture Initiation and Propagation in a Cylindrical Shell Containing an Initial Surface Flaw; presented at the Second International Conference on Structural Mechanics in Reactor Technology, Berlin, Germany (September 1973).
90. Yuceoglu, A., and F. Erdogan; A Cylindrical Shell with an Axial Crack Under Skew—Symmetric Loading; International Journal of Solids and Structures, Vol. 9 (1973) pp. 347 to 362.
91. Folias, E. S.; An Axial Crack in a Pressurized Cylindrical Shell; International Journal of Fracture Mechanics, Vol. 1 (1965) pp. 104 to 113.
92. Folias, E. S.; A Circumferential Crack in a Pressurized Cylindrical Shell; International Journal of Fracture Mechanics, Vol. 3 (1967) pp. 1 to 11.
93. Folias, E. S.; On the Effect of Initial Curvature on Cracked Flat Sheets; International Journal of Fracture Mechanics, Vol. 5, No. 4 (December 1969) pp. 327 to 346.
94. Folias, E. S.; On the Theory of Fracture of Curved Sheets; Engineering Fracture Mechanics, Vol. 2 (1970) pp. 151 to 164.
95. Folias, E. S.; A Finite Line Crack in a Pressurized Spherical Shell; International Journal of Fracture Mechanics, Vol. 1 (1965) pp. 20 to 46.
96. Folias, E. S.; The Stresses in a Cracked Spherical Shell; Journal of Mathematics and Physics, Vol. 44 (1965) pp. 164 to 176.
97. Copley, L. G., and J. L. Sanders, Jr.; A Longitudinal Crack in a Cylindrical Shell Under International Pressure; International Journal of Fracture Mechanics, Vol. 5, No. 2 (June 1969) pp. 117 to 131.
98. Duncan, M. E., and J. L. Sanders, Jr.; A Circumferential Crack in a Cylindrical Shell Under Tension; International Journal of Fracture Mechanics, Vol. 8 (1972) pp. 15 to 20.
99. Duncan, M. E., and J. L. Sanders, Jr.; The Effect of a Circumferential Stiffener on the Stress in a Pressurized Cylindrical Shell with a Longitudinal Crack; International Journal of Fracture Mechanics, Vol. 5, No. 2 (June 1969) pp. 133 to 155.

100. Sih, G. C., and H. C. Hagendorf; A New Theory of Spherical Shells with Cracks; presented at the Symposium on Thin Shell Structures, California Institute of Technology, Pasadena, California (29 to 30 June 1972).
101. Crichlow, W. J., and R. H. Wells; Crack Propagation and Residual Static Strength of Fatigue-Cracked Titanium and Steel Cylinders; in Fatigue Crack Propagation, ASTM STP 415 (1967) pp. 25 to 70.
102. Crichlow, W. J.; A Systems Approach to Material Selection and Design for Structural Integrity; presented at the Symposium on Crack Propagation of the 7000-Series Aluminum Alloys, McClelland Air Force Base, California (29 to 30 April 1969).
103. Adams, N. J. I.; The Influence of Curvature on Stress Intensity at the Tip of a Circumferential Crack in a Cylindrical Shell; in Damage Tolerance in Aircraft Structures, ASTM STP 486 (1970) pp 39 to 49.

APPENDIX

SYMBOLS AND SUBSCRIPTS

Symbols

a	an appropriate crack length depending on geometry	(inch)
A	cross-sectional area of the stiffener	(inch)
b	an appropriate crack length depending on geometry	(inch)
B	stiffener spacing also Bowie's Factor	(inch) (dimensionless)
c	an appropriate crack length depending on geometry	(inch)
E	Young's modulus	(ksi)
F_{tu}	material ultimate strength	(ksi)
F_{ty}	material tensile yield strength	(ksi)
F_{tys}	tensile yield strength for stiffener material	(ksi)
K	crack tip stress intensity factor	(ksi inch)
K_t	stress concentration factor	(dimensionless)
L	panel length or distance from edge of a hole	(inch)
l	total crack length of a through-the-thickness crack	(inch)
M_p	crack tip plasticity correction factor	(dimensionless)
p	rivet spacing also pressure	(inch) (psi)

Symbols

P	load	(pounds)
r	radius of a circular hole	(inch)
R	radius of the pressure vessel or shell	(inch)
t	sheet or plate thickness	(inch)
W	panel width	(inch)
σ	stress (tensional)	(ksi)
τ	shear stress	(ksi)
ν	Poisson's ratio	(dimensionless)

Subscripts

b	bending or broken
c	critical
cr	critical
e	effective
eff	effective
f	final
m	membrane or middle
net	net section
o	initial, original, or threshold
s	shell, stiffener or stiffened, or side
S	shell
1	Mode 1 or uniaxial or as defined in text
2	Mode 2 or biaxial or as defined in text